Università degli Studi di Torino

Scuola di Dottorato

Exploration of the phase diagram and the thermodynamic properties of QCD at finite temperature and chemical potential with the PNJL effective model with 2+1 flavors

Mario Motta

Università degli Studi di Torino
Scuola di Dottorato

Dottorato in Fisica ed Astrofisica

Exploration of the phase diagram and the thermodynamic properties of QCD at finite temperature and chemical potential with the PNJL effective model with 2+1 flavors

Mario Motta

Tutor:Wanda M. Alberico
Co-tutor: Andrea Beraudo

Introduction

In this PhD-thesis, I show the results of my research project developed in these last three years. This work is focused on the exploration of the QCD phase-diagram with an effective field model called PNJL: Nambu-Jona-Lasinio model with Polyakov Loop interaction. The starting point is Quantum Chromo-Dynamics (QCD), the theory of strong interactions, which is characterized by a non-trivial phase diagram. At ordinary conditions of temperature and density its elementary degrees of freedom, quarks and gluons, are confined into color-singlet objects, the hadrons. Furthermore, while the QCD Lagrangian is invariant under independent rotations of left/right-handed fields in flavor space (chiral symmetry), its ground state is not, chiral symmetry being spontaneously broken and the masses of scalar/pseudoscalar and vector/pseudovector meson multiplets being different.

QCD provides a beautiful tool to investigate the strongly interacting matter and then the smallest structures of the universe. Unfortunately, the most fundamental phenomena, i.e. color confinement and chiral-symmetry breaking, happen at small momentum exchange. The above phenomena occur in the so-called non-perturbative region where perturbation theory fails. Hence we need new tools to investigate these phenomena from the theoretical point of view. For this purpose, several theoretical methods are developed and experimental studies are pursued: lattice-QCD simulations, Effective Field Theory (EFT) calculations, heavy-ion collision experiments and astrophysical observation about neutron stars. In this thesis I focus on the EFT approach, presenting the results obtained with a particular low-energy chiral Lagrangian.

After a general discussion of the main features of QCD, in Sec. 1.5 I introduce the lattice-QCD approach in deeper details. Lattice-QCD simulations indicate that the confinement-deconfinement transition from a hadron gas to a plasma of quarks and gluons (QGP) is actually an analytic crossover at zero/small baryo-chemical potential μ_B, with a transition temperature T_c around 155 MeV. Unfortunately, at non-zero baryon density the lattice-QCD approach does not work. Hence, in order to study the transition in the region of non-vanishing chemical potential one has to rely on effective chiral Lagrangians: in this thesis I focus on the PNJL model, which is introduced in Sec. 3.

From the experimental side, the deconfined and chirally-symmetric phase of QCD is studied through relativistic heavy-ion collisions (HIC's) in experiments carried out at RHIC (BNL) and at the LHC (CERN). After the collision, for a very short time ($\tau \sim 10$ fm/c), one expects to produce a hot fireball of quarks and gluons, which expands and evolves until hadronization into final particles reaching the detectors.

In order to extract information on the active degrees of freedom, on the chemical freeze-out parameters (T_{FO} and μ_{FO}) of the matter produced in the collision and on the possible presence of a Critical End-Point (CEP) in the ($\mu_B - T$) plane (the end-point of the first-order phase transition occurring at large μ_B and relatively small T) several thermodynamic observables are used, described in Sec. 3.2.3. In particular, I discuss in detail the fluctuations of conserved charges (i.e. baryon-number, strangeness and electric charge), which are studied using the above mentioned PNJL effective Lagrangian. The comparison with lattice QCD results is shown in Sec. 4.1.

My thesis is organized as follows. In Chapter 1. I introduce the tools for the investigation of the QCD phase transition and the main features of its phase diagram. In Chapter 2 I provide a general introduction on the phenomenology of heavy-ion collisions. In Chapter 3 the PNJL model is studied, its mean-field equations are solved numerically and used to explore the phase diagram of stron interactions. Finally in Chapter 4 I show the comparisons between Lattice-QCD and the EFT results obtained starting from the PNJL Lagrangian. Finally, in Chapter 5 I draw my conclusions and illustrate possible future developments.

Contents

Chapter 1

Quantum Chromo-Dynamics: symmetries and phase diagram

In this chapter I introduce the basic aspects of Quantum Chromo-Dynamics (QCD), the fundamental theory of strong interactions. In particular I focus on its local and global symmetries and on its non-trivial phase diagram. I also introduce the major theoretical tools to study the latter, i.e. lattice-QCD simulations and Effective Field Theories (EFT).

1.1 The Quantum-Chromo-Dynamics Lagrangian

Today the scientific community agrees that matter is composed of a set of fermions interacting through the exchange of vector bosons. The elementary fermions include leptons and quarks. The bounds state of the latter form the particles feeling the nuclear interaction (hadrons). Quarks interact through electromagnetic, weak and strong interactions. The latter is responsible for nuclear binding and for the interaction of the constituents of nuclei. Its fundamental description is given by Quantum Chromo-Dynamics (QCD).

As in the case of electromagnetism, the guiding principle to describe strong interactions is the concept of *local* gauge invariance. However, at variance with QED, an Abelian gauge group is not sufficient and we need a more complicated one. We know that to build a nucleon we need three quarks. This suggests that we need a triplet instead of a singlet of Dirac fields with respect to some internal symmetry. In partial analogy with QED, we impose that the Lagrangian density is invariant under a local rotation of the triplet Dirac fields belonging to the $SU(3)$ group , i.e.

$$\psi(x) = \begin{pmatrix} \psi_1(x) \\ \psi_2(x) \\ \psi_3(x) \end{pmatrix} , \quad \psi(x) \to V(x)\psi(x), \quad V(x) = \exp\{ig\alpha^a(x)\lambda^a/2\} , \tag{1.1}$$

where α^a are arbitrary functions of x and λ^a are hermitian traceless 3×3 matrices. One constructs then a Lagrangian invariant under this non-Abelian symmetry. The mass term involves the quark bi-linear

$$\bar{\psi}(x)\psi(x) \to \bar{\psi}(x)V^\dagger(x)V(x)\psi(x) = \bar{\psi}(x)\psi(x) \quad \Leftrightarrow \quad V^\dagger(x)V(x) = \mathbb{1} \tag{1.2}$$

and is invariant since $V(x)$ belongs to the $SU(3)$ group.
The kinetic term contains the derivative of the Dirac spinor:

$$\bar{\psi}(x)\partial_\mu\psi(x) \to \bar{\psi}(x)\partial_\mu\psi(x) + \bar{\psi}(x)V^\dagger(x)\partial_\mu V(x)\psi. \tag{1.3}$$

The above expression is not invariant, therefore one adds a term to preserve the symmetry:

$$igA^a_\mu(x)\frac{\lambda^a}{2} \to igV(x)A^a_\mu(x)\frac{\lambda^a}{2}V^\dagger(x) + \partial_\mu V(x)V^\dagger(x), \tag{1.4}$$

where the derivative acts only on $V(x)$. Now, in analogy with QED, one defines the covariant derivative as

$$D_\mu \equiv \partial_\mu - igA^a_\mu(x)\frac{\lambda^a}{2}. \tag{1.5}$$

One gets then the transformation law

$$D_\mu\psi(x) \to V(x)D_\mu\psi(x) \tag{1.6}$$

and one can formally write

$$D_\mu \to V(x) D_\mu V^\dagger(x). \tag{1.7}$$

The matter part of the QCD Lagrangian reads then:

$$\mathcal{L}_{\text{matter}} = \bar{\psi}(x)(i\not{D} - \hat{m})\psi(x) \tag{1.8}$$

and is invariant under *local* $SU(3)$ transformations. Also the Lagrangian for the vector fields A^a_μ must be invariant under gauge transformations. Let us consider the transformation of the gauge field strength

$$F^{\mu\nu} \equiv F^a_{\mu\nu}\frac{\lambda^a}{2} \equiv \frac{i}{g}[D_\mu, D_\nu] \to V(x)[D_\mu, D_\nu]V^\dagger(x), \tag{1.9}$$

where the explicit expression of its components is given by

$$F^a_{\mu\nu} = \partial_\mu A^a_\nu - \partial_\nu A^a_\mu + g f^{abc} A^b_\mu A^c_\nu\ . \tag{1.10}$$

This term is not invariant but the trace of this term is. The latter however vanishes, due to the traceless nature of the λ^a matrices. The first non-trivial gauge-invariant quantity is the trace of the contraction of two field-strength tensors. In analogy with QED, the Lagrangian and the action for the gauge sector read then

$$\mathcal{L}_{\text{YM}} = -\frac{1}{4} F^a_{\mu\nu} F^{a\mu\nu}, \quad S_{\text{YM}} = -\frac{1}{4}\int d^4x F^a_{\mu\nu} F^{a\mu\nu}. \tag{1.11}$$

This is the Yang-Mills Lagrangian and, together with the matter part, it forms the QCD Lagrangian. In order to deal with different flavors of quarks one writes the Dirac spinor as a vector in flavor space. The complete QCD Lagrangian reads then:

$$\mathcal{L} = -\frac{1}{4} F^a_{\mu\nu} F^{\mu\nu a} + \sum_f \bar{\psi}_f (i\not{D} - m_f)\psi_f \tag{1.12}$$

and describes the interaction among quarks mediated by the exchange of vector bosons called gluons. Due to the non-Abelian nature of the theory, the gluons have also a self-interaction.

1.2 Global Symmetries and Conserved charge of QCD

The QCD Lagrangian (1.12), beyond the gauge invariance, has several global symmetries and, as a consequence, it has several conserved charges. In this section we show all the classical global symmetries of the massless QCD Lagrangian and we discuss which ones are conserved at the quantum level. From a general point of view, a global transformation acts at all points of spacetime in the same way. For example:

$$U = \exp\{i\alpha\}, \quad U = \exp\{i\alpha_a \lambda^a\} \tag{1.13}$$

are global rotations by an angle α for several groups of symmetry. In particular, in the QCD case, one can consider transformations that act on flavor space. Furthermore, it is convenient to introduce the left and right components of the Dirac spinors:

$$\begin{aligned} \psi_R &= \frac{1+\gamma^5}{2}\psi, \qquad & \psi_L &= \frac{1-\gamma^5}{2}\psi \\ \overline{\psi}_R &= \overline{\psi}\ \frac{1-\gamma^5}{2}, \qquad & \overline{\psi}_L &= \overline{\psi}\ \frac{1+\gamma^5}{2}\ . \end{aligned} \tag{1.14}$$

The matter part of the QCD Lagrangian (1.8) in the massless case becomes:

$$\mathcal{L}_{\text{matter}} = \overline{\psi}_R(i\not{D})\psi_R + \overline{\psi}_L(i\not{D})\psi_L\ . \tag{1.15}$$

The most general global transformation that leaves the massless QCD Lagrangian unchanged belongs to the following unitary group of transformations in flavor space:

$$U_R(N_f) \otimes U_L(N_f) = U_A(1) \otimes SU_A(N_f) \otimes U_V(1) \otimes SU_V(N_f), \tag{1.16}$$

the elements of this group being of the form

$$U = e^{i\alpha} e^{i\theta_a t^a} e^{i\alpha\gamma^5} e^{i\theta_a t^a \gamma^5}. \tag{1.17}$$

In the following, I focus on the different sectors of the above group of transformations and discuss to which conserved charge each invariance corresponds.

1.2.1 $U_V(1)$

The transformation rule for $U_V(1)$ reads:

$$\psi \to e^{-i\alpha}\psi, \qquad \overline{\psi} \to \overline{\psi} e^{i\alpha} \ . \tag{1.18}$$

The associated Noether current is called $U(1)$ vector current and reads:

$$j^\mu = \overline{\psi}\gamma^\mu\psi, \tag{1.19}$$

leading to the conserved charge

$$Q = \int d^3x j^0 = \int d^3x \ \psi^\dagger\psi = \int d^3x \ [\psi_R^\dagger\psi_R + \psi_L^\dagger\psi_L]. \tag{1.20}$$

The symbol Q represents the classical conserved charge, in this case Q is related to the *baryon-charge* B, in particular $B = Q/3$. The baryon charge is the net number of baryons (i.e. baryons minus anti-baryons) in the system. This quantity is exactly conserved in QCD. In the region of the QCD phase diagram in which quarks are confined into hadrons, the values of the baryon charge of the active degrees of freedom are ± 1 (baryons) or 0 (mesons); in the region where quarks are no longer confined into hadrons the active degrees of freedom carry baryon charge $\pm 1/3$ (quarks) or 0 (gluons). Therefore, this is a very important quantity for the exploration of the QCD phase diagram.

1.2.2 $U_A(1)$

The transformation rule for $U_A(1)$ reads:

$$\psi \to e^{-i\alpha\gamma^5}\psi, \qquad \overline{\psi} \to \overline{\psi} e^{-i\alpha\gamma^5} \ . \tag{1.21}$$

Left and right components are rotated by opposite angles ($\gamma^5\psi_{R/L} = \pm\psi_{R/L}$). $U_A(1)$ invariance is associated to the conservation of the axial charge:

$$Q_A = \int d^3x \; \psi^\dagger\gamma^5\psi = \int d^3x[\psi_R^\dagger\psi_R - \psi_L^\dagger\psi_L]. \tag{1.22}$$

However, though being a symmetry of the classical QCD action, $U_A(1)$ is not a symmetry of the theory, being broken by quantum fluctuations. Hence, the axial charge Q_A is not conserved. Quantum anomalies of the axial currents are responsible for the $\pi^0 \to \gamma\gamma$ decay and for the anomalously large mass of the pseudoscalar meson η'.

1.2.3 $SU_V(N_f)$

This symmetry corresponds to the invariance under the following transformation

$$\psi \to e^{i\theta_a t^a}\psi, \qquad \overline{\psi} \to \overline{\psi}e^{-i\theta_a t^a}, \quad \text{with} \quad t^a = \tau^a/2. \tag{1.23}$$

Here the τ^a matries belong to $\mathcal{SU}(N_f)$ algebra. In the simplest case, $N_f = 2$, they are the Pauli matrices. The conserved charges read:

$$Q_V^a = \int d^3x \; \psi^\dagger\frac{\tau^a}{2}\psi = \int d^3x[\psi_R^\dagger\frac{\tau^a}{2}\psi_R + \psi_L^\dagger\frac{\tau^a}{2}\psi_L]. \tag{1.24}$$

In the $N_f = 2$ case, these charges play the role of generators of isospin rotations. The latter is a symmetry of the Lagrangian and of the theory: the QCD vacuum and particle spectrum are invariant under isospin transformations. Isospin symmetry is only sligthly broken by the small mass difference of u and d quarks.

1.2.4 $SU_A(N_f)$

The transformation rule for $SU_A(N_f)$ rotations reads:

$$\psi \to e^{-i\theta_a t^a\gamma^5}\psi \quad , \quad \overline{\psi} \to \overline{\psi}e^{-i\theta_a t^a\gamma^5}. \tag{1.25}$$

The R and L components are rotated by opposite angles. The classical conserved charges are called *chiral charges* and read

$$Q^a_A = \int d^3x \; \psi^\dagger \frac{\tau^a}{2}\gamma^5\psi = \int d^3x \; [\psi^\dagger_R \frac{\tau^a}{2}\psi_R - \psi^\dagger_L \frac{\tau^a}{2}\psi_L]. \tag{1.26}$$

This symmetry of the Lagrangian is not realized in nature: the QCD vacuum is not invariant under chiral rotations. This phenomenon is known as spontaneous (or dynamical) chiral symmetry breaking. The chiral charges, applied to the QCD vacuum do not annihilate it, but create the pseudoscalar mesons, which can be considered the Goldstone bosons of QCD, associated to the spontaneous breaking of chiral symmetry. In the high-temperature/density region of the QCD phase diagram, a phase transition occurs and chiral symmetry gets restored. In this work, I will focus on the study of baryon-number fluctuations around the chiral-restoration transition.

1.3 Asymptotic freedom

From the QCD Lagrangian (1.12) one easily realizes that the coupling constant between fermions and vector bosons is dimensionless, thus implying that QCD is a renormalizable theory. The divergent diagrams are usually regularized through dimensional regularization, as in QED.

The Callan-Symanzik β-function, which describes the evolution of the coupling as a function of the energy scale μ, $\beta(g) = \frac{dg}{d\ln\mu}$ is given by:

$$\beta(g) = -\frac{b_0}{(4\pi)^2}g^3, \quad b_0 = 11 - \frac{2}{3}n_f, \tag{1.27}$$

here written for the $SU(3)$ gauge group and at the one-loop approximation. The overall minus sign implies that, for sufficiently small N_f , the theory is asymptotically free, i.e. that the running coupling tends to zero at large momenta according to

$$\alpha_s(Q) = \frac{\alpha_s(\mu)}{1 + \frac{b_0}{2\pi}\alpha_s(\mu)\ln\left(\frac{Q}{\mu}\right)} \tag{1.28}$$

where $\alpha_s \equiv g^2/4\pi$. As shown in Fig.1.1, at high momenta Q α_s is small, while at low momenta α_s is big and there exists a value of Q where the coupling becomes in principle infinitely large. This values of Q is called $\Lambda_{QCD} \sim 200$ MeV. Notice that this divergence of the coupling at low-momentum scale should be interpreted as a shortcoming of the one-loop perturbative calculation as α_s gets too large.

In QED the running of the electromagnetic coupling is due to the polarization of the vacuum stemming from the virtual electron-positron pair creation and this causes the effective electric charge to decrease at large distances. In QCD, according to Eq. (1.27), the fermions still produce such an effect, but there are additional corrections due to the gluons self-interaction. Accordingly, the net effect of gluons is opposite in sign. Eq. (1.28) implies that the coupling becomes strong at low momenta. Λ_{QCD} defines the boundary between the high energy $Q >> \Lambda_{QCD}$ (short distance) regime – in which the coupling is weak and perturbative calculations are possible – and a low

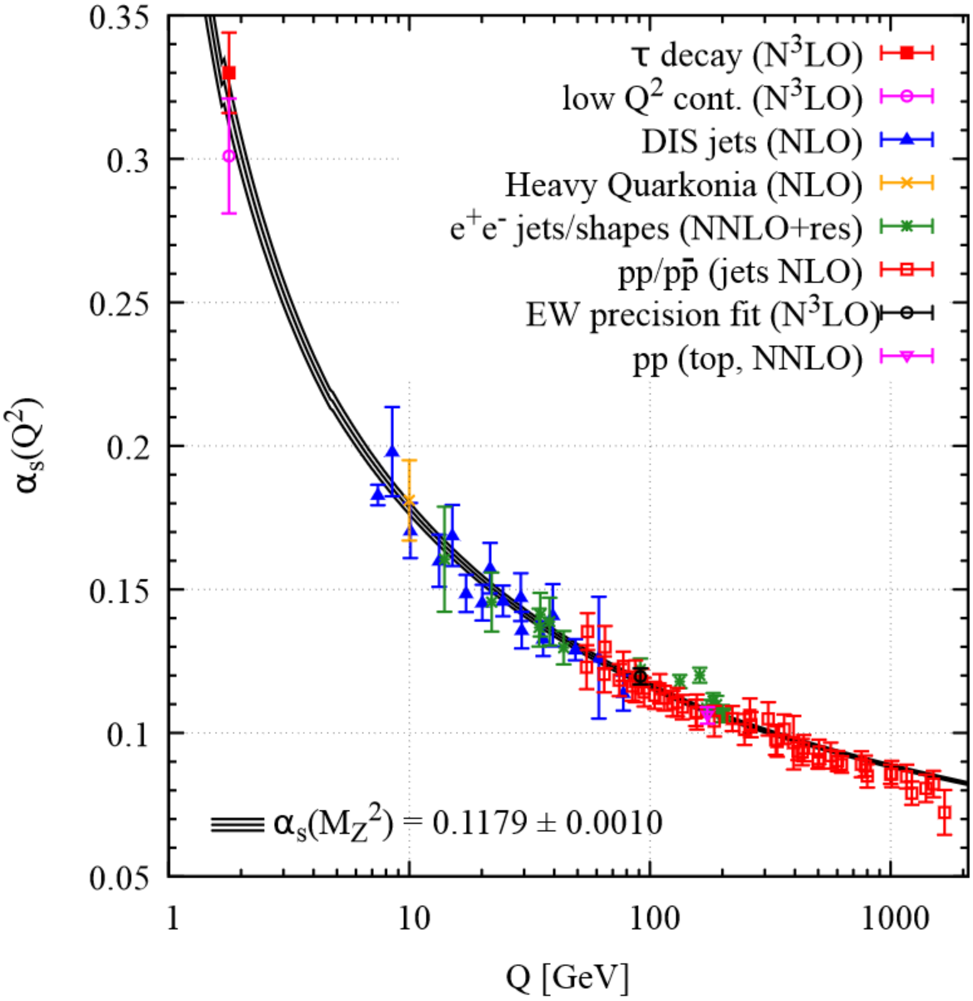

Figure 1.1: Summary of measurements of α as a function of the energy scale Q. The respective degree of QCD perturbation theory used in the extraction of α is indicated in brackets (NLO:next to leading order; NNLO: next to next to leading order; NNLO+res.: NNLO matched to are summed calculation; N^{3}LO: next to NNLO) [12].

energy $Q \lesssim \Lambda_{QCD}$ domain in which the coupling is strong and the theory displays a non-perturbative behavior. The most striking non-perturbative phenomenon is surely the confinement of quarks and gluons into color-singlet hadrons. There are interesting attempts to relate confinement to particular topological objects in the QCD vacuum, like monopoles or vortices, but it is fair to say that confinement is not yet fully understood. To investigate these phenomena other approaches have been developed like Lattice-QCD calculations and Effective Fields Theories. In the next sections, we outline these two approaches.

1.4 Phase diagram of QCD

The phase diagram of QCD is divided into two interesting regions. There is a “confined region”, in which one finds the ordinary hadronic matter composed of hadrons and, at high baryon density ($\sim 0.17\mathrm{fm}^{-3}$), of atomic nuclei. In this region, the elementary particles (quarks and gluon) are confined into hadrons. At higher temperature and/or baryon density the strongly interacting matter is deconfined. In this phase, quarks and gluons are not constrained into color-neutral hadrons but they are free to move, diffusing up to distances much larger then a typical hadronic size ($\sim$ 1 fm). From lattice-QCD we know that, at vanishing or small baryochemical potential, the phase transition is actually a crossover [52]; on the other hand at higher chemical potentials, one argues that the transition is of the first order, ending with a Critical End-Point (CEP). In figure 1.2 is show a schematic picture of QCD phase diagram. Unfortunately, lattice-QCD simulations cannot be extended to the

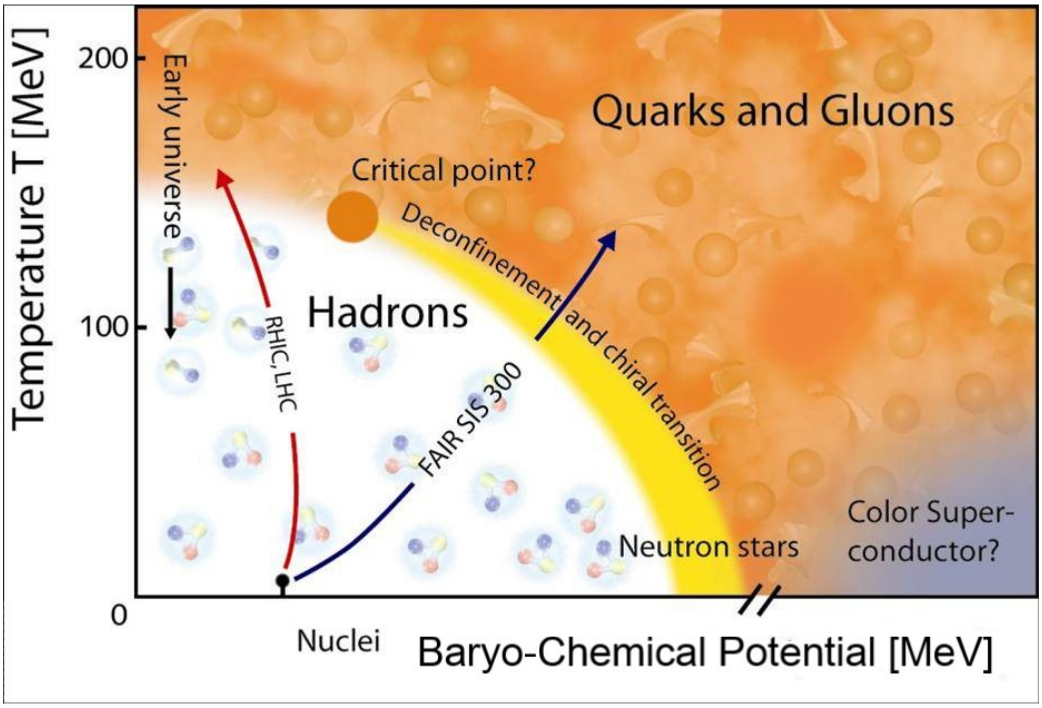

Figure 1.2: A schematic picture of the QCD phase-diagram elaborated from the picture of Ref [11].

region of high chemical potential, due to the sign problem: in the presence of light dynamical quarks, for non-vanishing baryon density, the euclidean QCD action, after performing the functional integral over the fermionic field, gives rise to a complex determinant which prevents the Monte Carlo sampling of the gauge field configurations. Due to this fact, it is necessary to use effective models to investigate the phase transition in this region. This approach, of course, can provide a nice qualitative picture, but quantitative prediction must be taken with caution.

There are two ways of producing a deconfined system of quarks and gluons. The first one is to excite matter to extremely high temperatures: this is what is realized in the experiments at the nuclear colliders RHIC and LHC. The second one is to "pack" nucleons into very dense regions so that they start overlapping and their partons are no longer confined into a single nucleon: this is what may occur in the core of neutron stars.

1.5 Lattice QCD

Lattice QCD (lQCD) calculations are a non-perturbative implementation of field theory using the Feynman path-integral approach. The starting point is the partition function in Euclidean space-time [48]. In lattice-QCD the 4-dimensional Euclidean space-time is discretized and it is replaced by a 4-dimensional lattice whose spacing provides a natural ultraviolet regularization of the theory. Such a partition function reads

$$Z = \int \mathcal{D}A_\mu \mathcal{D}\psi \mathcal{D}\overline{\psi}\ e^{-S_E}\ . \tag{1.29}$$

Here S_E is the QCD Action in a Euclidean space-time, in which the temporal dimension has undergone a Wick rotation:

$$t \rightarrow -i\tau, \quad A_0 \rightarrow iA_4\ . \tag{1.30}$$

The expectation values of physical observables can be calculated in the usual way:

$$\langle \mathcal{O} \rangle = \frac{1}{Z} \int \mathcal{D}A_\mu \mathcal{D}\psi \mathcal{D}\overline{\psi}\ \mathcal{O} e^{-S_E}\ . \tag{1.31}$$

The key of Lattice QCD is that the path integral is evaluated on a discretized Euclidean space-time and one can perform the computations of expectation values via a Montecarlo algorithm.

In 1974 Wilson formulated Euclidean gauge theories on the lattice as a tool to study confinement and carried out a non-perturbative analysis of QCD. The numerical implementation of the path-integral approach requires the following five steps:

- the discretization of space-time with lattice unit a: the lattice spacing;
- the transcription of the gauge and fermionic degrees of freedom;
- the construction of the action;
- the definition of the integration measure in the path integral;
- the transcription of the operators used to probe the physics.

Of these, the construction of the action and of the operators are the most complex ones.
A point of the grid is called vertex and a line between two points is called link. The vertex n is connected to the vertex $n+\hat{\mu}$ ($\hat{\mu}$ being the selected direction) by the operator:

$$U_\mu(n) = e^{iagt^a\mathcal{A}^a_\mu(n)}. \tag{1.32}$$

In this formula a is the lattice spacing, g is the coupling constant, t^a are the generator of the $SU(N)$ group ($N=3$ in QCD) and $\mathcal{A}^a_\mu$ are the components of the gauge field.

1.5.1 Yang-Mills action on the lattice

What is the gauge action in the case of the $SU(N)$ group? This section stretches its derivation and shows how, in the continuum limit, this action correctly reproduces the Yang-Mills action. The discretized action must be invariant under gauge transformations. The simplest one is the Wilson action:

$$S_W = -\frac{1}{g^2}\sum_{n,\mu\nu}\mathrm{Re}\{\mathrm{Tr}[U_{\mu\nu}(n)]\}, \tag{1.33}$$

where $U_{\mu\nu} \equiv U_{-\nu}(n)U_{-\mu}(n+\nu)U_\nu(n+\mu)U_\mu(n)$, with the link variable defined in Eq. (1.32). This action is invariant under local gauge transformations due to the trace over the color degrees of freedom. It is defined on the smallest path on the lattice: the plaquette. The plaquettes are "squares" of side a. It is possible to define:

$$U_\mu \equiv e^{iB_\mu(n)} \quad \text{with} \quad B_\mu(n) \equiv agt^a\mathcal{A}^a_\mu(n), \tag{1.34}$$

where a is the lattice spacing, g the coupling constant and $\mathcal{A}^a_\mu$, in the continuum limit, will become the standard vector gauge field of the Yang Mills theory. One may expand the fields appearing in the Wilson action keeping only terms up to order a^2 (B being of order a) as follows:

$$B_\nu(n+\mu) \sim B_\nu(n) + a\nabla_\mu B_\nu \tag{1.35}$$

$$B_{-\mu}(n+\nu) \equiv -B_\mu(n+\nu) \sim -B_\mu(n) - a\nabla_\nu B_\mu, \tag{1.36}$$

where $\nabla_\nu f(n) \equiv \frac{f(n+\nu)-f(n)}{a}$ is the finite-difference derivative on the lattice, whose continuum limit is the partial derivative. From the above expression one obtains:

$$U_{\mu\nu} \sim e^{-iB_\nu(n)} e^{-i(B_\mu(n)+a\nabla_\nu B_\mu(n))} e^{i(B_\nu(n)+a\nabla_\mu B_\nu(n))} e^{iB_\mu(n)}. \tag{1.37}$$

Now one can apply the Baker-Campbell-Hausdorff formula; keeping in the exponent only terms up to $O(a^2)$ one finds:

$$U_{\mu\nu}(n) \sim e^{\{ia(\nabla_\mu B_\nu - \nabla_\nu B_\mu)+[B_\mu,B_\nu]\}} \equiv e^{ia^2 g F_{\mu\nu}}. \tag{1.38}$$

In the above the $F_{\mu\nu}$ tensor is defined as before:

$$F_{\mu\nu} \equiv \nabla_\mu A_\nu - \nabla_\nu A_\mu - ig[A_\mu, A_\nu] \tag{1.39}$$

and $A_\mu \equiv t^a \mathcal{A}^a_\mu$. After inserting this result into Eq. (1.33) and expanding in powers of a, one finds:

$$S_W \sim -\frac{1}{g^2}\sum_{n,\mu\nu} \mathrm{Re}\ \mathrm{Tr}\Big(1 + ia^2 g F_{\mu\nu} - \frac{1}{2}a^4 g^2 F_{\mu\nu}F_{\mu\nu}\Big) \tag{1.40}$$

One can always normalize the $SU(N)$ generators to satisfy

$$\mathrm{Tr} t^a = 0 \qquad \mathrm{Tr}(t^a t^b) = \frac{1}{2}\delta^{ab}. \tag{1.41}$$

while $\mathrm{Tr}\mathbb{1}$ gives only an irrelevant constant which can be neglected. In this way one obtains

$$S_W = \frac{a^4}{4}\sum_{n,\mu\nu} F^a_{\mu\nu}F^{a,\mu\nu}. \tag{1.42}$$

In the $a \to 0$ limit one can set $\sum_n \to \int \frac{d^4x}{a^4}$ (for a 4-dimensional lattice) obtaining:

$$S_W \to \frac{1}{4} \int d^4x F^a_{\mu\nu} F^{a,\mu\nu}. \tag{1.43}$$

Hence, in the continuum limit one recovers the euclidean Yang-Mills action. The minus sign in front of the integral in Eq.(1.11) disappears due to the rotation in the Euclidean space-time. One can conclude that the Wilson action is the right action for the gauge fields on the lattice.

1.5.2 Lattice-QCD at $T = 0$

The Wilson action in Eq. (1.33), which reduces to the standard Yang-Mills action in the continuum $a \to 0$ limit, can be used to perform a Montecarlo sampling of the different gauge-field configurations, getting then the expectation value of the various observables of interest. Nowadays, for instance, lattice-QCD calculations successfully describe the hadron spectrum.

For the purpose of the present thesis, the main interest in lQCD results concerns the confinement of quarks, for which there is experimental evidence, but no first-principle theoretical derivation. For this purpose, the quantity to evaluate on the lattice is the Wilson loop, defined as

$$W_\gamma = \mathrm{Tr} \prod_{\mu,\nu \in \gamma} U_{\mu\nu}. \tag{1.44}$$

Here γ denotes the considered loop drawn in figure 1.3, followed in counterclockwise direction, and the group elements are ordered as they are encountered in going around the contour. The Wilson Loop is gauge invariant due to the trace over color degrees of freedom. The simplest non-trivial Wilson Loop is the plaquette. The Wilson Loop essentially measures the response of the gauge fields to an external quark-like source passing around its perimeter. For a time-like loop, this represents the production of an infinitely heavy quark-antiquark pair at the earliest time separated by the distance R and then annihilating at the latest time. If the loop is a rectangle of side T in the time direction and R in the space direction, a transfer matrix argument

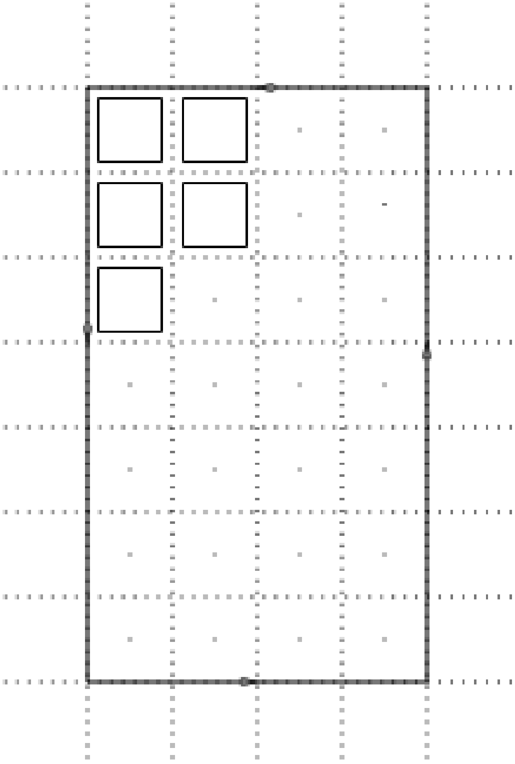

Figure 1.3: Sketch of a Wilson Loop on the lattice grid. The thick line is the chosen γ contour, the thin lines represent the plaquettes and the dashed lines the grid.

suggests that, for large T, one has for its expectation value the asymptotic behavior

$$\langle W(R,T)\rangle \underset{T\to\infty}{\sim} \exp(-V(R)T), \tag{1.45}$$

allowing one to identify the quark-antiquark potential $V(R)$. If the interquark energy for large separation grows linearly $V(R) \underset{R\to\infty}{\sim} \sigma R$, then the expectation value of the Wilson Loop becomes:

$$\langle W(R,T)\rangle \underset{T\to\infty}{\sim} \exp(-\sigma RT). \tag{1.46}$$

It decays with the exponential of the area with a coefficient given by the "string tension" σ of the linear part of the potential. Physically, this area law represents the action of the world sheet of a flux tube connecting the quark-antiquark sources. Exploiting Eq. (1.45) one can extract the $Q\bar{Q}$ potential from the expectation value of the Wilson loop:

$$V(R) = -\lim_{T\to\infty}\frac{1}{T}\ln\langle W(R,T).\rangle \tag{1.47}$$

The results of this calculation for infinitely massive quark are shown in Fig.1.4. The $Q\bar{Q}$ potential at large r is linear in r. Quarks are confined, since it would cost an infinite amount of energy to pull the two heavy quarks far apart. In the real world, as the $Q\bar{Q}$ separation increases above a given value, it becomes energetically more convenient to excite a light $q\bar{q}$ pair from the vacuum, so that quarks are always confined inside color-neutral mesons.

1.5.3 Lattice-QCD at finite Temperature

One can study QCD on the lattice also at finite temperature. For this purpose, one can use the statistical mechanics approach in the Grand-Canonical Ensemble, where the system is taken at finite temperature T and in a finite spatial volume V [61]. We start considering the case of vanishing baryochemical potential, $\mu_B = 0$. For this purpose, one formally starts from the partition function (here written for the $\mu_B\!=\!0$ case)

$$Z = \mathrm{Tr}e^{-H/T} = e^{-\Omega/T} \tag{1.48}$$

where H is the QCD Hamiltonian and Ω is the grand-canonical thermodynamic potential. For vanishing baryochemical potential the latter coincides with the free energy F. Other thermodynamics quantities follow by differentiation of Ω with respect to T or μ_B.

One can interpret the QCD partition function as a path-integral where the temporal dimension is compactified and its finite extension is set by the inverse temperature $\beta \equiv 1/T$, imposing appropriate (anti-)periodicity

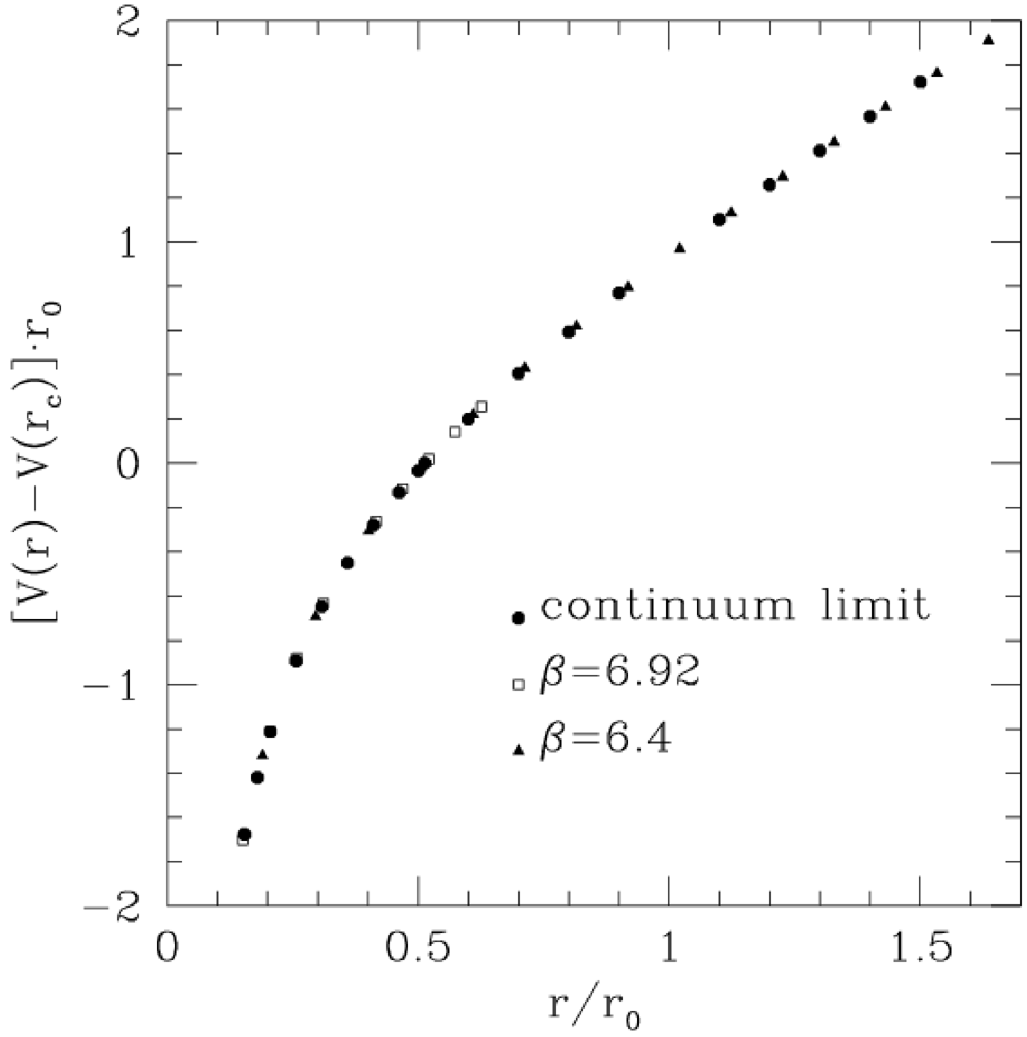

Figure 1.4: $Q\bar{Q}$ potential as a function of the distance [55]

conditions on the fields at $\tau = 0, \beta$. One has:

$$\mathrm{Tr}e^{-\beta H} = \int \mathcal{D}\overline{\psi}\mathcal{D}\psi\mathcal{D}A_\mu \exp\left\{ - \int_0^\beta d\tau \int d^3x \; \mathcal{L}[\psi, \overline{\psi}, A_\mu]\right\} . \tag{1.49}$$

In the lattice time direction $\beta \equiv N_\tau a$ (N_τ being the number of temporal links), whose length plays the role of the inverse temperature, and one imposes periodic boundary conditions for the link variables:

$$U_\mu(x, y, z, 1) \equiv U_\mu(x, y, z, N_\tau + 1). \tag{1.50}$$

A particularly interesting Wilson line in the $T \neq 0$ case is the Polyakov loop (a closed loop around the temporal direction), defined as

$$L \equiv \frac{1}{N_c} \mathrm{Tr}\, \mathcal{P} \prod_{t=1}^{N_\tau} U_4(x, y, z, t). \tag{1.51}$$

It is gauge invariant due to the trace in color space. The periodic boundary conditions on the link variable entail $U_4(x, y, z, N_\tau + 1) = U_4(x, y, z, 1)$. Physically, its expectation value is related to the free-energy change of the system after adding an isolated quark into thermal bath:

$$\langle L \rangle = e^{-\Delta F_Q / T}. \tag{1.52}$$

The possibility of having isolated charges in the theory requires a finite value of ΔF_Q and hence a non-vanishing expectation value of the Polyakov loop. On the other hand, in the confined phase $\Delta F_Q \to \infty$ and hence $\langle L \rangle = 0$. In addition to gauge invariance, $SU(N)$ gauge theories have a global $\mathbb{Z}_N$ invariance. It consists in multiplying all links on a given time slice by the same element $z \equiv e^{i \frac{2\pi}{N} k}$ of $\mathbb{Z}_N$. Such a transformation does not change the action since the latter is expressed in term of plaquettes, which are invariant under $\mathbb{Z}_N$. However, a non-vanishing expectation value of the Polyakov loop, $\langle L \rangle \neq 0$, gives rise to spontaneous breaking of the $\mathbb{Z}_N$ symmetry since the latter is not invariant, having $\langle L \rangle \to z \langle L \rangle$. Thus, in the case of $SU(N)$ pure gauge theory (light quarks explicitly break $\mathbb{Z}_N$ symmetry) $\langle L \rangle$ can be used as an order parameter for the transition to the deconfined phase.

On the lattice it is also possible to study the spontaneous breaking and restoration of chiral symmetry, whose order parameter is the chiral condensate $\langle \overline{\psi} \psi \rangle$. This physical observable reflects the correlation between quarks and anti-quarks. In the confined region the correlations are very strong, the expectation value of the chiral condensate is large and chiral symmetry is broken; on the contrary, in the deconfined region quarks and anti-quarks are uncorrelated and the expectation value of the chiral condensate is low or null.

In Fig.1.5 I show the expectation values of the Polyakov loop $\langle L \rangle$ and the normalized difference of light and strange quark chiral condensates defined as:

$$\Delta_{l,s}(T) = \frac{\langle\overline{\psi}\psi\rangle_l(T) - m_l/m_s\langle\overline{\psi}\psi\rangle_s(T)}{\langle\overline{\psi}\psi\rangle_l(T=0) - m_l/m_s\langle\overline{\psi}\psi\rangle_s(T=0)}\ . \tag{1.53}$$

The plots show that the deconfinement and chiral restorations occur in the same range of temperatures as a smooth crossover.

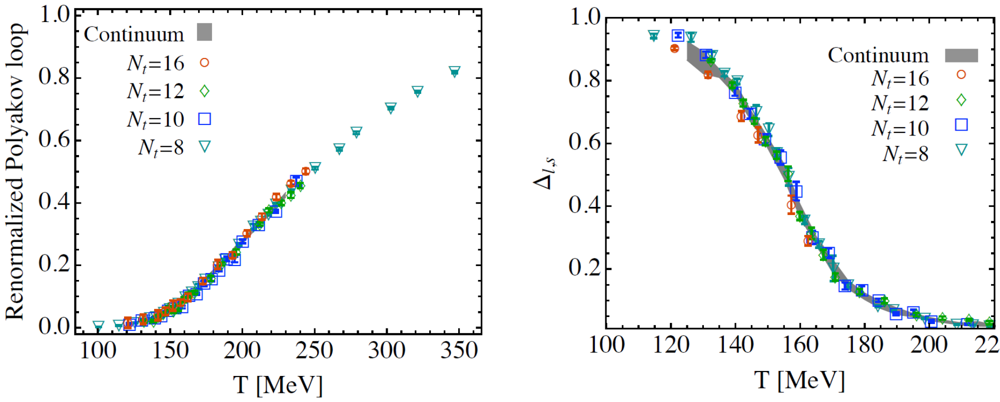

(a) (b)

Figure 1.5: Renormalized Polyakov loop as a function of the temperature (left panel). Subtracted chiral condensate $\Delta_{l,s}$ defined in Eq. (1.53) (right panel). In both figures, the different symbols correspond to different N_τ =8, 10, 12, 16. The grey band is the continuum limit [13].

1.5.4 Lattice-QCD at finite chemical-potential

For the study of compact stars and of heavy-ion collisions at lower center-of-mass energy, one has to explore the QCD phase-diagram at finite baryon density. In the Grand-Canonical Ensemble, this requires setting a non-vanishing value for the baryochemical potential. The corresponding grand-canonical partition function is given by:

$$Z = \mathrm{Tr} e^{-(H-\mu N)/T} = e^{-\Omega/T}\ . \tag{1.54}$$

From Eq. (1.54) one can see that the chemical potential plays the role of an imaginary part of the gauge fields A_4. It means that the Euclidean action becomes complex and hence it is not possible to compute the path-integral through a Montecarlo sampling algorithm. This problem is called *sign problem.* In this paragraph we show various attempts to bypass the sign problem in lQCD.

Taylor Expansion

The simplest idea to bypass the sign problem is to perform a Taylor expansion of the pressure in powers of μ/T around $\mu = 0$. The coefficients of the expansion can be calculated using conventional simulations at $\mu = 0$, where the sign problem is absent [28].

The pressure is related to the grand-canonical partition function by the usual equation

$$p = \frac{T}{V} \ln Z. \tag{1.55}$$

Due to the CPT symmetry, the pressure is an even function of the chemical potential. Hence, its Taylor expansion written in dimensionless form contains only even powers of (μ/T) and one has:

$$\frac{p(\mu,T)}{T^4} = \frac{p(\mu=0,T)}{T^4} + \sum_{n=1}^{+\infty} \frac{c_{2n}(T)}{(2n)!} \left(\frac{\mu}{T}\right)^{2n} \tag{1.56}$$

where the coefficients of the expansion are given by

$$c_{2n}(T) = \left.\frac{\partial^{2n} p(\mu,T)/T^4}{\partial(\mu/T)^{2n}}\right|_{\mu=0}. \tag{1.57}$$

These coefficients can be identified with the cumulants of the baryon-number distribution that we will meet in Sec. 3.3.1 studying event-by-event thermal fluctuations of conserved charges. For the first coefficients one has

$$\begin{aligned} c_1 &= \langle N \rangle|_{\mu=0} = 0 \\ c_2 &= (\langle N^2 \rangle - \langle N \rangle^2)_{\mu=0} = \langle N^2 \rangle|_{\mu=0}, \quad c_3 = 0 \\ c_4 &= \langle N^4 \rangle|_{\mu=0} - 3\langle N^2 \rangle^2|_{\mu=0} \end{aligned} \tag{1.58}$$

In Sec. 4.1 I will present a comparison between the lattice data and the results obtained in the effective models used in this work. The number of terms contributing to c_{2n} is proportional to the number of ways one can obtain $2n$ summing numbers $\leq 2n$, hence they grow very rapidly going to higher-order cumulants. Many of these terms are null but going to higher orders the Taylor expansion approach requires in any case the calculation of a large amount of terms. For example, in c_8 there are 27 terms and 5 of these are not null and the calculation takes very long time (see [46] for the details). Thus, the Taylor series is usually truncated at the $6^{\text{th}} - 8^{\text{th}}$ term. In summary the idea is simple, but the approach is limited to a region of the phase diagram in which μ/T is sufficiently small and does not allow to obtain information concerning the existence and location of the Critical End-Point.

Imaginary chemical potential

From the considerations written at the beginning of this section, it is clear that for an imaginary chemical potential the sign problem would disappear. One can thus set $\mu = i\mu_I$ and perform ordinary simulations employing importance sampling. In particular, one can obtain the transition line $T_c(\mu_I)$ at imaginary μ. Treating μ as a complex parameter, the transition line for real μ can then be obtained by analytic continuation. Since T_c is even in μ, this is particularly straightforward and amounts to map $\mu_I^2 \to -\mu^2$. Hence one can follow these steps, as illustrated in Fig. 1.6 from Ref. [4]:

- determine the phase boundary at $\mu^2 < 0$;
- parametrize and fit $T_c(-\mu^2)$
- obtain the phase boundary at $\mu^2 > 0$.

This approach has been carried out during the past decade in great detail. However, it turns out that at imaginary μ QCD has quite an intricate phase structure and that the topic is much richer than just applying analytical continuation around $\mu^2 \sim 0$.

In both the approaches we have just described (Taylor expansion and imaginary chemical potential), one can compute physical observables at non-

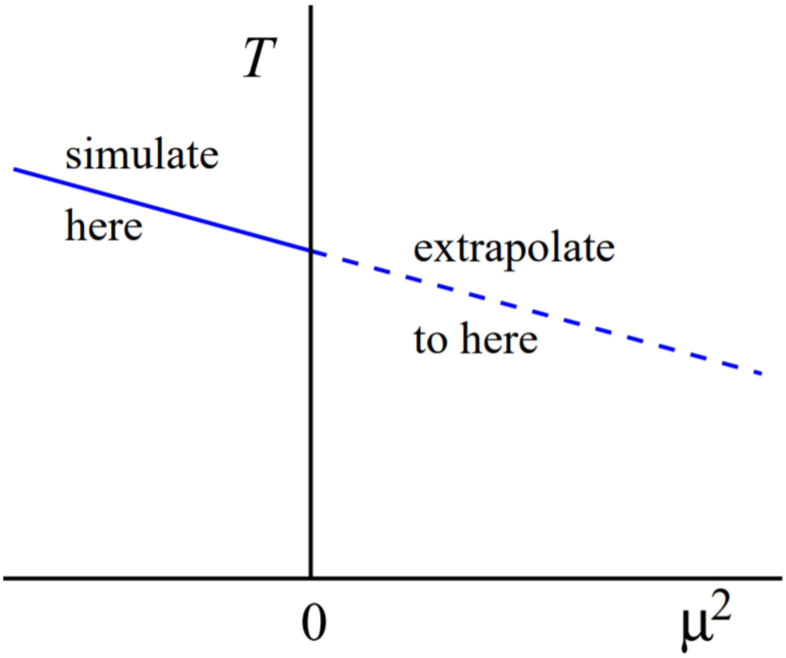

Figure 1.6: Phase boundary around $\mu^2 = 0$ in the $T - \mu^2$ plane [4].

vanishing chemical potential. However, lattice calculations are available only in a quite limited region of the phase diagram, for small values of μ/T. Beyond these two approaches there are further independent proposals to bypass the sign problem: for more details see Ref. [4].

1.6 Effective Field Theory

In this section I intoduce the basic ideas of Effective Field Theories and I show two notable examples of chiral effective models: the linear sigma model and the Nambu-Jona-Lasinio model. The second one is very important for the rest of this work, because it is the starting point for a more advanced implementation I am going to use.

The basic idea of an Effective Field Theory (EFT) is that, if one is interested in describing phenomena occurring to a certain (low) energy scale, one does not need to solve the exact microscopic theory in order to provide useful predictions. In general, Effective Field Theories are low-energy approximations of more fundamental theories. Instead of solving the underlying theory, low-energy physics is described with a set of variables that are suited to the particular energy region one is interested in. For example, one can use pions and nucleons instead of the more fundamental quarks and gluons as degrees of freedom in low-energy processes in hadronic and nuclear physics. This approach is more convenient since so far we do not know how to solve QCD in its non-perturbative domain, i.e. for energy scales below 1 GeV [63].

1.6.1 Linear Sigma-model

Section 1.2 deals with chiral symmetry in full generality. This section is focused on a specific model referring to the $N_f = 2$ case (for the 3-flavour case see Ref. [82]): the linear σ model.

First of all one introduces the current operators (expressed in terms of quark fields) having the quantum number to create/destroy the different light mesons (pion, sigma, rho and a_1):

$$\vec{\pi} = i\bar{\Psi}\vec{\tau}\gamma^5\Psi \qquad \sigma = \bar{\Psi}\Psi \qquad \vec{\rho} = i\bar{\Psi}\vec{\tau}\gamma^\mu\Psi \qquad \vec{a_1}^\mu = \bar{\Psi}\vec{\tau}\gamma^\mu\gamma^5\Psi\ . \tag{1.59}$$

Applying a $SU_A(N_f)$ transformation one gets:

$$\vec{\pi} \to \vec{\pi} - \vec{\theta}\sigma \quad \sigma \to \sigma + \vec{\theta}\cdot\vec{\pi} \quad \vec{\rho} \to \vec{\rho^\mu} + \theta \times \vec{a_1}^\mu \quad \vec{a_1}^\mu \to \vec{a_1}^\mu + \vec{\theta} \times \rho^\mu\ . \tag{1.60}$$

Scalar/pseudoscalar and vector/pseudovector mesons are mixed by chiral transformations. In Sec. 1.2 I showed that the QCD Lagrangian is invariant under $SU_A(N_f)$ transformations. However, such a chiral invariance is not found in the spectrum ($m_\pi \neq m_\sigma$ and $m_\rho \neq m_{a_1}$): the symmetry is spontaneously broken. In order to obtain a Lagrangian invariant under isospin and chiral transformations $SU_V(2) \times SU_A(2)$, one must take a potential of the form $V = V(\vec{\pi}^2 + \sigma^2)$. In the linear sigma-model, for the latter one chooses:

$$V(\vec{\pi}^2 + \sigma^2) = \frac{\lambda}{4}(\pi^2 + \sigma^2 - f_\pi^2)^2, \tag{1.61}$$

where $\vec{\pi}$ and σ will be interpreted as the pion and sigma fields and f_π is a parameter of the potential which can be identified with the pion decay constant. This potential is by construction invariant under chiral rotations. The mesonic Lagrangian reads then

$$\mathcal{L}_\sigma = \frac{1}{2}(\partial_\mu \vec{\pi} \cdot \partial^\mu \vec{\pi} + \partial_\mu \sigma \cdot \partial^\mu \sigma) - V(\vec{\pi}^2 + \sigma^2) \ . \tag{1.62}$$

Nucleons can be introduced and coupled to mesons preserving the $SU_V(2) \times SU_A(2)$ symmetry:

$$\mathcal{L}_\sigma^\Psi = i\bar{\Psi}\partial\!\!\!/\Psi - g_\pi \bar{\Psi}[i\gamma^5 \vec{\pi} \cdot \vec{\tau} + \sigma]\Psi \ , \tag{1.63}$$

where $\Psi \equiv (p, n)^T$ and g_π is the coupling constant between nucleons and mesons. They are introduced into the Lagrangian as massless fields, in order not to break chiral symmetry explicitly. The potential in Eq. (1.61) breaks chiral symmetry spontaneously (see Fig. 1.7). In fact, the latter displays a continuous set of minima that form a circle in the $\pi - \sigma$ plane: $\vec{\pi}^2 + \sigma^2 = f_\pi^2$. Nature chooses one of these minima and this spontaneously breaks the $SU_A(2)$ symmetry. One can define the meson fields in order for the minimum of the potential to lie at $\vec{\pi} = 0$ and $\sigma = f_\pi$. Fluctuations around the minimum are then performed,

$$\sigma \to f_\pi + s \qquad \vec{\pi} \to \vec{\pi}, \tag{1.64}$$

and allow one to find the masses of scalar and pseudoscalar mesons. The

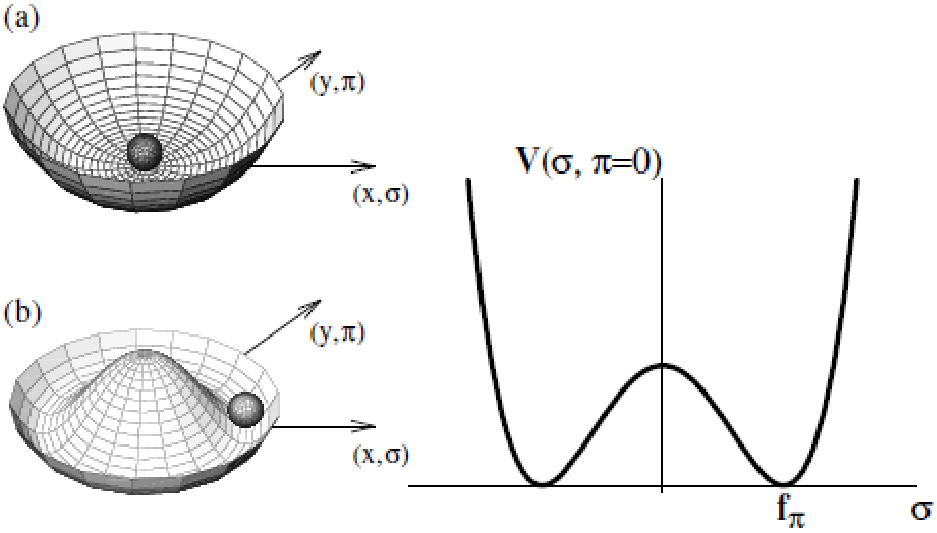

Figure 1.7: The potential responsible for chiral-symmetry breaking.

linear and constant terms in the fluctuations vanish and one gets

$$V = \frac{1}{2}(2\lambda f_\pi^2)s^2 + \lambda f_\pi s(\pi^2 + s^2) + \frac{\lambda}{4}(\pi^2 + s^2)^2 \ . \tag{1.65}$$

As one can see pions remain massless (there is no quadratic term in $\vec{\pi}$) and they are accordingly interpreted as Goldstone bosons. On the other hand the σ-meson gets a mass: $m_\sigma^2 = 2\lambda f_\pi^2$. Within the linear sigma model the nucleons, initially massless, get a mass from chiral-symmetry breaking:

$$\mathcal{L}_\sigma^\Psi = \bar{\Psi}[i\partial\!\!\!/ - M_n]\Psi - g_\pi \bar{\Psi}[i\gamma^5 \vec{\pi}\cdot\vec{\tau} + s]\Psi, \tag{1.66}$$

where $M_n = f_\pi g_\pi$ is the mass acquired by nucleons. Actually, in the Standard Model quarks are coupled to the Higgs field. Hence, due to this Yukawa coupling, after the electroweak symmetry-breaking also up and down quarks acquire a small mass. Hence the linear sigma model Lagrangian must contain a small term reflecting this explicit breaking of chiral symmetry. Nevertheless, the non-vanishing mass of light quarks produces only a small correction to the nucleons mass: around 95% of the nucleons mass is due to chiral symmetry breaking. It is now clear that chiral-symmetry restoration/breaking is a very important phenomenon to explore and one needs to develop the theoretical tools to investigate it.

1.6.2 Nambu-Jona-Lasinio Model

Today QCD has been accepted as the fundamental theory of strong interactions. Due to asymptotic freedom, predictions are possible in the kinematic range of large momentum transfer, where scattering processes are calculated with success. In this regime the coupling is small; hence the wealth of perturbative techniques that have been developed for the study of quantum electrodynamics may be confidently extended to describe QCD processes.

In contrast, away from large momentum transfer, or equivalently at large distances, QCD is not so well understood, although techniques (e.g. lQCD simulations) exist to perform first-principle calculations for some observables. Most of the quantities remain, however, out of reach and can only be measured in dedicated experiments. The problem lies in the fact that the coupling constant becomes large and a perturbative approach cannot be applied. Beside lattice-QCD calculations – in any case limited to some quantities – one has to rely on the description provided by Effective Field Theories.

A simple Lagrangian involving partonic degrees of freedom is the Nambu -Jona-Lasinio (NJL) model and this section is devolved to introduce this model. For more details I refer the reader to Ref. [63]. In its original form, this model was constructed as a pre-QCD theory of nucleons that interact via an effective two-body contact interaction. Today this is reinterpreted as a theory with quark degrees of freedom. Of primary importance is the fact that the Lagrangian density of this model is constructed respecting the global symmetries of QCD, in particular isospin and chiral symmetry. The NJL model allows one to describe the spontaneous breaking of chiral symmetry, which is essential for the comprehension of the lightest hadrons.

The NJL model has, of course, its shortcomings. The interaction between quarks is assumed to be point-like, so that the theory is not renormalizable.

Hence, an upper cutoff on the momenta is necessary for the regularization of the UV divergent integrals. A second shortcoming of the NJL model, physical rather than mathematical, is that its local interaction does not confine quarks. In this thesis, the NJL model will be generalized to include also the coupling with the so-called Polyakov fields (PNJL model), in order to introduce some features of confinement. However, its solution will be used both as a benchmark and as a starting point to look for the solutions of the PNJL mean-field equations.

NJL Lagrangian

The NJL Lagrangian is written in order to preserve the global $SU(N_f)_V \times SU(N_f)_A \times U(1)_V$ symmetry of QCD. The Lagrangian in the 3-flavour case reads

$$\begin{aligned}\mathcal{L} = i\overline{\psi}\partial\!\!\!/\psi + \frac{1}{2}G\sum_{a=0}^{8}[(\overline{\psi}\lambda^a\psi)^2 + (\overline{\psi}i\lambda^a\gamma^5\psi)^2]+ \\ + K\{\det[\overline{\psi}(1+\gamma^5)\psi] + \det[\overline{\psi}(1+\gamma^5)\psi]\}.\end{aligned} \tag{1.67}$$

Here λ^a (with $a = 1, ..., 8$) are the Gell-Mann matrices in flavour space, $\lambda^0 \equiv \sqrt{2/3}\mathbb{1}$ and the determinant is taken in flavour space. G and K are the coupling constant for the 4-fermion and 6-fermion interactions. The latter explicitly breaks the $U_A(1)$ symmetry, reflecting somehow the axial anomaly of QCD. The calculations are usually performed in mean-field approximation. In this case, the six-fermion term can be reduced to an effective four-fermion vertex, which can then be handled in the usual way. While there is little technical difference in the handling of the two- and three-flavor models, the six-fermion interaction vertex brings new physics with it. As we shall see, the flavor-mixing nature of this interaction leads to the mixing of the pure η_0 and η_8 modes to form the physical η and η' mesons, the latter characterized by a much larger mass. As above mentioned, in a 4-dimension spacetime the NJL-theory is not renormalizable: the coupling constant $[G] = [E]^{-2}$ and $K = [E]^{-4}$ are not dimensionless. The divergent integrals are regularized by an ultraviolet cutoff Λ. The coupling constant and the cutoff are the free parameters of the model. They are fixed by the values of some physical observables like the pion mass and decay constant.

NJL gap equation

This paragraph is devolved to illustrate the mean-field approximation and the mass gap equation. In principle, the mean-field approximation is a self-consistent resummation involving two different terms: the Hartree (direct) and Fock (exchange) terms. One can draw the resummed propagator of a quark interacting with a background due to the presence of all the other quarks in the system as in Fig. 1.8.

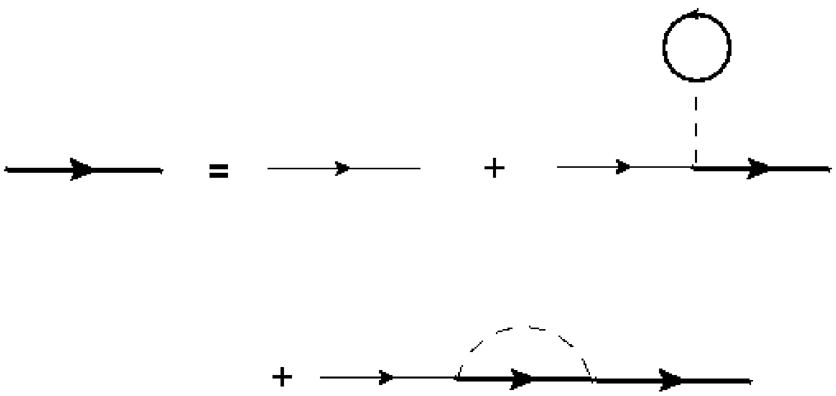

Figure 1.8: Dressed quark propagator in Mean Field Approximation. The first term is the free propagator, while the second and the third terms are respectively the Hartree and Fock terms.

In the case of 2+1 flavours, there are two different interaction vertices, but the 6- fermion vertex can be reduced to an effective 4-fermion interaction vertex in MF approximation, as shown in Fig. 1.9. One can write the self-energy arising from the 4-fermion interaction

$$\Sigma_f^{(4)} = iG[N_c + \frac{1}{2}] \sum_a (\lambda^a)_{ff} \sum_g \int \frac{d^4p}{(2\pi)^4} (\lambda^a)_{gg} \mathrm{tr} S^g(p). \tag{1.68}$$

Here f and g are flavour indices and tr indicate the trace over the Dirac space

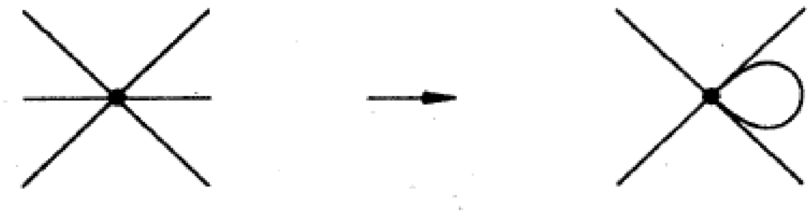

Figure 1.9: The 6-fermion interaction vertex is reduced to an effective 4-fermion coupling

of the quark propagator defined in the usual way:

$$S^f(p) = \frac{\not{p} + m_f}{p^2 - m_f^2 + i\epsilon}, \tag{1.69}$$

where m_f represent the self-consistent mass of the quark of flavour f. Due to the traceless nature of the Gell-Mann matrices, only the $a = 0$ term contributes to the sum. One obtains :

$$\Sigma_f^{(4)} = 2iG[N_c + \frac{1}{2}] \int \frac{d^4p}{(2\pi)^4} \mathrm{tr} S^f. \tag{1.70}$$

In the following we consider only the dominant term in the self-energy, i.e. the Hartree term, proportional to N_c, neglecting the sub-leading Fock term. The contribution to the self-energy arising from the 6-fermion interaction vertex reads:

$$\Sigma_f^{(6)} = K[2N_c^2 + 3N_c + 1] \int \frac{d^4p}{(2\pi)^4} \mathrm{tr} S^g \int \frac{d^4p}{(2\pi^4)} \mathrm{tr} S^h \quad (f \neq g \neq h). \tag{1.71}$$

In Mean-Field-Approximation one can rewrite the interaction term of the Lagrangian as a mass term for the quark:

$$\Delta\mathcal{L}_{\mathrm{int}}^{\mathrm{MF}} = -\overline{\psi}\Sigma\psi \ , \tag{1.72}$$

for which one can write the following self-consistent gap equation

$$m_f = +2iGN_c \int \frac{d^4p}{(2\pi)^4} \mathrm{tr} S^f(p) + 2KN_c^2 \int \frac{d^4p}{(2\pi)^4} \mathrm{tr} S^g \int \frac{d^4p}{(2\pi^4)} \mathrm{tr} S^h \ , \tag{1.73}$$

where the large-N_c approximation is assumed. It is useful to define the chiral condensate for flavour f as:

$$\phi_f \equiv -iN_c \int \frac{d^4p}{(2\pi)^4} \mathrm{tr} S^f(p). \tag{1.74}$$

If the Lagrangian contains an explicit mass term, the mass gap equation becomes:

$$m_f = m_{0,f} - 2G\phi_f - 2K\phi_g\phi_h. \tag{1.75}$$

Here $m_{0,f}$ is the current mass of the quark of flavor f appearing in the Lagrangian. In this case chiral symmetry is explicitly broken, although by a very small amount, since the current mass of light quarks is much smaller than the typical effective mass of a valence quark $>$ 300 MeV. From Eq. (1.75) one gets that light quarks acquire an effective mass and chiral symmetry is dynamically (or spontaneously) broken. In the chiral limit ($m_{0,f} = 0$), from the definition (1.74) and from Eq. (1.75), chiral symmetry is spontaneously broken if $\phi \neq 0$. Hence, one can use the chiral condensate as the order parameter for the chiral phase-transition. Since the explicit symmetry-breaking introduced by $m_{0,f}$ is small, this remains meaningful also in the case of non-vanishing currrent quark masses. The next paragraph is focused on the mesonic spectrum and on what happens to their chiral partners.

NJL hadronic spectrum

For the investigation of the mesonic spectrum predicted by the NJL model it is useful to rewrite the Lagrangian (1.67) in mean-field approximation in order to display explicitly the different meson operators:

$$\begin{aligned}\mathcal{L}_{MF} =& i\overline{\psi}\partial\!\!\!/\psi + \\ &+ \sum_{i=0}^{8} \Big\{ \mathcal{G}_i^-(\overline{\psi}\lambda^i\psi)^2 + \mathcal{G}_i^+(\overline{\psi}i\gamma^5\lambda^i\psi)^2 \Big\} + \\ &+ \frac{1}{2}\Big\{ \mathcal{K}^-(\overline{\psi}\lambda^8\psi)(\overline{\psi}\lambda^0\psi) + \mathcal{K}^+(\overline{\psi}i\gamma^5\lambda^8\psi)(\overline{\psi}i\gamma^5\lambda^0\psi) + \\ &\quad + \mathcal{K}^-(\overline{\psi}\lambda^0\psi)(\overline{\psi}\lambda^8\psi) + \mathcal{K}^+(\overline{\psi}i\gamma^5\lambda^0\psi)(\overline{\psi}i\gamma^5\lambda^8\psi) \Big\},\end{aligned} \tag{1.76}$$

where $\mathcal{G}^{\pm}$ and $\mathcal{K}^{\pm}$ are the flavour-dependent effective coupling constant, defined as:

$$\begin{aligned}
\mathcal{G}_0^{\pm} &= \frac{1}{2}G \pm \frac{1}{3}N_c K(i\mathrm{tr}S^s + 2i\mathrm{tr}S^u) \\
\mathcal{G}_1^{\pm} &= \mathcal{G}_2^{\pm} = \mathcal{G}_3^{\pm} = \frac{1}{2}G \mp \frac{1}{2}N_c K i\mathrm{tr}S^s \\
\mathcal{G}_4^{\pm} &= \mathcal{G}_5^{\pm} = \mathcal{G}_6^{\pm} = \mathcal{G}_7^{\pm} = \frac{1}{2}G \mp \frac{1}{2}N_c K i\mathrm{tr}S^u \\
\mathcal{G}_8^{\pm} &= \frac{1}{2}G \mp \frac{1}{6}N_c K(4i\mathrm{tr}S^u - i\mathrm{tr}S^s) \\
\mathcal{K}^{\pm} &= \mp\frac{\sqrt{2}}{6}N_c K(i\mathrm{tr}S^u - i\mathrm{tr}S^s) \ .
\end{aligned} \tag{1.77}$$

Notice that the effective coupling $\mathcal{K}$ is responsible for the mixing of the λ^0 and λ^8 modes, leading to the $\eta - \eta'$ mass splitting in the pseudoscalar spectrum. It is particularly interesting to focus on the pseudoscalar sector, since in the chiral limit these mesons can be interpreted as the Goldstone bosons associated to the spontaneous breaking of chiral symmetry. The different meson modes arise from the proper combination of flavour matrices and effective couplings, as follows:

$$T_i = \begin{cases}
\lambda^3 \to \mathcal{G}_3^{+} \to \pi^0 \\
\frac{1}{\sqrt{2}}(\lambda^1 \pm i\lambda^2) \to \mathcal{G}_1^{+} \pm i\mathcal{G}_2^{+} \to \pi^{\pm} \\
\frac{1}{\sqrt{2}}(\lambda^6 \pm i\lambda^7) \to \mathcal{G}_6^{+} \pm i\mathcal{G}_7^{+} \to K^0, \overline{K}^0 \\
\frac{1}{\sqrt{2}}(\lambda^4 \pm i\lambda^5) \to \mathcal{G}_4^{+} \pm i\mathcal{G}_5^{+} \to K^{\pm} \ .
\end{cases} \tag{1.78}$$

The effective interaction resulting from the exchange of a meson can be expressed to leading order in N_c as an infinite sum of terms in the random-phase approximation (RPA) that is recognized to be a geometric series. In Fig (1.10) I show the terms included in the series. The bubbles resummed in the series are called polarization propagators, $-i\Pi_I^J$, the index I referring to the kind of interaction (scalar, pseudoscalar, vector or pseudovector) and the index J referring to the kind of particle (pion, kaon, sigma, etc...). For

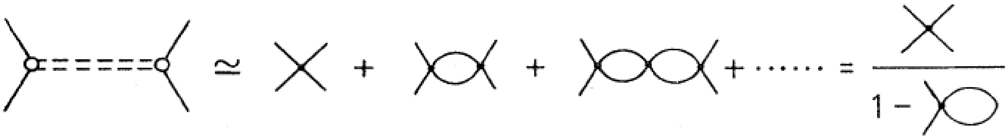

Figure 1.10: Effective $q\bar{q}$ scattering amplitude in the random phase approximation. Only the direct terms are considered.

instance, for the π^0, the polarization propagator reads:

$$-i\Pi^{\pi^0}_{ps}(k) = \mathrm{Tr}\int\frac{d^4p}{(2\pi)^4}\left[i\gamma^5\lambda^3 S^u(p+\frac{1}{2}k)i\gamma^5\lambda^3 S^u(p-\frac{1}{2}k)\right], \qquad (1.79)$$

where we exploited the exact isospin symmetry $m_u = m_d$ which makes the overall trace over flavor trivial. The resummation of the RPA series leads to the following effective interaction mediated by the exchange of a neutral pion. The effective propagator of the neutral pion reads:

$$\Gamma^{\pi^0}_{ps}(k) = \frac{2\mathcal{G}^+_3}{1-2\mathcal{G}^+_3\Pi^{\pi^0}_{ps}(k)}\,. \qquad (1.80)$$

The meson mass is defined as the value of k^0 that corresponds to the zero of the real part of the denominator evaluated at zero spatial momentum

$$1-2\mathcal{G}^+_3\mathrm{Re}\Pi^{\pi^0}_{ps}(m_\pi,\vec{k}=0) = 0. \qquad (1.81)$$

Using this methods one can obtain the spectrum of all the pseudoscalar mesons, as done by Klimt et al. in Ref. [64], and compare it with the PDG states. The results are shown in Table 1.1 and in Fig. 1.11.

In Appendix A I provide more details on the calculation of meson masses. The major finding of the NJL model is that, in the chiral limit, the pion and kaon become massless, while the scalar particles get a mass as in the Linear Sigma Model. Chiral symmetry is then dynamically broken. One can conclude that the NJL model is useful to investigate chiral-symmetry breaking. Actually, in order to reproduce the physical masses of the particles, one needs in the Lagrangian a small mass term for the quarks which breaks

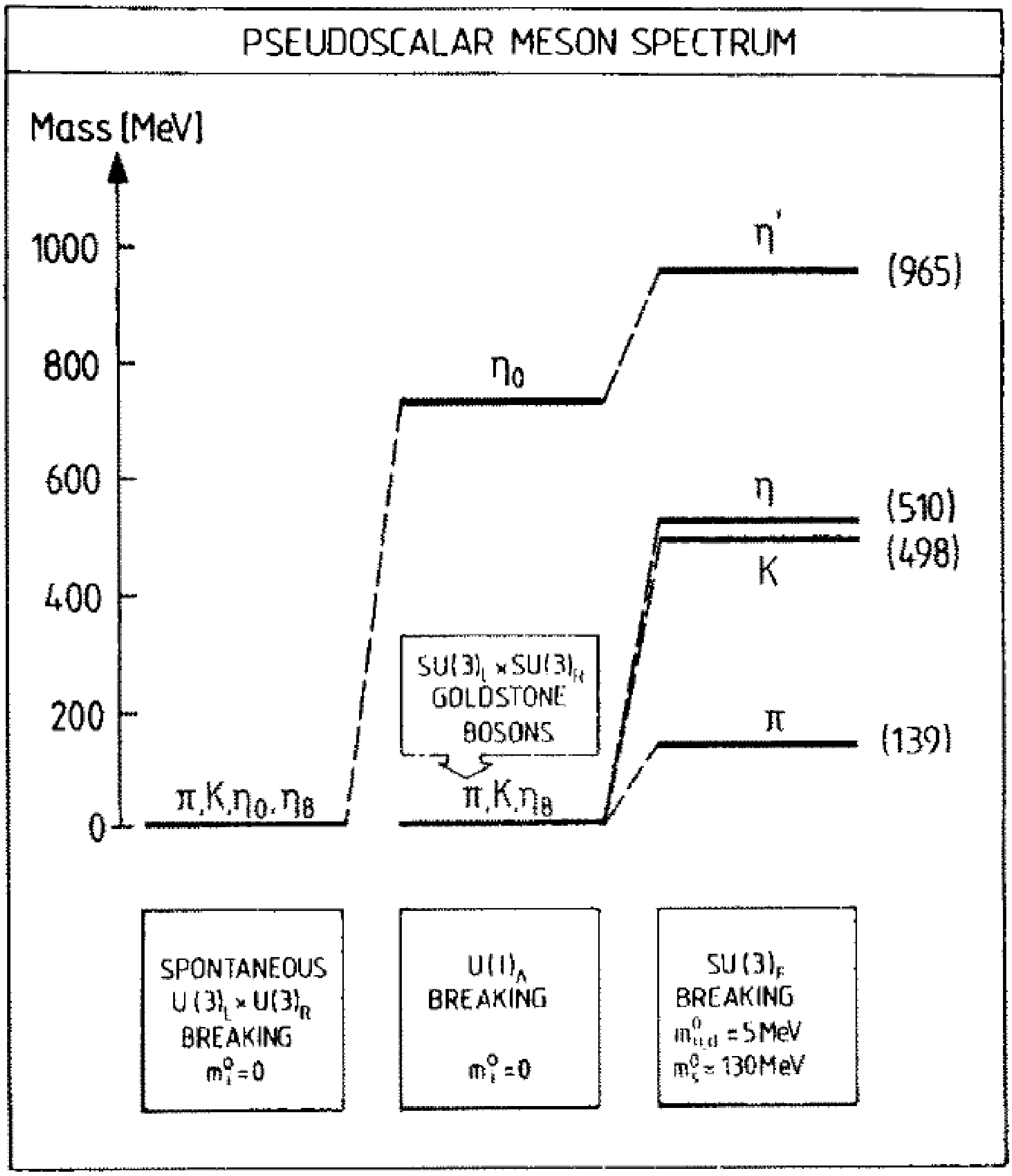

Figure 1.11: Pseudoscalar meson spectrum in the NJL model obtained in [64].

explicitly chiral symmetry by a small amount.

In the next chapter, starting from the NJL model, we present a more complex Effective Field Theory that considers also the interaction between quarks and a background color field. The latter will be used to investigate

	m_π MeV	m_K MeV	m_η MeV	$m_{\eta'}$ MeV
NJL predictions	139	498	509	969
PDG Mass	139	495	548	958

Table 1.1: Pseudoscalar meson masses predicted in the NJL model in Ref [64] compared to their PDG values.

the spontaneous breaking/restoration not only of chiral symmetry, but also of the center symmetry introduced in Sec. 1.5.

1.7 Hydrodynamics

This section is devolved to introduce some important concepts related to the hydrodynamic description of the QGP. The section is based on Refs. [57, 93, 98].

First of all, why is hydrodynamics relevant for the description of the Quark-Gluon Plasma? The only experimental way, available today, to study QCD under extreme conditions are heavy ion-collision experiments. Sec. 2 is devoted to describe this kind of experiments. The basic idea is that, after the collision, a hot and dense system of deconfined quarks and gluons is formed, which undergoes a rapid expansion and cools down. In light of its simplicity, one would like to describe such an expansion in terms of relativistic hydrodynamics (RHD). Hydrodynamics is applicable if the medium is locally thermalized (or close to local thermal equilibrium if viscous corrections are considered), condition which occurs if entropy is maximized and the microscopic collision time-scale is shorter than the macroscopic evolution time-scale. Since the fireball created in the heavy-ion collision is small and expands very fast, it seems that the above conditions are hardly satisfied. Surprisingly, several observables in relativistic heavy-ion collisions at RHIC and at the LHC are nicely reproduced by relativistic hydrodynamics, assuming that the fireball undergoes a collective expansion driven by pressure gradients: the hadron transverse-momentum spectra in central and non-central collisions; the anisotropy of their azimuthal distribution in non-central collisions, quantified by the elliptic-flow coefficient $v_2(p_T)$ and its dependence on the hadron rest mass; higher-order flow harmonics... All these observables are correctly described by hydrodynamic models for transverse momenta up to about 2 GeV [65].

From these observations one can infer that the Quark-Gluon Plasma created in heavy-ion collisions thermalizes very rapidly and must be strongly interacting. Therefore, the QGP is a strongly coupled plasma that behaves as an almost perfect fluid. For its description, perturbative QCD is not applicable and one needs a non-perturbative approach like lattice-QCD or an Effective Field Theory. Hydrodynamics can be considered an effective theory for the study of long-wavelength excitations of the system.

1.7.1 Relativistic hydrodynamics: general setup

Hydrodynamics describes a many-particle system in terms of a few fields obeying some conservation laws: the density of conserved charges $n_i(x)$ (if present), the energy density $\epsilon(x)$, the pressure $P(x)$ and the collective fluid four-velocity $u^\mu(x)$. We start considering the four-velocity, which is written as:

$$u^\mu = \gamma \begin{pmatrix} 1 \\ \vec{v} \end{pmatrix} \quad \text{with} \quad \gamma \equiv \frac{1}{\sqrt{1-\vec{v}^2}}, \tag{1.82}$$

which reduces to $u^\mu \approx (1, \vec{v})$ in the non-relativistic limit (NRL). In the *local rest frame* (LRF) $u^\mu = (1, \vec{0})$. The four-vector u^μ only contains three independent components, since it obeys the relation:

$$u^2 = u^\mu g_{\mu\nu} u^\nu = 1, \tag{1.83}$$

arising from the metric tensor $g_{\mu\nu} = \mathrm{diag}(1, -1, -1, -1)$ used in this thesis.

As mentioned above, hydrodynamic equations have the form of conservation laws for the energy, the momentum and, in the case of QCD, the baryon number (also strangeness and electric charge are conserved, but one usually neglects them in solving the equations).

In order to obtain the RHD equations, one must start from the energy-momentum tensor $T^{\mu\nu}$ for a relativistic fluid. Here we consider only the ideal case, neglecting dissipative effects. Hence, $T^{\mu\nu}$ just depends on the hydrodynamic degrees of freedom, namely two scalar quantities (ϵ, p) and one four-vector (u^μ). Since $T^{\mu\nu}$ must be symmetric and transform as a tensor under Lorentz transformations, its most general form is

$$T^{\mu\nu} = \varepsilon(c_0 g^{\mu\nu} + c_1 u^\mu u^\nu) + p(c_2 g^{\mu\nu} + c_3 u^\mu u^\nu). \tag{1.84}$$

In order to fix the coefficients, in the local rest frame, one requires the T^{00} component to represent the energy density ϵ of the fluid and the spatial components to be proportional to the pressure, $T^{ij} = p\delta^{ij}$. This implies

$c_0 = 0$, $c_1 = 1$, $c_2 = -1$ and $c_3 = 1$. Hence, the energy-momentum tensor reads:

$$T^{\mu\nu} = \varepsilon u^\mu u^\nu - p\Delta^{\mu\nu}, \tag{1.85}$$

where the transverse projector $\Delta^{\mu\nu}$ is defined as:

$$\Delta^{\mu\nu} = g^{\mu\nu} - u^\mu u^\nu. \tag{1.86}$$

This operator has the following properties:

- $\Delta^{\mu\nu} u_\mu = \Delta^{\mu\nu} u_\nu = 0$
- $\Delta^{\mu\nu} \Delta_\nu^\alpha = \Delta^{\mu\alpha}$.

$\Delta^{\mu\nu}$ acts then as a projection operator on the space orthogonal to the fluid four-velocity u^μ.

If there are no external sources (isolated system), the energy momentum tensor is conserved:

$$\partial_\mu T^{\mu\nu} = 0. \tag{1.87}$$

It is useful to project these equations along the directions parallel and perpendicular to the fluid four-velocity. For the parallel direction one finds

$$u_\nu \partial_\mu T^{\mu\nu} = u^\mu \partial_\mu \varepsilon + (\varepsilon + p)\partial_\mu u^\mu = 0, \tag{1.88}$$

while for the orthogonal direction one gets

$$\Delta_\nu^\alpha \partial_\mu T^{\mu\nu} = (\varepsilon + p) u^\mu \partial_\mu u^\alpha - \Delta^{\mu\alpha} \partial_\mu p = 0. \tag{1.89}$$

It is convenient to introduce the *comoving derivative* $D = u^\mu \partial_\mu$ and the perpendicular derivative $\nabla^\alpha = \Delta^{\mu\alpha}\partial_\mu$. The RHD equations written in a Lagrangian form become then:

$$\begin{aligned} &D\varepsilon + (\varepsilon + p)\partial_\mu u^\mu = 0 \\ &(\varepsilon + p) D u^\alpha - \nabla^\alpha p = 0. \end{aligned} \tag{1.90}$$

In the absence of conserved charges (which is approximately the case in heavy-ion collisions at the highest energies, with almost vanishing baryon number) these are the fundamental equations for a relativistic ideal fluid. This is a system of 4 independent equations with 5 unknowns: the 3 independent components of u^μ, the pressure and the energy density. One needs another equation to close the system: the Equation of State (EoS) $p = p(\epsilon)$. The equation of state depends on the nature of the system and, in this case, on the interaction between quarks and gluons. Due to the non-perturbative nature of these interactions, an analytic calculation of the EoS around the deconfinement transition starting from the QCD Lagrangian is infeasible. One needs a non-perturbative approach: Lattice QCD (Sec. 1.5 is devoted to this topic) or an Effective Field Theory (as described in Sec. 1.6).

The meaning of Eq.(1.90) becomes more transparent in the non-relativistic limit ($|\vec{v}| \ll 1$). One finds:

$$D = u^\mu \partial_\mu \sim \partial_t + \vec{v} \cdot \vec{\partial} + \mathcal{O}(|\vec{v}|^2), \quad \nabla^i = \Delta^{i\mu} \partial_\mu \sim -\partial_i - v^i u^0 \partial_0 + \mathcal{O}(|\vec{v}|^2). \tag{1.91}$$

In this limit, ∇^i reduces to (minus) the spatial derivative and pressure is much lower than the energy density $\epsilon \equiv \rho + \epsilon_{\rm th}$, which is dominated by the mass density ρ, much larger than the thermal energy density and playing the role of the inertial term. The set of Eqs. (1.90) becomes then:

$$\begin{aligned} (\partial_t + v^k \partial_k)\epsilon &= -(\epsilon + P)\,(\vec{\nabla} \cdot \vec{v}), \\ \rho(\partial_t + v^k \partial_k)\vec{v} &= -\vec{\nabla} P. \end{aligned} \tag{1.92}$$

The first equation contains a double information: the mass conservation

$$(\partial_t + v^k \partial_k)\rho = -\rho\,(\vec{\nabla} \cdot \vec{v})$$

and the evolution of the thermal energy density

$$(\partial_t + v^k \partial_k)\epsilon_{\rm th} = -(\epsilon_{\rm th} + P)\,(\vec{\nabla} \cdot \vec{v}),$$

which decreases both due to the dilution arising from the expansion of the system and due to the work done during the expansion (hence the role of the pressure). The second equation is the Euler equation and represents momentum conservation. This equation implies that an initial pressure anisotropy leads to an asymmetry in the fluid flow and hence in the momentum-distribution of final state particles.

The fireball produced in heavy-ion collisions is surrounded by the vacuum, which has zero pressure, while at its center one has the thermal pressure of a relativistic plasma. Considering the dynamics in the transverse plane, if the pressure gradient is isotropic the expansion is equal in all directions and one has simply a *radial flow.* On the contrary, if one has an initial deformation, in the final-state particles one can detect an *elliptic flow* or a *triangular flow* and so on.

The anisotropy in the initial pressure gradients is due to the asymmetric shape of the overlapping region of the colliding nuclei. This asymmetry arises both from the non-zero *impact parameter* (which will be introduced in Sec. 2) and from the fluctuations in the position of the nucleons in the nuclei. This topic will be treated in detail in Sec. 2.

If in the system there are some conserved charges, e.g. baryon number, associated to the conserved currents $J_i^\mu = n_i u^\mu$ (the latin index i labels the particular conserved charge) one has to consider new continuity equations:

$$\partial_\mu J_i^\mu = Dn_i + n_i\,\partial_\mu u^\mu = 0. \tag{1.93}$$

In full generality, in heavy-ion collisions the conserved charges are baryon number, electric charge and strangeness, although one usually considers only baryon number. Approximating the QGP as an ideal fluid, there is no energy dissipation and also entropy is conserved. In this case, one can write a continuity equation also for the entropy current, defined as $S^\mu = su^\mu$, where s is the entropy density in the local rest-frame of the fluid. The conservation equation reads then:

$$\partial_\mu S^\mu = Ds + s\,\partial_\mu u^\mu = 0. \tag{1.94}$$

Both baryon and entropy densities get diluted due to the expansion of the system expressed by the rate $\partial_\mu u^\mu$. One can combine Eq. (1.93) for the baryon density and Eq. (1.94) for the entropy density in order to define a new conserved quantity, the *entropy per baryon* $\sigma \equiv s/n_B$, that obeys the equation

$$D\sigma = 0. \tag{1.95}$$

During the evolution of the system, both the entropy and the baryon density can change, but their ratio in each fluid-cell followed along its motion remains constant. In heavy-ion collisions, one produces a system which – neglecting dissipative effects due to viscosity, heat conduction and charge diffusion – undergoes an approximate isentropic expansion moved by pressure gradients along trajectories of constant entropy per baryon: the higher the center-of-mass energy of the collision, the higher the s/n_B ratio.

One can define other conserved quantities used in theoretical calculations as constraints to satisfy fixing the values of the respective chemical potentials. One can define the *electric charge per baryon* $\xi \equiv n_Q/n_B$ and the *strangeness number per baryon* $\eta = n_s/n_B$. These two quantities can be used to fix the electric-charge and strangeness chemical potentials. In heavy-ion collisions, assuming that the non-zero charges arise from the partial stopping of the matter of the colliding nuclei, one has $\xi = 0.4$ and $\eta = 0.0$.

1.7.2 Speed of sound in an ideal fluid

Starting from the relativistic Euler equation (1.90) and considering that the evolution of an ideal fluid occurs along trajectories of constant entropy per baryon $\sigma \equiv s/n_B$, one can see that the speed of sound, defined as

$$c_s^2(\varepsilon, \sigma) \equiv \left.\frac{\partial P}{\partial \varepsilon}\right|_{\sigma}, \tag{1.96}$$

is responsible for the fluid acceleration, since it maps the energy-density gradient of the initial condition into a pressure gradient. In fact, in HIC's the viscosity and hence entropy production is found to be very low; then, in first approximation, one can neglect it and assume that the system evolves at a fixed value of σ. One has still to show that the quantity defined in Eq. (1.96) is actually the squared speed of sound. The hydrodynamics evolution of the fluid is driven by Eqs. (1.90). For small perturbations around the configuration of a fluid at rest at global equilibrium ($P = P_{\rm eq} + \delta P$, $\varepsilon = \varepsilon_{\rm eq} + \delta\varepsilon$), neglecting quadratic terms in the fluctuations, one obtains:

$$\partial_t \delta\varepsilon = -h_{\rm eq}\partial_i v^i \tag{1.97}$$

$$h_{\rm eq}\partial_t v^i = -\partial_i \delta P, \tag{1.98}$$

where $h_{\rm eq} \equiv (P_{\rm eq} + \varepsilon_{\rm eq})$ is the enthalpy density of the unperturbed system. One can consider the pressure as a function of the energy density ε and of the entropy-per-baryon σ. Since in the absence of dissipation σ is constant, the pressure fluctuation can be written as:

$$\delta P = \left.\frac{\partial P}{\partial \varepsilon}\right|_{\sigma} \delta\varepsilon \equiv c_s^2 \delta\varepsilon. \tag{1.99}$$

and hence one has

$$\partial_t \delta P = c_s^2 \partial_t \delta\varepsilon = -c_s^2 h_{\rm eq}\partial_i v^i. \tag{1.100}$$

After taking a second time derivative and using Eq. (1.98), one gets:

$$\frac{\partial^2}{\partial t^2}\delta P = c_s^2 \nabla^2 \delta P. \tag{1.101}$$

This is the d'Alembert wave equation, here for the particular case of a sound wave. Then one can conclude that c_s, defined in Eq. (1.96), can be identified with the speed of sound of a relativistic fluid. The speed of sound maps then a density gradient into a pressure gradient, which – if the evolution of the system can be described by hydrodynamics – is responsible for the fluid acceleration.

Eq. (1.96) gives the value of the speed of sound along a line of constant entropy per baryon. For practical purposes, it may be more useful to treat the speed of sound as a function of temperature and chemical potential as independent variables. One has:

$$c_s^2(T,\mu) = \frac{n^2\chi_{TT} - 2sn\chi_{T\mu} + s^2\chi_{\mu\mu}}{h(\chi_{TT}\chi_{\mu\mu} - \chi_{T\mu}^2)}, \tag{1.102}$$

where n is the baryon density, s is the entropy density and the symbols $\chi_{x,y}$

represent the following quantities:

$$\chi_{TT} = \left.\frac{\partial^2 P}{\partial T^2}\right|_{\mu}, \quad \chi_{T\mu} = \left.\frac{\partial}{\partial \mu}\right|_{T} \left.\frac{\partial P}{\partial T}\right|_{\mu}, \quad \chi_{\mu\mu} = \left.\frac{\partial^2 P}{\partial \mu^2}\right|_{T}. \tag{1.103}$$

Chapter 2

Heavy Ion Collisions

In this section **I introduce** the the motivations to use relativistic heavy-ion collisions for **the study of** the properties of hadronic matter at high temperature/density, **focusing on what** kind of observables are available in these experiments. This chapter is based on Ref.‘[30].

2.1 Motivations

In the past 50 years proton-proton and nucleus-nucleus collisions at higher and higher relative velocities have been studied in greater and greater details. These studies have been conducted because they may give us a more complete understanding of how particles are produced in high-energy collisions in QCD. This is a fundamental question that long predates QCD as Heisenberg [89] and Heitler et al [50] wrested with it in the 1930s and 1940s, Fermi [36] and Landau [66] did so in the 1940s and 1950s and Feynman [39] tried his hand in the 1960s. One can now gain new insight into these old questions by studying high-energy collisions in a new regime in which experiments have new knobs to dial, including the size of each of the colliding nuclei, the impact parameter, the final-state multiplicity and more.

Heavy-ion collision recreate a system of matter that filled the Universe few moments after the Big Bang. It has been understood since the 1970s [33, 68] that when the universe was only a few microseconds old it was filled with matter at temperatures above Λ_{QCD} and protons, neutrons and any hadrons were melt in a soup of quarks and gluons. Starting in the late 1990s, and culminating in classic works in the 2000s [15, 62], it became clear from first-principles lattice-QCD calculations at vanishing baryon density that the transition from the primordial hot deconfined QCD matter to the ordinary hadronic matter, which occurred in the first few microseconds after the Big Bang, proceed via continuous crossover, not as a first-order phase transition. One of the major goals of ultra-relativistic heavy ion-collisions (HIC's) is to use these experiments to recreate droplets of Big Bang in the laboratory.

One of the most important discoveries of HIC experiments is around the QCD transition that this matter – a few trillions of degrees hot – is an almost ideal fluid: the primordial matter is not a weakly-coupled system of quarks and gluons as originally expected but, on the contrary, it is a strongly-coupled system. The material property that quantifies the ideal fluid behaviour of a system made up of ultra-relativistic constituents is the ratio of its shear viscosity η to its entropy density s. The η/s ratio plays a central role in the equation of hydrodynamics, where it governs for instance the amount of entropy produced within the fluid as a sound wave propagates through it. The η/s ratio for the fluid of quarks and gluons produced in HIC's is close to the universal lower bound $1/4\pi$ conjectured by the gauge-gravity duality [87]. Such a small value of η/s justifies the estimate of the initial entropy of the system obtained from the final multiplicity of produced particles. In Chapter 4 this will be used to evaluate the adiabatic trajectories followed by the fireball in HIC's at different center-of-mass energies.

The main idea of HIC's is that two heavy nuclei collide at very high center-of-mass energy and after the collision a new state of matter called Quark-Gluon Plasma (QGP) is produced. This system is composed of quarks and gluons no longer confined into hadrons. The created system evolves in time and a large amount of particles ($\sim 10^3 - 10^4$ at the LHC) is found in the detectors. From the overall abundance and the relative yields of produced particles and their angular and momentum distribution it is possible to extract some information about the QGP and the QCD phase-diagram. This section is devolved to show which observables are experimentally accessible and which information can be extracted from their measurement.

One can scan the phase diagram of QCD starting from high energy heavy-ion collisions and move toward lower and lower collision energies, in which the initial baryon number carried by the incident nuclei provides a larger and larger contribution to the matter formed in the collision. High-energy AA experiments are under way at the LHC (Large Hadron Collider) at CERN in Geneva. Instead, lower energy AA studies were performed in the past at the SPS (Super Proton Synchrotron) [7] at CERN and are currently ongoing at the RHIC (Relativistic Heavy Ion Collider) Beam Energy Scan (BES) at Brookhaven National Laboratory (BNL) in New York. Extension of this program to even lower collision energies are planned at FAIR (Facility for Antiproton and Ion Research), an infrastucture devoted to the exploration of the high baryon-density region of the phase diagram which will be built at the GSI, in Darmstadt. The project devoted to this exploration is the CBM (Compressed Baryon Matter) experiment, where the projectile will have an energy of $10 - 45A$ GeV. This energy will allow one to create, in fixed-target collisions, the highest experimentally accessible net baryon densities, up to 10 times that of ground-state nuclear matter [53]. Other experiments about the exploration of the QCD phase-diagram at high baryon density are foreseen at the Nuclotron-Based Ion Collider Facility (NICA) in Dubna, Russia [101], and at the Japan Proton Accelerator Research Complex (J-PARC) in Tokai, Japan. The central question that these experiments aim to answer is whether the continuous crossover between the QGP fluid and hadronic matter turns into a first-order phase transition. The values of baryochemical potential μ_B and temperature where this occurs represent the coordinates of the Critical End Point (CEP) in 2-D QCD phase diagram. In Chapter 3 a theoretical model is introduced in order to explore the possible existence of this CEP.

2.2 Heavy-Ion Collision basic concepts

This section is devoted to introduce some basic concepts useful to describe the system produced in HIC's.

2.2.1 Transverse plane and impact parameter

The first two important concepts are the transverse plane and the reaction plane. The first one is orthogonal to the beam direction, the second one is generated by the beam direction and the vector that joins the centres of the colliding ions, as shown in Fig. 2.2.

In the study of heavy ion-collisions the only two quantities under direct experimental control are the ion species and the energy of the colliding beams. The energies are known to high precision. However, knowing the colliding ions is not equivalent to know the system arising from the collision. In fact, the two nuclei can collide either head-on or peripherally. The parameter that describes these different kinds of collisions is the impact parameters b, i.e. the transverse distance between the centers of mass of the two nuclei. One can focus only on the distance in the transverse plane because the ions are highly contracted due to the large Lorentz γ factor ($\gamma \sim 10^2 - 10^3$ at RHIC and LHC, respectively) and they look like two-dimensional disks; in common language they are called *pancakes*. Low values of b correspond to high-centrality events, large impact parameters correspond to peripheral ones. The main important differences between central and peripheral collisions are the number of *participant* or *wounded* nucleons (the number of nucleons that collide at least once) and, as a consequence, the number of binary collisions. The nucleons that do not collide with the others are called *spectators* and they continue travelling along the beam pipe and hence their number can in principle be directly measured through a devoted very forward detector. From this quantity one can determine the number of wounded nucleons ($N_{\text{spec}} + N_{\text{part}} = A_L + A_R$, A_i being the mass number of the two ions). In Fig. 2.1 an example of PbPb collision at the LHC is drawn.

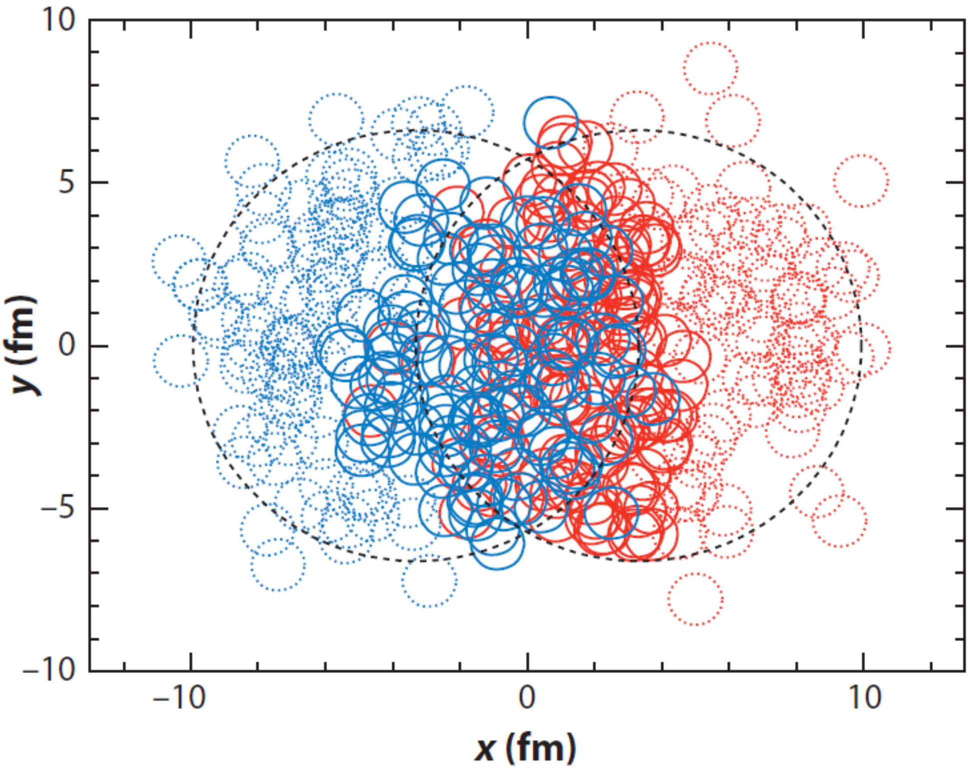

Figure 2.1: An example of a PbPb collision at the LHC with impact parameter $b \sim 7$ fm. The number of participants (solid) refers to the nucleons that collide at least once with any other nucleon, whereas the number of binary collisions counts all the overlapping blue/red nucleon pairs. Spectator nucleons (dashed) do not collide. [30]

2.2.2 Stopping power

Only the nucleons in the overlapping region of the two nuclei, the red bubble in Fig. 2.2, take part in the collision. At not so high energy ($\gamma \lesssim 10$) a lot of participant nucleons are stopped in the collision region and their presence can influence the experimental results, as we will discuss in the following: theoretical models must take this into account. At LHC energy there is essentially no stopping and the created system has vanishing baryon density; at the highest center-of-mass energies achieved at RHIC few participants are stopped and the system has small baryon density. Today a new experimental facility to study HIC's at high baryon-density is under construction at the

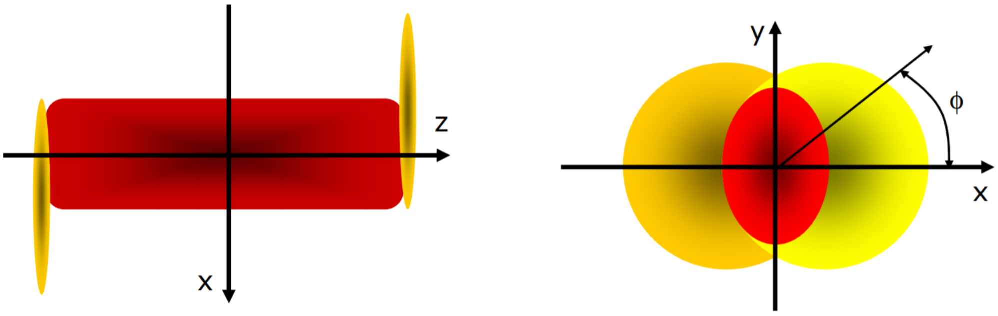

Figure 2.2: Illustration of a HIC: the reaction plane (left panel) and transverse plane (right panel) are shown [54].

GSI in Darmstadt, allowing the exploration of a different region of the QCD phase-diagram.

2.2.3 Time evolution

The time evolution of the fireball created in a heavy-ion collision is schematically shown in Fig. 2.3. One has first of all the rare hard processes involving high-momentum exchange occurring at the level of the individual nucleon-nucleon collisions before the formation of any medium, in which one produces high-p_T partons and heavy quarks. They go through the system and perform a tomography of QGP. The associated experimental observables are open heavy-flavour particles (e.g. D and B mesons), quarkonia and jets. These observables are the so-called hard probes.

Considering now the evolution of the bulk medium, one has an initial pre-equilibrium stage in which the energy stored in the colour-fields is converted into particles. After about 1 fm/c the system approaches local thermal equilibrium; at this stage quarks and gluons are free to move and exchange energy and momentum before the formation of confined states. The system expands and the temperature decreases until reaching the critical temperature T_c, at which quarks and gluons get confined into hadrons. Due to its rapid expansion the system immediately reaches chemical freeze-out, after which its chemical composition, i.e. the yields of the different hadron species, no longer

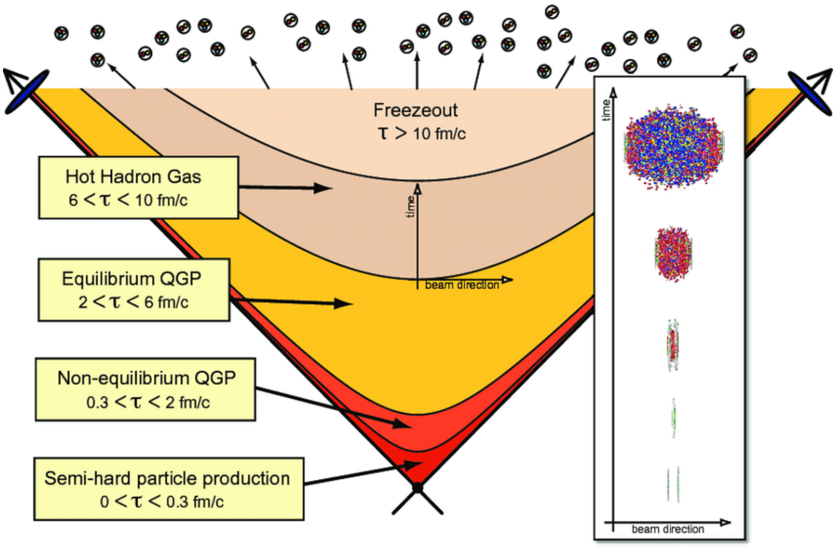

Figure 2.3: A cartoon depicting the space-time history of the QGP as generated in a heavy-ion collision at LHC energies. The overlay on the right shows the lab-frame evolution [99].

changes. Now, this Hadron-Resonance Gas made of mesons, baryons and resonances is still subject to elastic interactions, in which the different particles exchange energy and momentum. After about 10-15 fm/c the gas is so rarefied that the particles no longer interact and their energy and momenta get fixed: the kinetic freeze-out is thus achieved.

2.3 Soft probes

In this section I introduce the so called *soft probes.* These objects carry important information about the chemical composition and the collective motion of the system produced in HIC's.

2.3.1 Particle yields

In HIC experiments, beside the momentum spectra, one measures the yields of the different particle species. In Fig. 2.4 we show the multiplicity of several light hadrons as a function of the center-of-mass energy $\sqrt{s_{NN}}$. At low $\sqrt{s_{NN}}$ many nucleons are stopped in the region of the collision, hence the produced fireball has a large baryon number and the multiplicity of detected particles is dominated by protons (neutrons, having zero electric charge, cannot be directly measured); the number of anti-protons at that energy is low because of their large mass and of baryon-number conservation. Pions are the second most abundant particles at low energy, the different number of π^- compared to π^+ is due to the isospin conservation. The different multiplicity of kaons is caused by the different quark content of the two species. For K^+ one needs only an new anti-strange quark (hence the production of a $s\bar{s}$ pair) since light up-quarks are present in the colliding ions; instead, for K^- one needs both a $\bar{u}$ antiquark an a strange quark, both of them not present in the colliding ions, and hence the production of a $u\bar{u}$ and a $s\bar{s}$ pair. The same argument holds for the $\Lambda/\bar{\Lambda}$ hyperons. Furthermore, as above mentioned, the production of a Λ hyperon requires the exctitation of a $s\bar{s}$ pair; the s-quark gives rise to the Λ hyperon, while the $\bar{s}$-antiquark can recombine with a u quark from the medium contributing to the excess of K^+ mesons. At high $\sqrt{s_{NN}}$ incoming nucleons are not stopped and the particle multiplicity is dominated by pions because of their small mass; furthermore, the symmetry between matter and antimatter is recovered, since there is no stopping of the incoming matter and all the detected particles are produced during the collision. The system created at low $\sqrt{s_{NN}}$ is characterized by high baryon density (a lot of nucleons are stopped) and hence by a high value of the baryochemical potential μ_B; instead the system created at high center-of-mass energy is characterized by

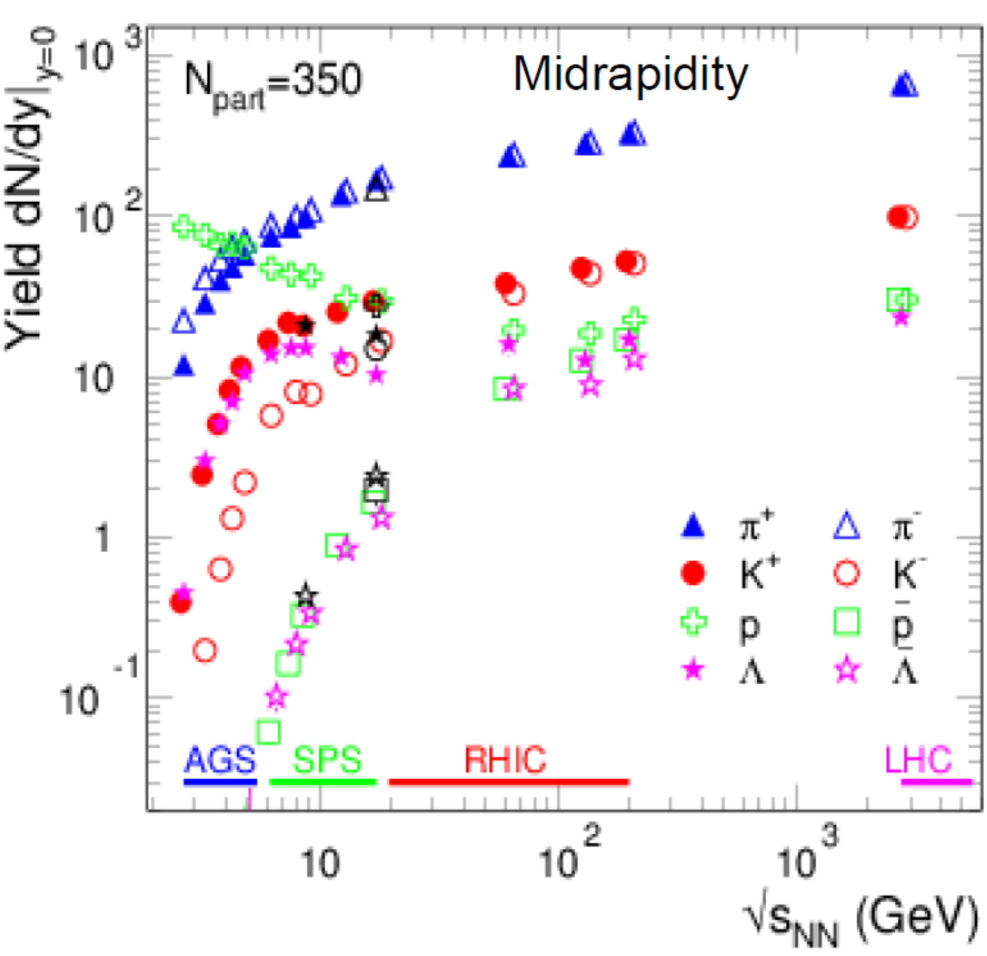

Figure 2.4: Particle multiplicity as a function of $\sqrt{s_{NN}}$ measured at different heavy-ion facilities. At high energy the number of produced particles and anti-particles is equal, while at low energy one detects more particles: this asymmetry is due to the stopped nucleons

.

low baryon density. One can see that at LHC energies the number of protons is the same as the number of anti-protons ($\mu_B = 0$).

2.3.2 Momentum distribution and collective flow

One important observable measured in HIC's is the transverse momentum distribution of produced particles. This quantity is often plotted in terms

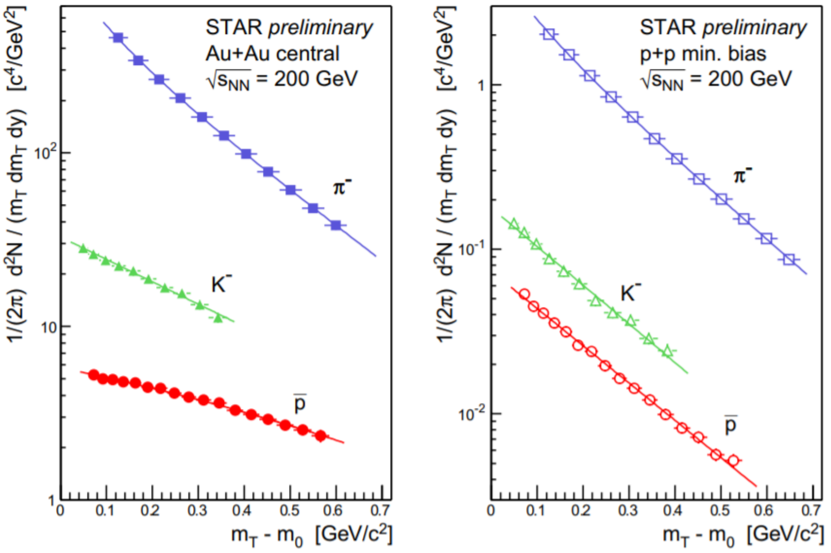

Figure 2.5: Transverse-mass distribution of identified particles measured by the STAR collaboration in Au-Au and p-p collisions [24].

of the so called transverse mass, defined as $m_T^2 = p_T^2 + m^2$, where p_T is the particle transverse momentum.

In Fig. 2.5 I show this observable for several identified particles (pions, kaons and protons) measured by the STAR experiment in A-A and p-p collisions. In p-p collisions the particle distribution is compatible with a Hagedorn one.

$$\frac{dN}{m_T dm_T} \propto e^{-m_T/T_{\text{slope}}}. \tag{2.1}$$

One can extract the value of T_{slope} from a fit, finding a result around 160 MeV. This quantity is universal for all particle species and for all values of $\sqrt{s_{NN}}$ and is called Hagedorn temperature T_H: the larger amount of available energy is used to produce more particles, not to increase their momentum. On the contrary, in A-A collisions T_{slope} is not universal but grows with m. In fact, in nuclear collisions a collective motion appears, that can change the shape of the distribution, explaining the harder spectrum found for heavier particles. In this case the relation between T_{slope} and the freeze-out temperature T_{fo} reads

$$T_{\text{slope}} = T_{\text{fo}} + \frac{1}{2} m\, v_{\text{T,flow}}^2. \tag{2.2}$$

Here $v_{\mathrm{T,flow}}$ is the collective transverse velocity of the medium, which gets larger and larger as $\sqrt{s_{NN}}$ increases. Actually, a real hydrodynamic calculation is needed for a correct interpretation of the experimental data.

In more peripheral events, with non-negligible impact parameter, the fireball is not azimuthally symmetric, but it dispalys an initial elliptic deformation, as shown in Fig. 2.6a. The presure gradient is asymmetric and bigger along the reaction plane than in the direction orthogonal to it. This pressure anisotropy is the cause of a complex collective motion. A convenient way of characterizing the angular pattern of this anisotropic flow is to perform a Fourier expansion of the invariant single-particle momentum distribution:

$$E\frac{d^3N}{d^3p} = \frac{1}{2\pi}\frac{d^2N}{p_T dp_T dy}\left\{1 + 2\sum_{n=1}^{+\infty} v_n \cos\left[n(\phi - \psi_{\mathrm{RP}})\right]\right\} . \tag{2.3}$$

The first non-trivial term of the expansion (one has $v_1 = 0$ for a symmetric rapidity window) is the $n = 2$ harmonic, the so-called elliptic flow, and its coefficient v_2 can be measured and compared to the results of hydrodynamic simulations, turning out to be a major feature of the azimuthal particle distribution. The comparison is shown in Fig. 2.6b.

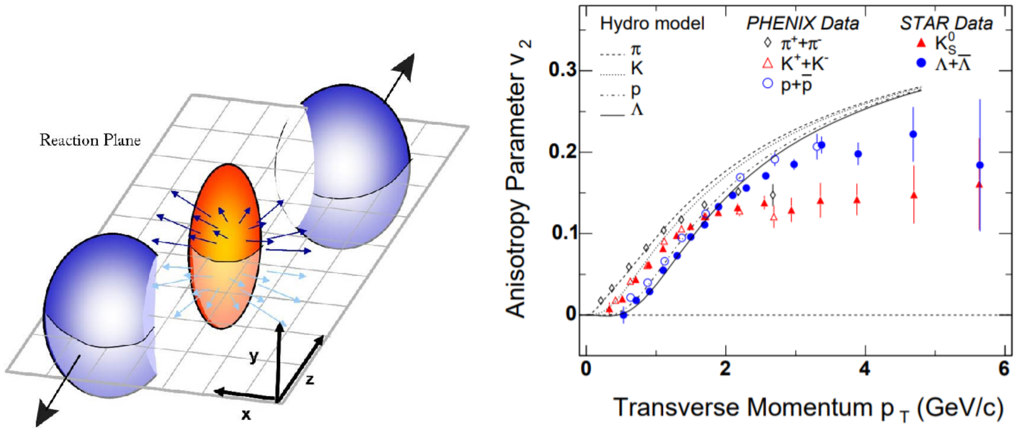

(a) *Cartoon of a peripheral collision.* (b) *Comparison between experimental data at RHIC and hydrodynamics simulations.*

Figure 2.6: Elliptic Flow in HIC's.

The hydrodynamic expansion is driven by the speed of sound according to

$$(\epsilon + P)\frac{dv^i}{dt} = -\frac{\partial P}{\partial x^i}, \quad \text{with} \quad \vec{\nabla} P = c_s^2 \vec{\nabla} \epsilon \tag{2.4}$$

and this allows one to get information on the Equation of State (EoS) of the system. The latter can be calculated with Lattice QCD at vanishing/small baryon density and with an Effective Field Theory approach at higher baryon density. In Chapter. 4 I show the results for the EoS and the speed of sound in the PNJL model. The comparison between experimental data and theoretical predictions in Fig. 2.6b is good up to 2 GeV. The reason of the discrepancy between the hydrodynamic predictions and experimental data as the transverse momentum gets larger, is that for high-momentum particles, the interaction rate is not sufficient to maintain them in kinetic equilibrium. The introduction of shear viscosity and the replacement of Eqs. (1.90) with the Israel-Steward second-order theory (for more details see [56]) produces a better agreement between theory and experimental data up to a bit larger transverse momentum.

2.4 Fluctuations

When one measures an observable in some thermal system, the results would take different values for different measurements, even if the measurement is performed with an ideal detector with an infinitesimal resolution. This distribution of the results of the measurement is referred to as fluctuations.

In HIC's the study of fluctuations concerns first of all the event-by-event yields of identified particles. In Fig. 2.7 one shows the net-charge (i.e. the difference between the number of positive and negative charged particles) distribution at several centralities and center-of-mass energies ($\sqrt{s_{NN}}$). At $\sqrt{s_{NN}} = 200$ GeV the distribution is symmetric and its maximum is close to zero. This is due to the fact that, at high energy, there is no stopping of the incoming nuclear matter and one produces the same number of particles and anti-particles; this occurs both in central and in peripheral events. On the contrary, in central collisions at low energy there is more stopping and the peak of the net-charge distribution is shifted from zero. The distributions can be characterized in terms of their cumulants. The first two

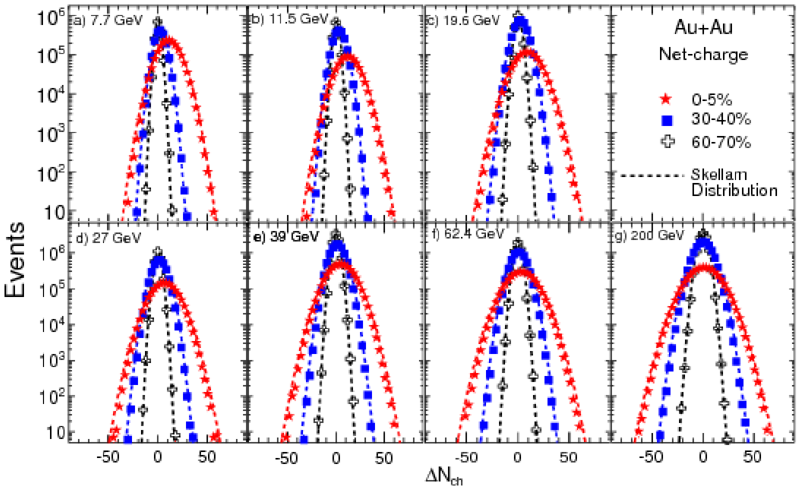

Figure 2.7: The net-charge distribution in Au+Au collisions for $\sqrt{s_{NN}}$ from 7.7 to 200 GeV with the kinematic cuts $|\eta| < 0.5$ and $0.2 < p_T < 2.0$ GeV/c for three different centralities (0 - 5%, 30 - 40%, 60 - 70%). The dashed curve is a Skellam distribution. Results are provided by the STAR collaboration [17].

are the mean M and the variance σ^2 (width of the distribution); the third and fourth cumulants are related to the skewness S and kurtosis κ, quantifying the asymmetry and sharpness of the distribution. These quantities are related to the first four moments of the distribution, as shown in the following in Eq. (3.71): for more details on these observables see Sec. 3.3.1 and Appendix B. In Fig. 2.8, taken from [17], one shows 3 combinations of these observables compared to the predictions of a Skellam distribution. The Skellam distribution is the distribution of the difference of two Poissonian stochastic variables and it can describe the net-charge or net proton number distribution in a classical ideal hadron-resonance gas.

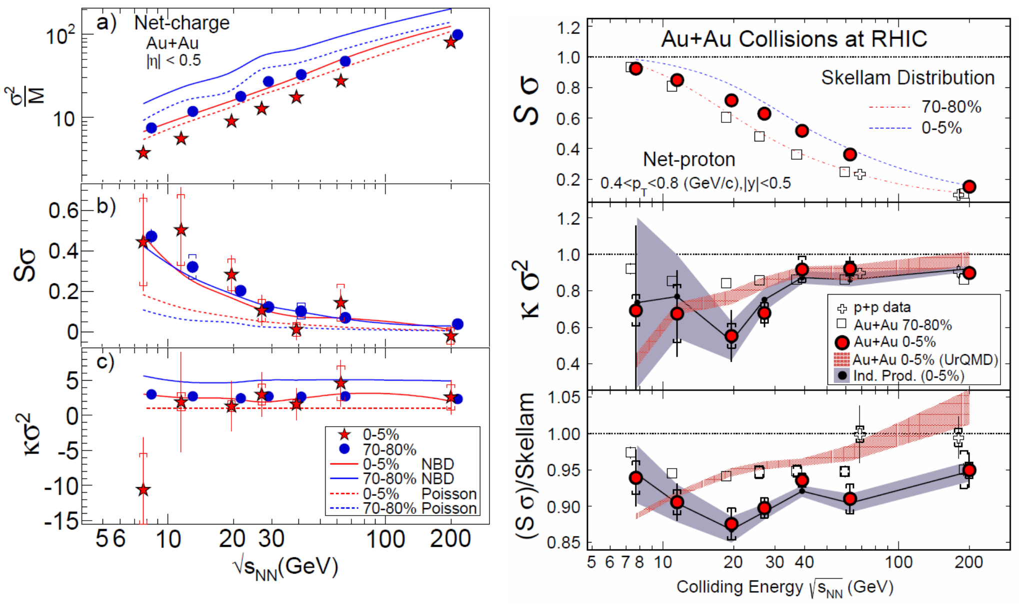

Figure 2.8: (left panel) Beam-energy dependence of (a) σ^2/M, (b) $S\sigma$ and (c) $\kappa\sigma^2$ for the net-charge distribution for a central (0-5%) and peripheral (70-80%) centrality bin. Results from a Poissonian and a Negative Binomial Distribution (NBD) baseline are superimposed. The value of $\kappa\sigma^2$ for a Poissonian distribution is always unity. (Right panel) Collision energy and centrality dependence of $S\sigma$ and $\kappa\sigma^2$ for the net-proton distribution in Au+Au and p+p collisions at RHIC. Expectations based on a Skellam distribution (dashed lines in the top panel), on UrQMD (red shaded band) and on independent particle production (shaded solid band) for the various collision centralities are shown [17].

A Skellam is the convolution of two Poisson distributions and reads:

$$S_{\lambda_1,\lambda_2}(m) = \sum_{m_1,m_2} \delta_{m,m_1-m_2} P_{\lambda_1}(m_1) P_{\lambda_2}(m_2). \tag{2.5}$$

The figure shows that, if higher order cumulants are considered, the system deviates from the predictions of a Hadron-Resonance Gas for certain values of the center-of-mass energy and one wonders whether one can interpret such a deviation as a signature of the crossing of the Critical End-Point.

From the theoretical point of view it is possible to calculate the fluctuations of net-charge and net-baryon number of the system at null/small chemical potential using lattice QCD taking higher order derivatives of the pressure with respect to the appropriate chemical potentials, but at high baryon density one needs an Effective Field Theory approach. In Chapter 3 we introduce an effective field model for this purpose.

2.5 Hard probes

The QGP formation in relativistic heavy ion collisions affects the production of hard particles: high$-p_T$ hadrons, heavy-flavor particles and quarkonia. They arise from high-energy partonic hard events described by pQCD occurring during the crossing of the two nuclei and they scale with the number of binary nucleon-nucleon collisions. The suppression of their yields (or momentum distributions) in AA collisions is quantified by the nuclear modification factor:

$$R_{AA} = \frac{N_{AA}}{\langle N_{\rm coll} \rangle N_{pp}}, \tag{2.6}$$

representing the ratio of particle yields (or kinematic distribution) in AA collisions with respect to the pp benchmark, rescaled by the average number of independent nucleon-nucleon collisions. An $R_{AA} \neq 1$ indicates a derivation from the pure $N_{\rm coll}$-scaling and hence the presence of medium effects.

One usually considers the case of the transverse-momentum spectrum of charged particles. The corresponding R_{AA} is plotted, for various collision centralities, in Fig. 2.9. As it can be seen, one always gets $R_{AA} < 1$. Actually, at very low p_T ($<$ 2 GeV) one has a violation of the $N_{\rm coll}$ scaling, since in this kinematic region particle production is proportional to $N_{\rm part}$. Hence, one must focus on the high-p_T region, where the energy loss suffered by the hard parton in the hot deconfined medium is responsible for the quenching of the distribution.

Also quarkonium production gets suppressed in high-energy nuclear collisions. This effect , interpreted as arising from the Debye screening of the $Q\bar{Q}$ interaction in the deconfined phase, was proposed by Matsui and Satz in 1986 [74]. Fig. 2.10 clearly displays strong indications of the suppression of the excited states of bottomonium Υ(2S) and Υ(3S), as can be seen from the di-muon invariant mass spectra in pp and PbPb collisions measured by CMS.

Further information on parton energy-loss can be obtained not only from single-particle observables but also from two-particle correlations. In the first stage of the fireball evolution, hard processes occur in which pairs of high-

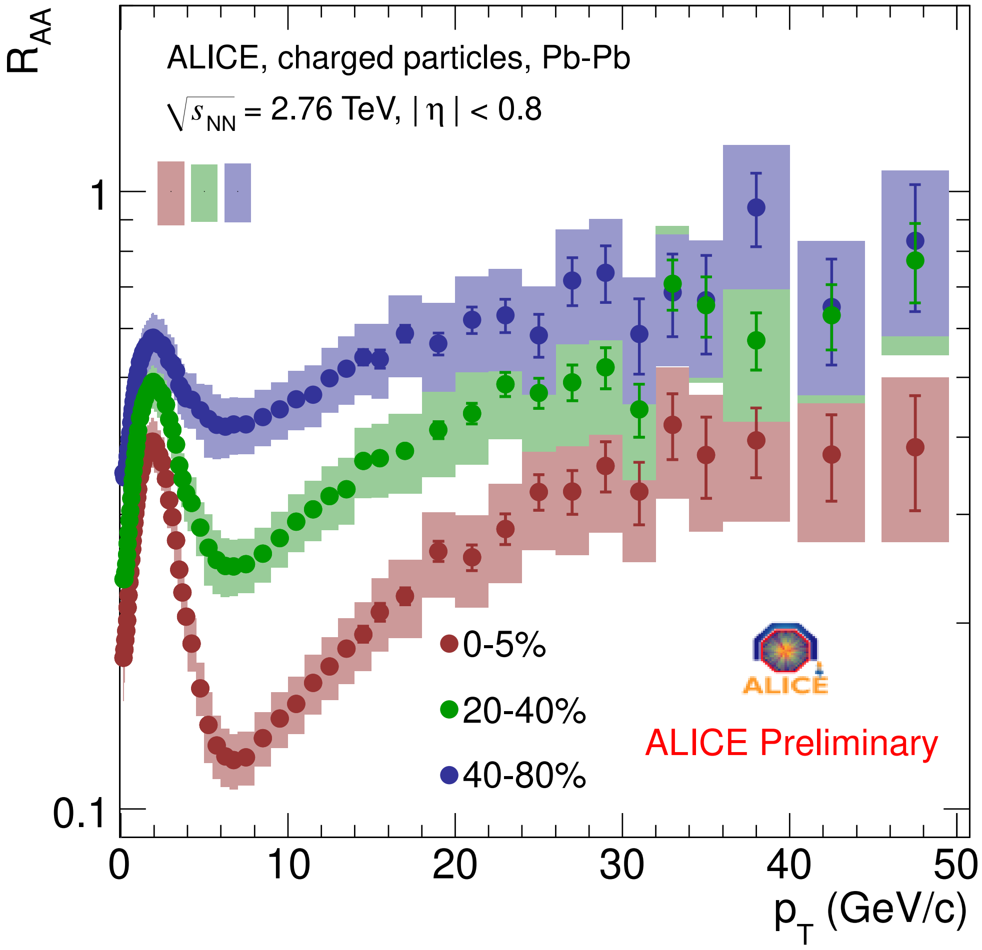

Figure 2.9: The nuclear modification factor R_{AA} for charged particles measured by the ALICE collaboration in PbPb collisions at $\sqrt{s_{NN}} = 2.76$ TeV with three different centrality selections [67].

momentum back-to-back partons are produced. The two partons propagate through the medium and interact with its constituents. In QCD a high-energy parton gives rise to a jet of collimated hadrons in the final state. Thus, in p-p collisions one can observe two jets in opposite azimuthal directions: if one measures a jet at a certain angle ϕ, one measures also another jet at an angle shifted by π, $\phi' = \phi + \pi$. Hence, taken a high-p_T trigger hadron, one will measure a lot of particles associated to it at angles $\Delta\phi \approx 0$ and $\Delta\phi \approx \pi$. In Fig. 2.11 the dark bars show the experimental results for pp

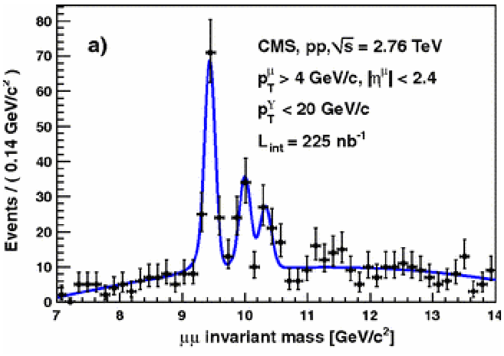

(a) *pp collion* (b) *PbPb Collision*

Figure 2.10: Di-muon invariant-mass distributions in pp and PbPb collisions at $\sqrt{s_{NN}} = 2.76$ TeV measured by the CMS collaboration [9].

collisions, in which two peaks are clearly visible. On the contrary in AA

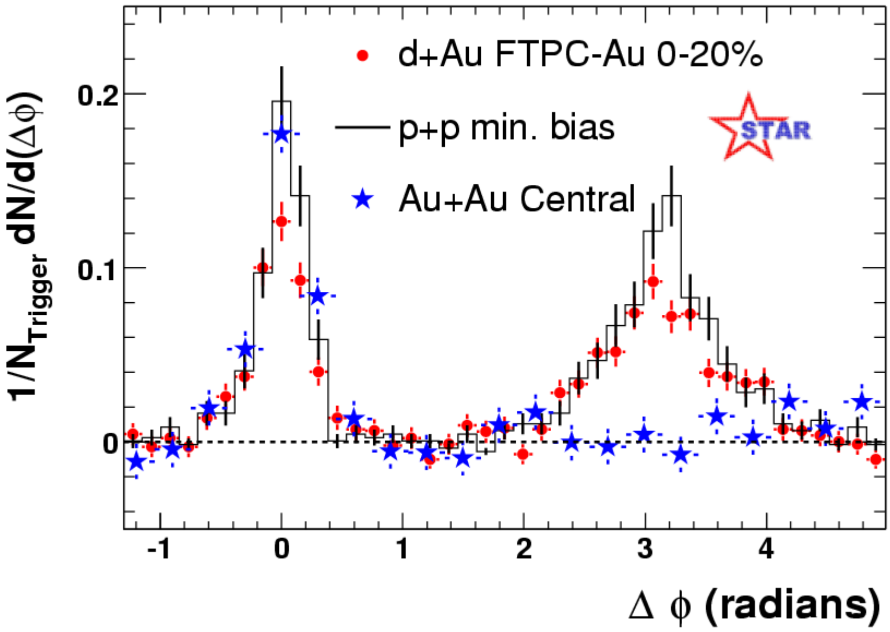

Figure 2.11: Two-particle azimuthal correlations in p-p (dark bars), d-Au (red points) and A-A (blue stars) collisions measured by the STAR collaboration. The p-p data show two peaks in opposite directions, while the A-A data display only one peak, because the second one is quenched by the presence of the medium.

collisions one can have a suppression of the away-side jet. At the level of the two-particle correlations displayed in Fig. 2.11 one observes a complete quenching of the away-side peak. The picture is the following: if two hard partons are produce near the border of the fireball, one goes out immediately and fragments in the vacuum, while the other one flies through the medium, interacts with its constituents and loses a lot of energy. The result is that the second peak in Fig. 2.11 gets suppressed, since the particles associated with the trigger hadron either have lost a lot of energy or have been moved to larger angles. From the suppression of jets and high-momentum hadrons one can extract further independent information on the size, temperature and transport coefficients of the medium.

Chapter 3

PNJL Model

As discussed in the previous chapter, for the description of the microscopic interactions that occur in the fireball and for the determination of the EoS necessary for the hydrodynamic simulations at non-zero baryon density one needs an Effective Field Theory compatible with lattice-QCD results at zero baryochemical potential.

For this purpose, during my PhD, I have focused my research on the Nambu-Jona-Lasinio model with Polyakov-loop corrections (PNJL model) with 2 light flavours (up and down) and 1 heavier quark (strange). The latter is an Effective Field Theory that can describe the low-energy interaction between quarks and, as discussed in the following, provide a dynamical mechanism for the breaking/restoration of chiral symmetry, embodying at the same time an effective confinement of quarks into color-singlet hadrons. The PNJL model is used in this thesis for the study of the chiral and deconfinement transitions, for the exploration of the QCD phase-diagram at high baryochemical potential and for the determination of the position of the Critical End Point (CEP) in such a Phase Diagram.

This chapter is organized as follow. In the next section I show the most general PNJL Lagrangian and I describe the symmetries and properties of the model. The regularization scheme used in this work and the fixing of the free parameters are also dealt with. Eventually, I discuss the different scenarios based on the possible relations among the three quark chemical potentials. In

Sec. 3.2 I introduce the Mean-Field approximation of the model, presenting the grand-canonical thermodynamic potential associated to the PNJL Lagrangian and its minimization with respect to the order parameters. In the end, in Secs. 3.2.3 and 3.3.1 I discuss the different thermodynamic quantities and the fluctuations of conserved charges, displaying their derivation from the grand-canonical potential.

3.1 PNJL Effective field theory

The PNJL effective model is based on the assumption that the only relevant gluon degree of freedom is the temporal component A_0 of the gauge field, which is replaced by the effective Polyakov field defined in the following. Moreover, the model includes several point-like quark vertices with quantum numbers suited to give rise to mesonic excitations in the different channels. In this section, I present the general formalism of the PNJL model and I discuss how the Polyakov potential is introduced, how the free parameters of the model are fixed and, finally, the different physical scenarios explored in the finite-density case.

3.1.1 Lagrangian

The results presented in this thesis are obtained within the framework of an extended $SU_f(3)$ PNJL Lagrangian, with 2+1 quark flavours. The quarks are coupled to a temporal background gauge field, more conveniently expressed in terms of the Polyakov loop [41–43]. The most general PNJL Lagrangian reads:

$$\begin{aligned} \mathcal{L} =& \bar{\psi}(i\not{D} - \hat{m})\psi + \frac{1}{2}G_S \sum_{a=0}^{8} \left[(\bar{\psi}\lambda^a\psi)^2 + (\bar{\psi}i\gamma^5\lambda^a\psi)^2\right] - \\ & - \frac{1}{2}G_V \sum_{a=0}^{8} \left[(\bar{\psi}\gamma_\mu\lambda^a\psi)^2 + (\bar{\psi}\gamma_\mu\gamma_5\lambda^a\psi)^2\right] + \\ & + K\{\det[\bar{\psi}(1+\gamma^5)\psi] + \det[\bar{\psi}(1-\gamma^5)\psi]\} - U(\Phi[A], \bar{\Phi}[A]; T) \end{aligned} \tag{3.1}$$

Here, $\psi = (u, d, s)^T$ is the quark-field in flavour space, with three flavours ($N_f = 3$) and tree colours ($N_c = 3$, not written explicitly), $\hat{m} = \mathrm{diag}(m_u, m_d, m_s)$ is the current-mass matrix of the quarks, λ^a are the $SU_f(3)$ Gell-Mann matrices ($a = 0, 1, ..., 8$) in flavour space, with $\lambda^0 \equiv \sqrt{\frac{2}{3}}\mathbb{1}$. The covariant derivative is defined as $D^\mu \equiv \partial^\mu - iA^\mu$, with $A^\mu = \delta^\mu_0 A^0$ (the so-called Polyakov Gauge); in Euclidean notation $A^0 = iA^E_4$. The usual QCD coupling g is absorbed in the definition of $A^\mu(x) \equiv g\mathcal{A}^\mu_a(x)\frac{\lambda^a}{2}$, where $\mathcal{A}^\mu_a(x)$ is the $SU_c(3)$ gauge field. The constants G_S and G_V are the coupling constants for the scalar/pseudoscalar and vector/axial-vector interaction respectively, K is the coupling constant for the six-fermion vertex responsible for the explicit breaking of the $U_A(1)$ symmetry. This last term is relevant to reproduce the correct masses of the pseudoscalar meson-octet and the $\eta - \eta'$ splitting.

Clearly, this Lagrangian is the generalization of the usual NJL Lagrangian of Ref. [63] already introduced in the previous chapters. As mentioned above, in this Lagrangian there are both 4-fermion and 6-fermion interactions, which provide independent contributions to the quark self-energy in the Hartree-Fock approximation. The last term in the Lagrangian is the effective Polyakov potential, which accounts for the gluon self-interaction. This object is a function of the Polyakov fields and of the temperature; in the next paragraph we discuss its functional form and its properties. It is easy to prove that the above PNJL Lagrangian – in the limit of vanishing current-mass of the quarks – is invariant under $U_V(N_f) \otimes SU_A(N_f)$ transformations. Then it is a convenient tool to study the dynamic breaking/restoration of chiral symmetry and the confinement/deconfinement transition.

Polyakov Potential

The Polyakov loop field Φ appearing in the potential term U in the Lagrangian is related to the gauge field through the following gauge-invariant average of the Polyakov line

$$\Phi(\vec{x}) \equiv \langle\langle l(\vec{x})\rangle\rangle = \frac{1}{N_c}\mathrm{Tr}_c\langle\langle L(\vec{x})\rangle\rangle, \tag{3.2}$$

where

$$L(\vec{x}) \equiv \mathcal{P}\exp\left[i\int_0^\beta d\tau A_4(\vec{x},\tau)\right]. \tag{3.3}$$

In the above, the symbol $\mathcal{P}$ represents the path-ordering of the operators appearing in the expansion of the exponential. The Polyakov loop is the order parameter used to identify the spontaneous breaking/restoration of the $\mathbb{Z}_3$ (the center of the $SU_c(3)$ group) symmetry of QCD, related to the deconfinement phase transition: the $\mathbb{Z}_3$ symmetry is broken in the deconfined phase ($\Phi \to 1$) and restored in the confined one ($\Phi \to 0$), as discussed in [1, 88, 100].

Here, it is important to make some remarks about the applicability of the PNJL model. An explicit gluon dynamics is absent in the model. The effects of gluons are hidden in the low-energy effective point-like interaction of quarks, in the potential U and in the coupling of quarks with the static background Polyakov-loop field Φ (see details in Refs. [51, 91]). This scenario cannot be expected to work outside a limited range of temperatures. Indeed, at large enough temperatures one expects that transverse gluons start to be active thermodynamic degrees of freedom, but they are not taken into account in the PNJL model. Since, as concluded in Ref.[75], transverse gluons start to contribute significantly to the thermodynamics for $T > 2.5T_c$, where T_c is the deconfinement temperature, we can assume that the range of applicability of the model is roughly limited to $T \lesssim 2T_c$.

One must provide an explicit expression for the effective potential U for the complex Φ field compatible with the $\mathbb{Z}_3$ symmetry of the Lagrangian and allowing the spontaneous breaking of the latter. Its coefficients must depend explicitly on the temperature (see e.g. Ref. [42, 86, 91, 94, 96]). Several parametrizations can be found in the literature. One possible parametrization for the Polyakov potential is the *polynomial* one of Ref. [91]. One has:

$$\frac{\mathcal{U}(\Phi,\bar{\Phi};T)}{T^4} = -\frac{b_2(T)}{2}\Phi\bar{\Phi} - \frac{b_3}{6}(\Phi^3+\bar{\Phi}^3) + \frac{b_4}{4}(\bar{\Phi}\Phi)^2, \tag{3.4}$$

where

$$b_2(T) = a_0 + a_1\left(\frac{T_0}{T}\right) + a_2\left(\frac{T_0}{T}\right)^2 + a_3\left(\frac{T_0}{T}\right)^3. \tag{3.5}$$

Another possible parametrization is the *logarithmic* one proposed in [94]:

$$\frac{\mathcal{U}(\Phi,\bar{\Phi};T)}{T^4} = -\frac{a(T)}{2}\bar{\Phi}\Phi + b(T)\ln[1-6\bar{\Phi}\Phi+4(\Phi^3+\Phi^3)-3(\bar{\Phi}\Phi)^2], \tag{3.6}$$

where

$$a(T) = a_0 + a_1\left(\frac{T_0}{T}\right) + a_2\left(\frac{T_0}{T}\right)^2 \qquad \text{and} \qquad b(T) = b_3\left(\frac{T_0}{T}\right)^3. \tag{3.7}$$

Polynomial	a_0	a_1	a_2	a_3	b_3	b_4
	6.75	-1.95	2.625	-7.44	0.75	7.5
Logarithmic	a_0	a_1	a_2	b_3		
	3.51	-2.47	15.22	-1.75		

Table 3.1: Parameters of the Polyakov potential $\mathcal{U}$

These parameters have been fixed in order to reproduce the results of lattice-QCD simulations for the expectation value of the Polyakov loop and for the various thermodynamic quantities in the pure gauge sector [59, 60]. The parameter T_0 is the critical temperature for the deconfinement phase transition in the pure-gauge theory: it was fixed to 270 MeV, according to lattice findings. Different criteria for fixing T_0 are available in the literature, like in Ref. [43], where an explicit N_f dependence of T_0 is proposed using renormalization group arguments. In this work, following Ref. [49], I fix $T_0 = 182$ MeV.

3.1.2 Regularization scheme

The Lagrangian (3.1) contains several point-like interaction terms that produce divergent integrals in the quark self-energy, in the thermodynamic quantities and in the calculation of mesonic masses. This kind of interactions in (3+1)D space-time makes the (P)NJL model a non-renormalizable theory with dimensionful couplings. A non-renormalizable model is not unique per se, but it depends on the regularization scheme chosen to perform the calculations preserving the symmetries of the theory. On the contrary, in a renormalizable theory the regularization is just a way of making divergent quantities finite in the intermediate calculations, but then any dependence on the ultraviolet regulator disappears in the final result.

The simplest regularization scheme in the (P)NJL model is the introduction of a three-momentum ultraviolet cutoff in the divergent integrals, as done in the original paper by Nambu–Jona-Lasinio [80]. The different regularization schemes proposed in the literature are: non-covariant three-momentum cutoff, four-momentum cutoff in Euclidean space, regularization in proper time and the Pauli-Villars methods. In all cases the value of the UV cutoff is one of the parameters of the model, together with the current quark masses m_f and the coupling constants G_i and K. In this thesis the simple three-momentum ultraviolet cutoff is adopted. The free parameters of the model are fixed (in the case of a simple scalar/pseudoscalar interaction) to reproduce the masses and decay constants of pions (m_π, and f_π) and kaons (m_K and f_K). Here I show how the ultraviolet cutoff is used to regularize the divergent integrals. The point-like interactions give rise to several terms in the mass gap-equation represented diagrammatically in Fig. 3.1. The bubbles in the figure, after the rotation to imaginary time and summation over the Matsubara frequencies, represent the following integral

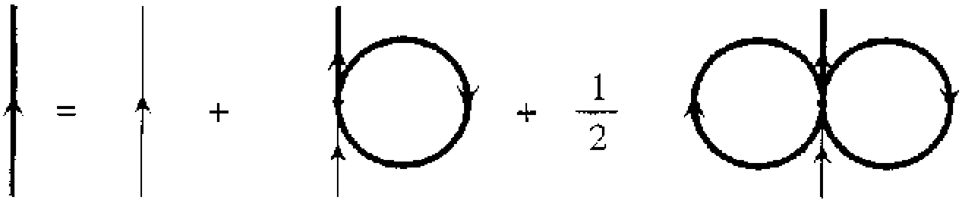

Figure 3.1: Feynman diagrams for the PNJL mass gap-equation

$$I_i = \int \frac{d^3p}{(2\pi)^3} \frac{M_i}{E_i} \big[1 - f_\Phi^{i+}(p,\mu_i) - f_\Phi^{i-}(p,\mu_i)\big], \tag{3.8}$$

where i is the quark flavor index, M_i is the dressed quark mass, $E_i = \sqrt{p^2 + M_i^2}$ is the single-particle energy, the functions $f_\Phi^{i\pm}$ are the modified Fermi functions defined in Sec. 3.1.3. These functions are exponentially suppressed for $|p| \to +\infty$. The first term in the integral diverges quadratically. To regularize the integral, the ultraviolet cutoff Λ is introduced. One then obtains

$$I_i = \int_0^\Lambda \frac{dpp^2}{2\pi^2} \frac{M_i}{E_i} - \int \frac{d^3p}{(2\pi)^3} \frac{M_i}{E_i} \big[f_\Phi^{i+}(p,\mu_i) + f_\Phi^{i-}(p,\mu_i)\big]. \tag{3.9}$$

The divergent part of the integral is regularized by the three-momentum cutoff (that breaks the Lorentz invariance). This criterium is adopted for all divergent integrals.

3.1.3 Gap equations

In this thesis the values of the couplings G_S, G_V and K, of the current masses m_i ($i = u, d, s$) of the quarks and of the UV cutoff Λ are fixed by the values of the pion and kaon masses ($m_\pi = 139$ MeV, $m_K = 495$ MeV) and of the pion and kaon decay constants ($f_\pi = 93.3$MeV, $f_K = 96.3$MeV) at zero temperature. In the case of non-zero vector interaction $G_V \neq 0$ one sets its value in order to reproduce also the spectrum of the lightest vector mesons. Notice that the presence of a vector interaction induces a mixing of the pseudoscalar and axial-vector channels in the quark-antiquark scattering matrix, so that all the parameters have to be refitted. The set of parameters is collected in Table 3.2 (for more details see Ref.[34]).

Λ (MeV)	$G_S\Lambda^2$	$K\Lambda^5$	G_V/G_S	$m_{u/d}$ (MeV)	m_s (MeV)
602.3	3.67	-12.36	0	5.5	140.7
750	3.647	-8.79	1.05	3.6	87.0

Table 3.2: Values of free parameters in the quark sector of the PNJL model adopted in this thesis with and without vector interaction.

In order to study in the grand-canonical ensemble a system composed by a large amount of particles that carry conserved charges (baryon number, electric charge and strangeness in the case of strong interactions) one should add a new term to the Lagrangian (3.1) which allows one to derive the proper thermodynamic potential. One has

$$\mathcal{L}_{\text{PNJL}}^{\text{GC}} = \mathcal{L}_{\text{PNJL}} + \psi^\dagger \hat{\mu} \psi, \tag{3.10}$$

where $\hat{\mu} = \text{diag}(\mu_u, \mu_d, \mu_s)$ is the chemical potential matrix. This matrix is diagonal in flavor space and it is associated to the conservation of the separate quark flavors i. As discussed in the following, this term can be absorbed in the covariant derivative as:

$$D^{\nu} = \partial^{\nu} - iA^{\nu}\delta^{0}_{\nu} - i\hat{\mu}\gamma^{\nu}\delta^{0}_{\nu}. \tag{3.11}$$

It means that one can consider the chemical potential as a correction to the temporal components of the gauge field.

Self-energy and Gap equations

In this thesis I use the Hartree-Fock approximation to calculate the self-energy of quarks that propagate in a static background Polyakov field, as introduced in Sec. 1.6.2. The resulting propagators are used to study the thermodynamics of the PNJL model.

Following Ref. [63] one can rewrite the Lagrangian (3.10) in terms of a self-energy arising from the 4-fermion and 6-fermion interaction terms as follows:

$$\mathcal{L} = \bar{\psi}(i\not{D} - \hat{m})\psi - \bar{\psi}\Sigma^{(4)}\psi - \bar{\psi}\Sigma^{(6)}\psi - U(\Phi, \bar{\Phi}; T). \tag{3.12}$$

The two contributions to the self-energy of the quarks of flavour i read

$$\Sigma^{(4)} = 2iG_S N_c \mathrm{Tr} S^{i} \tag{3.13}$$

and

$$\Sigma^{(6)} = K(2N_c^2 + 3N_c + 1)(\mathrm{Tr}S^{j})(\mathrm{Tr}S^{k}) \qquad i \neq j \neq k, \tag{3.14}$$

respectively, where S^i is the quark propagator of flavour i in coordinate space evaluated at zero separation. This leads to the bilinear terms in the Hartree-Fock mean-field Lagrangian

$$-\bar{\psi}_j[2iG_S N_c \mathrm{Tr}S^{j}]\psi_j \tag{3.15}$$

and

$$-\bar{\psi}_i[K(2N_c^2 + 3N_c + 1)(\mathrm{Tr}S^{j})(\mathrm{Tr}S^{k})]\psi_i \qquad i \neq j \neq k \tag{3.16}$$

where i, j, k are the flavor indices. The total quark self-energy in the Hartree-

Fock approximation, for a given quark flavour i, is then

$$\Sigma_i = 2iG_S N_c \mathrm{Tr} S^i + K(2N_c^2 + 3N_c + 1)\mathrm{Tr} S^j \mathrm{Tr} S^k \qquad i \neq j \neq k. \tag{3.17}$$

For more details see Ref. [63]. Assuming that $GN_c \sim O(1)$ and $KN_c^2 \sim O(1)$, a consistent $1/N_c$ expansion requires setting

$$\Sigma = M_i - m_i = 2iGN_c \mathrm{Tr} S^i + 2KN_c^2 \mathrm{Tr} S^j \mathrm{Tr} S^k \qquad i \neq j \neq k. \tag{3.18}$$

One can define $\phi_i \equiv -iN_c \mathrm{Tr} S_i$ and then the quark gap-equations read

$$M_i = m_i - 2G\phi_i - 2K\phi_j\phi_k \qquad i \neq j \neq k. \tag{3.19}$$

In this calculation, the vector interaction does not enter explicitly. This is due to the the fact that the expectation value of the spatial components $\langle \bar{\psi}\gamma^i\lambda^a\psi\rangle$, of relevance in the mean-field approximation, vanishes and the one of the diagonal elements of the temporal part $\langle \bar{\psi}\gamma^0\lambda^a\psi\rangle$ $(a = 0, 3, 8)$ contributes simply to a shift of the chemical potential of the various quark flavours. In the mean field approximation one obtains then:

$$\hat{\mu}_i = \mu_i - 2G_V n_i, \qquad n_i = \langle \psi_i^\dagger \psi_i \rangle. \tag{3.20}$$

Here i is the flavour index and n_i is the density of quarks of flavour i. At finite quark density, besides the 3 gap equations connecting the effective masses with the chiral condensates, there are other 3 equations connecting the densities with the chemical potentials. Notice that, in light of the shift of the chemical potentials in Eq. (3.20), in the presence of a vector interaction it is convenient to run the numerical code using temperature and density as independent variables instead of temperature and chemical potential as in the scalar/pseudoscalar case. A standard thermal-field-theory calculation provides the following form of the equations for the chiral condensate ϕ_i and the quark density n_i:

$$\phi_i(T,\hat{\mu}_i) \equiv -N_c \int \frac{dpp^2}{2\pi^2} \frac{M_i}{E_i} \left[\theta(\Lambda - p) - f_\Phi^{i+}(p,T,\hat{\mu}_i) - f_\Phi^{i-}(p,T,\hat{\mu}_i)\right] \quad (3.21)$$

$$n_i(T,\hat{\mu}_i) \equiv 2N_c \int \frac{dpp^2}{2\pi^2} \left[f_\Phi^{i+}(p,T,\hat{\mu}_i) - f_\Phi^{i-}(p,T,\hat{\mu}_i)\right] . \quad (3.22)$$

Here $\theta(\Lambda - p)$ is the Heaviside theta function that regularizes the divergent vacuum integral and $f_\Phi^{i\pm}$ are the modified Fermi functions arising from the coupling of the quarks with the background Polyakov field defined as:

$$f_\Phi^{+i}(E_i,T,\hat{\mu}_i) = \frac{\Phi e^{-\beta(E_i-\hat{\mu}_i)} + 2\bar{\Phi} e^{-2\beta(E_i-\hat{\mu}_i)} + e^{-3\beta(E_i-\hat{\mu}_i)}}{1 + N_c(\Phi + \bar{\Phi} e^{-\beta(E_i-\hat{\mu}_i)})e^{-\beta(E_i-\hat{\mu}_i)} + e^{-3\beta(E_i-\hat{\mu}_i)}} \quad (3.23)$$

$$f_\Phi^{-i}(E_i,T,\hat{\mu}_i) = \frac{\bar{\Phi} e^{-\beta(E_i+\hat{\mu}_i)} + 2\Phi e^{-2\beta(E_i+\hat{\mu}_i)} + e^{-3\beta(E_i+\hat{\mu}_i)}}{1 + N_c(\bar{\Phi} + \Phi e^{-\beta(E_i+\hat{\mu}_i)})e^{-\beta(E_i+\hat{\mu}_i)} + e^{-3\beta(E_i+\hat{\mu}_i)}} . \quad (3.24)$$

Here I set $\beta \equiv 1/T$. For more details on the derivation of these formulas one can see Appendix C.

3.1.4 Possible theoretical scenarios

In this thesis I explore the QCD phase-diagram in terms of the temperature and chemical potential. In the PNJL model with 2+1 light flavours there are three different chemical potentials, each one related to a different species of quark. Moreover, it is possible to rewrite these quark chemical potentials in terms of conserved-charge chemical potentials. The conserved charges considered in this work are the net baryon number (B), the electric charge (Q) and the net strangeness number (S). The term *net* indicates that they arise from the difference of the number of quarks and anti-quarks, that carry opposite charges. The relations between quark chemical potentials and conserved-charge chemical potentials are shown below and arise from the baryon number, electric charge and strangeness of each quark flavour (notice that, for historical reasons, the strangeness of a s quark is -1):

$$\mu_u = \frac{1}{3}\mu_B + \frac{2}{3}\mu_Q \tag{3.25}$$

$$\mu_d = \frac{1}{3}\mu_B - \frac{1}{3}\mu_Q \tag{3.26}$$

$$\mu_s = \frac{1}{3}\mu_B - \frac{1}{3}\mu_Q - \mu_S \; . \tag{3.27}$$

One must pay attention to the difference between μ_s and μ_S. The first one is the chemical potential associated to strange quarks, the second one is the chemical potential associated to net-strangeness number.

From a general point of view, the QCD phase-diagram is a 4-dimensional space (3 independent chemical potentials and the temperature). In order to simplify the exploration of this space it is useful to fix the values of two of the above chemical potentials according to the physical constraints posed by the system one is considering (e.g. heavy-ion collisions, compact stars...). One can refer to this choices as different *theoretical scenarios*. In this thesis 4 different theoretical scenarios are explored:

- **Fully-symmetric scenario** $\mu_Q = 0, \;\; \mu_S = 0$

  All quark chemical potentials are equal, the phase diagram is a plane spanned by the axis of baryo-chemical potential μ_B and the one of temperature. This is the most common scenario found in the literature.

- **Quasi-Neutral-Strangeness scenario** $\mu_Q = 0, \;\; \mu_S = \frac{1}{3}\mu_B$

  The up and down quark chemical potentials (as well as their current masses) are equal and then also their self-consistent effective masses. The strange quark chemical potential is zero. Again there is only one independent chemical potential: the net-baryon one μ_B. In the pure NJL model this scenario would correspond to a situation of zero net-strangeness, since there would be an equal density of strange quarks and antiquarks. Notice that at finite baryon density the zero-strangeness scenario does not corresponds to $\mu_S = 0$, since a fraction a particles carrying baryon number carry also non-zero strangeness. However, in the PNJL model, in this scenario the net-strangeness density does not vanish, since the Polyakov fields mix the various chemical potentials as discussed in Sec. 3.2.1.

- **Neutral-strangeness scenario** $\mu_Q = 0,\ \mu_S \mid n_S = 0$
  We still take the up and down chemical potentials (and current masses) equal, but now we impose the constraint of vanishing net-strangeness density. This means that in solving the mean-field equations one must impose a new condition, $n_S = 0$, that promotes the net-strangeness chemical potential to an implicit function of μ_B and T defining the surface $\mu_S = \mu_S(T, \mu_B)$. In the NJL model this scenario coincides with the previous one due to the absence of mixing induced by the Polyakov fields.

- **Heavy-Ion Collision scenario** $\mu_Q \mid n_Q/n_B = 0.4,\ \mu_S \mid n_S = 0$
  Taking the baryo-chemical potential μ_B and the temperature T as independent variables, μ_Q and μ_S are obtained solving the self-consistent mean-field equations setting the physical constraints $n_Q/n_B = 0.4$ and $n_S = 0$. This is the scenario closer to the situation at nuclear colliders, the ratio between the net-electric-charge density and net-baryon density being fixed to the proton-to-nucleon ratio in the $^{208}_{82}\mathrm{Pb}$ and $^{197}_{79}\mathrm{Au}$ nuclei used in heavy-ion collisions and the initial net-strangeness being zero. Due to the conservation of B, Q and S, the produced fireball has the same ratios among conserved charges as the stopped incoming matter. In this case, the up and down quarks do not have the same density and effective mass.

In Sec. 4 I show the results of calculations of various thermodynamic quantities in the different scenarios just discussed and how the phase diagram of the corresponding systems changes.

3.2 PNJL Thermodynamics

In order to explore the behaviour of a hot and dense system composed of a large number of particles, it is useful to introduce some thermodynamics concepts. In particular the concept of Grand Canonical Ensemble: a statistical ensemble that is used to represent the possible states of a mechanical system of particles that are in thermodynamic equilibrium with a reservoir. The system is open, in the sense that it can exchange particles and energy with the external environment. The number of particles and energy are not conserved exactly but only their average values are. This concept is useful for the study of the QGP, because the system created in HIC's is large, the detector does not cover the full solid angle and hence the measured particles can fluctuate event-by-event. As discussed in the previous section, in this case the conservation of particle number has to be interpreted as referring to the net number of quarks of different flavours.

From a mathematical point of view, the Grand Canonical Ensemble is described by the grand canonical partition function

$$\mathcal{Z} = \mathrm{Tr}\{e^{-\beta(H-\mu N)}\}, \tag{3.28}$$

where H is the Hamiltonian of the system and N is the number of particles. In the relativistic case one has to replace

$$\mu N \quad \longrightarrow \quad \sum_i \mu_i Q_i, \tag{3.29}$$

where the index i refers to the different charges conserved by the Lagrangian of the system. For the present general discussion I consider the case of a single conserved charge. Starting from the grand canonical partition function defined in Eq. (3.28), one can derive all the different thermal averages:

$$\langle E\rangle = \frac{1}{\mathcal{Z}}\mathrm{Tr}\{He^{-\beta(H-\mu N)}\} \tag{3.30}$$

$$\langle N\rangle = \frac{1}{\mathcal{Z}}\mathrm{Tr}\{Ne^{-\beta(H-\mu N)}\} \tag{3.31}$$

These two equations can be rewritten in terms of partial derivatives of $\mathcal{Z}$. Defining $\tilde{\mu} \equiv \mu/T$ one has

$$\langle E\rangle = -\frac{\partial}{\partial\beta}\log\mathcal{Z}\bigg|_{\tilde{\mu}} \tag{3.32}$$

$$\langle N\rangle = \frac{\partial}{\partial\tilde{\mu}}\log\mathcal{Z}\bigg|_{T}. \tag{3.33}$$

It is useful to introduce a new function called grand-canonical thermodynamic potential Ω:

$$\Omega \equiv -T\log\mathcal{Z}. \tag{3.34}$$

The latter will be the quantity to minimize to derive the mean-field equations and which will be used as the starting point for the study of the thermodynamics of the PNJL model

Grand Canonical Potential in the PNJL model

From the complete PNJL Lagrangian of Eq. (3.10) it is possible to obtain the grand-canonical thermodynamic potential, for instance via the method of coupling constant integration explained by Fetter and Walecka in Ref. [38]. The grand canonical potential is an extensive quantity, directly proportional to the volume of system. It is useful to factorize this trivial dependence, introducing the grand canonical potential density $\omega \equiv \Omega/V$. In full generality, the grand-canonical potential density of the PNJL model in mean-field approximation reads

$$\begin{aligned}\omega(\Phi,\bar{\Phi},\phi_i,n_i;T,\mu_i) &= \mathcal{U}[\Phi,\bar{\Phi};T] + G_S\sum_{i=u,d,s}\phi_i^2 - G_V\sum_{i=u,d,s}n_i^2 + 4K\phi_u\phi_d\phi_s \\ &-2\sum_{i=u,d,s}\int_\Lambda\frac{d^3p}{(2\pi)^3}\Big\{N_cE_i + T\big[z_\Phi^{i+}(E_i,T,\hat{\mu}_i) + z_\Phi^{i-}(E_i,T,\hat{\mu}_i)\big]\Big\};,\end{aligned} \tag{3.35}$$

where, in order to deal with the case of non-vanishing vector coupling G_V, the effective chemical potentials $\hat{\mu}_i \equiv \mu_i - 2G_Vn_i$ are introduced. Here two new function $z_\Phi^{i\pm}$, related to the modified Fermi functions already discussed, are introduced. Their analytic expression is:

$$z_\Phi^{i+}(E_i,T,\hat{\mu}_i) = \log\left\{1+N_c(\Phi+\bar{\Phi}e^{-\beta(E_i-\hat{\mu}_i)})e^{-\beta(E_i-\hat{\mu}_i)}+e^{-3\beta(E_i-\hat{\mu}_i)}\right\} \quad (3.36)$$

$$z_\Phi^{i-}(E_i,T,\hat{\mu}_i) = \log\left\{1+N_c(\bar{\Phi}+\Phi e^{-\beta(E_i+\hat{\mu}_i)})e^{-\beta(E_i+\hat{\mu}_i)}+e^{-3\beta(E_i+\hat{\mu}_i)}\right\}. \quad (3.37)$$

From a mathematical point of view, the grand canonical potential density ω is a function of 12 variables: the temperature, 3 quark chemical potentials (μ_i), 3 chiral condensates (ϕ_i), 3 quark densities (n_i) and 2 Polyakov fields ($\bar{\Phi}$, Φ). However, not all of them are really independent. For instance, minimizing the thermodynamic potential with respect to the quark densities n_i, one gets back Eq. (3.22), connecting flavour densities and chemical potentials. Notice that, depending on the considered scenario, it may be more convenient to use as independent variables either the quark chemical potentials μ_i, or the quark densities $n_i \equiv \langle\psi_i^\dagger\psi_i\rangle$ or the effective chemical potentials $\hat{\mu}_i$. Furthermore, applying physical constraints like the knowledge of the n_S/n_B and n_Q/n_B ratios, only one of the chemical potentials (the one associated to baryon number) is really independent of the others. One is left with 7 independent variables. At fixed temperature T and baryochemical potential μ_B one can fix the physical values of the other 5 variables by minimizing the grand-canonical potential with respect to the quark condensates ϕ_i and the Polyakov fields Φ and $\bar{\Phi}$. The equations obtained in this way are called Mean Field Equations (MFE's) and they will be discussed in the following section.

3.2.1 Mean field equations

As discussed in the previous section, the grand canonical thermodynamic potential depends on two kinds of variables: the internal ones (chiral condensates, Polyakov fields and quark densities) and the external ones (chemical potentials and temperature). The physical values of the internal variables are obtained by minimizing the grand canonical potential Ω. From the minimization one obtains a system of 8 (5 in the case of only scalar/pseudoscalar interaction, in which the quark densities do not enter explicitly into the evaluation of the other quantities) coupled equations. Together they form the set of mean-field equations. In the following I show the MFE's for the case $G_V = 0$. In this case the internal variables are the 3 chiral condensates and the 2 Polyakov fields; the quark densities are not involved in the minimization of the thermodynamic potential and can be calculated a posteriori from Eq. (3.22). When one performs the derivative of Ω defined in Eq. (3.35) with respect to the chiral condensates, one obtains a coupled system of 3 equations. It is possible to reorganize the system as follows

$$\begin{cases} 2G(\phi_u + 2N_c I_u) + 2K\phi_s(\phi_d + 2N_c I_d) + 2K\phi_d(\phi_s + 2N_c I_s) = 0 \\ 2G(\phi_d + 2N_c I_d) + 2K\phi_s(\phi_u + 2N_c I_u) + 2K\phi_u(\phi_s + 2N_c I_s) = 0 \\ 2G(\phi_s + 2N_c I_s) + 2K\phi_u(\phi_d + 2N_c I_d) + 2K\phi_d(\phi_u + 2N_c I_u) = 0, \end{cases} \tag{3.38}$$

where the *quark mass integral* I_i defined as

$$I_i \equiv \int_\Lambda \frac{d^3p}{(2\pi)^3} \frac{M_i}{E_i} [1 - f_\Phi^{i+}(E_i, T, \mu_i) - f_\Phi^{i-}(E_i, T, \mu_i)] \tag{3.39}$$

was introduced. In the above the effective quark mass of flavour i is expressed in terms of all the quark condensates according to the definition in Eq. (3.19). It is clear that the system is solved if all the brackets are zero. It is possible to prove this using Gauss method for a coupled system of equations. The procedure is not difficult but is boring and is shown in Appendix D.

The system of MFE's becomes then:

$$\begin{cases} \phi_u + 2N_c \int_\Lambda \frac{d^3p}{(2\pi)^3} \frac{M_u}{E_u} [1 - f_\Phi^{+u}(E_u, \mu_u) - f_\Phi^{-u}(E_u, \mu_u)] = 0 \\ \\ \phi_d + 2N_c \int_\Lambda \frac{d^3p}{(2\pi)^3} \frac{M_d}{E_d} [1 - f_\Phi^{+d}(E_d, \mu_d) - f_\Phi^{-d}(E_d, \mu_d)] = 0 \\ \\ \phi_s + 2N_c \int_\Lambda \frac{d^3p}{(2\pi)^3} \frac{M_s}{E_s} [1 - f_\Phi^{+s}(E_s, \mu_s) - f_\Phi^{-s}(E_s, \mu_s)] = 0 \\ \\ \frac{\partial \mathcal{U}}{\partial \Phi} + \frac{2Nc}{T^3} \sum_i \int_\Lambda \frac{d^3p}{(2\pi)^3} [g_\Phi^{+i} + g_\Phi^{-i}] = 0 \\ \\ \frac{\partial \mathcal{U}}{\partial \bar{\Phi}} + \frac{2Nc}{T^3} \sum_i \int_\Lambda \frac{d^3p}{(2\pi)^3} [h_{\bar{\Phi}}^{+i} + h_{\bar{\Phi}}^{-i}] = 0 \ . \end{cases} \tag{3.40}$$

In writing this system I have introduced the following new functions

$$\begin{aligned} f_\Phi^{+i}(E_i, \mu_i) &\equiv -\frac{T}{N_c} \frac{\partial}{\partial E_i} z_\Phi^{+i}(E_i, \mu_i) = \\ &= \frac{\Phi e^{-\beta(E_i-\mu_i)} + 2\bar{\Phi} e^{-2\beta(E_i-\mu_i)} + e^{-3\beta(E_i-\mu_i)}}{1 + N_c(\Phi + \bar{\Phi} e^{-\beta(E_i-\mu_i)}) e^{-\beta(E_i-\mu_i)} + e^{-3\beta(E_i-\mu_i)}} \end{aligned} \tag{3.41}$$

$$\begin{aligned} f_\Phi^{-i}(E_i, \mu_i) &\equiv -\frac{T}{N_c} \frac{\partial}{\partial E_i} z_\Phi^{-i}(E_i, \mu_i) = \\ &= \frac{\bar{\Phi} e^{-\beta(E_i+\mu_i)} + 2\Phi e^{-2\beta(E_i+\mu_i)} + e^{-3\beta(E_i+\mu_i)}}{1 + N_c(\bar{\Phi} + \Phi e^{-\beta(E_i+\mu_i)}) e^{-\beta(E_i+\mu_i)} + e^{-3\beta(E_i+\mu_i)}} \end{aligned} \tag{3.42}$$

$$\begin{aligned} g_\Phi^{+i}(E_i, \mu_i) &\equiv \frac{1}{N_c} \frac{\partial}{\partial \Phi} z_\Phi^{+i}(E_i, \mu_i) = \\ &= \frac{e^{-\beta(E_i-\mu_i)}}{1 + N_c(\Phi + \bar{\Phi} e^{-\beta(E_i-\mu_i)}) e^{-\beta(E_i-\mu_i)} + e^{-3\beta(E_i-\mu_i)}} \end{aligned} \tag{3.43}$$

$$\begin{aligned} g_\Phi^{-i}(E_i, \mu_i) &\equiv \frac{1}{N_c} \frac{\partial}{\partial \Phi} z_\Phi^{-i}(E_i, \mu_i) = \\ &= \frac{e^{-2\beta(E_i+\mu_i)}}{1 + N_c(\bar{\Phi} + \Phi e^{-\beta(E_i+\mu_i)}) e^{-\beta(E_i+\mu_i)} + e^{-3\beta(E_i+\mu_i)}} \end{aligned} \tag{3.44}$$

$$\begin{aligned} h_\Phi^{+i}(E_i,\mu_i) &\equiv \frac{1}{N_c}\frac{\partial}{\partial\bar{\Phi}} z_\Phi^{+i}(E_i,\mu_i) = \\ &= \frac{e^{-2\beta(E_i-\mu_i)}}{1+N_c(\Phi+\bar{\Phi}e^{-\beta(E_i-\mu_i)})e^{-\beta(E_i-\mu_i)}+e^{-3\beta(E_i-\mu_i)}} \end{aligned} \tag{3.45}$$

$$\begin{aligned} h_\Phi^{-i}(E_i,\mu_i) &\equiv \frac{1}{N_c}\frac{\partial}{\partial\bar{\Phi}} z_\Phi^{-i}(E_i,\mu_i) = \\ &= \frac{e^{-\beta(E_i+\mu_i)}}{1+N_c(\bar{\Phi}+\Phi e^{-\beta(E_i+\mu_i)})e^{-\beta(E_i+\mu_i)}+e^{-3\beta(E_i+\mu_i)}}\ . \end{aligned} \tag{3.46}$$

Notice that in the $\Phi \to 1$ and $\bar{\Phi} \to 1$ limit, i.e. when confinement effects are absent, the functions $f_\Phi^{\pm i}$ reduce to standard Fermi distributions for quarks/antiquarks of flavour i.

To solve these equations one needs a numerical implementation, but it is possible to extract some analytical properties of the internal variables. The most important are:

1. $\Phi(\mu_i = 0) = \bar{\Phi}(\mu_i = 0)$
2. $\left.\frac{\partial\phi_i}{\partial\mu_i}\right|_{\mu_i=0} = 0$
3. $\Phi(-\mu_i) = \bar{\Phi}(\mu_i)$
4. $\phi_i(\mu_i)$ is an even function of μ_i

The last two proprieties are the realization of the CPT symmetry in the PNJL model. These analytical proprieties provide a check of the correct numerical solution of the system.

The MFE's perform a reduction of the grand-canonical thermodynamic potential density as shown in the follow diagram:

$$\begin{aligned} &\{\phi_i,\Phi,\bar{\Phi}\} \xrightarrow{\text{MFE's}} \{\phi_i(T,\mu_i),\Phi(T,\mu_i),\bar{\Phi}(T,\mu_i)\} \\ &\omega:\mathbb{R}^9\to\mathbb{R} \xrightarrow{\text{MFE's}} \bar{\omega}:\mathbb{R}^4\to\mathbb{R} \end{aligned} \tag{3.47}$$

The internal variables are promoted to real functions of the external variables and the grand canonical potential density now depends only on external variables. The relation of the general grand canonical potential and the minimized one is given by

$$\bar{\omega}(T,\mu_i) \equiv \omega(\phi_i,\Phi,\bar{\Phi};T,\mu_i)|_{\text{MFE's}}\ . \tag{3.48}$$

If one could solve the MFE's analytically, one would know the dependence of the chiral condensates and of the Polyakov fields on the external variables, as well as the analytic expression of the minimized grand canonical potential. Unfortunately this is not possible and the analytic form of $\bar{\omega}$ is not known. It is important to take this into account when performing higher order derivatives of the mean-field grand canonical potential density with respect to the external variables, taking into account both the explicit dependence and the one contained in the internal variables.

Numerical Algorithm

To find the solution of the MFE's at fixed values of temperature and chemical potentials I developed a numerical code based on the Newton-Raphson algorithm. In this algorithm, an important role is played by the Jacobian matrix of the coupled system of equations. Its expression, in the absence of a vector/axial-vector interaction, is shown below:

$$J = \begin{pmatrix}
1-2GC_{1,1} & -2K\phi_s C_{1,1} & -2K\phi_d C_{1,1} & -C_{1,4} & -C_{1,5} \\[2ex]
2K\phi_s C_{2,2} & 1-2GC_{2,2} & -2K\phi_u C_{2,2} & -C_{2,4} & -C_{2,5} \\[2ex]
-2K\phi_d C_{3,3} & -2K\phi_u C_{3,3} & 1-2GC_{3,3} & -C_{3,4} & -C_{3,5} \\[2ex]
\begin{array}{l} -2GC_{1,4}- \\ -2K\phi_s C_{2,4}- \\ -2K\phi_d C_{3,4} \end{array} &
\begin{array}{l} -2K\phi_s C_{1,4}- \\ -2GC_{2,4}- \\ -2K\phi_u C_{3,4} \end{array} &
\begin{array}{l} -2K\phi_d C_{1,4}- \\ -2K\phi_u C_{2,4}- \\ -2GC_{3,4} \end{array} &
\frac{\partial^2\mathcal{U}(\Phi,\bar{\Phi},T)}{\partial\Phi^2} - C_{4,4} &
\frac{\partial^2\mathcal{U}(\Phi,\bar{\Phi},T)}{\partial\Phi\partial\bar{\Phi}} - C_{4,5} \\[2ex]
\begin{array}{l} -2GC_{1,5}- \\ -2K\phi_s C_{2,5}- \\ -2K\phi_d C_{3,5} \end{array} &
\begin{array}{l} -2K\phi_s C_{1,5}- \\ -2GC_{2,5}- \\ -2K\phi_u C_{3,5} \end{array} &
\begin{array}{l} -2K\phi_d C_{1,5}- \\ -2K\phi_u C_{2,5}- \\ -2GC_{3,5} \end{array} &
\frac{\partial^2\mathcal{U}(\Phi,\bar{\Phi},T)}{\partial\Phi\partial\bar{\Phi}} - C_{4,5} &
\frac{\partial^2\mathcal{U}(\Phi,\bar{\Phi},T)}{\partial\Phi^2} - C_{5,5}
\end{pmatrix}$$

In the above matrix I introduced the following functions ($i = 1, 2, 3$):

$$\begin{aligned}
C_{i,i} &= \frac{N_c}{\pi^2}\left\{\int_0^{\Lambda} dp\, \frac{p^4}{E_i^3} - \int_0^{+\infty} dp\, \frac{p^4 - M_i^4}{E_i^3}\left[f_\Phi^{+i}(E_i,\mu_i) + f_\Phi^{-i}(E_i,\mu_i)\right]\right\}\\
C_{i,4} &= \frac{N_c}{\pi^2}\int_0^{+\infty} dp\, p^2\frac{M_i}{E_i}\left[c_\Phi^{+i}(E_i,\mu_i) + c_\Phi^{-i}(E_i,\mu_i)\right]\\
C_{i,5} &= \frac{N_c}{\pi^2}\int_0^{+\infty} dp\, p^2\frac{M_i}{E_i}\left[d_\Phi^{+i}(E_i,\mu_i) + d_\Phi^{-i}(E_i,\mu_i)\right],
\end{aligned} \tag{3.49}$$

where

$$\begin{aligned}
c_\Phi^{+i}(E_i,\mu_i) &= \frac{e^{-\beta(E_i-\mu_i)} - 3\bar{\Phi}e^{-3\beta(E_i-\mu_i)} - 2e^{-4\beta(E_i-\mu_i)}}{(1 + N_c\Phi e^{-\beta(E_i-\mu_i)} + N_c\bar{\Phi}e^{-2\beta(E_i-\mu_i)} + e^{-3\beta(E_i-\mu_i)})^2}\\
c_\Phi^{-i}(E_i,\mu_i) &= \frac{2e^{-2\beta(E_i+\mu_i)} + 3\bar{\Phi}e^{-3\beta(E_i+\mu_i)} - e^{-5\beta(E_i+\mu_i)}}{(1 + N_c\Phi e^{-\beta(E_i+\mu_i)} + N_c\bar{\Phi}e^{-2\beta(E_i+\mu_i)} + e^{-3\beta(E_i+\mu_i)})^2}\\
d_\Phi^{+i}(E_i,\mu_i) &= \frac{2e^{-2\beta(E_i-\mu_i)} + 3\Phi e^{-3\beta(E_i-\mu_i)} - e^{-5\beta(E_i-\mu_i)}}{(1 + N_c\Phi e^{-\beta(E_i-\mu_i)} + N_c\bar{\Phi}e^{-2\beta(E_i-\mu_i)} + e^{-3\beta(E_i-\mu_i)})^2}\\
d_\Phi^{-i}(E_i,\mu_i) &= \frac{e^{-2\beta(E_i+\mu_i)} - 3\Phi e^{-3\beta(E_i+\mu_i)} - 2e^{-4\beta(E_i+\mu_i)}}{(1 + N_c\Phi e^{-\beta(E_i+\mu_i)} + N_c\bar{\Phi}e^{-2\beta(E_i+\mu_i)} + e^{-3\beta(E_i+\mu_i)})^2}
\end{aligned} \tag{3.50}$$

and

$$\begin{aligned}
C_{4,4} &= \frac{N_c^2}{T^3\pi^2}\sum_i\int_0^{+\infty} dp\, \left\{\left[g_\Phi^{+i}(E_i,\mu_i)\right]^2 + \left[g_\Phi^{-i}(E_i,\mu_i)\right]^2\right\}\\
C_{5,5} &= \frac{N_c^2}{T^3\pi^2}\sum_i\int_0^{+\infty} dp\, \left\{\left[h_{\bar{\Phi}}^{+i}(E_i,\mu_i)\right]^2 + \left[h_{\bar{\Phi}}^{-i}(E_i,\mu_i)\right]^2\right\}\\
C_{4,5} &= \frac{N_c^2}{T^3\pi^2}\sum_i\int_0^{+\infty} dp\big\{g_\Phi^{+i}(E_i,\mu_i)h_{\bar{\Phi}}^{+i}(E_i,\mu_i) + g_\Phi^{-i}(E_i,\mu_i)h_{\bar{\Phi}}^{-i}(E_i,\mu_i)\big\}.
\end{aligned} \tag{3.51}$$

An important observation is that the Jacobian matrix of the system is not the Hessian matrix for the grand canonical potential density. Using the Newton-Raphson algorithm it is possible to obtain the solution of the system via an iterative approach, until reaching the desired accuracy. Moreover, it is possible to obtain the numerical error of solution. Let ϵ_i be the numerical accuracy for the i-th equation; then, the numerical error of the solution x_j reads:

$$\delta x_j = (J^{-1})_{ji}\epsilon_i \, . \tag{3.52}$$

3.2.2 Order parameters

In the first chapter of this thesis I discussed the spontaneous breaking/restoration of two global symmetries of the QCD action: the $SU_A(N_f)$ chiral-symmetry and the $\mathbb{Z}_3$ symmetry, the latter linked to the deconfinement of quarks. For their study one introduces two order parameters that can acquire a non-vanishing expectation value as one varies the temperature and the chemical potentials. The two order parameters are the chiral condensate and the Polyakov Loop. In the following I present some properties of these quantities.

Chiral condensate

The spontaneous breaking of chiral symmetry accounts for about 98% of the dressed mass of the quarks. From Eq. (3.19) one can infer that, for a big and negative value of the chiral condensates, the effective quark masses are large and chiral symmetry is dynamically broken. When the chiral condensates become small, the quark masses approach their current values and chiral symmetry gets almost restored: only the explicit breaking due to the small current masses of the quarks survives. The chiral condensate is a meaningful order parameter even in the presence of a small explicit symmetry breaking in the Lagrangian. How the chiral condensate varies as a function of the temperature and chemical potentials defines the order of the phase transition. If it is a smooth function, the transition is actually a crossover and for the estimate of the transition temperature one can choose the inflection point of the chiral condensate. If, instead, the chiral condensate is a function with a jump discontinuity, one has a first-order transition. The transition temperature corresponds to the location of this discontinuity.

Polyakov loop

The confinement/deconfinement transition is linked to the breaking of the center symmetry of the $SU_c(3)$ group. The natural order parameter of this transition is the Polyakov loop. One can remember that the single Polyakov-loop is not invariant under $\mathbb{Z}_3$ rotations and its average value is related to the free energy F_Q of an isolated quark:

$$\langle P \rangle \propto e^{-\beta F_Q}. \tag{3.53}$$

Hence, the Polyakov loop is invariant under a $\mathbb{Z}_3$ transformation only if its expectation value vanishes, which occurs when $F_Q \to +\infty$. This happens in the confined region, where an infinite amount of energy is needed to add an isolated quark into the system. In the deconfined region one needs only a very small amount of energy to create an isolated quark, i.e. $F_Q \to \infty$ and hence $\langle P \rangle \to 1$, so that the $\mathbb{Z}_3$-symmetry is broken. One can conclude that a null value of the Polyakov loop and, as a consequence, a null value of the Polyakov fields in the PNJL Lagrangian, indicate the absence of free quarks in the system. Instead, a value of the Polyakov fields close to unity indicates the deconfinement of quarks. As for the chiral condensate, the behaviour of the Polyakov field as a function of the temperature and chemical potentials marks the kind of transition of the system.

These two are the only linearly independent order parameters. In the study of the QCD phase-diagram it can be convenient in numerical calculations (for instance on the lattice) to introduce other quantities used as order parameters (since closer to some experimental observable or displaying a sharper behaviour). In the crossover region, depending on the above choice one can obtain slightly different transition temperatures. However, all of them are related to the chiral condensate and to the Polyakov fields.

3.2.3 Thermodynamic Quantities

The grand canonical potential Ω, calculated in the mean-field approximation, is a function of the temperature T and of the quark chemical potentials μ_i

or alternatively of the ones associated to the conserved charges of the theory μ_B, μ_Q, μ_S. The relation among these two sets of chemical potentials is defined in Eq. (3.25). From this function it is possible to calculate all the thermodynamics quantities of interest, which we summarize in this section. It is convenient to subtract from the thermodynamic potential density its vacuum value at $T = \mu_i = 0$, since the latter is not observable. In this case, by definition, the pressure and energy density of the vacuum vanish. One can define

$$\widetilde{\omega}(T, \{\mu_i\}) \equiv \bar{\omega}(T, \{\mu_i\}) - \bar{\omega}(T = 0, \{\mu_i = 0\}). \tag{3.54}$$

From the latter one derives all other thermodynamic quantities

$$P(T, \{\mu_i\}) = -\widetilde{\omega}(T, \{\mu_i\}) \tag{3.55}$$

$$s(T, \{\mu_i\}) = \left.\frac{\partial P(T, \{\mu_i\})}{\partial T}\right|_{\mu_i} \tag{3.56}$$

$$n_j(T, \{\mu_i\}) = \left.\frac{\partial P(T, \{\mu_i\})}{\partial \mu_j}\right|_{T} \tag{3.57}$$

$$\varepsilon = -P + Ts + \sum_{i=u,d,s} \mu_i n_i \; . \tag{3.58}$$

In this work, beside the above thermodynamic quantities, also the specific heat, the trace anomaly and the subtracted chiral condensate are calculated. In the following, these quantities are introduced.

Equation of State, speed of sound and isentropic lines

As already discussed, in the study of the fireball created in HIC's a lot of information, of particular relevance for the hydrodynamic expansion of the system, is carried by the Equation of State $P = P(\epsilon, n_B)$ and by the speed of sound. The EoS closes the system of hydrodynamic equations; in Chapter 4 I show some results for the EoS along different isentropic trajectories. The squared speed of sound c_s^2 governs the response of the system to the initial energy-density gradients, leading to the collective acceleration of the fireball. Moreover, in a non-dissipative system, the fireball evolves along trajectories of constant entropy per baryon $\sigma \equiv s/n_B$. Along these lines the calculation of the speed of sound is particularly easy. The squared speed of sound reads

$$c_s^2 = \left.\frac{\partial P}{\partial \varepsilon}\right|_{\sigma} , \tag{3.59}$$

which differs from its non-relativistic expression since the partial derivative (at constant entropy per baryon) is taken with respect to the energy density rather than the mass density. In the numerical results in Sec. 4 I will show the comparison between the speed of sound calculated in the PNJL model and the one provided by lattice-QCD calculations.

Specific heat

The specific heat at constant volume in the grand canonical ensemble is defined as

$$C_V = T \left(\frac{\partial S}{\partial T}\right)_{V,N} \tag{3.60}$$

whose physical meaning can be understood from

$$T\Delta S + \mu \Delta N = \Delta E + P\Delta V \; . \tag{3.61}$$

Keeping N and V constant, the increase in thermal energy of the system can only come from the heat exchange with a reservoir – not from an exchange of particles – and, at the same time, all this heat flux is converted into disordered thermal motion and not into work. Since one assumes V to be constant, one can consider the heat-capacity per unit volume

$$c_V \equiv \frac{C_V}{V} = T \left(\frac{\partial s}{\partial T}\right)_{n} \; . \tag{3.62}$$

Employing the temperature and the chemical potential as independent variables requires introducing some Jacobians. One has

$$\left(\frac{\partial s}{\partial T}\right)_{n} = \frac{\partial(s,n)}{\partial(T,n)} = \frac{\dfrac{\partial(s,n)}{\partial(T,\mu)}}{\dfrac{\partial(T,n)}{\partial(T,\mu)}} \; , \tag{3.63}$$

which leads to

$$c_V = T\left[\left(\frac{\partial s}{\partial T}\right)_\mu - \frac{\left(\dfrac{\partial N}{\partial T}\right)_\mu^2}{\left(\dfrac{\partial N}{\partial \mu}\right)_T}\right] \tag{3.64}$$

One can intuitively characterize the QCD deconfinement transition as the sudden liberation around a certain temperature of many new degrees of freedom, giving rise to a rapid increase in the energy density and entropy density, ideally with an infinite slope at the CEP. This rapid rise would then manifest as a peak (or even a divergence) in the specific heat, which could serve as an indicator for the pseudo-critical (or critical) temperature.

Numerical results for the specific heat obtained in the PNJL model and their comparison with lattice-QCD findings are shown in the following chapter.

Trace Anomaly

In a thermodynamic system composed of massless non-interacting particles (Stefan-Boltzmann gas), like one expects to be the case for a QGP at asymptotically high temperature, the EoS is very simple: $\varepsilon = 3P$. This is the EoS for a conformal fluid, in which there is no mass scale. In the fluid rest frame the stress-energy tensor is diagonal and its trace in this limit, due to the particular form of the EoS, is null: $\varepsilon - 3P = 0$. In the presence of interaction this is in general not true and the trace of the stress-energy tensor can be used to quantify how much the system is far from the Stefan-Boltzmann limit. A comparison between the PNJL calculations and lattice results for this quantity, written in dimensionless units as $(\varepsilon - 3P)/T^4$, is shown in Chapter 4.

Subtracted chiral condensate

As above discussed, the chiral condensate of light quarks can be used as an order parameter to identify the chiral transition. However, in lattice QCD, one must deal with renormalized quantities with a well defined continuum limit. For this purpose, an important quantity calculable from the solution of the MFE's and suited to a comparison with lattice-QCD calculations is the subtracted chiral condensate $\Delta_{l,s}$. This quantity is the difference between the chiral condensates of light and strange quarks, normalized to its value at zero temperature, in the vacuum. Its expression is

$$\Delta_{l,s} \equiv \frac{\phi_l(T,\mu_i) - \phi_s(T,\mu_i) m_u/m_s}{\phi_l(T=0) - \phi_s(T=0) m_u/m_s} \; . \tag{3.65}$$

This quantity measures how much the system is far from the restoration of chiral symmetry. In chapter 4 I shown the comparison between PNJL results for this quantity and lattice-QCD data.

3.2.4 Phase Diagram

Employing lattice-QCD simulations, it is possible to explore the QCD phase diagram at null/small chemical potential. In this region, one finds that the transition is a smooth crossover and the order parameters display, at most, a steep but continuous variation which occurs within a broad range of temperatures around $T_c \sim 155$ MeV [18, 22], the chiral transition a bit below the deconfinement one. At higher chemical potential, the transition is supposed to become become a first-order one and the order parameters are discontinuous. Along the first-order transition line in the μ_B–T plane, the hadronic and quark phases coexist in the same volume in thermal, chemical and mechanical equilibrium, corresponding to two different degenerate minima of the thermodynamic potential. It means that there are portions of volume occupied by hadronic matter and other portions of volume occupied by deconfined quarks and gluons. The region where this happens is called *coexistence* region. Here the system cannot exist as a single homogeneous stable phase and the transition occurs via the nucleation of bubbles of the new phase surrounded by the matter in the old one. It is however possible to have metastability. This occurs in the region where the grand canonical potential has two different local minima corresponding to different values of the order parameters and of the dynamical quark masses. In this region the system, depending on its evolution, can remain in the local minimum

To find the stationary points of Ω, one can use the eigenvalues of the Hessian matrix. In particular, if all the eigenvalues are strictly positive the point is a local minimum; on the contrary, for all eigenvalues strictly negative the point is a local maximum. For eigenvalues of different sign one has a saddle point. For given values of temperature and chemical potentials, the stable phase of the system corresponds to the absolute minimum of Ω. In the presence of two minima, the minimum with the lower value is called *stable minimum*, the other one is the *metastable minimum.* Below the transition line in the $\mu_B - T$ plane the stable minimum corresponds to the confined chirally-broken phase, instead above the transition line the stable minimum corresponds to the deconfined chirally-restored phase. The first-order transition line starts from the chemical potential axis and ends at the Critical End Point. The position of this point is today a matter of debate.

Unfortunately, due to the introduction of the Polyakov fields, the PNJL grand canonical potential has only saddle points. In this work, to study the coexistence region I consider the Hessian matrix corresponding to the second derivatives of the grand canonical potential with respect to the chiral condensates. This matrix is completely defined (positive or negative); then one can find the local/global minima of Ω. In Appendix D the Hermitian matrix used in the calculation is shown.

3.3 Fluctuations

This section is devoted to introduce the issue of fluctuations, previously mentioned in Sec. 2, from the theoretical point of view and to show how it is possible to calculate these quantities in the framework of the PNJL with 2+1 flavours.

As already discussed, fluctuations are related to the impossibility of obtaining the same value for a given observable in a series of repeated measurements. One can refer to the distribution of the results of the set of measurements as fluctuations. In contrast to standard observables, fluctuations are sometimes regarded as the noise associated with the measurement and thus are obstacles; however, fluctuations can sometimes become invaluable physical observables. Here, in order to spur the motivations of the reader, I list three examples of the physics in which fluctuations play a crucial role [19].

- Brownian Motion
  In 1827 Brown discovered that small objects, such as pollen, floating on water show a quick and random motion. Due to this motion, the position of the pollen after a long several time duration fluctuates even if the initial position is fixed. Einstein attributed the origin of this phenomenon to the thermal motion of water molecules [3]. This prediction was confirmed by Perrin, who calculated the Avogadro constant based on this picture [84]. These works contributed to the proof of the existence of molecules and atoms.

- Cosmic Microwave Background
  As a remnant of the Big Bang and as a result of its transparency to radiation, our Universe has a 2.7 K thermal radiation called cosmic microwave background (CMB) [2]. The temperature of this radiation is uniform in all directions, but has tiny fluctuations at different angles. These fluctuations are related to the quantum fluctuations of the primordial Universe. The spectrum of these fluctuations carries information about the primordial Universe. For example, our Universe has

started with an inflational expansion 13.8 billion years ago. In other words, one can see the hot primordial Universe behind the fluctuations of the CMB [21].

- Shot Noise

  The current in a resistor R generally fluctuates, even if no voltage is applied. The current has a thermal noise proportional to T/R which is called the Johnson-Nyquist noise [58],[81]. On the other hand, there is a noise which occurs when a voltage is applied and which is proportional to the average current $\langle I\rangle$. When a circuit has a potential barrier the variance of the above noise is proportional to $\hat{e}\langle I\rangle$, where $\hat{e}$ is the electric charge of the elementary degrees of freedom carrying electric current. This noise is called shot noise [97]. From the analysis of the fluctuations in particular electric systems, for example circuits at very low temperature, one can quantify the electric charge carried by the elementary degrees of freedom. This procedure led for instance to discover that the elementary degrees of freedom in superconductivity are the Cooper pairs, with the electric charge of two electrons, and that in the fractional quantum Hall effect the elementary charges become fractional.

These three examples tell us that the fluctuations are powerful tools to diagnose the microscopic physics and investigate the elementary active degrees of freedom in the system although they are macroscopic observables. Furthermore, they can be used to trace back the history of a system, like in the analysis of CMB fluctuations.

3.3.1 A briefly introduction to cumulants

Fluctuations are mathematically represented by probability distribution functions. For example, if one repeats a measurement of an observable in an equilibrated medium many times, the result of the measurement would fluctuate event by event. This distribution is nothing other than the fluctuation. One usually starts from a probability distribution $P(x)$ for a continuous stochastic variable x, satisfying the normalization condition $\int P(x)dx=1$. A probability distribution can be characterized by its moments. The n-th moment of a distribution is defined as:

$$\langle x^n \rangle = \int x^n P(x)dx. \tag{3.66}$$

To calculate the moments of a given probability distribution it is convenient to introduce the moment generating function:

$$G(\theta) = \int e^{\theta x} P(x)dx \tag{3.67}$$

The moments are given by the derivatives of $G(\theta)$ evaluated at $\theta = 0$:

$$\langle x^n \rangle = \frac{d^n}{d\theta^n} G(\theta)\bigg|_{\theta=0} . \tag{3.68}$$

For many practical purposes, it is more convenient to use cumulants rather than moments to characterize a probability distribution. One defines the cumulant generating function as

$$K(\theta) = \log G(\theta) \ . \tag{3.69}$$

The cumulants of order n-th is then defined as

$$\langle x^n \rangle_c = \frac{d^n}{d\theta^n} K(\theta)|_{\theta=0}. \tag{3.70}$$

The cumulants are useful to describe the non-Gaussianity of the distribution. For more information about this topic see Appendix B. The relation between the first four cumulants of a distribution and its first four moments is shown below:

$$\begin{cases} \langle x\rangle_c = \langle x\rangle \equiv M \\ \langle x^2\rangle_c = \langle x^2\rangle - \langle x\rangle^2 = \langle(\delta x)^2\rangle \equiv \sigma^2 \\ \langle x^3\rangle_c = \langle x^3\rangle - 3\langle x\rangle\langle x^2\rangle + 2\langle x\rangle^3 = \langle(\delta x)^3\rangle \\ \langle x^4\rangle_c = \langle x^4\rangle - 4\langle x^3\rangle\langle x\rangle + 12\langle x^2\rangle\langle x\rangle^2 - 3\langle x^2\rangle^2 - 6\langle x\rangle^4 = \langle(\delta x)^4\rangle - 3\langle(\delta x)^2\rangle^2 \,. \end{cases} \tag{3.71}$$

To estimate how much a probability distribution deviates from a Gaussian one can use two ratios of cumulants, the skewness γ and the kurtosis κ, defined as

$$\gamma \equiv \frac{\langle x^3\rangle_c}{\langle x^2\rangle^{\frac{3}{2}}} = \frac{\langle x^3\rangle_c}{\sigma^3} \tag{3.72}$$

$$\kappa \equiv \frac{\langle x^4\rangle_c}{\langle x^2\rangle^2} = \frac{\langle x^4\rangle_c}{\sigma^4} \,. \tag{3.73}$$

These two quantities express the asymmetry and the sharpness of the distribution per unit of standard deviation. In other words, they are the third and the fourth the cumulants of renormalized stochastic variable $\tilde{x} = x/\sigma$. For a Gaussian distribution, one has $\gamma = \kappa = 0$. In the next section I present the calculation of the cumulants of QCD conserved charges considered in this thesis.

3.3.2 Calculations of cumulants in the PNJL model

In this section I focus on the study of baryon-number fluctuations, but the treatment can be easily generalized to other conserved charges like electric charge and strangeness. In statistical mechanics, cumulants of extensive variables are also extensive quantities, but in HIC's one wants to avoid introducing a source of systematic uncertainty connected to the volume of the system, only indirectly accessible. Hence it is useful to define cumulants per unit volume. These quantities are called generalized susceptibilities and they are calculated starting from the pressure of the system. The n^{th}-order generalized susceptibility χ_B^n is defined in full generality as

$$\chi_B^n(T,\mu_B) = \left.\frac{\partial^n P(T,\mu_B)/T^4}{\partial(\mu_B/T)^n}\right|_T , \tag{3.74}$$

where μ_B is the baryochemical potential and we have used the temperature to make the quantities dimensionless. In the following, in our calculations based on the PNJL model, the pressure is evaluated in mean-field approximation where

$$P(T,\mu_i) = P[\Phi(T,\mu_i),\bar{\Phi}(T,\mu_i),\phi_i(T,\mu_i),;T,\mu_i]_{\mathrm{MFE}} . \tag{3.75}$$

Hence in taking the derivatives one must consider also the implicit dependence on the chemical potentials hidden in the chiral condensates and in the Polyakov fields, imposing furthermore the constraints $\partial P/\partial\phi_i = \partial P/\partial\Phi = \partial P/\partial\bar{\Phi} = 0$ set by the mean-field approximation. In the above the functions $\Phi(T,\mu_i)$, $\bar{\Phi}(T,\mu_i)$ and $\phi_i(T,\mu_i)$ are the solutions of the MFE's. Since they are not known analytically, but arise from the self-consistent numerical solution of the MFE's, it is more convenient to perform higher-order derivatives in Eq. (3.74) numerically, evaluating the incremental ratio of the pressure at μ_B/T and $\mu_B/T+h$. The first-order susceptibility provides the baryon density of the system, according to the thermodynamic identity $n_B = \partial P/\partial\mu_B$, and due to the MFE's for its derivation one must simply consider the explicit dependence on the chemical potentials. In HIC's the volume of the system undergoes an expansion and is different event-by-event. For these reasons one would like to deal with volume-independent observables. One can define particular combinations of cumulants which do not depend on the system volume and which correspond to ratios of the generalized susceptibilities just introduced. These observables are:

$$\frac{\gamma_B \sigma_B^3}{M} = \frac{\chi_B^3(T, \mu_B)}{\chi_B^1(T, \mu_B)} \,, \tag{3.76}$$

$$\kappa_B \sigma_B^2 = \frac{\chi_B^4(T, \mu_B)}{\chi_B^2(T, \mu_B)} \,. \tag{3.77}$$

In the above, the mean, variance, skewness and kurtosis are obtained substituting the net baryon number to the continuous variable x in Eqs. (3.71). Experimentally the net baryon number is replaced by the net proton distribution, since neutrons cannot be detected. Eqs. (3.76) and (3.77) allow one to access the temperature and baryochemical potential at chemical freezeout. Assuming that net-particles (i.e. particles minus antiparticles) follow a Skellam distributions (i.e. the difference of two Poissonian distributions), net baryon number cumulants are given by

$$\langle N_{B,\mathrm{net}}^n \rangle_c = B^n [\langle N \rangle + (-1)^n \langle \overline{N} \rangle], \tag{3.78}$$

where N counts the number of active degrees of freedom carrying baryon charge B. One gets then

$$\frac{\chi_B^{n+2}}{\chi_B^n} = \frac{\langle N_{B,\mathrm{net}}^{n+2} \rangle_c}{\langle N_{B,\mathrm{net}}^n \rangle_c} = \frac{B^{n+2}[\langle N \rangle + (-1)^n \langle \overline{N} \rangle]}{B^n [\langle N \rangle + (-1)^n \langle \overline{N} \rangle]} = B^2, \tag{3.79}$$

In the confined region the correct elementary degrees of freedom are hadrons and baryon number is carried by baryons, which have unitary baryon charge $B = 1$. In the deconfined region the degrees of freedom carrying baryon number are quarks, hence $B = 1/3$. This means that the above ratios of cumulants decrease by a factor 9 when one goes through the transition line (or crossover band). In chapter 4 this topic is widely treated.

Fluctuations of conserved charges might provide an insight on the QGP thermal properties and on the nature of the chiral transition. In fact, one expects that near the transition the fluctuations become larger and larger as the latter gets sharper when approaching the CEP where from a continuous crossover it turns into a first-order. These quantities are experimentally accessible through the fluctuations of detected particles, at variance with the chiral condensates and the Polyakov fields. In this thesis I use the susceptibilities associated to the QCD conserved charges and calculated along lines of constant temperature, chemical potential or entropy-per-baryon to explore, in several scenarios, the QCD phase diagram. The results of these calculations are shown in the following chapter.

Chapter 4

Numerical Results

In this part of my thesis I show the numerical results obtained in the PNJL effective model. First of all, in Sec. 4.1, I compare the PNJL results at zero chemical potential for several thermodynamic quantities and for the order parameters of the transition with the lattice data. Afterwards, I show the results of the MFE's at finite chemical potential with two different versions of the Polyakov potential: logarithmic and polynomial.

In the second part of this chapter I consider isentropic trajectories of relevance for the BES undergoing at RHIC and for future experiments at SPS, NICA and FAIR. The corresponding values of s/n_B are estimated starting from the data provided by the STAR collaboration in [14] and [8]. I study the values taken by the Equation of State, by the speed of sound and by the generalized susceptibilities during the isentropic evolution of the system until the estimated freeze-out point, looking for differences among cases in which the QCD transition occurs via a smooth crossover, via a first-order transition or crossing a possible CEP. These results are shown for four different scenarios in Secs. 4.3-4.6, trying to get closer and closer to the situation met in HIC's. Finally, in Sec. 4.7 I show the results of the exploration of the PNJL phase diagram in the presence of a vector interaction.

4.1 Comparison with lattice data at $\mu_B = 0$

In this section I compare the results for various thermodynamic quantities calculated at $\mu_B = 0$ in the PNJL model with a polynomial and logarithmic Polyakov potential and lattice data: pressure, speed of sound, specific heat, trace anomaly and subtracted chiral condensate $\Delta_{l,s}$. The parameters of the PNJL model are collected in Tables 3.1 and 3.2 and have been fixed in order to reproduce the properties of the light pseudoscalar mesons. These quantities and the predictions for the scalar meson mass and the dressed quark masses in vacuum are collected in Table 4.1.

The two different Polyakov potentials produce a different behaviour near the transition. The agreement with lattice data is not always good from the quantitative point of view, but overall the PNJL model produces a good qualitative description of the phase transition. Asymptotically, both in the PNJL model and in lattice-QCD, all quantities for high temperatures tend to their Stefan-Boltzmann limit, the pressure more slowly, dispaying a ∼20% deviation in the considered temperature range.

Fitted quantities	m_π	m_K	$m_{\eta'}$	f_π
Value [MeV]	135	497.7	957.8	92.4
Predictions	m_σ	m_l	m_s	
Value [MeV]	728.9	367.7	549.5	

Table 4.1: The fitted quantities used to fix the model parameters and the predictions of the present PNJL calculation with the parameter set in Tables 3.1 and 3.2.

In Fig. 4.1 I display the pressure of the system: the qualitative behaviour of the PNJL curves is similar to the one of lattice-QCD results, although there are quantitative differences: PNJL curves overshoot lattice data at high temperature; moreover the inflection point of the lQCD curve does not coincide with the one of the PNJL calculations. This, probably, is due to the fact that the PNJL model has only a few free parameters used to reproduce

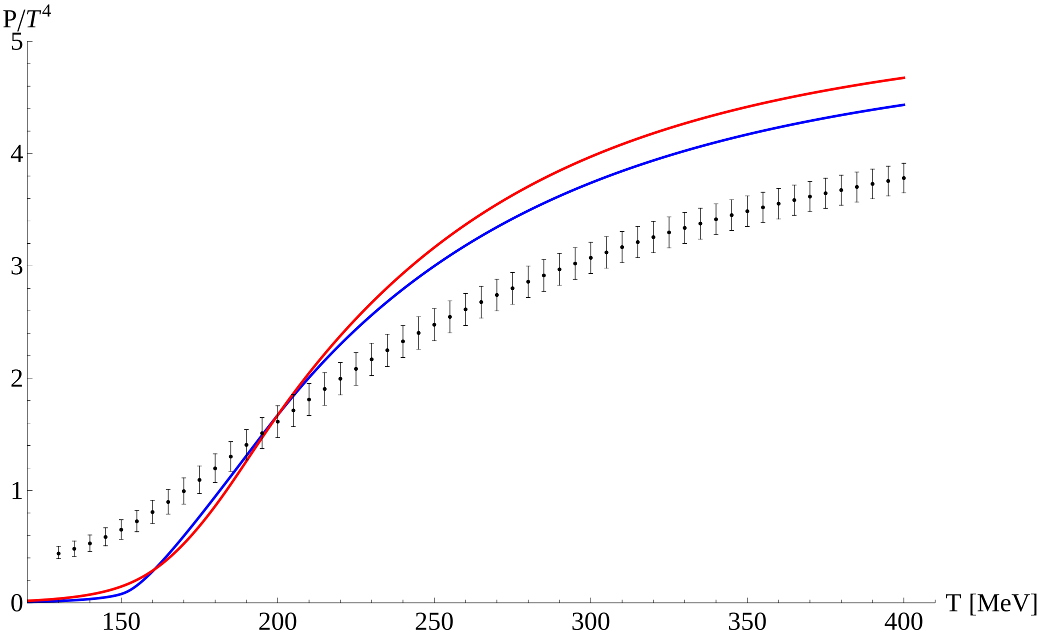

Figure 4.1: Comparison between the results of the PNJL model with a polynomial (red line) and a logarithmic (blue line) Polyakov potential and the lattice-QCD [23] data (black points) for the pressure of the system at $\mu_B = 0$.

the meson spectrum at $T = 0$ and not the thermodynamic quantities, for which it provides genuine predictions, but not necessarily in close quantitative agreement with the fundamental theory.

In Fig.4.2a I show the heat-capacity per unit volume, defined in Sec. 3.2.3. One can observe that the logarithmic version of the Polyakov potential produces two separated peaks, while the polynomial one gives rise to a single peak but higher than the others. This is due to the fact that, in the PNJL model, the crossover temperatures for the deconfinement and chiral transitions are not equal, although close to each other. With the polynomial potential the two temperatures are closer than in the logarithmic case. On the contrary, the lattice data do not shown any peak; this difference between PNJL and lattice-QCD results can mean that the PNJL model produces a sharper crossover.

Another difference between the polynomial and logarithmic Polyakov potentials is shown in the speed of sound plot in Fig. (4.2b). The minimum in

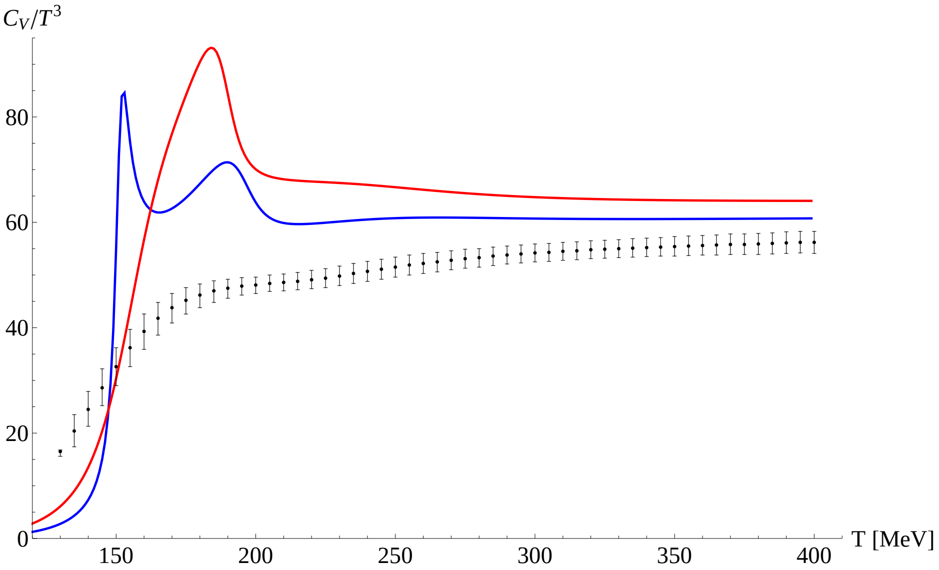

(a) *Heat capacity per unit volume.*

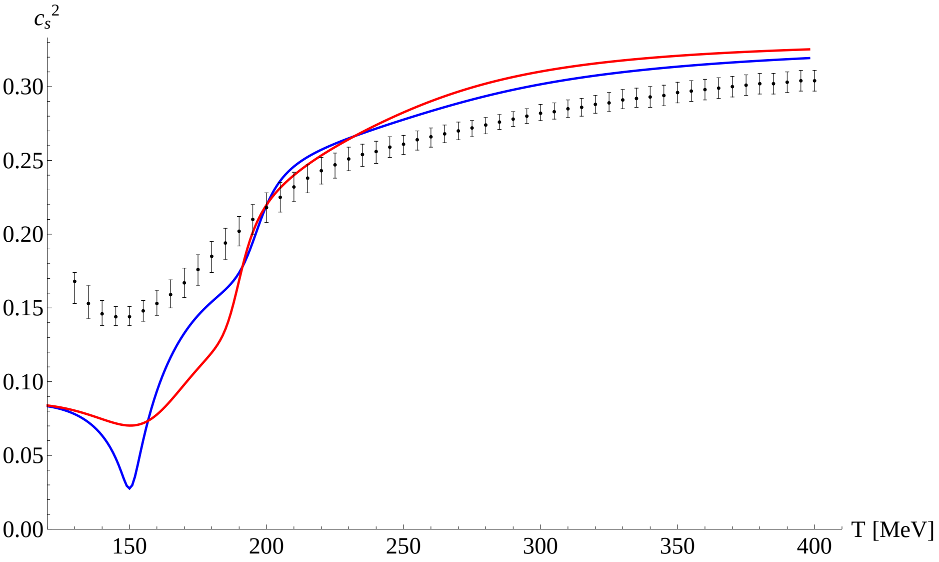

(b) *Squared speed of sound.*

Figure 4.2: Comparison between the results of the PNJL model with a polynomial (red line) and a logarithmic (blue line) Polyakov potential and the lattice-QCD [23] data (black points) for the heat capacity per unit volume (a) and the squared speed of sound at $\mu_B = 0$ (b).

the logarithmic case is sharper and is reached through two well defined knees in the curve. Notice that lattice data display a milder drop of c_s^2 around the crossover temperature.

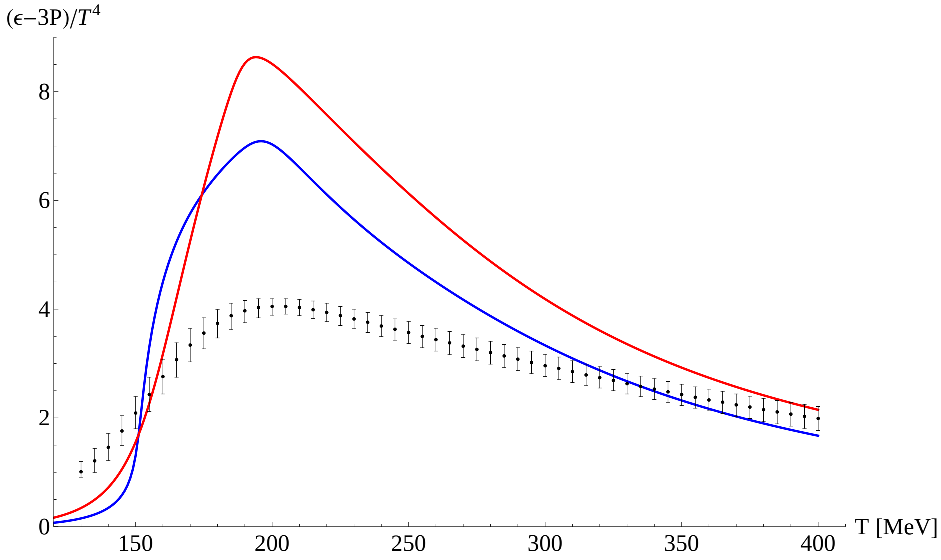

Figure 4.3: Comparison between the results of the PNJL model with a polynomial (red line) and a logarithmic (blue line) Polyakov potential and the lattice-QCD [23] data (black points) for the trace anomaly at $\mu_B = 0$.

In Fig. 4.3 I show the trace anomaly $(\varepsilon - 3P)/T^4$. This quantity measures how far the system is from an ideal gas of relativistic non-interacting massless particles, for which the Equation of State is $\varepsilon = 3P$. This is also known as the conformal-fluid limit, since it is what one expects for a theory with no mass scale different from the temperature. Both lattice data and PNJL results show a maximum around the same temperature, although in the PNJL model the latter is much more pronounced.

Finally, in Fig. 4.4 I show the subtracted chiral condensate $\Delta_{l,s}$ in two different plots. This quantity, defined in Eq. (3.65), measures how far the system is from chiral-symmetry restoration. The definition in Eq. (3.65) is used in lattice-QCD calculations in order to deal with a properly renormalized dimensionless quantity. Being the quantity normalized to the vacuum result, theoretical calculations at low temperature provide values close to unity, while at high temperature $\Delta_{l,s}$ drops to zero, signalling chiral-symmetry restoration. In the PNJL model, the inflection point occurs around a temperature about 30 MeV larger than in continuum-extrapolated lattice-QCD calculations. In

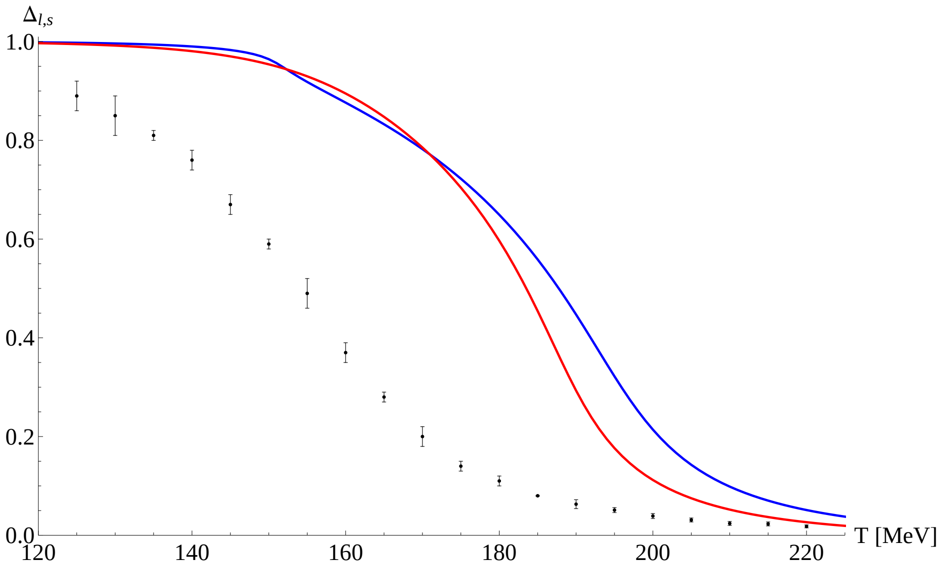

(a) *The subtracted chiral condensate* $\Delta_{l,s}$ *as a function of the temperature.*

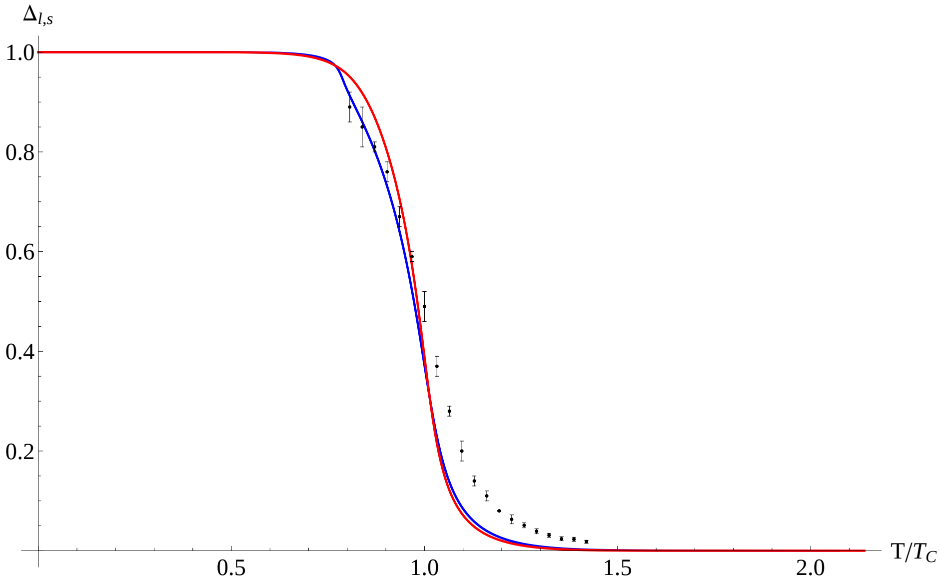

(b) *The subtracted chiral condensate* $\Delta_{l,s}$ *as a function of the* T/T_c.

Figure 4.4: Comparison between the results of the PNJL model with a polynomial (red line) and a logarithmic (blue line) Polyakov potential and the lattice-QCD [13] data (black points) for the subtracted chiral condensate at $\mu_B = 0$.

figure 4.4a the PNJL predictions are far from lattice data; this shortcoming can be explained as due to the different transition temperature T_c in the two calculations. As mentioned before, the transition temperature of the NJL model is about 30 MeV higher than lattice data, hence in Fig. 4.4b I show the comparison as a function of the reduced temperature T/T_c: the results of the two approaches look in much better agreement, although the transition in the PNJL model is a bit sharper.

In the next section there are still comparisons between results for different thermodynamic quantities obtained with the logarithmic and polynomial potentials. On the contrary, in Secs. 4.3-4.7 I focus on the search for the Critical End-Point and I use only the polynomial Polyakov Potential.

4.2 PNJL results at $\mu_B \neq 0$

In this section I display the results of the PNJL model in the case of finite baryochemical potential, $\mu_B \neq 0$. These calculations are performed in the fully symmetric scenarios (all quark chemical potentials are equal to $\mu_B/3$) with two different parameterizations of the Polyakov potential (logarithmic and polynomial). The solution of the MFE's provides the values of the order parameters of the deconfinement and chiral transitions, i.e. the Polyakov fields and the quark condensates, respectively.

One can then evaluate the various thermodynamics quantities like the pressure, the entropy density and the baryon density. In the rest of this section I'm going to display these results, together with the ones for the generalized susceptibilities.

4.2.1 Order parameters

The behaviour of the order parameter defines the order of a phase transition. Here, I show the order parameters of the deconfinement and chiral transitions as functions of the temperature for different values of the baryochemical potential μ_B.

In Figs. 4.5 and 4.6 I show the mean-field results for the Polyakov fields in the logarithmic and polynomial versions of the Polyakov potential. The difference between the two cases is that, with the logarithmic potential, the expectation values of the Polyakov fields approach unity from below, while in the other version they overshoot unity as already observed in Ref. [69], probably approaching it from above at very high temperatures, beyond the theoretical limits of validity of the PNJL model.

In Figs. 4.7 and 4.8 I show the chiral condensates for light (up and down) and strange quarks normalized to their values in the vacuum in the logarithmic and polynomial versions of the Polyakov potential.

All the order parameters in Figs. 4.5-4.8 are smooth until $\mu_B = 862$ MeV. After this value of chemical potential the order parameters have a jump discontinuity around $T \sim 122$ MeV for both versions of the Polyakov potential. Then the possible Critical End-Point is approximately located around $T^{\mathrm{CEP}} = 122$ and $\mu_B^{\mathrm{CEP}} = 862$ MeV.

It is useful to identify the position of the CEP in the QCD phase diagram studying the behaviour of quantities with a more direct connection with experimental observables, like fluctuations of conserved charges. In this connection, in Sec.4.2.3 I display the results for the baryon-number generalized susceptibilities obtained in the PNJL model.

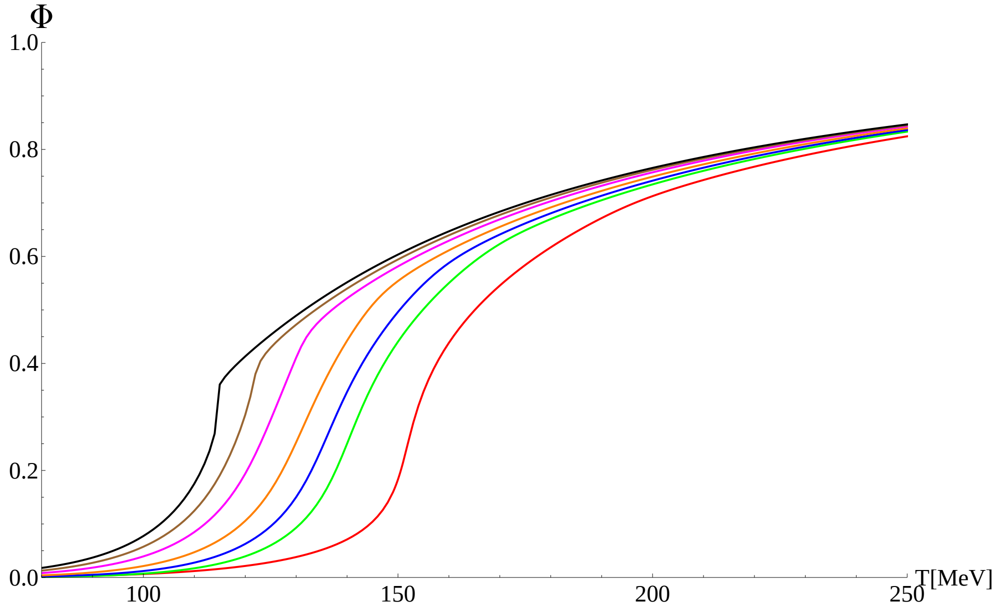

(a) *Polyakov field with the logarithmic Polyakov potential.*

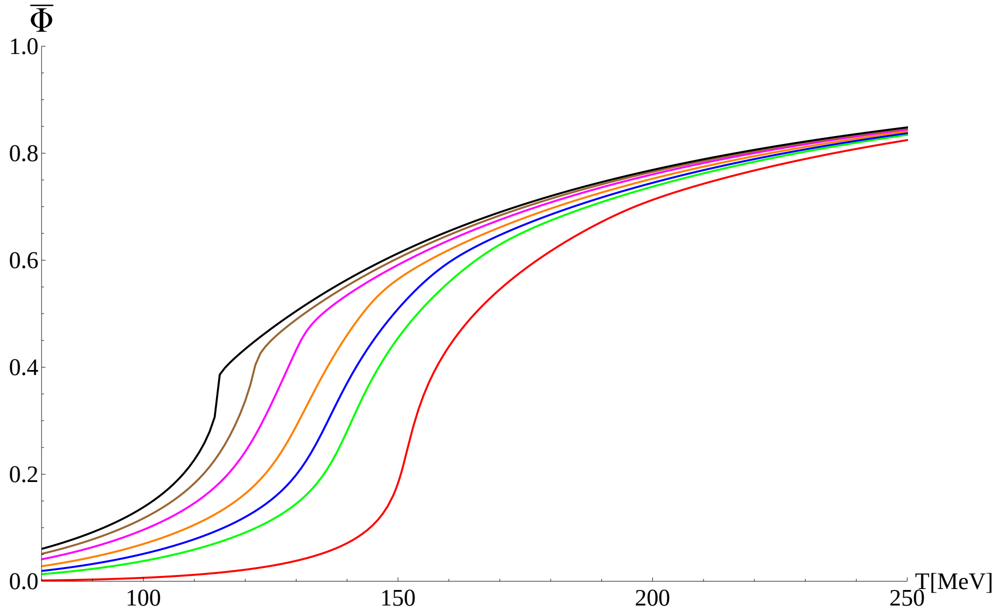

(b) *Adjoint Polyakov field with the logarithmic Polyakov potential.*

Figure 4.5: Expectation values of the Polyakov fields in the PNJL model at different baryochemical potentials: $\mu_B = 0$ (red line), 540 MeV (green line), 630 MeV (blue line), 720 MeV (orange line), 810 MeV (magenta line), 862 MeV (brown line), 900 MeV (black line).

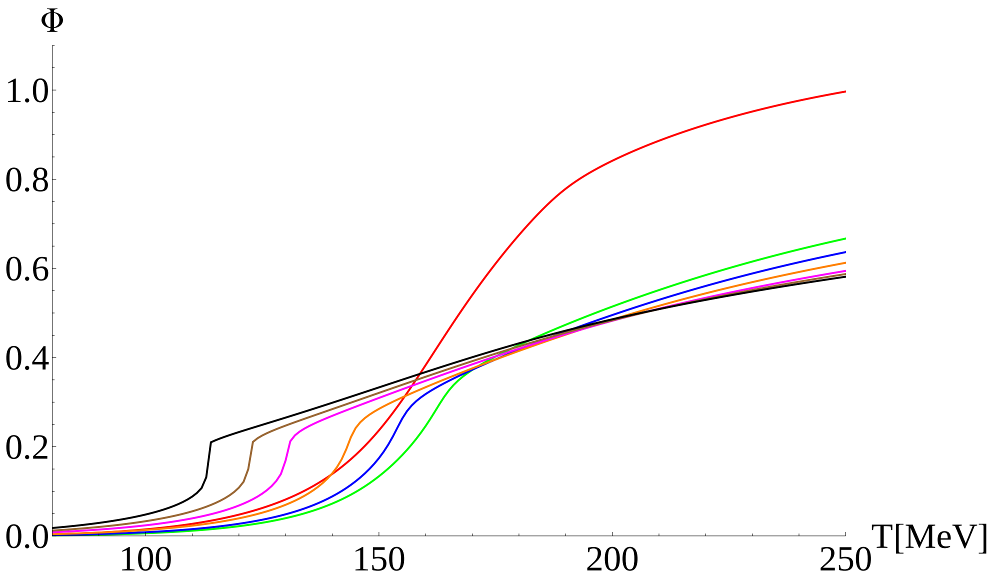

(a) *Polyakov field with the polynomial Polyakov potential.*

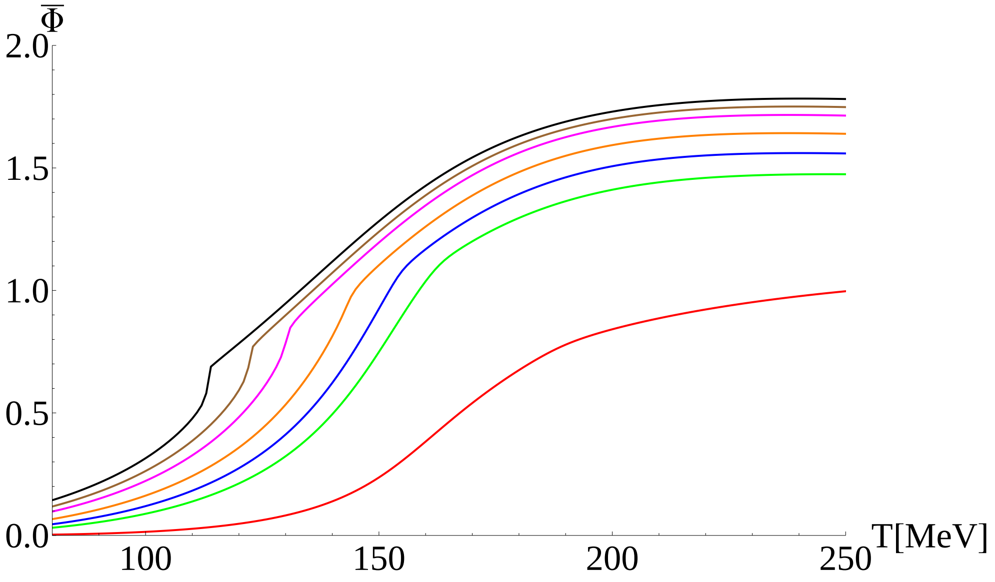

(b) *Adjoint Polyakov field with the polynomial Polyakov potential.*

Figure 4.6: Expectation values of the Polyakov fields in the PNJL model at different baryochemical potentials: $\mu_B = 0$ (red line), 540 MeV (green line), 630 MeV (blue line), 720 MeV (orange line), 810 MeV (magenta line), 862 MeV (brown line), 900 MeV (black line).

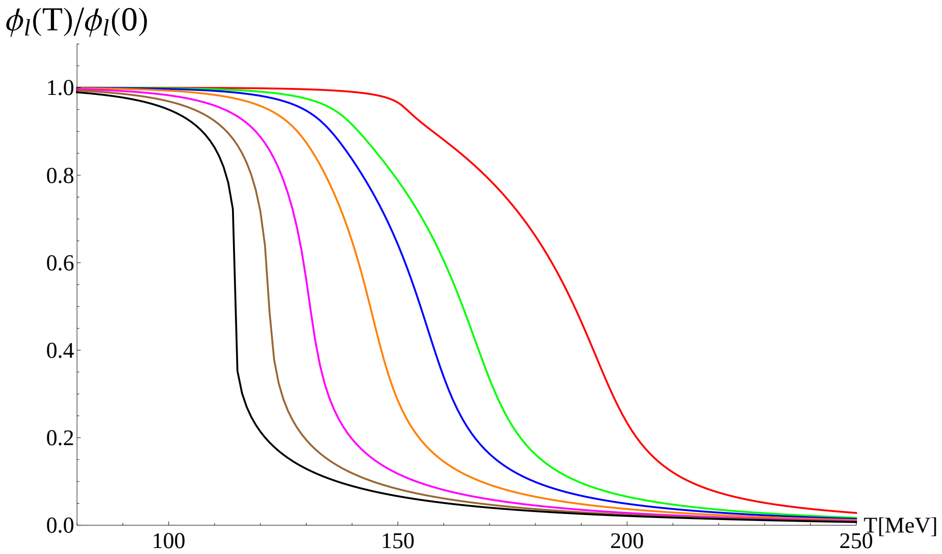

(a) *Light-quark chiral condensate normalized to its vacuum value, with the logarithmic Polyakov potential.*

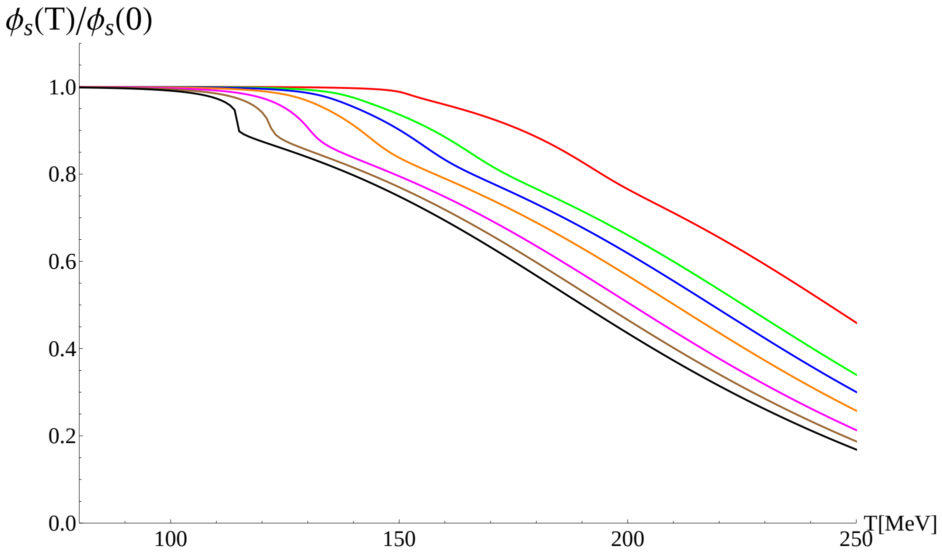

(b) *Strange-quark chiral condensate, normalized to its vacuum value, with the logarithmic Polyakov potential.*

Figure 4.7: Mean-field results for the chiral condensates in the PNJL model (with logarithmic Polyakov potential) for several values of the baryochemical potential: $\mu_B = 0$ (red line), 540 MeV (green line), 630 MeV (blue line), 720 MeV (orange line), 810 MeV (magenta line), 862 MeV (brown line), 900 MeV (black line).

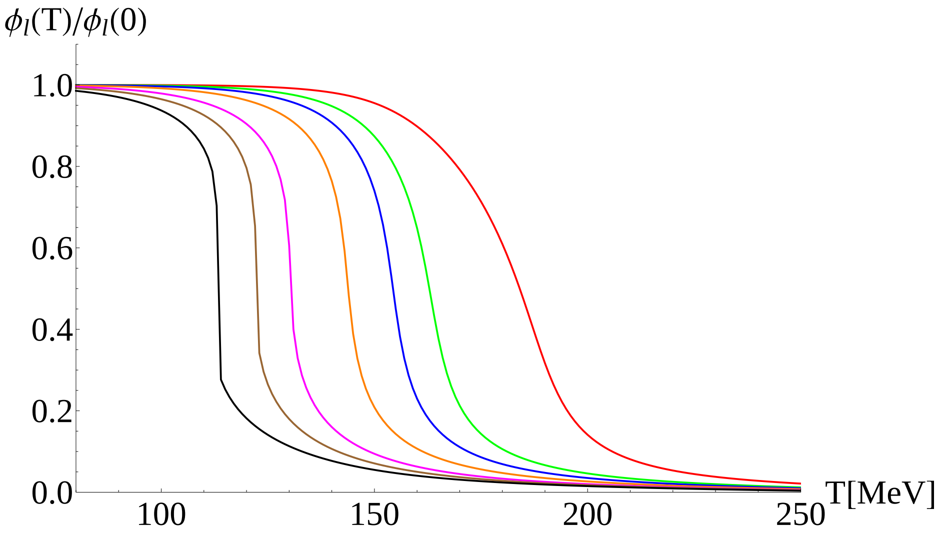

(a) *Light-quark chiral condensate normalized to its vacuum value, with the polynomial Polyakov potential.*

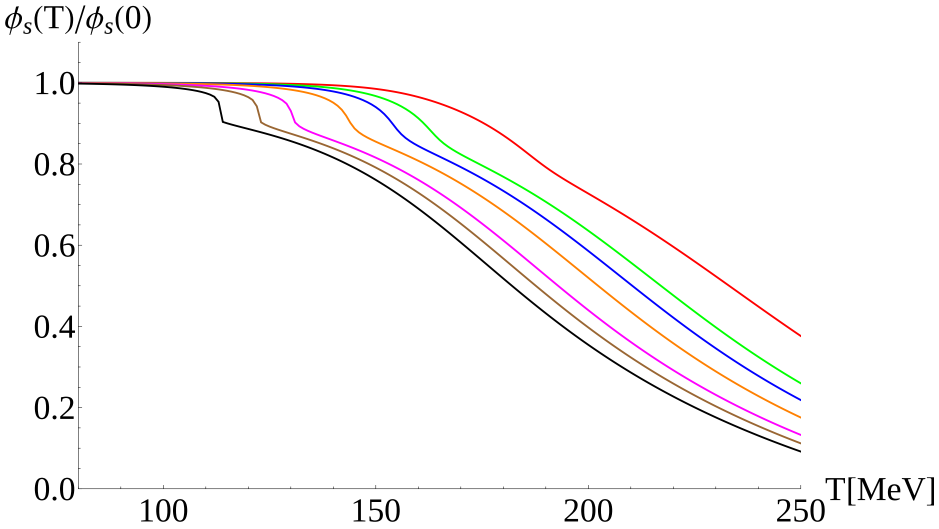

(b) *Strange-quark chiral condensate normalized to its vacuum value, with the polynomial Polyakov potential.*

Figure 4.8: Mean-field results for the chiral condensates in the PNJL model (with polynomial Polyakov potential) for several values of the baryochemical potential: $\mu_B = 0$ (red line), 540 MeV (green line), 630 MeV (blue line), 720 MeV (orange line), 810 MeV (magenta line), 862 MeV (brown line), 900 MeV (black line).

4.2.2 Thermodynamics Observables

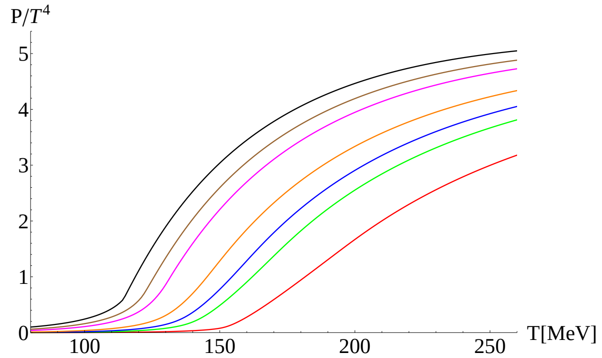

(a) *Pressure*

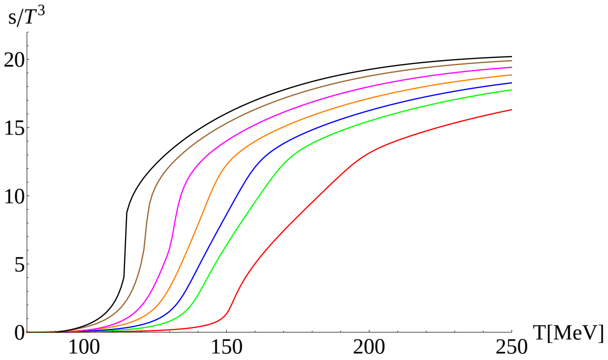

(b) *Entropy density*

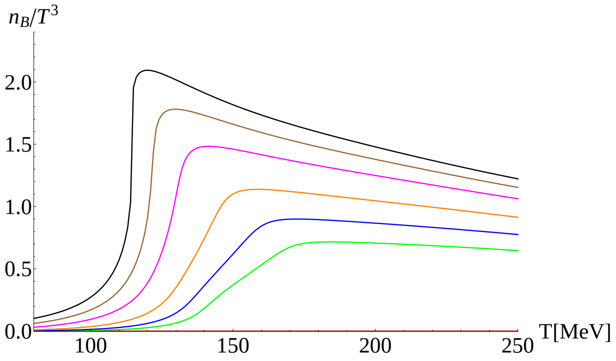

(c) *Net-Baryon density*

Figure 4.9: Mean-field results for the pressure, entropy density and baryon density in the PNJL model (with logarithmic potential) as functions of the temperature for different values of the baryochemical potential: $\mu_B = 0$ (red line), 540 MeV (green line), 630 MeV (blue line), 720 MeV (orange line), 810 MeV (magenta line), 862 MeV (brown line), 900 MeV (black line).

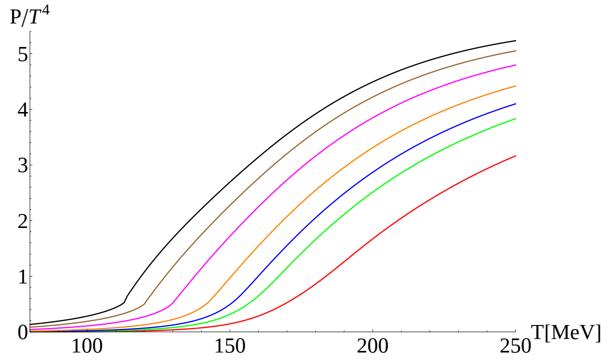

(a) *Pressure*

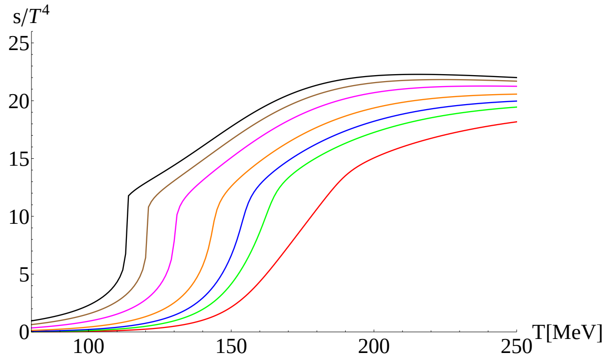

(b) *Entropy density*

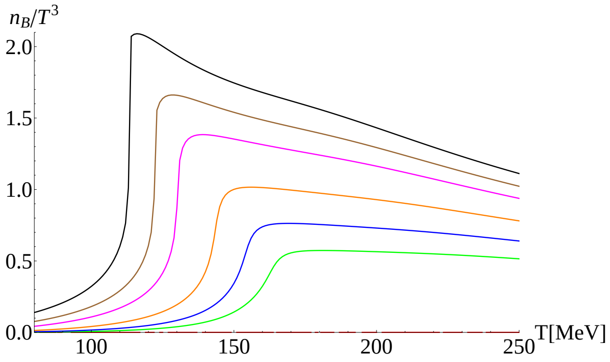

(c) *Net-Baryon density*

Figure 4.10: Mean-field results for the pressure, entropy density and baryon density in the PNJL model (with polynomial potential) as functions of the temperature for different values of the baryochemical potential: $\mu_B = 0$ (red line), 540 MeV (green line), 630 MeV (blue line), 720 MeV (orange line), 810 MeV (magenta line), 862 MeV (brown line), 900 MeV (black line).

Pressure, entropy density and baryon density in the PNJL model are plotted in Fig. 4.9, which refers to the case of logarithmic Polyakov potential and in Fig. 4.10, which refers to the case of polynomial Polyakov potential. For all values of the chemical potential at low-temperature, both the pressure and the entropy density are negligibly small. This reflects the fact that the temperature is so low to make the thermal excitation of quarks, dressed by their dynamical mass, very unlikely. An important role is also played by the Polyakov fields Φ and $\bar{\Phi}$, which in the confined phase suppress the contribution of states with one or two quarks to the thermodynamics of the medium. The pressure gets steeper and steeper progressively as the baryochemical potential increases and above a certain value of μ_B a temperature for which the derivative of the curve is discontinuous appears. The nature of the transition has changed, becoming first-order. Concerning the entropy density, where the pressure curve has a non-derivable point the entropy density shows a jump discontinuity. This fact is in agreement with the statistical mechanics definition of the entropy density as $s \equiv (\partial P/\partial T)_\mu$: the two different values of the entropy density refer to the two different phases which coexist in thermal, chemical and mechanical equilibrium. Similar considerations hold for the baryon density, also shown in Fig. 4.9. This observable is very important for the study of the deconfinement transition. The baryochemical potential μ_B describes the excess of quarks over antiquarks: for a given temperature, the larger μ_B the larger the baryon density of the system. However, for the same reasons discussed above, for low temperature the baryon density is very small. Above a certain value of chemical potential (μ_B^{CEP}), as the temperature increases also the baryon density shows a discontinuity, where the dynamical masses of the quarks suddenly drop and where the Polyakov fields no longer suppress the excitation of coloured quarks. Below μ_B^{CEP}, the transition is a smooth crossover while above this value it is first order. The presence of two degenerate minima of the thermodynamic potential Ω, corresponding to the same value of the pressure, signals the occurrence of a first-order transition. It is possible to draw a first-order line in the phase diagram, which ends at the Critical End-Point. In the present implementation of the PNJL model, from the above plots, one obtains $\mu_B^{\mathrm{CEP}} \sim 862$ MeV and $T^{\mathrm{CEP}} \sim 122$ MeV. A more accurate determination of the location of CEP is performed in the following paragraph using the Logarithmic Polyakov Potential and in the following sections with the Polynomial Polyakov Potential in several scenarios. For a determination of the CEP location of closer phenomenological interest, it is useful to study fluctuations of conserved charges like net-baryon number, as explained in Sec. 3.3.1. In the following I show some results about these quantities.

4.2.3 Generalized baryon-number susceptibilities

In this section I present some results for higher-order baryon number susceptibilities obtained in the fully symmetric scenario in which all quark chemical potentials are equal to $\mu_B/3$ with the logarithmic parameterization of the Polyakov potential. A summary of these results was shown in Ref. [78]. Besides various higher-order susceptibilities, I also show their ratios as functions of the temperature for several values of the baryochemical potential μ_B. At variance with the Polyakov fields, the quark condensates and the previous thermodynamic quantities, generalized susceptibilities – being functions not only of the order parameters but also of their derivatives – display divergences in correspondence of the CEP.

2$^{\text{nd}}$-order susceptibility

In Fig. 4.11 one can see the plot of the 2$^{\text{nd}}$-order baryon-number susceptibility χ_B^2 as a function of the temperature for different values of the baryochemical potential μ_B. According to the definition of generalized susceptibilities introduced in Sec. 3.3.1, one has

$$\chi_B^2(\mu_B, T) \equiv \left. \frac{\partial^2 (P/T^4)}{\partial(\mu_B/T)^2} \right|_T . \tag{4.1}$$

In mean-field approximation this corresponds to:

$$\begin{aligned}\chi^2_B(\mu_B, T) = \left.\frac{d(n_B/T^3)}{d(\mu_B/T)}\right|_T = \\ &= \left(\frac{\partial(n_B/T^3)}{\partial(\mu_B/T)} + \frac{\partial(n_B/T^3)}{\partial\Phi}\frac{\partial\Phi}{\partial(\mu_B/T)} + \right. \\ &\left. + \frac{\partial(n_B/T^3)}{\partial\bar{\Phi}}\frac{\partial\bar{\Phi}}{\partial(\mu_B/T)} + \frac{\partial(n_B/T^3)}{\partial\phi^i}\frac{\partial\phi^i}{\partial(\mu_B/T)}\right)_T . \end{aligned} \tag{4.2}$$

Here the "total derivative" with respect to (μ_B/T) means that, beside the explicit dependence on μ_B, one must consider also the implicit dependence contained in the order parameters Φ, $\bar{\Phi}$ and ϕ_i. From the analytic proprieties of Eq.(3.2.1), at null baryochemical potential, one gets:

$$\chi^2_B(\mu_B = 0, T) = \left(\left.\frac{\partial n_B/T^3}{\partial \mu_B/T}\right|_T\right)_{\mu_B=0} = \frac{2}{3\pi^2 T^3}\sum_i \int_0^{+\infty} dp p^2 \mathcal{F}(p, T)$$

$$\mathcal{F}(p) = \frac{e^{-\beta E_i}\Phi(1 + 4e^{-\beta E_i} + 3\Phi e^{-2\beta E_i} - 5e^{-3\beta E_i} - 8e^{-4\beta E_i})}{(1 + 3e^{-\beta E_i}\Phi(1 + e^{-\beta E_i}) + e^{-3\beta E_i})^2} \tag{4.3}$$

At vanishing chemical potential, χ^B_2 is an increasing function of the temperature without any particular structure except some changes of slope. The curve has an inflection point around $T_c \sim 155$ MeV in correspondence with the transition from confined to deconfined phase.

At finite chemical potential, χ^2_B starts displaying a local maximum associated to the chiral transition: in fact, in Eq. (4.2) the derivatives of the chiral condensates appear, which become larger and larger as the crossover gets sharper and the transition approaches the CEP. As the baryochemical potential grows, the peak increases and moves to lower temperatures following the critical line in the phase diagram. At a given μ_B, the position of the peak can be used as an estimator for the temperature of the chiral transition. Notice that the deconfinement transition occurring at a slightly smaller temperature leaves a much milder signature on χ^2_B, giving rise simply to a double change of curvature on the left of the peak associated to the chiral transition.

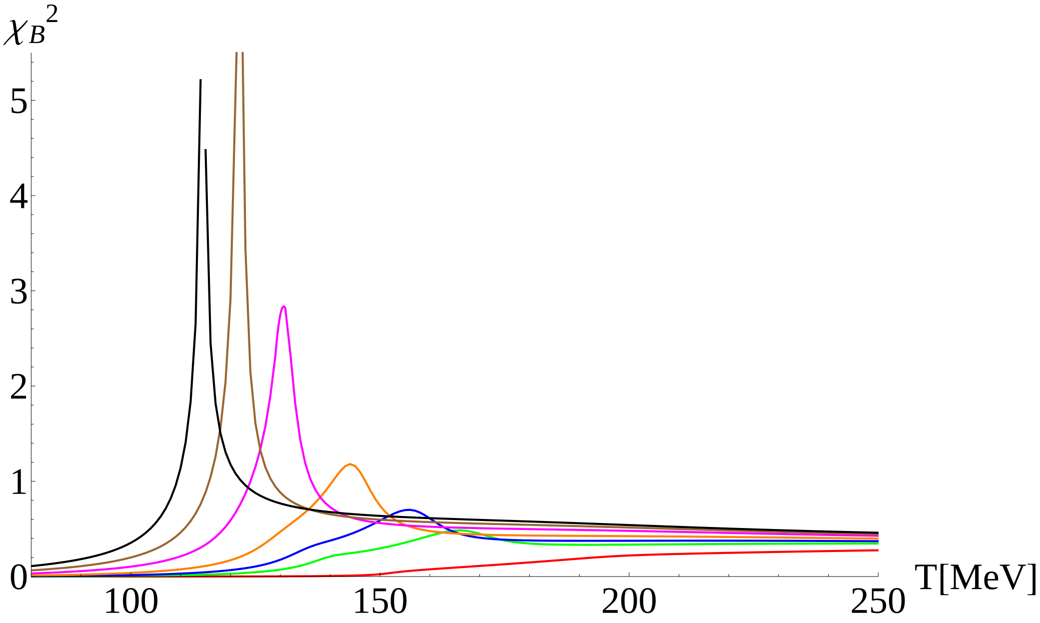

Figure 4.11: Second-order baryon-number susceptibility as a function of the temperature in the PNJL model (with logarithmic potential) for different values of the baryochemical potential: $\mu_B = 0$ (red line), 540 MeV (green line), 630 MeV (blue line), 720 MeV (orange line), 810 MeV (magenta line), 862 MeV (brown line), 900 MeV (black line).

Around $\mu_B = 862$ MeV, the curve displays a divergence. The discontinuity temperature is the first estimator of the Critical End-Point temperature $T_1^{CEP} \approx 122$ MeV. This is due to the fact that χ_2^B depends on the derivatives of the order parameters, which diverge around the CEP. At higher chemical potential, the fluctuations are discontinuous but no longer divergent. This difference is crucial to distinguish between the CEP and the first-order transition line. Indeed, the phase transition, when the system is at the CEP, is of second-order and the derivatives of the order parameters are divergent; on the other hand, along the first-order transition line, their derivatives are discontinuous but finite [45, 95].

3^{rd}-order susceptibility

In Fig. 4.12 I plot the 3^{rd}-order baryon-number susceptibility as a function of the temperature. The qualitative structure of the curves is essentially given

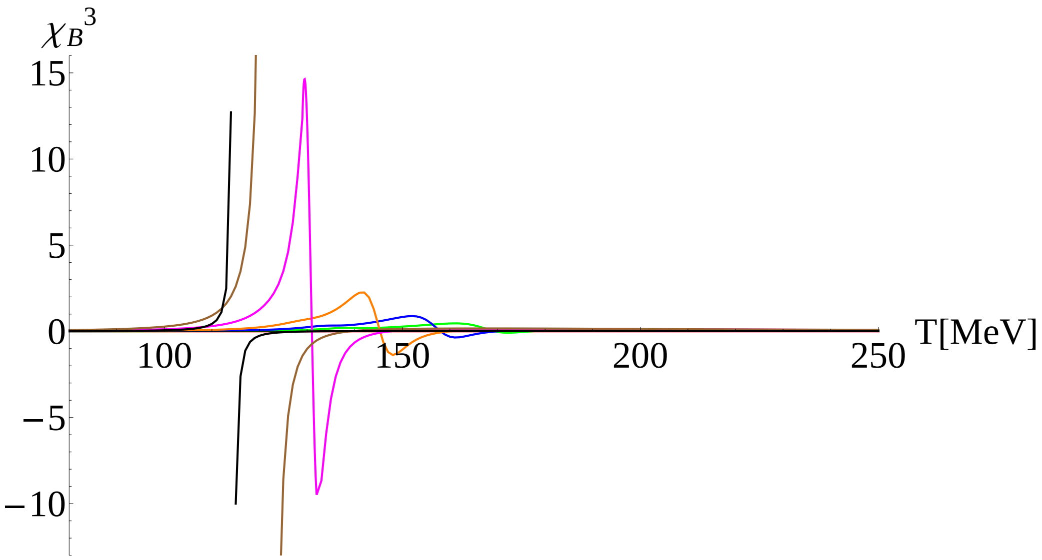

Figure 4.12: Third-order baryon-number susceptibility as a function of the temperature in the PNJL model (with logarithmic potential) for different values of the baryochemical potential: $\mu_B = 0$ (red line), 540 MeV (green line), 630 MeV (blue line), 720 MeV (orange line), 810 MeV (magenta line), 862 MeV (brown line), 900 MeV (black line).

by the chiral transition. The main feature of the curves is the presence of a positive maximum and a negative minimum separated by a sudden change of sign, associated to the peak of χ_B^2. When the baryochemical potential grows the maximum and the minimum move to lower temperatures, get more pronounced and the change of sign gets steeper. This is in agreement with the peak in χ_B^2 getting sharper and sharper. The location of the zero of χ_B^3 is the second estimator for the chiral transition temperature. Around $\mu_B = 862$ MeV an essential discontinuity appears. The position of the discontinuity is the second estimator of the Critical End-Point temperature $T_2^{CEP} \approx 122$ MeV.

4^{th}-order susceptibility

The plot of the 4^{th}-order baryon-number susceptibility as a function of temperature, for different values of μ_B, is shown in Fig. 4.13. The main feature of the curves is the presence of a more and more pronounced negative minimum as μ_B gets larger, associated to the sharper and sharper peak of

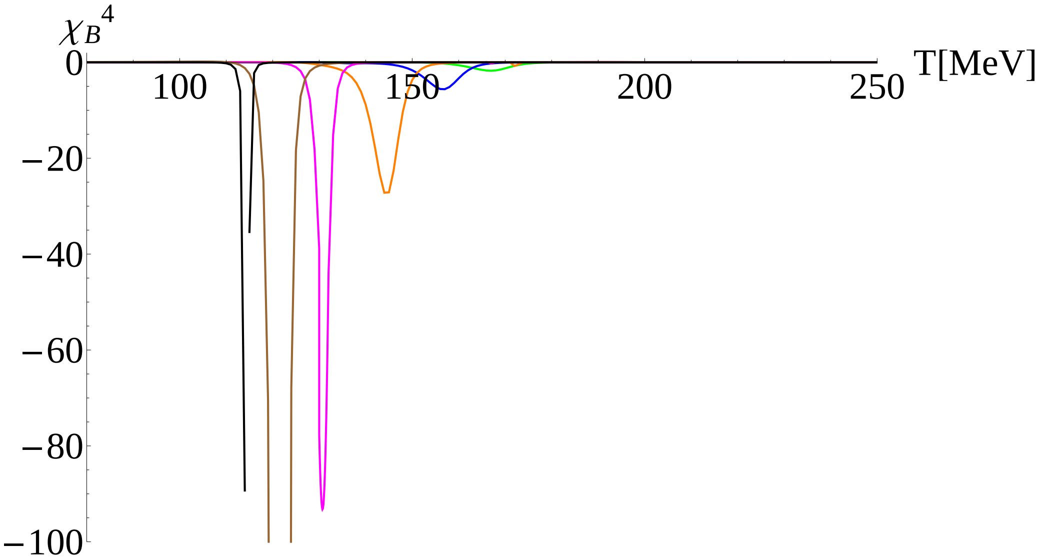

Figure 4.13: Fourth-order baryon-number susceptibility as a function of the temperature in the PNJL model (with logarithmic potential) for different values of the baryochemical potential: $\mu_B = 0$ (red line), 540 MeV (green line), 630 MeV (blue line), 720 MeV (orange line), 810 MeV (magenta line), 862 MeV (brown line), 900 MeV (black line).

χ_B^2, which has a negative curvature as a function of μ_B. As the baryochemical potential increases, the minimum moves to lower temperatures, following the crossover line in the phase diagram. The position of this minimum is a third estimator for the chiral transition temperature. At $\mu_B = 862$ MeV there is an essential discontinuity that can be used as a third estimator of the Critical End-Point temperature $T_3^{CEP} \approx 122$ MeV.

Ratio of generalized susceptibilities: χ_B^4/χ_B^2

The ratio of the 4th and 2nd-order baryon-number susceptibilities is related to the kurtosis via Eq. (3.77) and, in the classical limit, turns out to be proportional to the square of the baryon charge carried by the active degrees of freedom in the system, according to Eq. (3.79). At low temperature, the baryon charge of the active degrees of freedom is unitary: quarks are confined into hadrons and particles carrying baryon number have $B = 1$. In the PNJL model this is implemented through the Polyakov fields, which

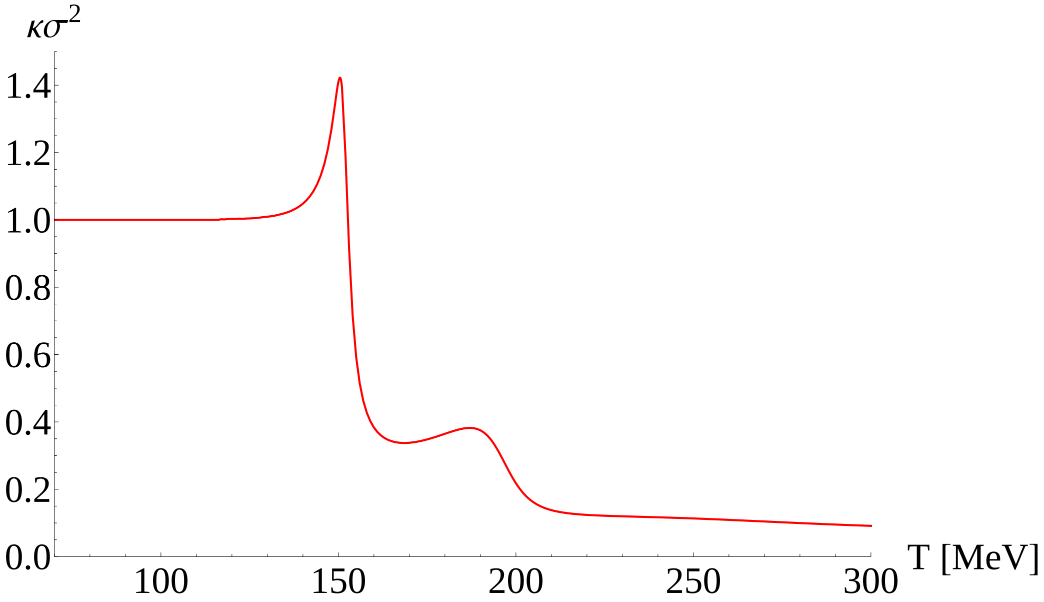

Figure 4.14: χ_B^4/χ_B^2 as a function of temperature at zero baryochemical potential.

suppress coloured combinations of quarks, leaving only colourless clusters of 3 quarks or antiquarks to contribute to the thermodynamics of the system. At high temperature, the baryon charge of the active degrees of freedom is 1/3 (free quarks and antiquarks). As one can see in Fig. 4.14, the value of the kurtosis at high temperature is around 1/9 and at low temperature its value is around 1: the PNJL model correctly captures the active degrees of freedom of the system. Beside these two flat regions, the kurtosis has two local maxima, associated to the deconfinement of quarks and to the chiral transition, which, in the present implementation of the PNJL model, occur at two slightly different temperatures $T_c^{\mathrm{dec}} \sim 155$ MeV, $T_c^{\chi} \sim 192$ MeV. These two estimators of the pseudo-critical temperature are in agreement with the positions of the inflection point of the Polyakov fields and of the light chiral condensate in Figs. 4.5 and 4.7.

The study of the kurtosis can be extended to finite chemical potential. In Fig. 4.15 I show the corresponding results, which still display the correct low-temperature behaviour associated to the effective confinement of the quark colour charges. The χ_B^4/χ_B^2 ratio has an essential discontinuity around $\mu_B =$

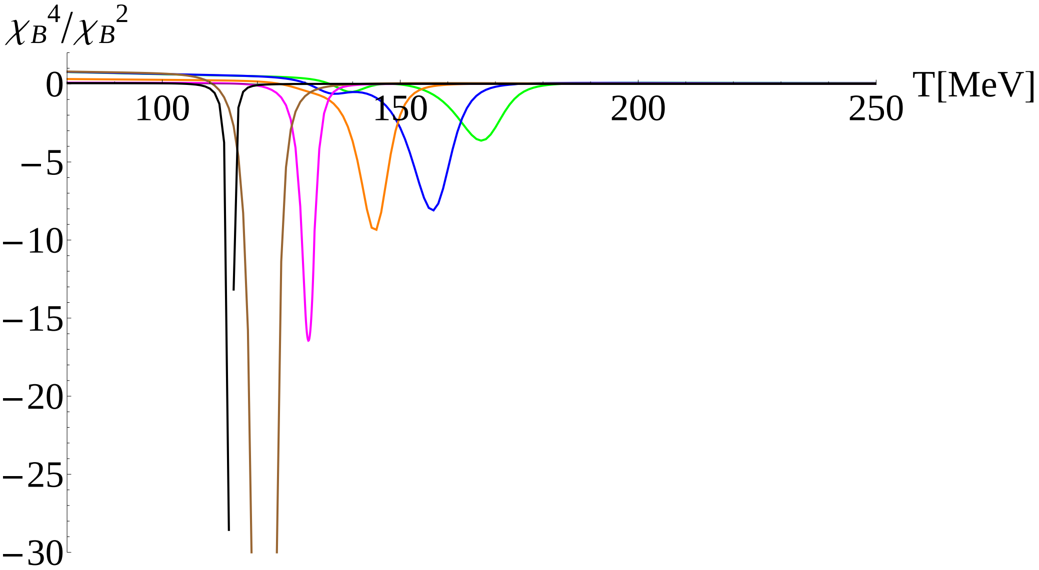

Figure 4.15: χ_B^4/χ_B^2 as a function of the temperature for different values of the baryochemical potential: $\mu_B = 0$ (red line), 540 MeV (green line), 630 MeV (blue line), 720 MeV (orange line), 810 MeV (magenta line), 862 MeV (brown line), 900 MeV (black line).

862 MeV and $T = 122$ MeV, in agreement with other observables. Notice that both χ_B^4 and χ_B^2 have an essential discontinuity at the CEP, but higher-order susceptibilities have a stronger dependence on the diverging correlation length.

Ratio of generalized susceptibilities: χ_B^3/χ_B^1

The second important ratio of generalized susceptibilities is χ_B^3/χ_B^1 and it is related to the skewness by Eq. (3.77). At $\mu_B = 0$, the skewness is zero. At finite chemical potential also χ_B^3/χ_B is proportional to the squared baryon charge of the active degrees of freedom. In fact, the curves plotted in Fig. 4.16 start from 1 at low temperature (where coloured quark states are suppressed), then show some bumps due to deconfinement and chiral transitions and eventually converge at high temperature to 1/9 (where quarks are active degrees of freedom). At $\mu_B = 862$ MeV an essential discontinuity appears at $T \approx 122$ MeV, in agreement with other observables.

In conclusion, from the study of the divergences of the above general-

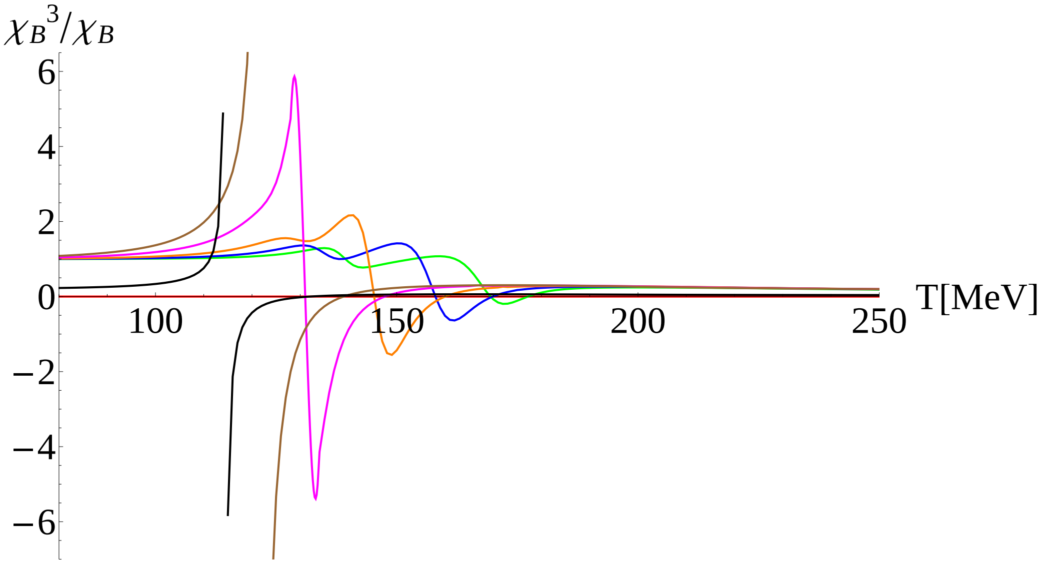

Figure 4.16: χ_B^3/χ_B^1 as a function of temperature for different values of the baryochemical potential: $\mu_B = 0$ (red line), 540 MeV (green line), 630 MeV (blue line), 720 MeV (orange line), 810 MeV (magenta line), 862 MeV (brown line), 900 MeV (black line).

ized susceptibilities, one can affirm that the Critical End-Point is located at CEP $\approx (862, 122)$ MeV. The two crossover temperatures at zero chemical potential are $T_c^\chi = 192$ MeV and $T_c^{\rm dec} = 155$ MeV.

4.3 Fully symmetric scenario

The matter produced in HIC's, if dissipative effects are negligible, evolves along isentropic trajectories of constant entropy per baryon. In this section I explore the phase diagram of the PNJL model along these adiabatic lines focusing on the Equation of State, the speed of sound and the baryon-number fluctuations. I also identify the crossover/first-order transition line and the location of the CEP. In the presence of a first-order transition, I also display the metastability region. In this sections calculations are performed in the fully symmetric scenario (SYM), in which all quark chemical potentials are equal: $\mu_u = \mu_d = \mu_s = \mu_B/3$.

4.3.1 Equation of State and speed of sound

In heavy-ion collisions, one produces a system which – neglecting dissipative effects due to viscosity, heat conduction and charge diffusion – undergoes an approximate isentropic expansion moved by pressure gradients along trajectories of constant entropy per baryon (s/n_B = const), the higher the center-of-mass energy of the collision the higher the s/n_B ratio. Hence, in performing theoretical calculations of experimental relevance, the quantities of physical interest must be evaluated along the above trajectories. To compute the entropy density and the net-baryon density, one can use the equations given in Appendix C. To find the points that belong to an isentropic trajectory, one starts from a point in the phase diagram of a given entropy per baryon; one looks for the next point along a small circle centered around the first one corresponding to the same value of s/n_B and then iterates the procedure. Some interesting theoretical studies about isentropic lines are Ref.[35, 37, 83].In these works are introduced a vectors interaction in the Lagrangian and is explored the phase transition with the presence of a magnetic field.

In order to provide results of phenomenological relevance, we need to estimate both the entropy-per-baryon ratio S/B and the initial entropy density of the system arising from the heavy-ion collisions at the various nucleon-nucleon center-of-mass energies explored in the BES at RHIC, from 7.7 GeV to 200 GeV. We start estimating the initial entropy density s_0, assuming that its value is proportional to the measured rapidity density of charged particles $dN^{\rm ch}/d\eta$. For Au-Au collisions at $\sqrt{s_{\rm NN}} = 200$ GeV the value $s_0 = 84\,{\rm fm}^{-3}$, once inserted in the initial condition of hydrodynamic calculations, was shown to satisfactorily reproduce soft-hadron distributions [71] and, later on, it was widely employed in the literature, e.g. [16, 25]. Taking $\tau_0 = 1$ fm/c as an estimate of the initial thermalization time and integrating over the transverse plane the profile provided by a Glauber calculation one gets $dS/dy \approx 4700$ for the entropy per unit rapidity in central Au-Au collisions; taking into account that, for a pion gas around the chemical freeze-out temperature, one has $S \gtrsim 4N$, this compares well with the observed rapidity density of charged particles [20]. The initial entropy density s_0 at lower center-of-mass energies is obtained rescaling the estimate at $\sqrt{s_{\rm NN}} = 200$ GeV according to the lower values of $dN^{\rm ch}/dy$ [5, 6]. Also the S/B ratio at the various center-of-mass energies is estimated from the yields of identified hadrons – $\pi^{\pm}$, $K^{\pm}$, $p/\overline{p}$ – quoted in Refs. [5, 6], still assuming that each particle carries about 4 unit of entropy. Our results for s_0 and S/B are collected in Table 4.2, where we also quote the values of the kinetic freeze-out temperatures obtained in [5, 6] through a blast-wave fit of the transverse-momentum distributions of identified hadrons.

Along these isentropic lines, then, it is interesting to evaluate the physical quantities entering hydrodynamics calculations, as discussed in Sec. 1.7. For this reason, one can focus on the Equation of State and on the squared speed of sound c_s^2, which can be derived from the latter. In Fig. 4.17 I plot the EoS calculated along various isentropic trajectories, corresponding to values of s/n_B of interest for HIC's at RHIC center-of-mass energies. In this figure one can see that, employing logarithmic scales for the axis, the curves have an approximate straight-line behaviour, except in a very limited region of energy density around the chiral crossover where the EoS looks softer. The softening of the EoS is particularly evident for small values of the entropy-per-baryon ratio, corresponding to small center-of-mass energies of the HIC's and to large stopping of the matter of the colliding nuclei. Anyway, the EoS's are smoothly increasing functions of ε (hence $c_s^2 > 0$) for all the values of

$\sqrt{s_{\rm NN}}$ [GeV]	s_0 [fm^{-3}]	S/B	$T_{\rm kin}^{\rm fo}$
7.7	29.6	17.5	116
11.5	35.3	26.7	118
19.6	43.0	45.8	113
27.0	45.8	56.8	117
39.0	47.6	84.3	117
62.4	60.2	123.9	99
130	70	277.6	98
200	84	331.6	89

Table 4.2: Estimate of the initial entropy density and of the entropy per baryon in Au-Au collisions at different center-of-mass energies. We also quote the kinetic freeze-out temperature obtained in Refs. [5, 6] through a blast-wave-fit.

entropy per baryon of phenomenological interest I explored. This means that, for these values of s/n_B, the system changes phase smoothly and no first-order transition appears. One does not have bubbles of deconfined matter in a hadronic background or vice versa.

In Fig. 4.18 I plot the squared speed of sound c_s^2 for several values of s/n_B. The curves are positive and smooth for all the considered values of entropy per baryon. This means that in this domain the system changes phase smoothly, with a crossover and not with a first-order transition. One observes that, around the crossover region, c_s^2 displays a minimum, which gets deeper as s/n_B decreases. Moreover, from Eq. (2.4) one can see that the system decreases the acceleration of its expansion and that there is a value of temperature for which such an acceleration is minimal. The squared speed of sound, as one expects, at high temperature converges to the Stefan-Boltzmann limit $c_s^2 = 1/3$. This fact suggests that, at very high temperature, the QGP can be approximated as a gas of free massless particle.

4.3.2 Net baryon-number fluctuations

In Fig. 4.19 the ratios of higher-order net baryon-number susceptibilities (χ_B^4/χ_B^2 and χ_B^3/χ_B^1) for the different isentropic trajectories are displayed.

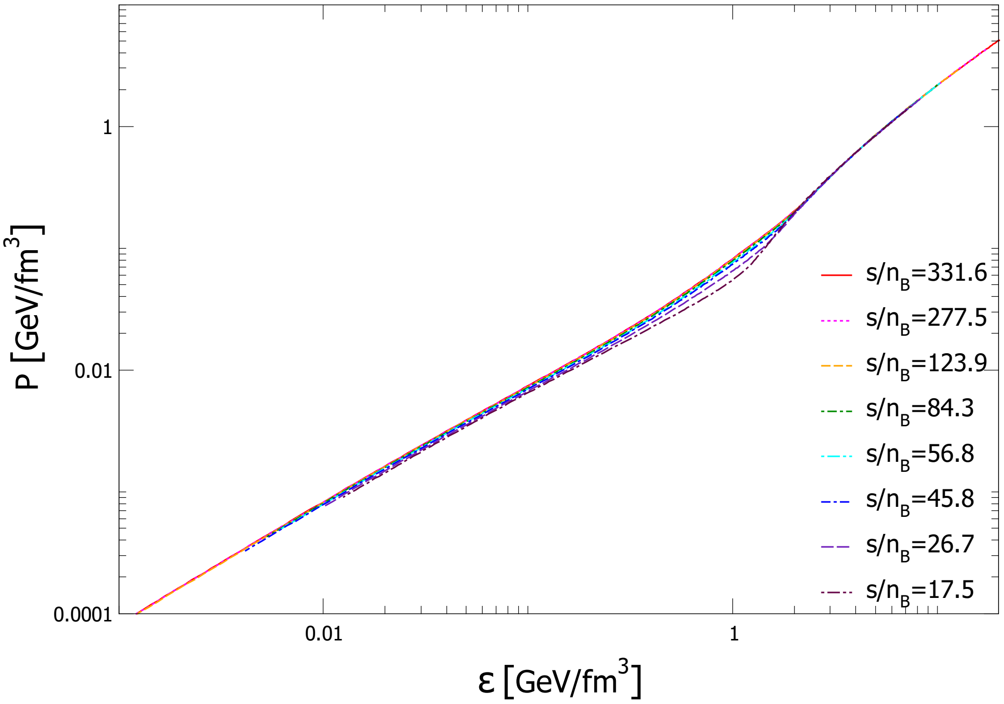

Figure 4.17: Equation of State $P(\varepsilon, s/n_B)$ evaluated along isentropic trajectories for several values of s/n_B in the fully symmetric scenario for the entropy per baryon values: $s/n_B = 331.6$ (red line), 277.6 (magenta line), 123.9 (orange line), 84.3 (green line), 56.8 (cyan line), 45.8 (blue line), 26.7 (purple line), 17.5 (indigo line).

One can see that these quantities display huge fluctuations around the transition temperature, which get larger and larger as the entropy per baryon decreases. However, the various susceptibilities remain continuous functions. This means that the CEP and the first-order region are not achieved for these values of s/n_B, representative of the collisions during the Beam Energy Scan (BES) at RHIC. The growth of fluctuations is easy to understand if one remembers the link between the generalized susceptibilities and the cumulants of the distributions of conserved charges and their different dependence on the correlation length of the order parameter, which is stronger for higher-order susceptibilities. In particular, the χ_B^3/χ_B^1 ratio is proportional to the skewness, that represents the asymmetry of the distribution. The χ_B^4/χ_B^2 ratio is proportional to the kurtosis, which quantifies how tailed the distri-

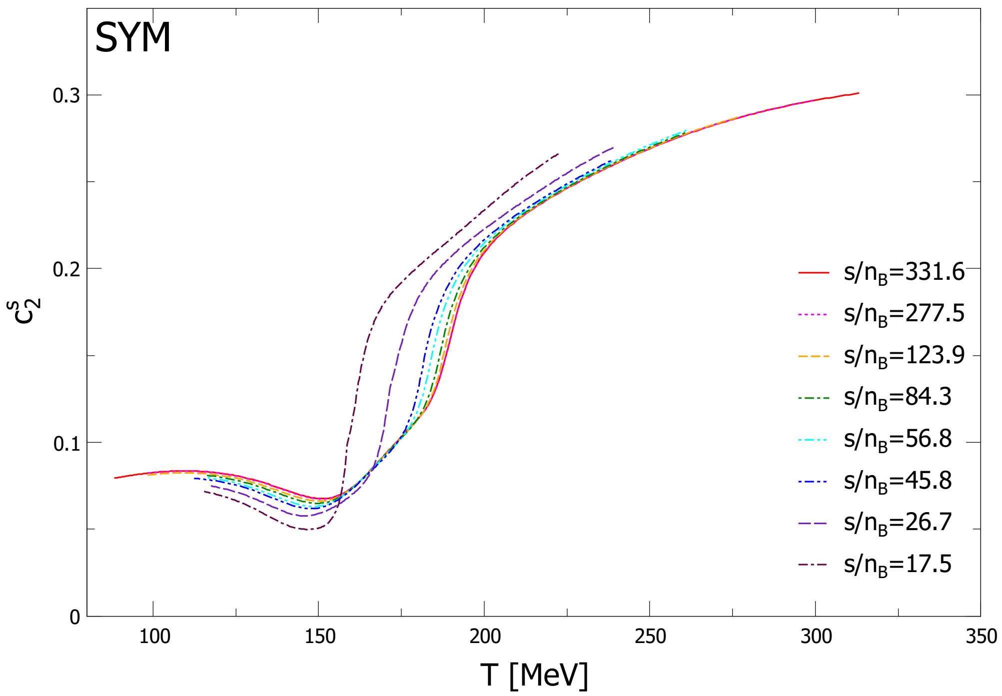

Figure 4.18: Squared speed of sound c_s^2 evaluated along isentropic trajectories for several values of s/n_B in the fully symmetric scenario entropy per baryon values: $s/n_B = 331.6$ (red line), 277.6 (magenta line), 123.9 (orange line), 84.3 (green line), 56.8 (cyan line), 45.8 (blue line), 26.7 (purple line), 17.5 (indigo line).

bution is. In this case, the distribution of interest is the net-baryon number distribution. Isentropic trajectories corresponding to lower values of s/n_B pass closer to the CEP and hence, around the crossover, are characterized by a larger correlation length. Equivalently, the crossover for them is steeper. This explains the huge fluctuations and sharp peaks of the χ_B^3/χ_B^1 and χ_B^4/χ_B^2 ratios around the transition temperature.

Notice also the expected values close to 1 and 1/9 in the low and high-temperature limits, respectively.

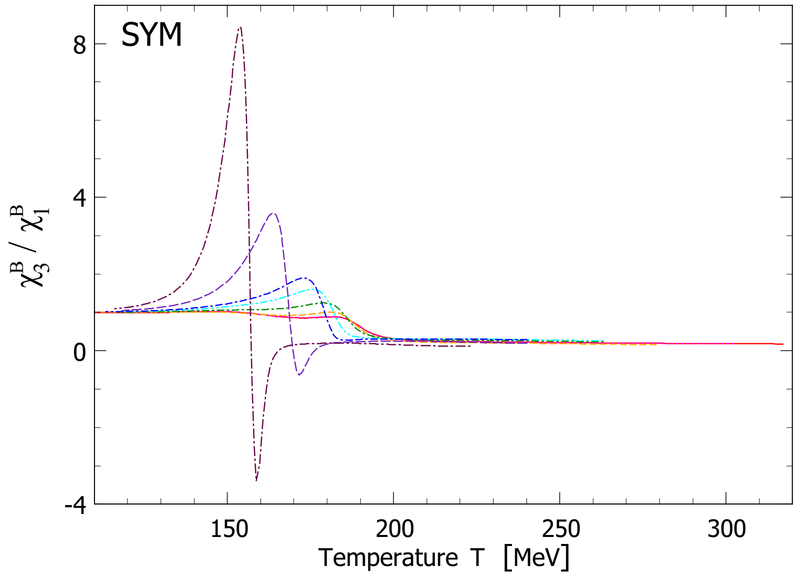

(a) χ_B^3/χ_B^1 *ratio along different isentropic trajectories*

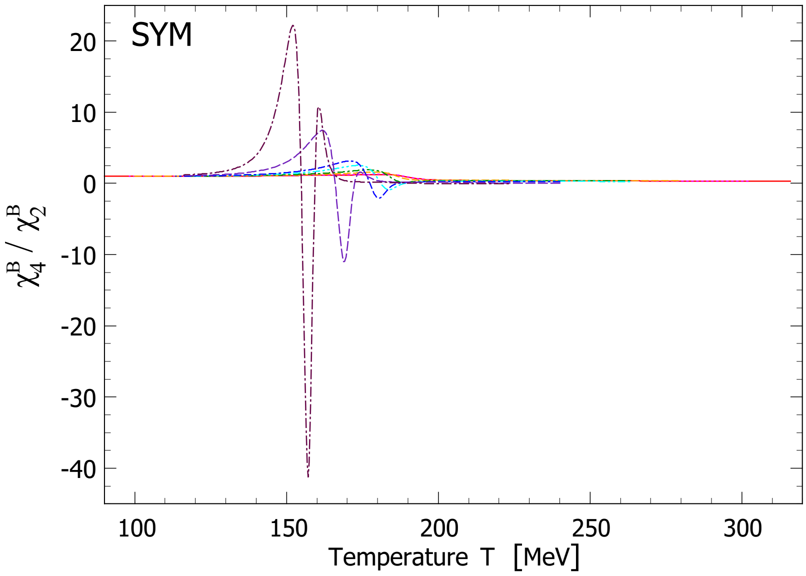

(b) χ_B^4/χ_B^2 ratio along different isentropic trajectories

Figure 4.19: Ratios of higher-order baryon-number susceptibilities along isentropic trajectories for several values of s/n_B in the SYM quark chemical potential scenario: $s/n_B = 331.6$ (red line), 277.6 (magenta line), 123.9 (orange line), 84.3 (green line), 56.8 (cyan line), 45.8 (blue line), 26.7 (purple line), 17.5 (indigo line).

4.3.3 Phase diagram in the SYM scenario

From the stationary points and the rapid oscillations of the baryon-number susceptibilities one can define the transition line between the phases of broken and restored chiral symmetry and identify, through their divergences, the CEP predicted by the model.

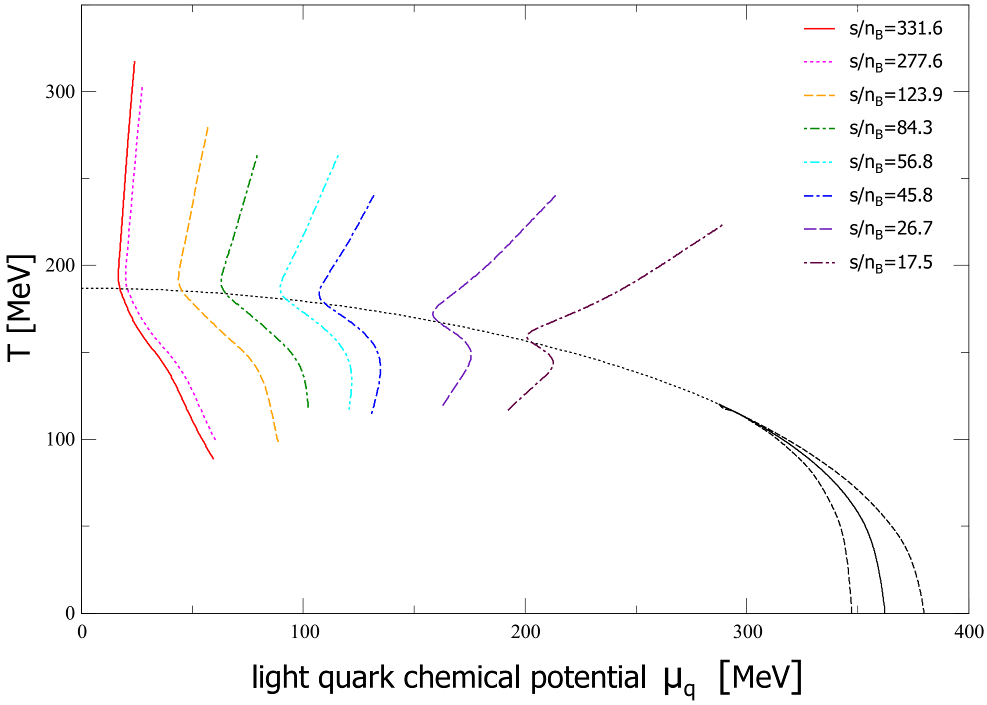

Figure 4.20: Phase diagram of the PNJL model in the SYM scenario $\mu_u = \mu_d = \mu_2 = \mu_B/3$. The black dotted curve represents the chiral crossover line, the black solid curve is the fist-order transition line, the two black dashed lines are the borders of the metastability regions. The colored lines are the isentropic trajectories for several values of s/n_B: 331.6 (red line), 277.6 (magenta line), 123.9 (orange line), 84.3 (green line), 56.8 (cyan line), 45.8 (blue line), 26.7 (purple line), 17.5 (indigo line).

In Fig. 4.20 I show the phase diagram of the model together with several isentropic trajectories that correspond to the entropy per baryon representative of HIC's at the RHIC Beam-Energy Scan [6, 32]. The curves have been plotted down to the kinetic freeze-out temperatures estimated in Au-Au collisions at RHIC from the momentum distributions of the detected particles and quoted in Table 4.2. For more information about this topic see [79]. As one can see, for all values of s/n_B the isentropic trajectories display a change of direction around the crossover line, but this bend is sharper for higher values of the chemical potential. All the adiabatic trajectories pass through the crossover region, where the chiral transition occurs smoothly and there is no coexistence of two different phases. The present implementation of the PNJL model predicts that the current experiments carried out with the BES program at RHIC are not able to reach the QCD CEP. This might be achieved only through the collisions of heavy nuclei at lower center-of-mass energies, characterized by a larger stopping of the incoming nucleons. For this purpose, experiments were performed in the past at AGS [14] and SPS [8], a rich physics program is scheduled for the present and the near future at SPS [76] and new infrastructures like NICA [10] and FAIR are under construction.

In order to compare the results for the transition line of this effective chiral model with the findings of lattice-QCD simulations, one can fit the small μ_B region of the PNJL crossover line (up to $\mu_q = 100$ MeV or, in other words, up to $\mu_B = 300$ MeV) with a quartic polynomial in the dimensionless variable μ_B/T_c^0, where $T_c^0 \equiv T_c(\mu_B = 0)$ is the pseudo-critical temperature of the model (still referring to the chiral phase transition) at zero chemical potential:

$$\frac{T_c(\mu_B)}{T_c^0} = 1 - \kappa_2\left(\frac{\mu_B}{T_c^0}\right)^2 - \kappa_4\left(\frac{\mu_B}{T_c^0}\right)^4 + \mathcal{O}\left[\left(\frac{\mu_B}{T_c^0}\right)^6\right] . \tag{4.4}$$

From the PNJL model in the SYM scenario one obtains:

$$T_c^0 = (186.5 \pm 0.1)\text{MeV}, \quad \kappa_2 = (170 \pm 3)10^{-4}, \quad \kappa_4 = (-17 \pm 3)10^{-4}. \tag{4.5}$$

These results will be compared with lattice-QCD predictions in Chapter 5.

The two dashed lines in Fig. 4.20 are the boundaries of the metastability region, where the thermodynamic potential has two local minima that correspond to the “hadronic” (broken chiral symmetry) and quark (restored chiral symmetry) phases. The solid line is the first-order transition line, where the two minima have the same value, i.e. the two phases have the same pressure and can coexist in mechanical equilibrium. This means that, along the first-order line, a certain volume of the system is occupied by the quark phase and the rest by bubbles of hadronic matter or vice versa. When drawn in the density-temperature plane, the first order line is the border of a coexistence region in which the system cannot exist as a single stable phase. Depending on the cases, it is however possible that the medium remains as a whole in a local metastable minimum. This occurs if the nucleation rate of bubbles of the new stable phase is not fast enough compared to the expansion rate of the system. One has then super-heating or super-cooling.

The first-order line, characterized by the presence of two degenerate minima of the thermodynamic potential, ends at the CEP. In the SYM scenario for the quark chemical potentials (i.e. $\mu_Q = \mu_S = 0$ for the conserved charges) with the polynomial Polyakov potential, the CEP is found at $T^{\rm CEP} = 120$ MeV and $\mu_B^{\rm CEP} = 863$ MeV.

From a general point of view, the phase diagram is a four-dimensional space and the CEP's form an hypersurface defined by $T^{\rm CEP}(\mu_S, \mu_Q)$ and $\mu_B^{\rm CEP}(\mu_S, \mu_Q)$. One interesting question is what kind of surface the one spanned by the CEP's is. It can be an open or a closed surface. In the first case for any value of μ_S and μ_Q there exists, somewhere, a CEP. In the second case the CEP exists only in some specific region of the 4D phase diagram.

4.4 Quasi-Neutral Strangeness Scenario

Here I repeat the study performed in Sec. 4.3, extending it to the Quasi-Neutral Strangeness (QNS) scenario. The QNS condition is obtained setting the electric-charge chemical potential μ_Q to zero, so that $\mu_u = \mu_d$, and imposing a vanishing strange-quark chemical potential, i.e. $\mu_s = 0$, which entails the following relation:

$$\mu_S = 1/3\mu_B \qquad \text{when} \qquad \mu_Q = 0\ . \tag{4.6}$$

In the NJL model, these conditions lead to a vanishing strange-quark density, but in the PNJL model this does not occur. This fact is due to the presence of the Polyakov fields that provide a mixing of the flavours, as evident in Eq.(3.40). In this scenario, therefore, the strange-quark density is small as compared to the one of up and down quarks, but not null.

4.4.1 Equation of State and speed of sound

In this scenario I calculate the same isentropic trajectories considered for the SYM case, plus two new adiabatic lines at lower values of s/n_B, in order to display what happens when the system during its evolution crosses the first-order line. These two isentropic lines do not correspond to values of the entropy per baryon representative of current HIC's at RHIC, but they are important from the theoretical point of view since they allow one to appreciate quite general aspects of the behaviour of a strongly interacting system undergoing a first-order transition. The values of the entropy per baryon for these two new isentropic lines are $s/n_B = 5$ and $s/n_B = 2$.

As in the SYM scenario, isentopic curves are plotted down to the kinetic freeze-out temperatures estimated in Au-Au collisions at RHIC from the momentum distributions of the detected particles and quoted in Table 4.2. Since the Polyakov fields strongly suppress the contribution of quarks to the thermodynamics of the system in the confined phase, the latter corresponds to unrealistically small values of the energy density.

In Fig. 4.21 I show the EoS for a few isentropic trajectories. The first lines

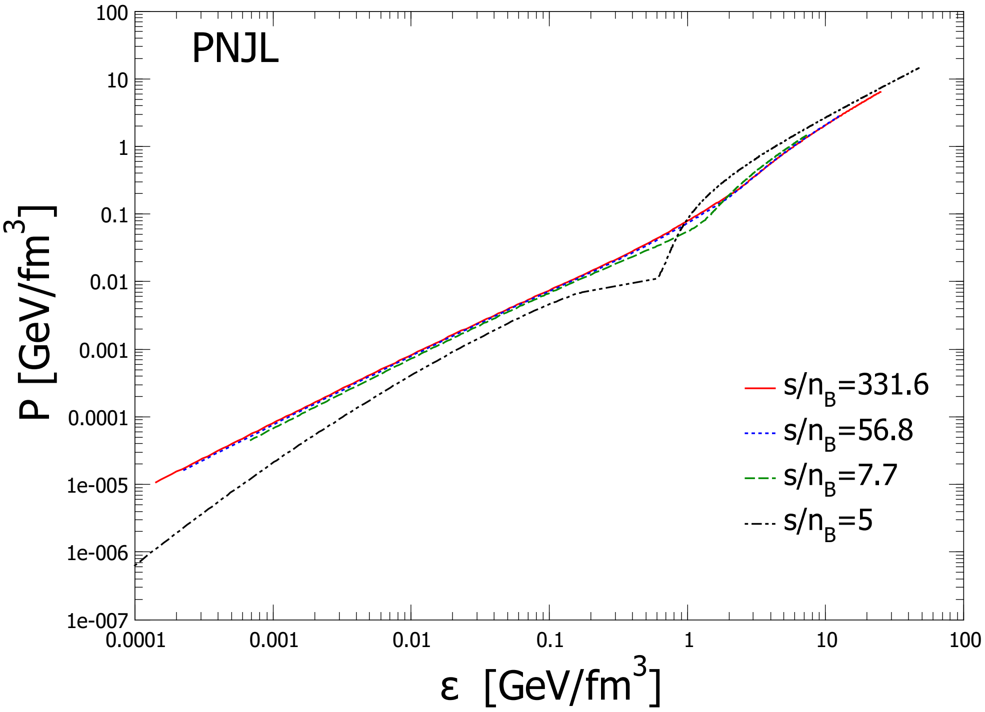

Figure 4.21: Equation of State $P = P(\varepsilon, s/n_B)$ in the QNS scenario evaluated along adiabatic lines corresponding to different values of entropy per baryon s/n_B: 331.6 (red line), 56.8 (blue line), 26.7 (green line), 5 (black line)

are smooth and show just some changes of slope (a flattening followed by a steepening) for energy densities around 1 GeV/fm^3, more evident for lower s/n_B. The last EoS, referring to $s/n_B = 5$, shows an almost flat behaviour in the region $0.2 \lesssim \varepsilon \lesssim 0.7$ GeV/fm^3 ending with a non-derivable point, where its slope suddenly changes. Here the speed of sound displays a discontinuity and this can be interpreted as a signal of a first-order phase transition. One can conclude that below some critical value of the entropy per baryon the system undergoes a first-order phase transition.

In Fig. 4.22 I plot the squared speed of sound along various isentropic trajectories. The behaviour of the curves is similar to what found in the SYM scenario, with the minimum of the speed of sound getting deeper and moving to lower temperatures as s/n_B decreases. The last two plots correspond to the trajectories with $s/n_B = 5$ and $s/n_B = 2$. Here the speed of sound

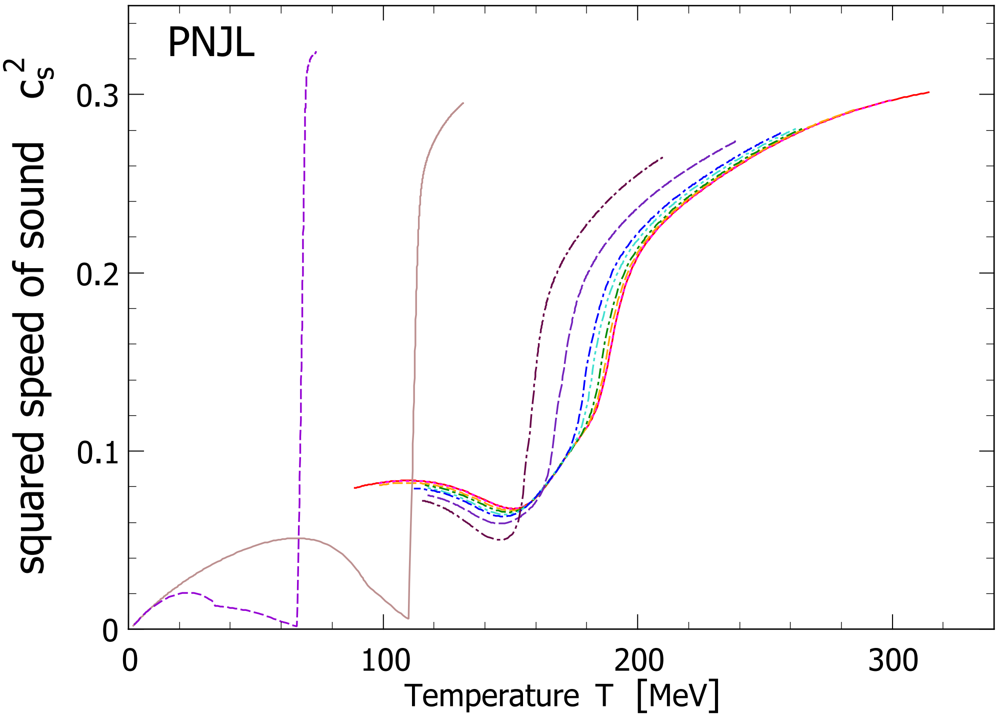

Figure 4.22: Squared speed of sound in the QNS scenario along isentropic trajectories corresponding to different values of s/n_B: 331.6 (red line), 277.6 (magenta line), 123.9 (orange line), 84.3 (green line), 56.8(cyan line), 45.8 (blue line), 26.7 (purple line), 17.5 (indigo line), 5 (brown line), 2 (violet line).

displays a discontinuous behaviour, with a sudden drop as the system cools down in correspondence of the coexistence phase. Notice that the two curves crossing the first-order transition approach faster the ideal gas limit at high temperature.

4.4.2 Net baryon-number fluctuations

In Fig. 4.23 one can see the results for the ratios of baryon-number susceptibilities along adiabatic trajectories passing through the crossover region in the QNS scenario. The curves display a behaviour very similar to the one found in the SYM scenario and the same considerations hold to interpret their main qualitative features. The analysis of the huge peaks and oscilla-

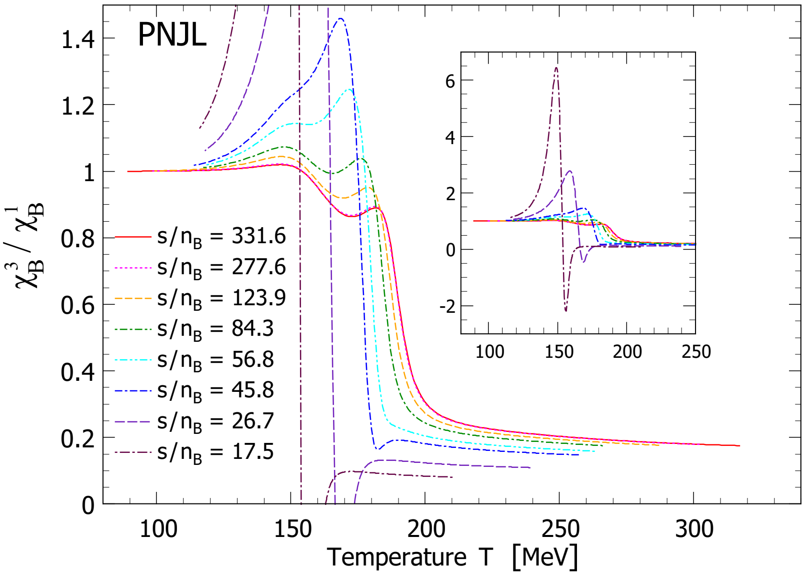

(a) χ_B^3/χ_B^1 *along the isentropic trajectories*

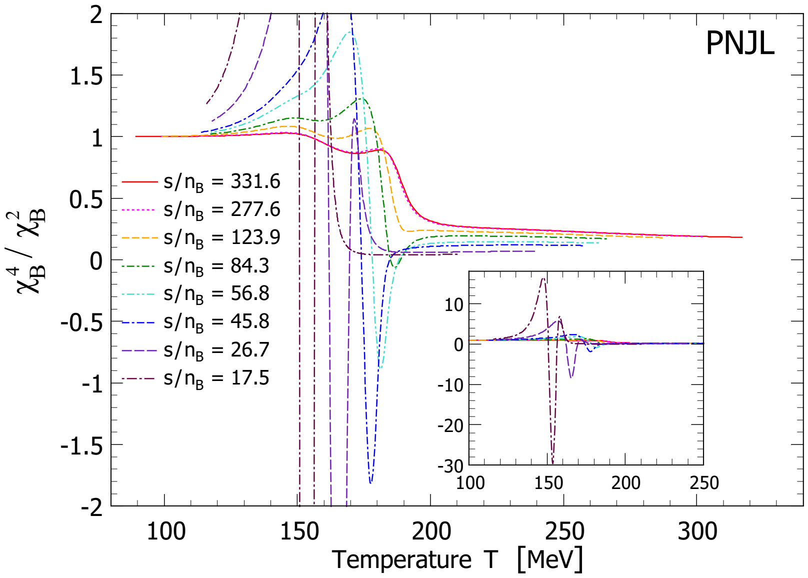

(b) χ_B^3/χ_B^1 along the isentropic trajectories

Figure 4.23: Ratios of higher-order baryon-number susceptibilities along isentropic trajectories for several values of s/n_B in the QNS scenario: $s/n_B =$ 331.6 (red line), 277.6 (magenta line), 123.9 (orange line), 84.3 (green line), 56.8 (cyan line), 45.8 (blue line), 26.7 (purple line), 17.5 (indigo line).

tions around the chiral crossover can be used to extract the parameters of the transition and to draw the phase diagram of the model as done for the SYM scenario.

4.4.3 Phase diagram in the QNS scenario

In figure 4.24 I show two different versions of the phase diagram. The first one is given in a plane spanned by the temperature and chemical potential, the second one in a plane spanned by the temperature and quark density. In the figure I also plot two isentropic lines at low entropy per baryon ($s/n_B = 5$ and 2) which cross the first-order region. In particular, the first isentropic curve ($s/n_B = 5$) meets the first-order line in the $\mu_q - T$ plane, it flows along this critical line and it reappears on the other side of the transition line, in the chirally broken phase. The other one ($s/n_B = 2$) meets the first-order line but does not enter into the confined region. It means that the system created at $s/n_B = 2$, once met the first-order line, remains in the coexistence region.

Also in this case one can perform a fit of the crossover line getting

$$T_c^0 = (187.0 \pm 0.1)\text{MeV}, \quad \kappa_2 = (143 \pm 17)10^{-4}, \quad \kappa_4 = (-1 \pm 20)10^{-4}. \quad (4.7)$$

These results will be compared with lattice-QCD findings in Chapter 5.

The CEP is located where the two borders of the metastable regions meet the first-order line, i.e. when the termodynamic potential no longer has two local minima. In the QNS scenario the CEP is found at $T^{\text{CEP}} = 120.7$ MeV and $\mu_B^{\text{CEP}} = 875.0$ MeV.

The second plot in Fig. 4.24 shows the phase diagram in the $n_q - T$ plane. In this plot, the first-order line encloses the coexistence region. In the coexistence region no *stable* homogeneous phase can exist, but a fraction α of the volume is occupied by the chirally-restored phase and a fraction $(1 - \alpha)$ is occupied by the chirally-broken one. They are characterized by the same pressure, temperature and chemical potential, expressing the mechanical, thermal and chemical equilibrium between the two phases. For each T and μ_B the value of α, which is determined through a Maxwell construction,

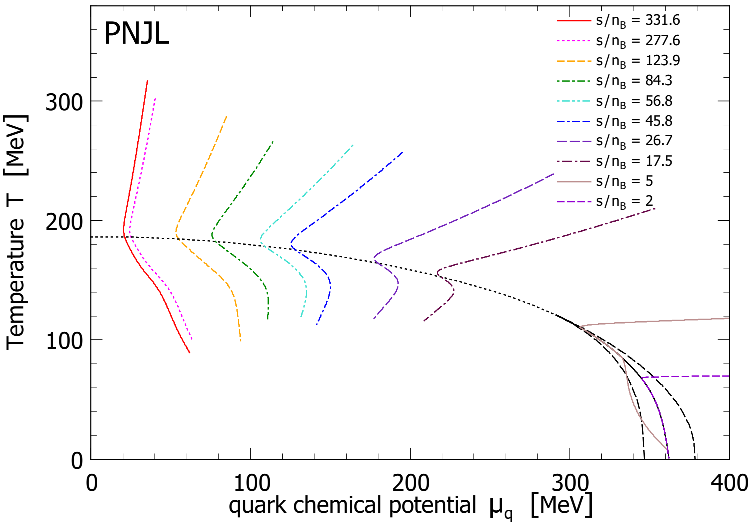

(a) *Phase diagram in the $\mu_q - T$ plane.*

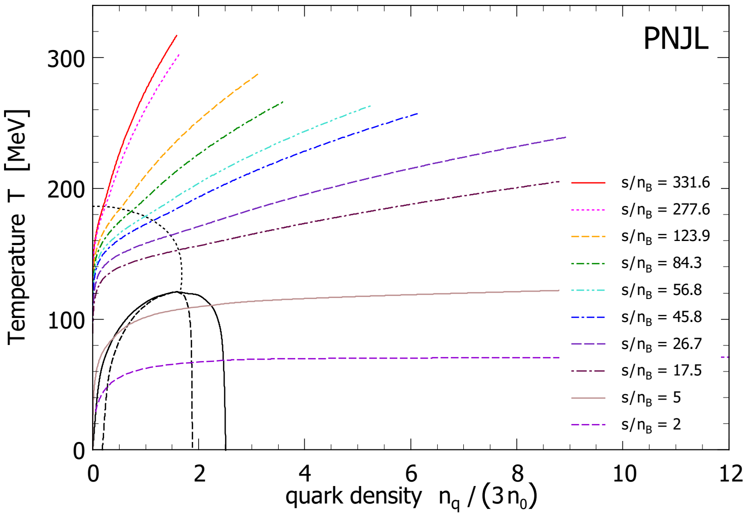

(b) Phase diagram in the $n_q - T$ plane.

Figure 4.24: The phase diagram of the PNJL model in the QNS scenario. In the lower panel densities are measured in units of the nuclear-matter density. The black dotted curve is the chiral crossover line, the black solid curve is the first-order line, the two black dashed lines are the borders of the metastable regions. The colored lines are isentropic trajectories corresponding to several values of s/n_B: 331.6 (red line), 277.6 (magenta line), 123.9 (orange line), 84.3 (green line), 56.8 (cyan line), 45.8 (blue line), 26.7 (purple line), 17.5 (indigo line), 5 (brown line), 2 (violet lines).

depends on the history and kind of evolution of the system. Usually in thermodynamics one considers phase transitions occurring along isothermal lines, however in heavy-ion collisions there is no thermal bath with which the fireball is in contact. The system follows then an isentropic expansion at fixed s/n_B and one has

$$\frac{s}{n_B} = \frac{\alpha s_Q(T,\mu_B) + (1-\alpha)s_H(T,\mu_B)}{\alpha n_Q(T,\mu_B) + (1-\alpha)n_H(T,\mu_B)}, \tag{4.8}$$

where $s_{Q/H}$ and $n_{Q/H}$ are the entropy and baryon density in the chirally restored/broken phase. One has $\alpha = 1$ when the isentrope crosses the high-density branch of the critical line and $\alpha = 0$ when it crosses the low-density branch. Hence, a given value of T and μ_B does not fix α: one has to specify also the isentrope followed by the system. Notice that, considering this kind of evolution, one is implicitly assuming that the nucleation rate of bubbles of the low-density, chirally-broken phase is larger than the expansion rate of the fireball and we are not addressing the case of super-heating/cooling, which occurs if the system remains in a metastable minimum. Establishing whether this is a realistic assumption or whether the transition occurs via a different dynamics (spinodal decomposition) would need a deeper study of the rate of bubble nucleation, requiring in particular the evaluation of the surface tension of the interface between the two phases [40, 77, 85, 90], which is out of the scope of the present thesis. For the sake of completeness, in the second panel of Fig. 4.24, I display the regions in which a homogeneous metastable phase can exist, extending between the continuous first-order line and the dashed isothermal spinodal lines. In the region enclosed by the two isothermal spinodal lines any homogeneous phase is unstable.

The phase diagram plotted in terms of the quark density rather than of the chemical potential reveals how, in both models, the first-order coexistence region extends down to the origin. In the low-temperature regime the behaviour of the model is then unphysical, since it does not leave room for the existence of a self-bound homogeneous nuclear-matter phase, which we know to exist, but whose experimental density $n_B \approx 0.16\,\mathrm{fm}^{-3}$ would lie here in the coexistence region. Furthermore, there is no room for the liquid-gas

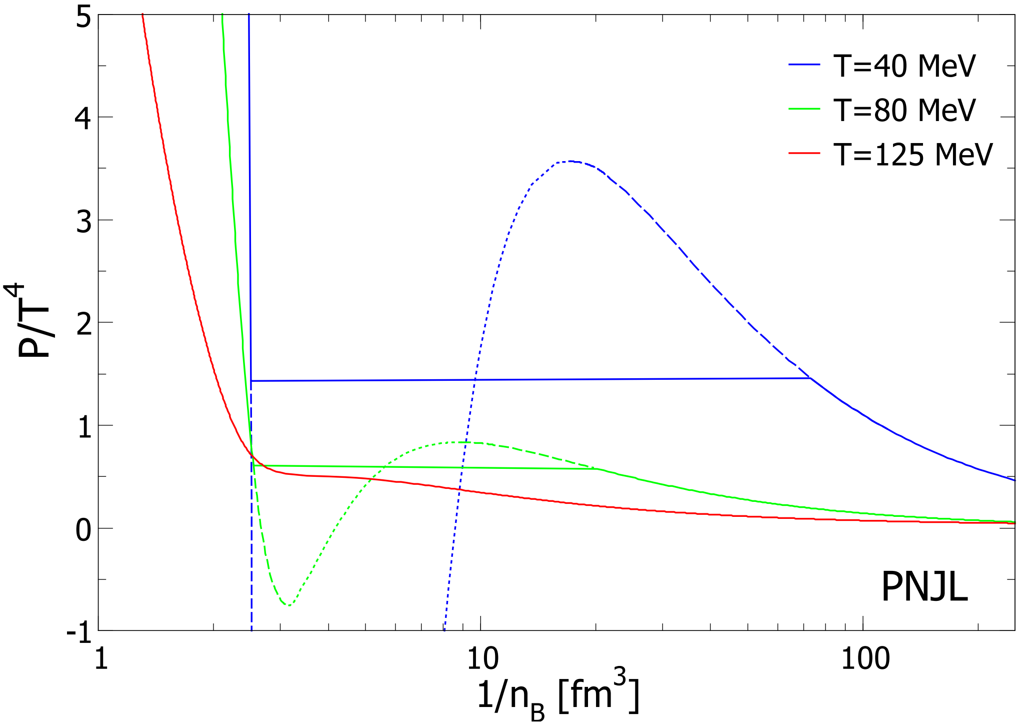

Figure 4.25: Pressure vs specific volume for a few isothermal transformations in the PNJL model. The isothermal lines cross the phase diagram above and below the critical isothermal T^{CEP} passing through the CEP. In the case of a first-order transition I also display the Maxwell construction. The stationary points of the isothermal curves lie on top of the isothermal spinodal lines: between them the system gets unstable and cannot be found in a homogeneous phase, not even metastable.

phase transition of nuclear matter, which is a characteristic feature of strong interactions in the low-temperature ($T \lesssim 20$ MeV), high-density regime for low values of the entropy per baryon [26, 44, 47]. This must be viewed as a shortcoming of the model due to the pure scalar/pseudoscalar interaction and to the mean field approximation. We expect that the inclusion of a vector interaction and of hadrons as dynamical degrees of freedom in the confined, chirally-broken phase should improve the description of this region of the phase diagram.

Finally, in Fig. 4.25, I show a few isothermal curves for the PNJL model, plotting the pressure as a function of the specific volume $1/n_B$. We choose values of T either above or below the critical value T^{CEP}. In this last case, in which a first-order transition occurs, I show also the Maxwell construction. Notice that the isothermal curves with $T < T^{\text{CEP}}$ display two stationary points. Between the two stationary points, the pressure is a decreasing function of the density and the system is thus unstable. This part of the curves actually corresponds to effective quark masses arising from the maximum of the thermodynamic potential; this is also the region enclosed by the isothermal spinodal lines in Fig. 4.24 in which a single homogeneous phase cannot exist.

4.5 Neutral Strangeness Scenario

In the Neutral Strangeness (NS) scenario the MFE's are solved adding a new equation which sets to zero the net density of strange quarks. One still assumes exact up-down symmetry, setting $\mu_Q = 0$. One has

$$n_s(T, \mu_B, \mu_S(T, \mu_B)) = 0. \tag{4.9}$$

This equation imposes a non-trivial relation between strangeness and baryochemical potential, while the electric-charge chemical potential, as above mentioned, is fixed to zero.

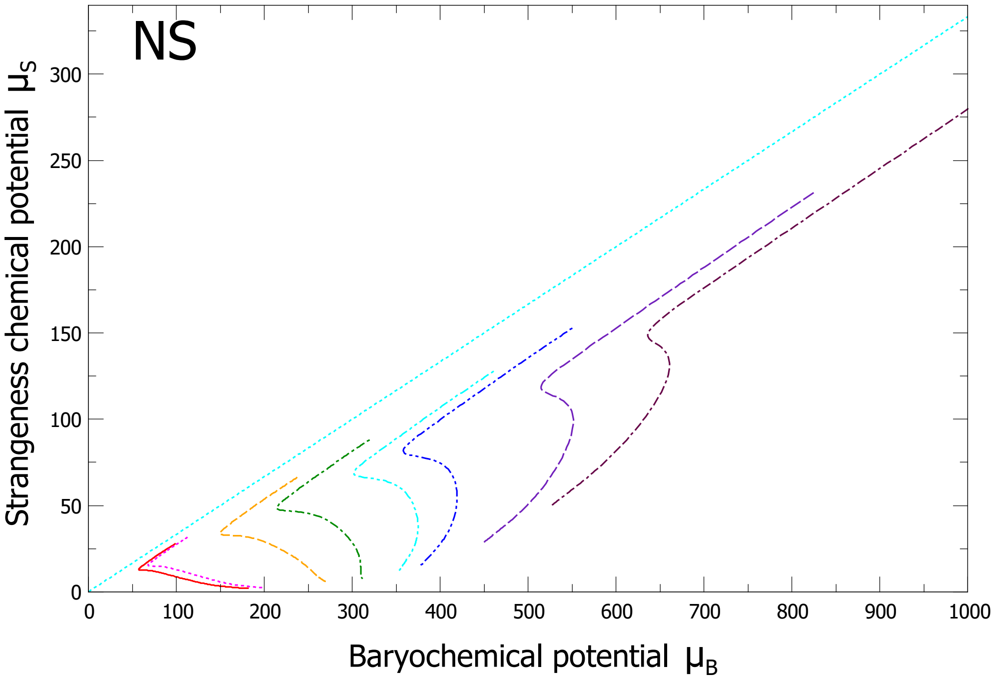

Figure 4.26: Neutral-strangeness trajectories along various adiabatic lines corresponding to different values of s/n_B: 331.6 (red line), 277.6 (magenta line), 123.9 (orange line), 84.3 (green line), 56.8 (cyan line), 45.8 (blue line), 26.7 (purple line), 17.5 (indigo line).

In this scenario the calculation of isentropic trajectories is more complex than the previous one. In fact at each step, in evaluating the next point of the trajectory, besides setting s/n_B equal to the desired value one needs to solve Eq. (4.9) to fix the strangeness chemical potential in order to satisfy the NS condition. In other words, in the NS scenario the isentropic trajectories are trajectories in the 3D space $(T - \mu_B - \mu_S)$ and not in the 2D plane $(T - \mu_B)$. The points in the phase diagram in the $\mu_B - T$ plane have then different values of strangeness chemical potential. In Fig. 4.26 I show the NS lines along different isentropic trajectories. Each point of the curves correspond to a different temperature. One can see that, for all lines, the values of the strangeness chemical potential are lower than $\mu_B/3$ (dotted blue line), which would correspond to the QNS scenario. In this figures one can observe a double change of direction, after which the NS trajectories become approximate straight lines with slope 1/3, like for the QNS case.

4.5.1 Equation of State and speed of sound

In Figs. 4.27a and 4.27b I show the Equation of State and the squared speed of sound of the PNJL model in the NS scenario calculated along different isentropic trajectories. The curves are qualitatively and quantitatively very similar to the ones found in the SYM and QNS cases and the same physical interpretation of their behaviour holds.

4.5.2 Fluctuations in the NS scenario

In the NS scenario, the fluctuations of net baryon number show the same properties found for the previous two scenarios. Hence here I focus on the off-diagonal fluctuations of conserved charges. In particular, I consider the ratio between the off-diagonal susceptibility of net-baryon and net-strangeness number and the second-order strangeness susceptibility. In Fig. 4.28 I show the numerical results of the PNJL model in mean-field approximation for this quantity. The off-diagonal susceptibilities I am interested in, related to the corresponding off-diagonal cumulants of the particle distributions, are

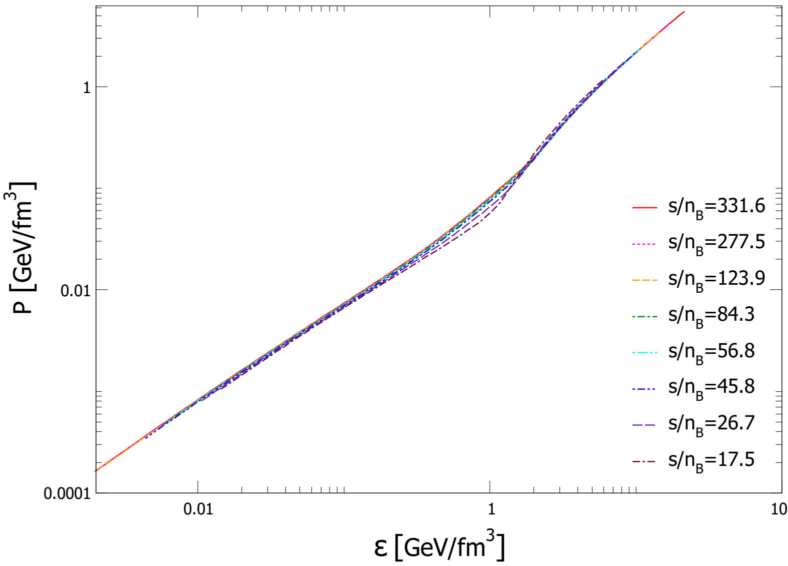

(a) *EoS in the NS scenario.*

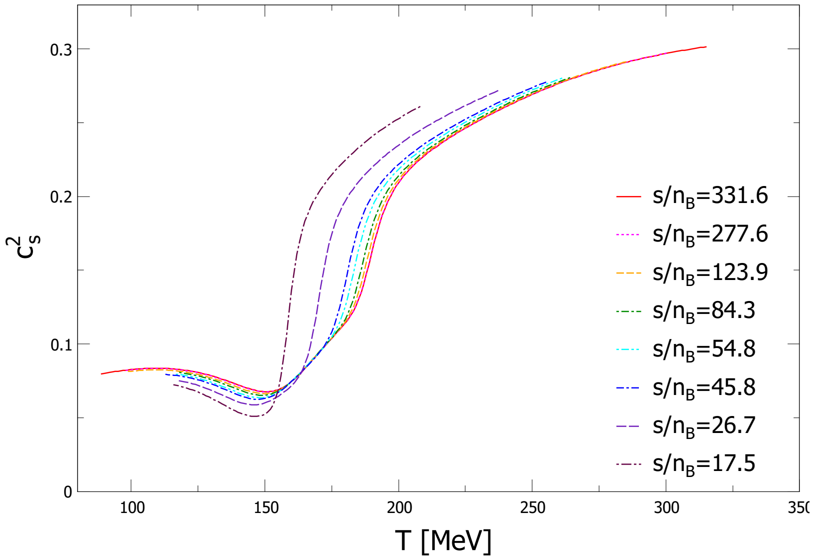

(b) *Squared speed of sound in the NS scenario.*

Figure 4.27: Equation of state (upper panel) and squared speed of sound (lower panel) in the NS scenario along isentropic trajectories corresponding to different values of s/n_B: 331.6 (red line), 277.6 (magenta line), 123.9 (orange line), 84.3 (green line), 56.8 (cyan line), 45.8 (blue line), 26.7 (purple line), 17.5 (indigo line).

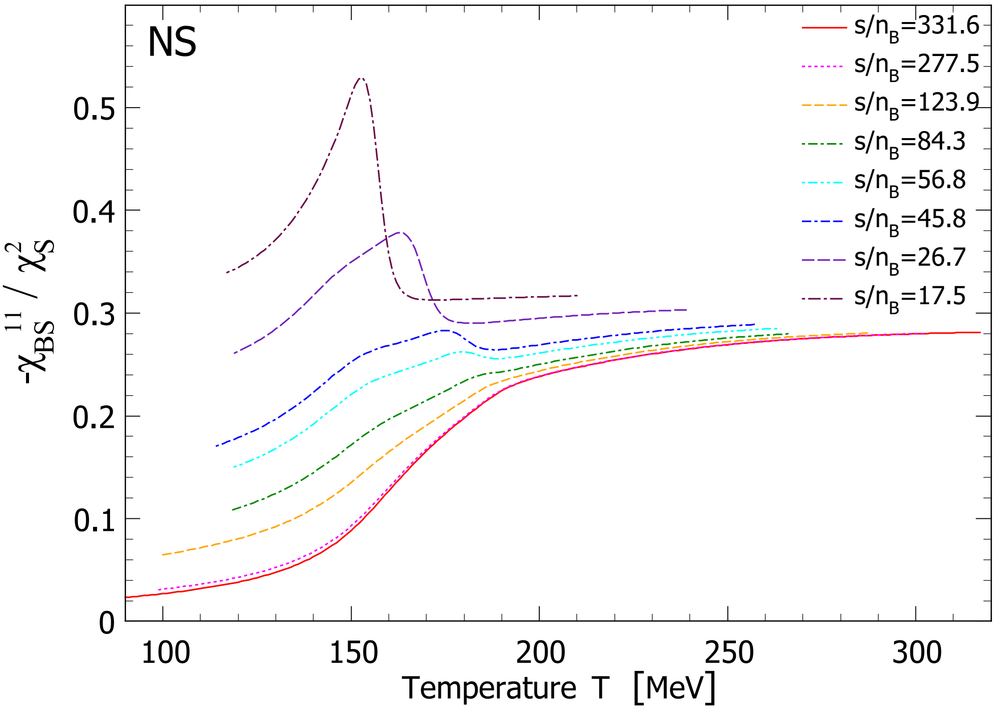

Figure 4.28: The $-\chi^{11}_{BS}/\chi^2_S$ ratio in the NS scenario evaluated along various adiabatic lines corresponding to different values of s/n_B: 331.6 (red line), 277.6 (magenta line), 123.9 (orange line), 84.3 (green line), 56.8 (cyan line), 45.8 (blue line), 26.7 (purple line), 17.5 (indigo line).

defined as:

$$\langle \chi^{nk}_{BS} \rangle \equiv \frac{\partial^{k+n}}{\partial(\mu_B/T)^n \partial(\mu_S/T)^k} \left[P(T, \mu_B, \mu_S)/T^4 \right] \Bigg|_T \sim \langle B^n S^k \rangle_c. \tag{4.10}$$

In Appendix B I show the relation between the off-diagonal cumulants and moments of the particle distributions. If the particles obey classical statistics, the first off-diagonal cumulant is given by:

$$\langle BS \rangle_c = \sum_i B_i S_i \langle N_i \rangle \ , \tag{4.11}$$

where the sum runs over all particle species, B_i and S_i are the baryon and strangeness charges carried by the i-th species and $\langle N_i \rangle$ is the average number of particles of species i. This makes very interesting the evaluation of the ratio $\chi_{BS}/\chi^2_S = \langle BS \rangle_c / \langle S^2 \rangle_c$, whose behaviour can be estimated from the above equation and whose value provides information on the active degrees of freedom of the system. In the deconfined phase, strangeness is carried by s-quarks (with $S = -1$), which carry also baryon number 1/3. Antiquarks provide the same contribution, since the product of their baryon and strangeness charges is the same. In this case one has then $-\chi_{BS}/\chi^2_S \sim 1/3$. This is the asymptotic high-temperature behaviour observed in Fig. 4.28 and also found in lattice-QCD simulations. The behaviour in the confined phase is also interesting, since one expects a strong suppression of this quantity, which is actually observed in lattice-QCD. In the hadronic phase only strange baryons, quite heavy, carry both non-vanishing B and S, but strangeness fluctuations in the denominator are mainly driven by kaons, which are much lighter. Unfortunately in the present implementation of the PNJL model we cannot capture this aspect of the problem, since hadrons do not contribute directly to the thermodynamics and the suppression at low temperature is mainly driven by the coupling with the Polyakov field.

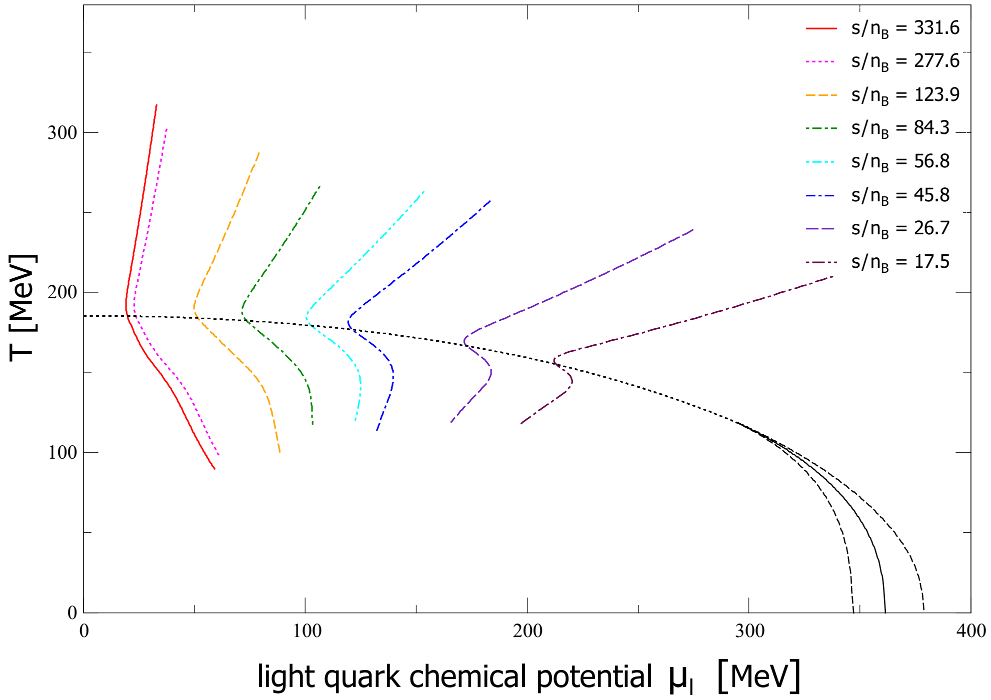

Figure 4.29: Phase diagram of the PNJL model in the NS scenario. The black dotted curve is the chiral crossover, the black solid curve is the first-order transition line, the two black dashed lines are the borders of the metastable regions. The colored lines are isentropic trajectories corresponding to several values of s/n_B: 331.6(red line), 277.6 (magenta line), 123.9 (orange line), 84.3 (green line), 56.8 (cyan line), 45.8 (blue line), 26.7 (purple line), 17.5 (indigo line).

4.5.3 Phase diagram in the NS scenario

In this section I address the PNJL phase diagram in the Neutral Strangeness scenario, which is shown in Fig. 4.29. As in the previous two scenarios, the isentropic lines of current experimental interest are located in the crossover region. The first-order region could be investigated only with experiments that produce a system with lower values of entropy per baryon. From the fluctuations of conserved charges and the inflection points of the order parameters one can obtain the crossover line. Also in this case one can try to fit this line with a polynomial containing even powers of μ_B/T_c^0, like in

Eq. (4.4), obtaining

$$T_c^0 = 186.2 \text{ MeV}, \quad \kappa_2 = 0.120 \pm 2 \quad \kappa_4 = 0.00047 \pm 70 \; . \tag{4.12}$$

These values will be compared with the values of others scenarios in Chapter 5. The first-order transition region and the Critical End-Point are found through a fine scan at high baryochemical potential. The CEP coordinates for this scenarios are: $T^{\text{CEP}} = 121.0 \pm 0.1$ and $\mu_B^{\text{CEP}} = 885.1 \pm 0.1$.

4.6 HIC Scenario

In this section I discuss the scenario which provides the most realistic description of the matter produced in heavy-ion collisions. In this kind of experiments, a couple of heavy ions (usually lead or gold) are accelerated up to the speed of light and made collide. These nuclei do not contain strange quarks and the proton to nucleon ratio is about 0.4. To perform realistic theoretical calculations, one needs to introduce these two features. Then one imposes two new equations in the numerical code:

$$\begin{cases} n_s(\mu_B, \mu_Q, \mu_S, T) = 0 \\ n_Q(\mu_B, \mu_Q, \mu_S, T)/n_B(\mu_B, \mu_Q, \mu_S, T) = 0.4. \end{cases} \tag{4.13}$$

These two equations impose a relation among the strangeness chemical potential, the electric-charge chemical potential, the baryochemical potential and the temperature. In this scenario the isentropic trajectories are lines in a 4D space. The conditions in Eqs. (4.13) together with the isentropic condition $s/n_B = \text{const.}$, can reduce the number of independent parameters allowing one to identify a point in the phase space through a single parameter, the temperature. In this scenario the calculation of isentropic curves is then more complex, since it requires solving a larger number of equations and since, as above mentioned, adiabatic lines are trajectories in the 4D space ($T - \mu_B - \mu_S - \mu_Q$) and not in the 2D plane ($T - \mu_B$). The points in the phase diagram in the $\mu_B - T$ plane have different values of strangeness and electric-charge chemical potential, fixed in order to satisfy the conditions in Eqs. (4.13). For each isentropic curve one can visualize the relation among the three chemical potentials as a trajectory in the $\mu_B - \mu_Q$ plane, as done in Fig. 4.30.

From the baryon number and electric charge of each quark flavour one can write

$$\frac{n_Q}{n_B} \equiv \frac{2n_u - n_d - n_s}{n_u + n_d + n_s} \,, \tag{4.14}$$

where n_i is the net-density of quark of a given flavour. In the Neutral Strangeness scenario ($n_s = 0$ and $\mu_Q = 0$, i.e. $n_u = n_d = n_l$) this ratio is equal to 0.5. In the HIC scenario, for which $n_Q/n_B = 0.4$ and $n_u/n_d < 1$, one expects the electric-charge chemical potential μ_Q to be negative. This can be easily understood in the low-density classical limit, for which $n_u/n_d = \exp[(\mu_u - \mu_d)/T] = \exp[\mu_Q/T]$, which entails $\mu_Q < 0$ in order to have $n_u/n_d < 1$. In figure 4.30 I show some trajectories with $n_Q/n_B = 0.4$. As one expects, the electric-charge chemical potential is negative, but two order of magnitude smaller than the baryochemical potential. As found in the NS scenario, after the phase transition the relation between the chemical potentials becomes linear.

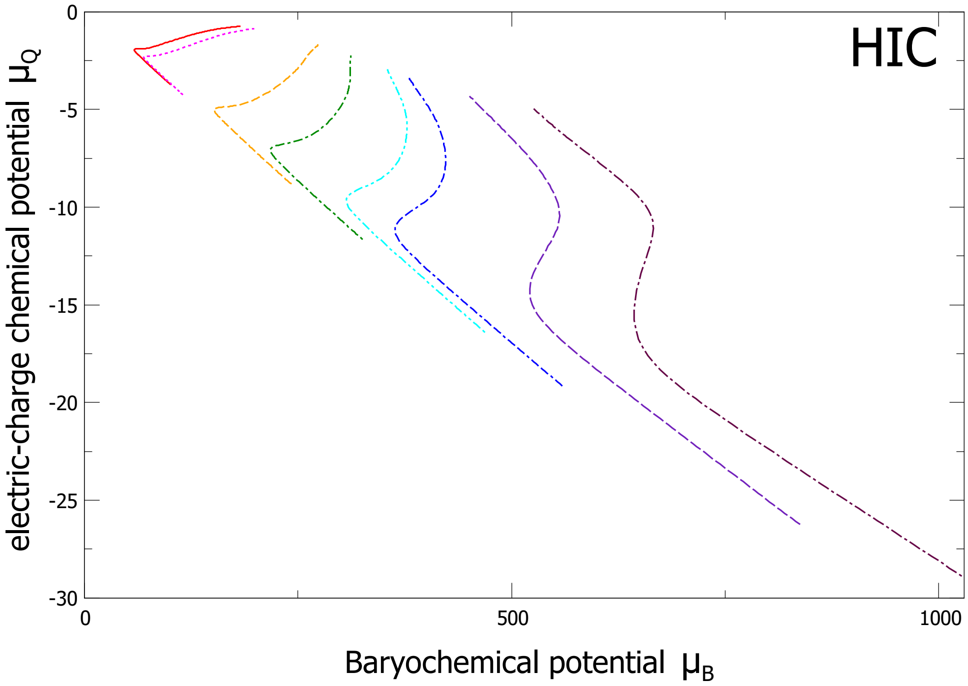

Figure 4.30: Evolution of the electric-charge chemical potential μ_Q in the HIC scenario with $n_Q/n_B = 0.4$ and $n_S = 0$ along isentropic trajectories corresponding to different values of s/n_B: 331.6 (red line), 277.6 (magenta line), 123.9 (orange line), 84.3 (green line), 56.8(cyan line), 45.8 (blue line), 26.7 (purple line), 17.5 (indigo line).

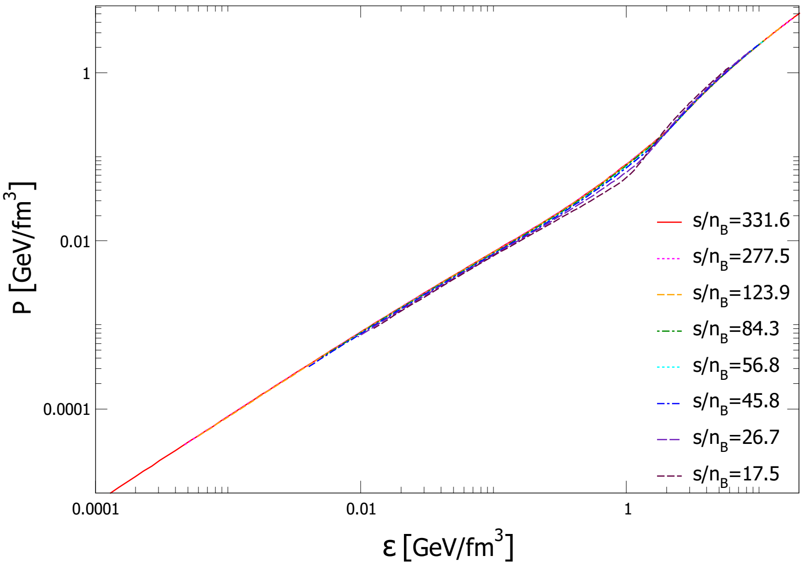

(a) *EoS in the HIC scenario.*

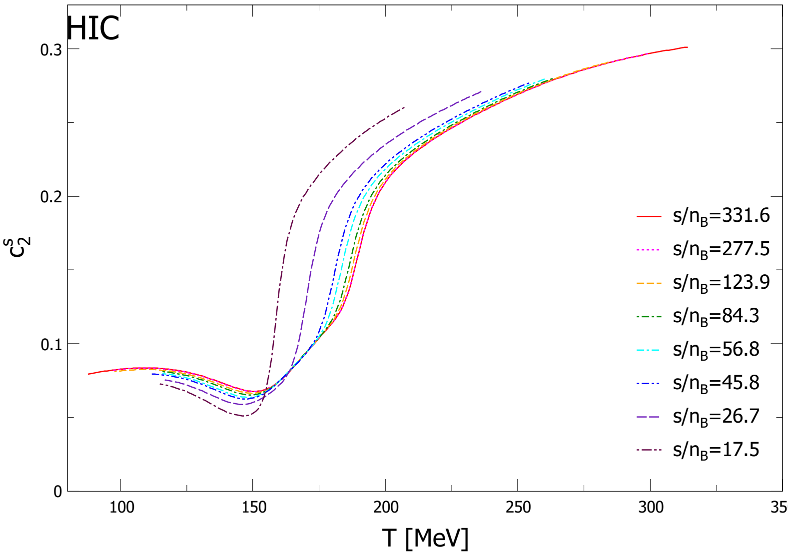

(b) *Squared speed of sound in the HIC scenario.*

Figure 4.31: Equation of state (upper panel) and squared speed of sound (lower panel) in the HIC scenario along isentropic trajectories corresponding to different values of s/n_B: 331.6 (red line), 277.6 (magenta line), 123.9 (orange line), 84.3 (green line), 56.8 (cyan line), 45.8 (blue line), 26.7 (purple line), 17.5 (indigo line).

4.6.1 Equation of State and speed of sound

In Figs. 4.31a and 4.31b I show the Equation of State and the squared speed of sound calculated along various isentropic trajectories in the HIC scenario. The results are very similar to the ones found in the other scenarios both at a qualitative and quantitative level. In particular, for all values of entropy per baryon of current experimental relevance, the transition between the two phases occurs smoothly.

4.6.2 Fluctuations in the HIC scenario

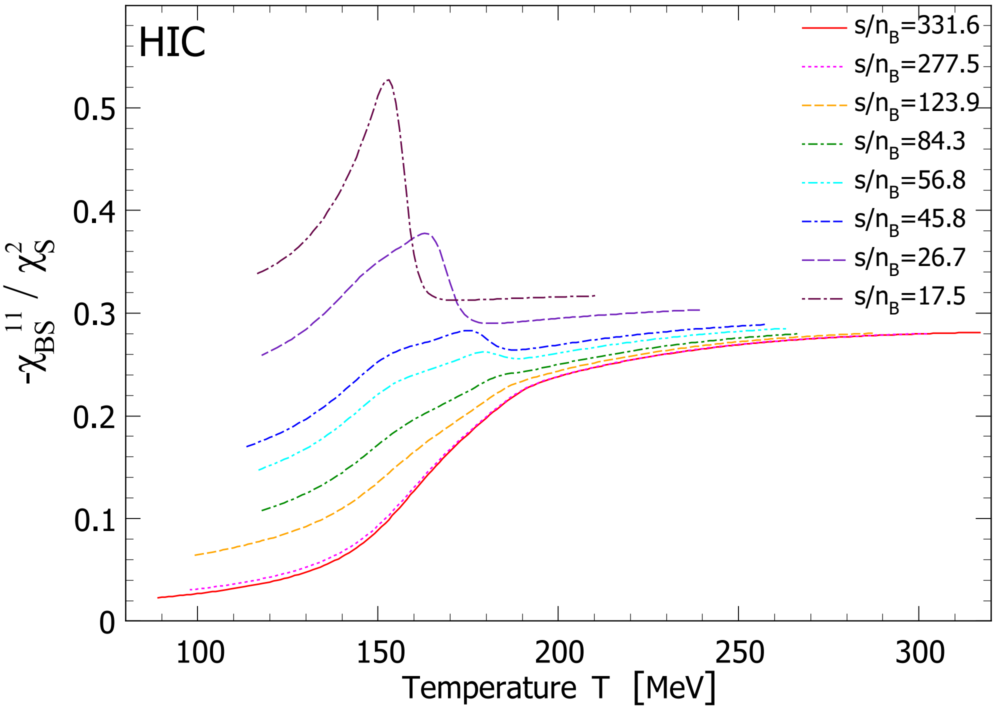

Figure 4.32: The $-\chi_{BS}^{11}/\chi_S^2$ ratio in the HIC scenario evaluated along various adiabatic lines corresponding to different values of s/n_B: 331.6 (red line), 277.6 (magenta line), 123.9 (orange line), 84.3 (green line), 56.8 (cyan line), 45.8 (blue line), 26.7 (purple line), 17.5 (indigo line).

In the HIC scenario, the generalized baryon-number susceptibilities display the same behaviour found in the first three scenarios. Also in this case, from their peaks and fluctuations one can find the crossover line. In this section I show the off-diagonal fluctuations of conserved charges. In particular I focus again on the ratio between the off-diagonal susceptibility of baryon-number and strangeness and the second-order strangeness susceptibility. In Fig. 4.32 I show the numerical results, very similar to what found in the NS scenario and for which the same interpretation holds.

4.6.3 Phase diagram in the HIC scenario

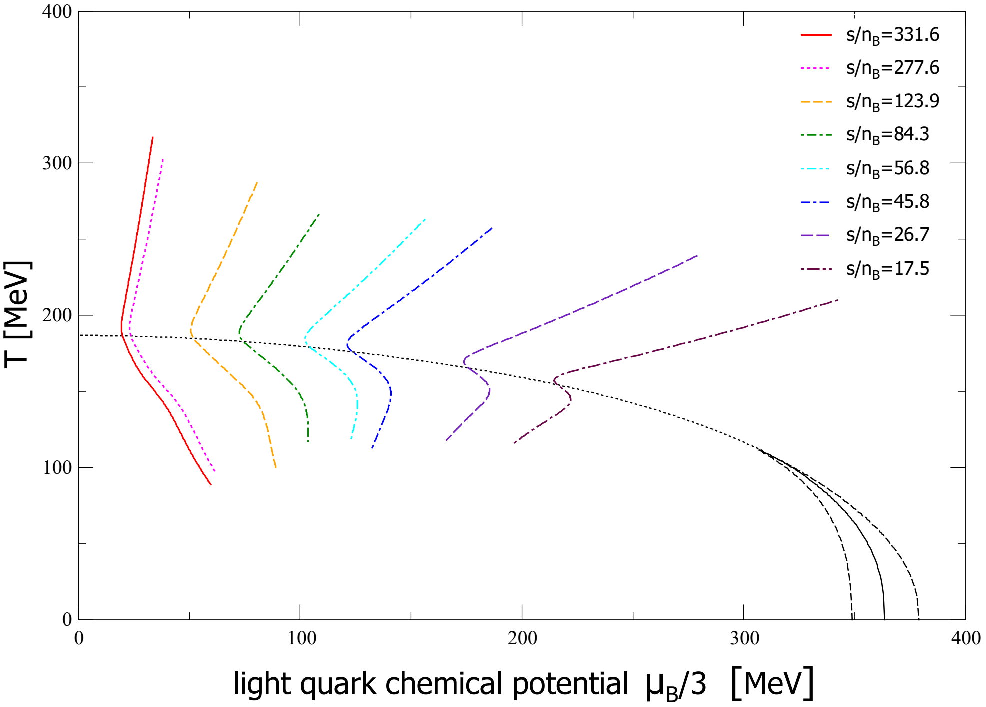

Figure 4.33: Phase diagram of the PNJL model in the HIC scenario. The black dotted curve is the chiral crossover, the black solid curve is the first-order transition line, the two black dashed lines are the borders of the metastable regions. The colored lines are isentropic trajectories corresponding to several values of s/n_B: 331.6(red line), 277.6 (magenta line), 123.9 (orange line), 84.3 (green line), 56.8 (cyan line), 45.8 (blue line), 26.7 (purple line), 17.5 (indigo line).

In this section I display the PNJL phase diagram in the HIC scenario, which is shown in Fig. 4.33. As in the previous scenarios, the isentropic trajectories currently explored by the experiments are located in the crossover region. To explore the first-order region, one needs to reach lower values of entropy per baryon. From the fluctuations of conserved charges and the derivative of the order parameters one can obtain the crossover line. Also in this case, one can try to fit this line with a polynomial containing even powers of μ_B/T_c^0 like in Eq. (4.4), obtaining

$$\begin{aligned} &\frac{T_c(\mu)}{T_c^0} = 1 - 0.0146\Big(\frac{\mu}{T_c^0}\Big)^2 + 0.00011\Big(\frac{\mu}{T_c^0}\Big)^4 + \mathcal{O}\Big[\Big(\frac{\mu}{T_c^0}\Big)^6\Big] \\ &T_c^0 = T_c(\mu = 0) = 186.79 \text{ MeV} . \end{aligned} \tag{4.15}$$

The first-order region and the Critical End-Point are found through a fine scan at high baryochemical potential. The CEP coordinates for this scenario are: $T^{\text{CEP}} = 118.1 \pm 0.1$ and $\mu_B^{\text{CEP}} = 921.0 \pm 0.1$. These values will be compared with the ones obtained in other scenarios in Chapter 5.

4.7 PNJL with vector interaction

In this section I show the results of the exploration of the PNJL phase diagram in the presence of a vector/axial-vector interaction. Calculations are performed in the SYM scenario. The parameters of the model have been fixed in order to reproduce the properties of pseudoscalar and vector mesons in the vacuum. Since the vector interaction introduces a mixing between different channels into the Bethe-Salpeter equation for the quark-antiquark scattering matrix, this requires refitting all the parameters of the model. For this purpose, I employ the parameter set given in Ref. [70] and shown in Table 3.2. In this model, the presence of the vector interaction leads to a shift of the quark chemical potentials proportional to the net-quark density:

$$\hat{\mu}_q = \mu_q - 2G_V n_q \tag{4.16}$$

The shift in the effective quark chemical potentials induced by the vector interaction and the different values of the model parameters produce some differences in the phase diagram. In Fig 4.34 I show the comparison of the phase diagrams of the PNJL model with and without a vector interaction. First of all, the chiral crossover temperature at zero chemical potential is higher in the $G_V > 0$ case. Notice however that, from a quantitative point of view, already the original version of the model, with a pure scalar/pseudoscalar interaction, overshoots the QCD crossover temperature obtained in lattice simulations. Also the curvature of the crossover line changes. Performing a new fit in the vector case one gets:

$$\begin{aligned} &\frac{T_c(\mu_B)}{T_c^0} = 1 - 0.010\Big(\frac{\mu}{T_c^0}\Big)^2 - 0.0017\Big(\frac{\mu_B}{T_c^0}\Big)^4 + \mathcal{O}\Big[\Big(\frac{\mu_B}{T_c^0}\Big)^6\Big] \\ &T_c^0 = T_c(\mu = 0) = 197.6 \text{ MeV} \end{aligned} \tag{4.17}$$

The CEP moves to a higher chemical potential μ_B and to a lower temperature. The location of CEP is:

$$T^{\text{CEP}} = 72.1\text{MeV} \qquad \mu_B^{\text{CEP}} = 1098\text{MeV} \tag{4.18}$$

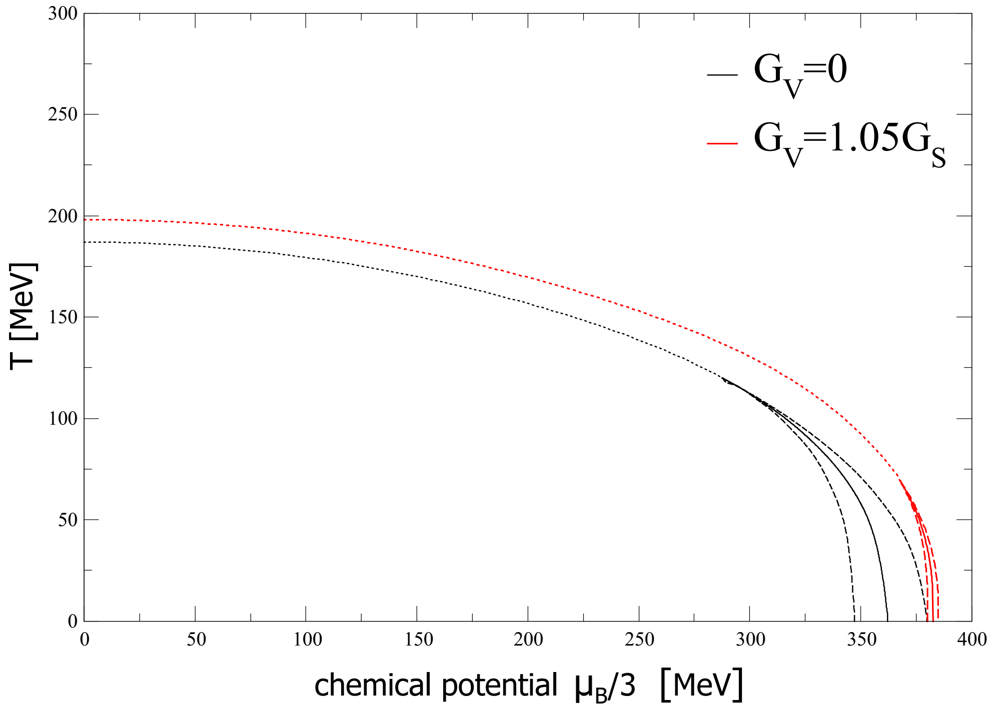

Figure 4.34: Comparison of the phase diagrams of the PNJL model in the SYM scenario without (black curves) and with (red curves) vector interaction.

This effect is due to the shifted chemical potential: in fact the quantity entering the equations is the effective chemical potential $\hat{\mu}_q$, but eventually the phase diagram has to be expressed in terms of the true chemical potential, receiving a positive correction proportional to the temperature. In particular, the first-order transition line in the vector case occurs at such a so high baryochemical potential to produce a region at zero temperature in the n_B-T plane that contains only hadronic matter, as one can see in Fig. 4.35. This feature, which surely makes the model closer to reality, is not present in the scalar version of the model, as one can see in Fig. 4.24.

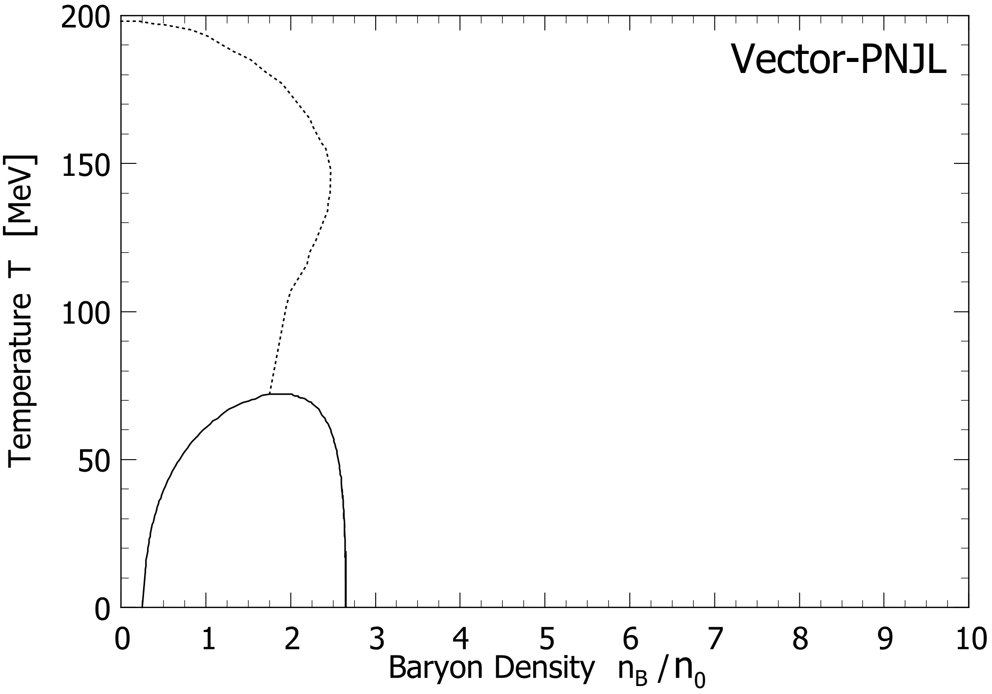

Figure 4.35: Phase diagram of the PNJL model with vector interaction in the SYM scenario plotted in the $n_B - T$ plane.

Chapter 5

Conclusions and outlook

This chapter is devoted to summarize and compare the numerical results and features of the different implementations of the PNJL model and to explain what can be the outlook for the future.

5.1 Comparison with lattice-QCD calculations

The numerical results in Figs. 4.1-4.4 show that the PNJL model allows one to capture the main features of the chiral and deconfinement transitions and of their effects on the thermodynamics of the system, but it is not able to provide an accurate quantitative description of the most recent continuum-extrapolated lattice-QCD data at zero chemical potential.

This shortcoming of the PNJL model is due to the simplicity of the model, which – in particular in the present mean-field implementation – misses some important degrees of freedom: hadrons (which can be obtained as poles of the quark scattering matrix in the different channels, but whose contribution to the pressure of the system is not included) at low temperature and transverse gluons at high temperature. The effective model is able, however, to correctly describe the qualitative behaviour of the physical observables as a function of the temperature. In conclusion, one can use the PNJL model as a guidance to explore general features of the thermodynamics of strong interactions in regions of the phase diagram today not accessible to lattice-QCD simulations.

5.2 The choice of the Polyakov potential

In the literature there exist more versions of the effective Polyakov potential, for which the only first-principle constraints are the respect of the global Z_3 symmetry, its spontaneous breaking, and the agreement with pure-gauge lattice simulation. The two main choices adopted in the literature are the polynomial potential and the logarithmic potential introduced in Eq. (3.4) and Eq. (3.5), respectively. In Figs. 4.1-4.4, I compared the predictions obtained with the two versions of the Polyakov potential to lattice-QCD data at vanishing baryochemical potential. The main difference between the polynomial and the logarithmic potential is that, in the last case, the chiral and deconfined transitions are separated, the chiral occurring at a temperature 30-40 MeV larger than the deconfinement one. This leads to the appearance of two distinct peaks in some quantities like the specific heat, which are not observed in lattice-QCD simulations. The polynomial potential still produces two different crossover temperatures, but much closer to each other. In Sec. 4.2 I showed the numerical results for several thermodynamic quantities arising from the solutions of the mean field equations. Quantities involving derivatives of the order parameters, like fluctuations of conserved charges, display peaks in correspondence of the deconfinement and chiral transitions, which do not coincide in the case of a logarithmic Polyakov potential. The major effect is in any case given by the chiral crossover of the light-quark condensate.

5.3 Fluctuations of conserved charges

The cumulants of conserved charges, as discussed in Sec. 3.3.1, are useful tools to diagnose the elementary degrees of freedom of a system and to investigate the location and kind of phase transition. For the first purpose, one looks at the asymptotic values of certain ratios of cumulants in a determinate range of temperature and chemical potential; for the second purpose, one focuses on the fluctuating behaviour of certain cumulants around the phase transition.

In this thesis I considered several higher-order generalized susceptibilities of conserved charges (in most cases baryon number) and their ratios: χ_B^n, χ_B^3/χ_B^1, χ_B^4/χ_B^2 and also the off-diagonal fluctuations of net-baryon and net-strangeness number, χ_{BS}^{11}/χ_S^2. The first quantities were studied through the entire phase diagram and the corresponding results are shown in Sec. 4.2. Up to a certain value of baryochemical potential, they show a rapid but smooth variation of their values around the critical temperature, signalling a steep but continuous crossover; above a certain chemical potential the cumulants display a discontinuity at a critical temperature. This fact signals a change in the order of the phase transition, which from a smooth crossover turns into a first-order phase transition. The two regimes are separated by a Critical End-Point, where the transition is of second order, the cumulants of conserved charges diverge and the correlation length of the fluctuations of the order parameter is infinite. In all the explored scenarios, only along the isentropic trajectories of very low entropy per baryon s/n_B (much lower than the values of current experimental interest) the cumulants of conserved charges display an actual discontinuity, associated to a first-order phase transition.

Concerning the identification of the active degrees of freedom in the different regions of the phase diagram, both the ratios of diagonal cumulants χ_B^{n+2}/χ_B^n and of off-diagonal ones χ_{BS}/χ_S^2 support a picture in which, at high temperature, baryon number is carried by particles with $B = 1/3$, while at low temperature – due to the coupling with the Polyakov field – only clusters of three quarks with $B = 1$ are not suppressed by confinement.

5.4 Comparison of different scenarios

In Secs. 4.3-4.6 I showed the results of the exploration of the PNJL phase diagram in four different scenarios: SYM ($\mu_u = \mu_d = \mu_s = \mu_B/3$), QNS ($\mu_u = \mu_d$, $\mu_s = 0$), NS ($\mu_u = \mu_d$, $n_s = 0$) and HIC ($n_s = 0$, $n_Q/n_B = 0.4$). These four scenarios reduce the four-dimensional phase diagram to a two-dimensional plane spanned by the baryochemical potential μ_B and the temperature T, imposing some physical constraints. In Table 5.1 I collect the coordinates of the CEP and the parameters of the fit of the crossover line according to Eq. (4.4).

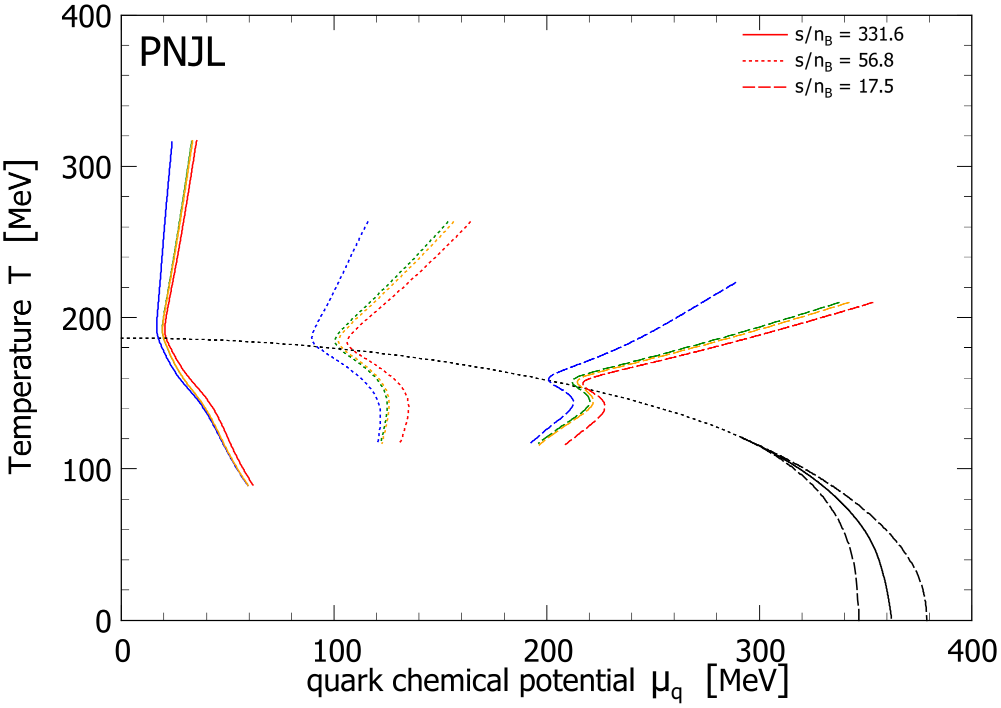

Figure 5.1: Isentropic lines in several scenarios: SYM (blue lines), QNS (red lines), NS (green lines) and HIC (orange lines). Three values of s/n_B are shown: 331.6 (solid lines), 56.8 (dotted lines) and 17.5 (dashed lines).

Observable	SYM	QNS	NS	HIC	V
T_0^χ[MeV]	186.5	187.0	186.2	186.8	197.6
κ_2	0.0170(3)	0.0143(17)	0.012(2)	0.0146(1.4)	0.010
κ_4	−0.0017(3)	0.0001(20)	0.00047(7)	−0.00011(6)	−0.0017
T^{CEP}[MeV]	120.0	120.7	121.0	118.1	72.1
μ_B^{CEP}[MeV]	863.0	875.0	885.1	921.0	1098

Table 5.1: Parameters of the fit of the crossover line and CEP coordinates in the PNJL model for the different scenarios explored in this thesis.

From the comparison of the different scenarios, one can see that the crossover line does not change its shape and the values of the coefficient of the quadratic term in the fit (κ_2) in the last three scenarios are all compatible within the numerical uncertainties. Furthermore, the fit parameters are compatible with the lattice-QCD results of Refs. [27, 29, 31] summarized in Table 5.2.

Observable	SYM	QNS	HIC
κ_2	0.020(4)	0.0135(20)	0.0153(18)
κ_4	/	/	0.00032(67)

Table 5.2: Parameters of the fit of the crossover line obtained in lattice-QCD simulations [27, 29, 31]

The location of the CEP changes in the different scenarios; in particular the introduction of a non-vanishing strangeness chemical potential $\mu_S \neq 0$ shifts the CEP to higher baryochemical potential without affecting the critical temperature. Furthermore, the introduction of a non-vanishing electric-charge chemical potential $\mu_Q \neq 0$ shifts the CEP to an even larger baryochemical potential and to a lower temperature. In Fig. 5.1 I display the differences obtained for the isentropic lines in the different scenarios (the transition lines referring to the QNS case).

5.5 Outlook

In light of the quite strong sensitivity of the CEP location on the value of the electric-charge chemical potential previously discussed, it may be interesting to explore the phase diagram of the PNJL model in regions of high electric-charge chemical potential, in order to find the values (if they exist) of μ_Q for which the CEP disappears. This exploration is of interest in light of the study of the initial fluctuations of conserved charges in HIC's, implemented for instance in the ICCING model presented in Refs. [72, 73]. Different cells of the fireball created in HIC's can have different chemical composition, with a local excess of quarks of a given flavour. Then, during the expansion and cooling of the system, some cells of the fireball can cross the region around the CEP (or Critical End-Surface in a 4D phase diagram) and some others may cross a region of the phase diagram where the CEP is not present.

Hence, for the future one can plan a scan of the full 4D phase diagram focusing in particular on large values of the electric-charge and strangeness chemical potentials, to find the possible borders (if any) of the Critical End-Surface.

Appendix A

Meson masses

In this appendix I explain the method to obtain the pion and kaon masses in the vacuum ($T = \mu_B = 0$) in the NJL model setting $m_u = m_d$. The equations are based on Ref. [92]. One can start from the following Lagrangian:

$$\begin{aligned}\mathcal{L}_{\mathrm{NJL}} = \bar{\Psi}(i\not{\partial} - \hat{m})\Psi + \frac{1}{2}G\big[(\bar{\Psi}\lambda^a\Psi)^2 + (\bar{\Psi}i\gamma^5\lambda^a\Psi)^2\big] - \\ - K\big\{\det\big[\bar{\Psi}(1+\gamma^5)\Psi\big] + \det\big[\bar{\Psi}(1+\gamma^5)\Psi\big]\big\},\end{aligned} \tag{A.1}$$

where Ψ and $\bar{\Psi}$ are the quark spinors and λ^a $(a = 0, ..., 8)$ are the Gell-Man matrices in flavour space. In order to obtain effective meson propagators corresponding to physical particles it is useful to combine the Gell-Man matrices to obtain the following meson-interaction vertices:

$$\pi^0 : \lambda^3 \tag{A.2}$$

$$\pi^\pm : \frac{1}{\sqrt{2}}(\lambda^1 \pm i\lambda^2) \tag{A.3}$$

$$K^0, \overline{K^0} : \frac{1}{\sqrt{2}}(\lambda^6 \pm i\lambda^7) \tag{A.4}$$

$$K^\pm : \frac{1}{\sqrt{2}}(\lambda^4 \pm i\lambda^5). \tag{A.5}$$

It is useful to rewrite the NJL Lagrangian in mean field approximation in the following form

$$\mathcal{L}_{\mathrm{NJL}} = \bar{\Psi}(i\not{\partial} - \hat{m})\Psi + \sum_{a=0}^{8} \left[K_a^-(\bar{\Psi}\lambda^a\Psi)^2 + K_a^+(\bar{\Psi}i\gamma^5\lambda^a\Psi)^2\right] + \\ + 2\mathcal{K}^-(\overline{\psi}\lambda^0\psi)(\overline{\psi}\lambda^8\psi) + 2\mathcal{K}^+(\overline{\psi}i\gamma^5\lambda^0\psi)(\overline{\psi}i\gamma^5\lambda^8\psi)\ . \tag{A.6}$$

The $K_a^{\pm}$ factors are the effective two-body interaction constants, occurring as an effective point-like vertex. For the calculation of the pion and kaon masses the relevant effective couplings are K_3^+ and K_4^+, defined as:

$$K_3^+ = G + \frac{1}{2}iKN_c\mathrm{tr}S^s(x,x) \tag{A.7}$$

$$K_4^+ = G + \frac{1}{2}iKN_c\mathrm{tr}S^d(x,x)\ , \tag{A.8}$$

where $S^i(x,y)$ is the propagator of quark i from y to x.

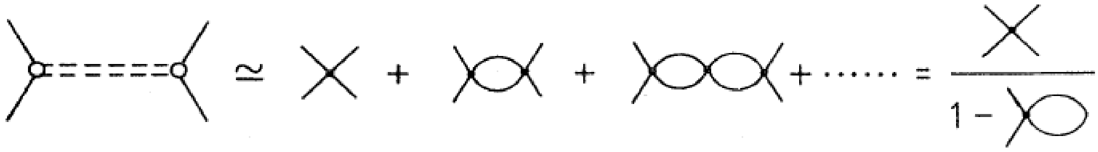

Figure A.1: RPA approximation for the $\bar{q}q$ scattering amplitude.

The quantity which allows one to extract the meson masses in the NJL model is the $\bar{q}q$ scattering amplitude $M(k_0, \vec{k})$. One can calculate it in the Random Phase Approximation, diagrammatically displayed in Fig. A.1, which yields the results:

$$M_\pi(k_0, \vec{k}) = \frac{2K_3^+}{1 - 2K_3^+\Pi_{q\bar{q}}^{\pi}(k_0, \vec{k})} \tag{A.9}$$

$$M_K(k_0, \vec{k}) = \frac{2K_4^+}{1 - 2K_4^+\Pi_{q\bar{q}}^{K}(k_0, \vec{k})}. \tag{A.10}$$

The term $\Pi_{q\bar{q}}^{\pi}$ is the irreducible bubble, which is iterated in the diagrams

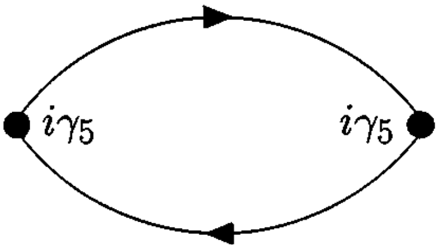

Figure A.2: Irreducible quark-antiquark bubble contributing to the pseudoscalar meson propagator. Depending on the considered particle, different Gell-Mann matrices in flavour space must appear in the vertices.

in Fig.1.10. It is drawn in Fig. A.2. For the pion channel one gets

$$\Pi^{\pi}(k) = 2N_c \mathrm{tr} \int_{\Lambda} \frac{d^4p}{(2\pi)^4} \left\{ i\gamma^5 S^u(p+\frac{1}{2}k) i\gamma^5 S^u\big(p-\frac{1}{2}k\big) \right\}, \tag{A.11}$$

while for the kaon channel one has

$$\Pi^{K}(k) = 2N_c \mathrm{tr} \int_{\Lambda} \frac{d^4p}{(2\pi)^4} \left\{ i\gamma^5 S^s(p+\frac{1}{2}k) i\gamma^5 S^u\big(p-\frac{1}{2}k\big) \right\}. \tag{A.12}$$

The trace in the above equations is performed on Dirac space. After some easy calculations one gets:

$$\begin{aligned} \Pi^{\pi}(k) = 8N_c &\int_{\Lambda} \frac{d^4p}{(2\pi)^4} \frac{1}{p^2-m_u^2} - \\ &- 4N_c k^2 \int_{\Lambda} \frac{d^4p}{(2\pi)^4} \frac{1}{\left[(p+\frac{1}{2}k)^2-m_u^2\right]\left[(p-\frac{1}{2}k)^2-m_u^2\right]} \end{aligned} \tag{A.13}$$

$$\begin{aligned} \Pi^{K}(k) = 4N_c &\int_{\Lambda} \frac{d^4p}{(2\pi)^4} \frac{1}{p^2-m_u^2} + 4N_c \int_{\Lambda} \frac{d^4p}{(2\pi)^4} \frac{1}{p^2-m_s^2} - \\ &- 4N_c k^2 \int_{\Lambda} \frac{d^4p}{(2\pi)^4} \frac{1}{\left[(p+\frac{1}{2}k)^2-m_u^2\right]\left[(p-\frac{1}{2}k)^2-m_s^2\right]} \end{aligned} \tag{A.14}$$

The pion and kaon masses are given by the poles of the effective propagators arising from the iteration of the elementary quark-antiquark bubbles. They are obtained solving the following equations at zero momentum:

$$1 - 4K_3^+ \Pi^\pi(m_\pi, 0) = 0 \tag{A.15}$$

$$1 - 4K_4^+ \Pi^K(m_K, 0) = 0\ . \tag{A.16}$$

For the calculation of the η and η' masses, the situation is more complicated. Due to the mixing in Eq. (A.6), the scattering amplitude $M_{\eta,\eta'}$ is not diagonal. Within the RPA it can be expressed as

$$M_{\eta,\eta'} = \frac{2\mathcal{K}^+}{1 - 2\Pi^{\eta\eta'}\mathcal{H}}. \tag{A.17}$$

Here $\mathcal{H}$ is a 2x2 matrix that contains the coupling

$$\mathcal{H} = \begin{pmatrix} \mathcal{G}_0^+ & \mathcal{K}^+ \\ \mathcal{K}^+ & \mathcal{G}_8^+ \end{pmatrix} \tag{A.18}$$

and $\Pi^{\eta\eta'}$ is a 2x2 matrix that contains the integrals

$$\Pi^{\eta\eta'} = \begin{pmatrix} \Pi_{00}^{\eta\eta'} & \Pi_{08}^{\eta\eta'} \\ \Pi_{80}^{\eta\eta'} & \Pi_{88}^{\eta\eta'} \end{pmatrix} \tag{A.19}$$

defined as

$$\Pi_{00}^{\eta\eta'} = \frac{2}{3}[2\Pi_{u\bar{u}}(k) + \Pi_{s\bar{s}}(k)] \tag{A.20}$$

$$\Pi_{80}^{\eta\eta'} = \Pi_{08}^{\eta\eta'} = \frac{2\sqrt{2}}{3}[\Pi_{u\bar{u}}(k) - \Pi_{s\bar{s}}(k)] \tag{A.21}$$

$$\Pi_{88}^{\eta\eta'} = \frac{2}{3}[\Pi_{u\bar{u}}(k) + 2\Pi_{s\bar{s}}(k)]. \tag{A.22}$$

$$\tag{A.23}$$

In the above, $\Pi_{u\bar{u}}$ is defined in Eq. (A.13). Then the η and η' meson masses are now defined as:

$$\det[1 - \Pi^{\eta\eta'}(m_{\eta,\eta'}, 0)\mathcal{H}] = 0. \tag{A.24}$$

One can use these equation to fix the free parameters of (P)NJL model in order to reproduce the experimental values of the mesons masses and decay constants.

Appendix B

Moments and cumulants

In Sec. 2 I discussed the topic of cumulants and moments of a distribution. In this appendix I discuss the relation between these quantities.

Moments of a distribution

Let $P(m)$ be some probability distribution of a discrete stochastic variable m. Of course, the sum of $P(m)$ over all possible values of m is 1. To characterize a distribution one can use its moments. The moment of order n of P is defined as:

$$\langle m^n \rangle = \sum_m m^n P(m). \tag{B.1}$$

The direct computation of these quantities can be difficult and boring. For this reason, it is useful to introduce a moment generating function $G(\theta)$, defined as:

$$G(\theta) \equiv \sum_m e^{\theta m} P(m), \quad G(\theta = 0) = 1\ . \tag{B.2}$$

The moment of order n of the distribution $P(m)$ is given by:

$$\langle m^n \rangle = \left. \frac{d^n G(\theta)}{d\theta^n} \right|_{\theta=0} . \tag{B.3}$$

This methods is very powerful when one is able to compute $G(\theta)$.

Cumulants of a distribution

For many practical purposes, it is more convenient to use *cumulants* rather than moments to characterize a probability distribution. To define the cumulants, we start from the cumulant generating function

$$K(\theta) \equiv \ln G(\theta) \; . \tag{B.4}$$

The cumulant of order n of $P(m)$ reads:

$$\langle m^n \rangle_c = \left. \frac{d^n K(\theta)}{d\theta^n} \right|_{\theta=0} . \tag{B.5}$$

Cumulants have several useful features; in particular, it is easy to estimate from them the non-gaussianity of a distribution. It is also easy to compute the cumulants of the distribution of the sum (or difference) of two stochastic variables.

Relation between moments and cumulants

Here I show the relation between cumulants and moments. To perform the calculation, one can insert Eq. (B.5) into Eq. (B.4) and perform the calculation of the first four cumulants:

$$\begin{aligned}
\langle m \rangle_c &= \left(\frac{1}{G(\theta)} \frac{dG(\theta)}{d\theta} \right)_{\theta=0} \\
\langle m^2 \rangle_c &= \left[\frac{1}{G} \frac{d^2G}{d\theta^2} - \frac{1}{G^2} \frac{dG}{d\theta} \right]_{\theta=0} \\
\langle m^3 \rangle_c &= \left[\frac{1}{G} \frac{d^3G}{d\theta^3} - \frac{3}{G^2} \frac{dG}{d\theta} \frac{d^2G}{d\theta^2} + \frac{2}{G} \left(\frac{dG}{d\theta} \right)^3 \right]_{\theta=0} \\
\langle m^4 \rangle_c &= \left[\frac{1}{G} \frac{d^4G}{d\theta^4} - \frac{4}{G^2} \frac{dG}{d\theta} \frac{d^3G}{d\theta^3} - \frac{3}{G^2} \left(\frac{d^2G}{d\theta^2} \right)^2 + \frac{12}{G^3} \left(\frac{dG}{d\theta} \right)^2 \frac{d^2G}{d\theta^2} + \right. \\
&\qquad \left. - \frac{6}{G^4} \left(\frac{dG}{d\theta} \right)^4 \right]_{\theta=0} .
\end{aligned} \tag{B.6}$$

One can rewrite these relations in terms of the moments and, for compact notation, in terms of the central moments $\langle \delta m^n \rangle \equiv \langle (m - \langle m \rangle)^n \rangle$. One gets:

$$\begin{aligned}
\langle m \rangle_c &= \langle m \rangle = M \\
\langle m^2 \rangle_c &= \langle m^2 \rangle - \langle m \rangle^2 = \langle (\delta m)^2 \rangle = \sigma^2 \\
\langle m^3 \rangle_c &= \langle m^3 \rangle - 3\langle m \rangle \langle m^2 \rangle + 2\langle m \rangle^3 = \langle (\delta m)^3 \rangle \\
\langle m^4 \rangle_c &= \langle m^4 \rangle - 4\langle m^3 \rangle \langle m \rangle + 12\langle m^2 \rangle \langle m \rangle^2 - 3\langle m^2 \rangle^2 - 6\langle m \rangle^4 \\
&= \langle (\delta m)^4 \rangle - 3\langle (\delta m)^2 \rangle^2 \, .
\end{aligned} \tag{B.7}$$

The first cumulant coincides with the first moment, the second one is the variance, the third one is the third central moment. All higher order ($n \geq 3$) cumulants are functions only of the central moments and are exactly zero for a Gaussian distribution. Of course, one can invert these relations and obtain the moments as functions of the cumulants:

$$\begin{aligned}
\langle m \rangle &= \langle m \rangle_c \\
\langle m^2 \rangle &= \langle m^2 \rangle_c + \langle m \rangle_c^2 \\
\langle m^3 \rangle &= \langle m^3 \rangle_c + 3\langle m \rangle_c \langle m^2 \rangle_c + \langle m \rangle_c^3 \\
\langle m^4 \rangle &= \langle m^4 \rangle_c + 4\langle m^3 \rangle_c \langle m \rangle_c + 6\langle m^2 \rangle_c \langle m \rangle_c^2 + 3\langle m^2 \rangle_c^2 + \langle m \rangle_c^4
\end{aligned} \tag{B.8}$$

Skewness and kurtosis

So far, I have discussed cumulants as quantities characterizing a distribution function. When one needs to describe the deviations from a Gaussian distribution, it is sometimes convenient to use two quantities called skewness γ and kurtosis κ. These quantities are defined as:

$$\gamma = \frac{\langle x^3 \rangle_c}{\langle x^2 \rangle_c^{3/2}} = \frac{\langle x^3 \rangle_c}{\sigma^3}, \quad \kappa = \frac{\langle x^4 \rangle_c}{\langle x^2 \rangle_c^2} = \frac{\langle x^4 \rangle_c}{\sigma^4}. \tag{B.9}$$

For the renormalized stochastic variables $\tilde{x} = x/\sigma$ these two quantities correspond to the third and fourth cumulants: $\gamma = \langle \tilde{x}^3 \rangle_c$, $\kappa = \langle \tilde{x}^4 \rangle_c$. The skewness quantifies the asymmetry of a distribution, while the kurtosis its sharpness compared with a Gaussian. As one can see in the next paragraph, these two quantities for a Gaussian distribution exactly vanish.

Cumulants of some important distributions

In this paragraph I show the calculation of the cumulants of a Gaussian, a Poisson and a Skellam distribution.

A Guassian probability density with average μ and variance σ reads:

$$P(x) = \frac{1}{\sqrt{2\pi\sigma^2}} e^{-\frac{1}{2}\left(\frac{x-\mu}{\sigma}\right)^2} . \tag{B.10}$$

The moment generating function for a continuous variable is defined as:

$$G(\theta) \equiv \int_{-\infty}^{+\infty} e^{\theta x} P(x) dx . \tag{B.11}$$

The computation of the integral is very simple. One simply needs to complete the square obtaining

$$G(\theta) = \exp\left[\frac{1}{2}\theta^2\sigma^2 + \mu\theta\right] \tag{B.12}$$

One can obtain all the moments by taking derivatives of G at $\theta = 0$. The cumulant generating function follows immediately:

$$K(\theta) = \frac{1}{2}\sigma^2\theta^2 + \mu\theta . \tag{B.13}$$

From the derivatives of K, one obtains the cumulants of a Gaussian distribution. The only non-vanishing cumulants are the first two, that correspond to the average and the variance, respectively. In particular, for a Gaussian distribution, the skewness and kurtosis are exactly zero.

The Poisson distributions for a discrete stochastic variable m is:

$$P(m) = \frac{\lambda^m}{m!} e^{-\lambda}, \quad \sum_{m=0}^{\infty} P(m) = 1 \tag{B.14}$$

One can repeat the steps for the Gaussian case and obtain the moment generating function and the cumulant generating function:

$$\begin{aligned} G(\theta) &= \sum_{m=0}^{\infty} e^{\theta m} \frac{\lambda^m}{m!} e^{-\lambda} = \\ &= \sum_{m=0}^{\infty} \frac{(\lambda e^{\theta})^m}{m!} e^{-\lambda} = \\ &= \exp\{\lambda e^{\theta} - \lambda\} \end{aligned} \tag{B.15}$$

$$K(\theta) = \ln G(\theta) = \lambda e^{\theta} - \lambda \; . \tag{B.16}$$

From Eq. (B.16) it easy to verify that all cumulants are equal to λ and from Eq. (B.8) one obtains for the first four moments:

$$\begin{aligned} \langle m \rangle &= \lambda \\ \langle m^2 \rangle &= \lambda^2 + \lambda \\ \langle m^3 \rangle &= \lambda^3 + 3\lambda^2 + \lambda \\ \langle m^4 \rangle &= \lambda^4 + 6\lambda^3 + 7\lambda^2 + \lambda \; . \end{aligned} \tag{B.17}$$

Due to the fact that all cumulants are equal, the skewness and kurtosis of a Poissonian distribution are given by

$$\gamma = \lambda^{-1/2} \quad \text{and} \quad \kappa = \lambda^{-1}. \tag{B.18}$$

For asymptotically large values of λ these quantities tend to zero, as in the case of a Gaussian distribution. This feature is related to the central limit theorem in statistics.

Finally, one can compute the cumulants for a Skellam distribution. This is the distribution followed by the difference of two stochastic variables, each of which follows a Poissonian distribution. One has:

$$S(m) = \sum_{m_1, m_2} \delta_{m, m_1 - m_2} P_{\lambda_1}(m_1) P_{\lambda_2}(m_2) \tag{B.19}$$

where $P_{\lambda_i}(m_i)$ is the Poisson distribution for the stochastic variable m_i with average λ_i. Of course the sum of $S(m)$ over all possible values of m is 1:

$$\begin{aligned} \sum_{m=-\infty}^{+\infty} \sum_{m_1,m_2} \delta_{m,m_1-m_2} P_1(m_1) P_2(m_2) = \\ = \sum_{m_1} P_1(m_1) \sum_{m_2} P_2(m_2) = 1 \ . \end{aligned} \tag{B.20}$$

The moment generating function is easily calculated:

$$\begin{aligned} G(\theta) &= \sum_{m=-\infty}^{+\infty} \sum_{m_1,m_2} \delta_{m,m_1-m_2} e^{\theta m} P_1(m_1) P_2(m_2) = \\ &= \sum_{m_1=0} e^{\theta m_1} P_1(m_1) \sum_{m_2=0} e^{-\theta m_2} P_2(m_2) = \\ &= G_1(\theta) G_2(-\theta) \ , \end{aligned} \tag{B.21}$$

where G_i is the moment generating function for the Poissonian distribution of variable m_i. The computation of the moments of the Skellam distribution is difficult. On the contrary, the computation of cumulants is very easy. The cumulant generating function is:

$$K(\theta) = \ln G_1(\theta) + \ln G_2(-\theta). \tag{B.22}$$

Hence, the odd cumulants for a Skellam distribution are the difference of cumulants of the two Poisson distribution, while the even cumulants are given by the sum of the two Poissonian cumulants:

$$\langle m^n \rangle_c = \lambda_1 + (-1)^n \lambda_2 \ . \tag{B.23}$$

From Eq.(B.8), the moments of a Skellam distribution read:

$$\begin{aligned}
&\langle m\rangle = \lambda_1 - \lambda_2 \\
&\langle m^2\rangle = (\lambda_1 - \lambda_2)^2 + \lambda_1 + \lambda_2 \\
&\langle m^3\rangle = (\lambda_1 - \lambda_2)[1 + 3(\lambda_1 + \lambda_2) + (\lambda_1 - \lambda_2)^2] \\
&\langle m^4\rangle = (\lambda_1 - \lambda_2)\big\{1 + (\lambda_1 - \lambda_2)[1 + 3(\lambda_1 + \lambda_2) + (\lambda_1 - \lambda_2)^2] + \\
&+ 6(\lambda_1^2 - \lambda_2^2) + (\lambda_1 - \lambda_2)^3\big\} + 3(\lambda_1 + \lambda_2)^2 \; .
\end{aligned} \tag{B.24}$$

The skewness and kurtosis for a Skellam distribution read:

$$\gamma = \frac{\lambda_1 - \lambda_2}{(\lambda_1 + \lambda_2)^{3/2}} \qquad \kappa = \frac{1}{\lambda_1 + \lambda_2} \; . \tag{B.25}$$

Again, for large values of λ_i, the skewness and kurtosis become arbitrarily small and also the Skellam distribution approaches a Gaussian.

In the next paragraph I discuss how one can use cumulants in statistical mechanics.

Cumulants in statistical mechanics

This paragraph is focused on cumulants in statistical mechanics, in particular the cumulants of conserved charges. One can consider a physical system described by the Hamiltonian $\hat{H}$ enclosed in a volume V and assume that this system has an observable $\hat{N}$ which is a conserved charge. Of course $\hat{H}$ and $\hat{N}$ commute. The grand canonical partition function for this system at temperature T and chemical potential μ is defined as

$$\mathcal{Z} = \mathrm{tr}[e^{-(\hat{H}-\mu\hat{N})/T}] \; , \tag{B.26}$$

where the trace is taken over all quantum states of the system. The expectation value of an observable $\hat{O}$ is given by:

$$\langle\hat{O}\rangle = \frac{1}{\mathcal{Z}}\mathrm{tr}[\hat{O}e^{-(\hat{H}-\mu\hat{N})/T}] \; . \tag{B.27}$$

For example, the expectation value for the conserved charge $\hat{N}$ is:

$$\langle \hat{N} \rangle = \frac{1}{\mathcal{Z}} \mathrm{tr}[\hat{N} e^{-(\hat{H}-\mu\hat{N})/T}] \ . \tag{B.28}$$

Now one can define the grand canonical thermodynamics potential as:

$$\Omega \equiv -T \ln \mathcal{Z} \ . \tag{B.29}$$

From the latter one can derive the cumulants of the distribution of the conserved charge $\hat{N}$:

$$\langle \hat{N}^n \rangle_c = -\frac{\partial^n \Omega/T}{\partial(\mu/T)^n} \tag{B.30}$$

One can easily check this definition by evaluating the lowest-order cumulants.

Similarly, one can define the off-diagonal fluctuations of two different conserved charge, Q_1 and Q_2, associated to two chemical potentials μ_1 and μ_2. In this case, the grand canonical partition function reads:

$$\mathcal{Z} = \mathrm{tr}\left[e^{-(\hat{H}-\mu_i\hat{Q}_i)/T}\right]. \tag{B.31}$$

The off-diagonal moments of the distribution are

$$\langle \hat{Q}_1^n \hat{Q}_2^k \rangle = \frac{1}{\mathcal{Z}} \mathrm{tr}[\hat{Q}_1^n \hat{Q}_2^k e^{-(\hat{H}-\mu_i\hat{Q}_i)/T}] \ , \tag{B.32}$$

while the corresponding cumulants are given by

$$\langle \hat{Q}_1^n \hat{Q}_2^k \rangle_c = -\frac{\partial^{n+k} \Omega/T}{\partial(\mu_1/T)^n \partial(\mu_2/T)^k}. \tag{B.33}$$

It is an easy exercise to find the relation between the first off-diagonal moments and the first off-diagonal cumulants.

In some cases it is more convenient to express the fluctuations of conserved charges in terms of the ones of their carriers. The charge is expressed in terms of the particle number through the equation

$$\langle \hat{Q} \rangle = \sum_i Q_i \langle \hat{N}_{i,\mathrm{net}} \rangle \ , \tag{B.34}$$

where the sum runs over all particle species and $\langle \hat{N}_{i,\mathrm{net}} \rangle$ is the average net number of particles i (i.e. particles minus antiparticles), carrying charge Q_i. For the expectation values of higher-order cumulants one has:

$$\langle \hat{Q}^n \rangle_c = \sum_i Q_i^n \langle \hat{N}_{i,\mathrm{net}}^n \rangle_c = \sum_i Q_i^n [\langle \hat{N}_{Q_i} \rangle + (-1)^n \langle \hat{N}_{-Q_i} \rangle], \tag{B.35}$$

where in the last step we assumed that the net particle number obeys a Skellam statistics. These last considerations applied to baryon-number fluctuations in QCD lead to:

$$\frac{\langle B^{2n+2} \rangle_c}{\langle B^{2n} \rangle_c} = B^2 \frac{\sum_i \langle N_{i,\mathrm{net}}^{2n+2} \rangle_c}{\sum_i \langle N_{i,\mathrm{net}}^{2n} \rangle_c} = B^2 \ , \tag{B.36}$$

which holds since, depending on the phase, all particles carry the same baryon number, either 1/3 or 1. Also in this case we assumed that the net-particle distribution follows a Skellam statistics.

Appendix C

Matsubara sums and Fermi functions

In this Appendix I show the thermal field theory calculations used to derive the expression for the chiral condensate in Eq. (3.19). In Chapter 3 I introduced the chiral condensate as:

$$\phi_i \equiv -i\mathrm{Tr}S^i, \tag{C.1}$$

where the trace is performed over the Dirac and color indices and S^i is the quark propagator of flavour i in coordinate space evaluated at zero separation:

$$S^i(x,x) = \int \frac{d^4p}{(2\pi)^4} \frac{1}{\not{p} - m_i + \gamma^0(\mu + A_0)}. \tag{C.2}$$

In order to study the problem at finite temperature and baryon density in the imaginary time formalism ($t = -i\tau$ with $\tau \in [0,\ \beta]$), the τ-ordered product of the operators replaces the usual time-ordering and all the expectation values are taken in the grand-canonical ensemble. Then one needs to operate the following substitutions

$$p_0 \to i\omega_n = (2n+1)i\pi/\beta; \tag{C.3}$$

$$A_0 \to iA_4 \tag{C.4}$$

$$\int \frac{dp_0}{(2\pi)} \to \frac{i}{\beta} \sum_{n=-\infty}^{+\infty} . \tag{C.5}$$

The discrete energies ω_n take the name of Matsubara frequencies. The quark propagator, then, becomes:

$$S^i = -\frac{i}{\beta} \sum_{n=-\infty}^{+\infty} \int_\Lambda \frac{d^3p}{(2\pi)^3} \frac{1}{(i\omega_n + \mu + iA_4)\gamma^0 - \vec{\gamma}\vec{p} - m_i}. \tag{C.6}$$

The chiral condensate now becomes:

$$\phi_i = -\frac{4}{\beta}\mathrm{Tr}_c \sum_{n=-\infty}^{+\infty} \int_\Lambda \frac{d^3p}{(2\pi)^3} \frac{m_i}{(i\omega_n + \mu + iA_4)^2 - E_i^2} . \tag{C.7}$$

The fraction can be decomposed into a sum of two different fractions:

$$\begin{aligned} \frac{1}{(i\omega_n + \mu + iA_4)^2 - E_i^2} &= \\ &= \frac{1}{2E_i}\left(\frac{1}{i\omega_n + \mu + iA_4 - E_i} - \frac{1}{i\omega_n + \mu + iA_4 + E_i}\right). \end{aligned} \tag{C.8}$$

One can compute the Matsubara sum of the two fractions separately, using the following trick:

$$-\frac{1}{2\pi i}\int_C \frac{dz}{e^{\beta z}+1}\frac{e^{\eta z}}{z-x} = \sum_{n=-\infty}^{+\infty} \frac{e^{\eta i\omega_n}}{i\omega_n - x} , \tag{C.9}$$

where the contour of the integral runs around the imaginary axis in the complex z-plane and η is a positive infinitesimal factor that ensures convergence and accounts also for the correct ordering of the quark fields in the zero-distance propagator. The integral can be evaluated through the residue of the pole at $z = x$ and one gets:

$$\sum_{n=-\infty}^{+\infty} \frac{e^{\eta i\omega_n}}{i\omega_n - x} = \frac{1}{1+e^{\beta x}} \ . \tag{C.10}$$

Applying this trick to Eq. (C.8) one gets:

$$\sum_{n=-\infty}^{+\infty} \frac{1}{i\omega_n + \mu + iA_4 - E_i} = \frac{1}{1+\exp\{\beta(E_i - \mu - iA_4)\}} \tag{C.11}$$

$$\sum_{n=-\infty}^{+\infty} \frac{1}{i\omega_n + \mu + iA_4 + E_i} = \frac{1}{1+\exp\beta(-E_i - \mu - iA_4)}. \tag{C.12}$$

After computing the trace over colors one obtains

$$\phi_i = -2N_c \int_\Lambda \frac{d^3p}{(2\pi)^3} \frac{m_i}{E_i} [1 - f_\Phi^{+i}(E_i, \mu_i) - f_\Phi^{-i}(E_i, \mu_i)] \ , \tag{C.13}$$

where the functions $f_\Phi^\pm$ were defined in the main text.

Appendix D

The Mean Field Equations

In this chapter I present some technical details concerning the solution of the mean field equation.

D.1 Mean Field Equations: getting the system

In section 3.2.1 I introduced the five coupled equations of the mean field approximation, in the case in which the vector interaction is neglected. In this section I show the steps to reduce Eq. (3.38) to Eq. (3.40). To prove this, one can use the Gauss reduction method.

$$\begin{cases} 2G(\phi_u + 2N_cI_u) + 2K\phi_s(\phi_d + 2N_cI_d) + 2K\phi_d(\phi_s + 2N_cI_s) = 0 \\ 2G(\phi_d + 2N_cI_d) + 2K\phi_s(\phi_u + 2N_cI_u) + 2K\phi_u(\phi_s + 2N_cI_s) = 0 \\ 2G(\phi_s + 2N_cI_s) + 2K\phi_u(\phi_d + 2N_cI_d) + 2K\phi_d(\phi_u + 2N_cI_u) = 0. \end{cases} \tag{D.1}$$

One can replace the first equation, called R_1 with the following expression:

$$R_1 \to \phi_u R_1 - \phi_d R_2 \;, \tag{D.2}$$

where R_2 is the second equation, and one gets:

$$(2G\phi_u - 2K\phi_d\phi_s)(\phi_u + 2N_cI_u) - (2G\phi_d - 2K\phi_u\phi_s)(\phi_d + 2N_cI_d) = 0. \tag{D.3}$$

Then, the second equation can be replaced by:

$$R_2 \to \phi_d R_2 - \phi_s R_3 \tag{D.4}$$

where R_3 is the third equation and one gets:

$$(2G\phi_d - 2K\phi_u\phi_s)(\phi_d + 2N_cI_d) - (2G\phi_s - 2K\phi_u\phi_d)(\phi_s + 2N_cI_s) = 0\ . \tag{D.5}$$

From these expressions one can obtain the following equations

$$(\phi_u + 2N_cI_u) = \frac{2G\phi_d - 2K\phi_u\phi_s}{2H\phi_u - 2K\phi_d\phi_s}(\phi_d + 2N_cI_d) \tag{D.6}$$

$$(\phi_s + 2N_cI_s) = \frac{G\phi_d - 2K\phi_u\phi_s}{2G\phi_s - 2K\phi_u\phi_d}(\phi_d + 2N_cI_d)\ . \tag{D.7}$$

Now, substituting these two expressions into the third equation one can conclude that the parenthesis involving the condensate of down quarks is null. One obtains then the first three MFE's in Eq. (3.40).

D.2 The Hessian matrix of the quark-mass sector of the PNJL model

In this work, in studying the region of the phase diagram around the first-order transition I consider the Hessian matrix corresponding to the second derivatives of the grand canonical potential with respect to the chiral condensates. This matrix is completely defined (positive or negative); then one can find the local/global minima of Ω. The Hermitian matrix used in the calculation is:

$$
\begin{pmatrix}
2G - 4G^2 A + & 2K\phi_s - 4GK\phi_s A - & 2K\phi_d - 4GK\phi_d A - \\
-\,4K^2\phi_s^2 B - 4K^2\phi_d^2 C & -\,4GK\phi_s B - 4K^2\phi_u\phi_d C & -\,4K^2\phi_u\phi_s^2 B - 4GK\phi_d^2 C \\
& & \\
2K\phi_s - 4GK\phi_s A - & 2G - 4K^2\phi_s^2 A - & 2K\phi_d - 4GK\phi_d A - \\
-\,4GK\phi_s B - 4K^2\phi_u\phi_d C & -\,4G^2 B - 4K^2\phi_u C & -\,4K^2\phi_u\phi_s^2 B - 4GK\phi_d^2 C \\
& & \\
2K\phi_d - 4GK\phi_d A - & 2K\phi_d - 4GK\phi_d A - & 2G - 4K^2\phi_d^2 A + \\
-\,4K^2\phi_u\phi_s^2 B - 4GK\phi_d^2 C & -\,4K^2\phi_u\phi_s^2 B - 4GK\phi_d^2 C & -\,4K^2\phi_u^2 B - 4G^2 C
\end{pmatrix}
$$

where A,B,C are numerical integrals defined as:

$$
\begin{aligned}
A &= \frac{N_c}{\pi^2}\int dp \frac{p^2 - M_u^2}{E_u}\Big[\theta(\Lambda - |p|) - f_\Phi^{+u}(E_u,\mu_u) - f_\Phi^{-u}(E_u,\mu_u)\Big] \\
B &= \frac{N_c}{\pi^2}\int dp \frac{p^2 - M_d^2}{E_d}\Big[\theta(\Lambda - |p|) - f_\Phi^{+d}(E_d,\mu_d) - f_\Phi^{-d}(E_d,\mu_d)\Big] \\
C &= \frac{N_c}{\pi^2}\int dp \frac{p^2 - M_s^2}{E_s}\Big[\theta(\Lambda - |p|) - f_\Phi^{+s}(E_s,\mu_s) - f_\Phi^{-s}(E_s,\mu_s)\Big]\ .
\end{aligned}
\tag{D.8}
$$

Appendix E

Abbreviations

In the following I list in alphabetic order all the abbreviations used in this thesis.

- AGS: Alternating Gradient Synchrotron is a particle accelerator located at Brookhaven National Laboratory.
- BNL: Brookhaven National Laboratory located in New York.
- CBM: Compressed Baryon Matter, the experiment devoted to the exploration of the QCD phase diagram located at the GSI Helmholtz Centre for Heavy Ion Research in Darmstadt (Germany).
- CEP: Critical End Point.
- CERN: Conseil Européen pour la Recherche Nucléaire or, in English, European Organization for Nuclear Research, located in Geneva (Switzerland).
- CMB: Cosmic Microwave Background.
- EFT: Effective Field Theory.
- EoS: Equation of State.
- FAIR: the Facility for Antiproton and Ion Research is a future particle accelerator located at the GSI Helmholtz Centre for Heavy Ion Research in Darmstadt (Germany).

- HIC: Heavy Ion Collision.
- LHC: the Large Hadron Collider, sited at CERN, is the biggest particle accelerator in the world.
- LHS: Left Hand Side, usually referred to equations.
- lQCD: Quantum Chromo Dynamics on the Lattice.
- LRF: Local Rest Frame.
- MFE: Mean Field Equation.
- NICA: the Nuclotron-based Ion Collider fAcility is a particles accelerator, currently under construction, near Moscow (Russia).
- NJL: Nambu-Jona-Lasinio.
- NLO: Next-to Leading Order. It usually refers to the first subleading term in a perturbative series.
- NNLO: Next-to-Next-to Leading Order. It usually refers to the second subleading term in a perturbative series.
- NRL: Non Relativistic Limit.
- NS: Neutral Strangeness. It refers to a system with vanishing net number of strange particles.
- PD: Phase Diagram.
- PDG: Particle Data Group.
- PNJL: NJL model with Polyakov-loop correction.
- QCD: Quantum Chromo-Dynamics.
- QED: Quantum Electro-Dynamics.
- QGP: Quark Gluon Plasma.

- QNS: Quasi Neutral Strangeness. It refers to a system with a small net number of strange particles.
- RHD: Relativistic Hydro-Dynamics.
- RHIC: the Relativistic Heavy Ion Collider is a particle accelerator located at BNL.
- RHS: Right Hand Side, usually referred to equations.
- SPS: the Super Proton Synchrotron is a particle accelerator of synchrotron type at CERN.
- SYM: Symmetric. In this thesis it is the scenario with all quark chemical potentials set equal.
- YM: Yang-Mils, usually referred to the gauge-field Lagrangian.

Bibliography

[1] G. 't Hooft. "On the phase transition towards permanent quark confinement". In: *Nuclear Physics B* 138.1 (1978), pp. 1–25. ISSN: 0550-3213. DOI: `https://doi.org/10.1016/0550-3213(78)90153-0`. URL: `http://www.sciencedirect.com/science/article/pii/0550321378901530`.

[2] P. A. R. Ade et al. [Planck Collaboration]. "Planck 2013 results. I. Overview of products and scientific results". In: *Astronomy & Astrophysics* 571 ().

[3] A.Einstein. "On the Motion of Small Particles Suspended in Liquids at RestRequired by the Molecular-Kinetic Theory of Heat". In: *Annalen der Physik* 17 (), pp. 549–560.

[4] Gert Aarts. "Introductory lectures on lattice QCD at nonzero baryon number". In: *Journal of Physics: Conference Series* 706 (Apr. 2016), p. 022004. ISSN: 1742-6596. DOI: `10.1088/1742-6596/706/2/022004`. URL: `http://dx.doi.org/10.1088/1742-6596/706/2/022004`.

[5] B. I. Abelev et al. "Systematic Measurements of Identified Particle Spectra in pp, d^+ Au and Au+Au Collisions from STAR". In: *Phys. Rev.* C79 (2009), p. 034909. DOI: `10.1103/PhysRevC.79.034909`. arXiv: `0808.2041 [nucl-ex]`.

[6] L. Adamczyk et al. "Bulk Properties of the Medium Produced in Relativistic Heavy-Ion Collisions from the Beam Energy Scan Program". In: *Phys. Rev.* C96.4 (2017), p. 044904. DOI: `10.1103/PhysRevC.96.044904`. arXiv: `1701.07065 [nucl-ex]`.

[7] A. Aduszkiewicz et al. "Measurements of π^{pm}, K^{pm}, p and $\bar{p}$ spectra in proton-proton interactions at 20, 31, 40, 80 and 158 GeV /c with the NA61/SHINE spectrometer at the CERN SPS." In: *Eur. Phys. J. C* 77 (2017), p. 671. URL: `https://doi.org/10.1140/epjc/s10052-017-5260-4`.

[8] C.Alt et al. "Pion and kaon production in central Pb + Pb collisions at $20A$ and $30A$ GeV: Evidence for the onset of deconfinement". In: *Phys. Rev. C* 77 (2 Feb. 2008), p. 024903. DOI: `10.1103/PhysRevC.77.024903`. URL: `https://link.aps.org/doi/10.1103/PhysRevC.77.024903`.

[9] Chatrchyan et al. "Indications of Suppression of Excited Υ States in Pb-Pb Collisions at $\sqrt{s_{\mathrm{NN}}} = 2.76$ TeV". In: *Phys. Rev. Lett.* 107 (5 June 2011), p. 052302.

[10] D.Blaschke et al. "Topical issue on Exploring Strongly Interacting Matter at High Densities - NICA White Paper". In: *Eur. Phys. J A* (), p. 267. DOI: `https://doi.org/10.1140/epja/i2016-16267-x`.

[11] H. Reinhardt et al. "Hamiltonian approach to QCD in Coulomb gauge: From the vacuum to finite temperatures". In: *EPJ Web of Conferences* 126 (Oct. 2015). DOI: `10.1051/epjconf/201612601002`.

[12] P.A Zyla et al. "Particle Data Group". In: *Progress of Theoretical and Experimental Physics* 2020.8 (Aug. 2020). 083C01. ISSN: 2050-3911. DOI: `10.1093/ptep/ptaa104`. eprint: `https://academic.oup.com/ptep/article-pdf/2020/8/083C01/34673722/ptaa104.pdf`. URL: `https://doi.org/10.1093/ptep/ptaa104`.

[13] S.Borsányi et al. "Is there still any T_c mystery in lattice QCD? Results with physical masses in the continuum limit III". In: *Journal of High Energy Physics* 73 (9). DOI: `10.1007/JHEP09(2010)073`.

[14] Y. Akiba et al. "Particle production in Au + Au collisions from BNL E866". In: *Nuclear Physics A* 610 (1996). Quark Matter '96, pp. 139–152. ISSN: 0375-9474. DOI: `https://doi.org/10.1016/`

`S0375-9474(96)00350-8`. URL: `https://www.sciencedirect.com/science/article/pii/S0375947496003508`.

[15] Y.Aoki et al. "The order of the quantum chromodynamics transition predicted by the standard model of particle physics". In: *Nature* 443 (2006). DOI: `10.1038/nature05120`. URL: `https://doi.org/10.1038/nature05120`.

[16] W. M. Alberico et al. "Heavy-flavour spectra in high energy nucleus-nucleus collisions". In: *Eur. Phys. J.* C71 (2011), p. 1666. DOI: `10.1140/epjc/s10052-011-1666-6`. arXiv: `1101.6008 [hep-ph]`.

[17] Nihar Ranjan Sahoo and. "Recent results on event-by-event fluctuations from the RHIC Beam Energy Scan program in the STAR experiment". In: *Journal of Physics: Conference Series* 535 (Sept. 2014), p. 012007. DOI: `10.1088/1742-6596/535/1/012007`.

[18] Y. Aoki et al. "The QCD transition temperature: Results with physical masses in the continuum limit". In: *Physics Letters B* 643.1 (2006), pp. 46–54. ISSN: 0370-2693. DOI: `https://doi.org/10.1016/j.physletb.2006.10.021`. URL: `https://www.sciencedirect.com/science/article/pii/S0370269306012755`.

[19] M. Asakawa and M. Kitazawa. "Fluctuations of conserved charges in relativistic heavy ion collisions: An introduction". In: *Progress in Particle and Nuclear Physics* 90 (2016), pp. 299–342. ISSN: 0146-6410. DOI: `https://doi.org/10.1016/j.ppnp.2016.04.002`. URL: `https://www.sciencedirect.com/science/article/pii/S0146641016300023`.

[20] B. B. Back et al. "Centrality dependence of charged anti-particle to particle ratios near mid rapidity in d + Au collisions at s(NN)**(1/2) = 200-GeV". In: *Phys. Rev.* C70 (2004), p. 011901. DOI: `10.1103/PhysRevC.70.011901`. arXiv: `nucl-ex/0309013 [nucl-ex]`.

[21] Daniel Baumann. *TASI Lectures on Inflation.* 2009. arXiv: `0907.5424 [hep-th]`.

[22] A. Bazavov et al. “Chiral and deconfinement aspects of the QCD transition”. In: *Phys. Rev. D* 85 (5 Mar. 2012), p. 054503. DOI: `10.1103/PhysRevD.85.054503`. URL: `https://link.aps.org/doi/10.1103/PhysRevD.85.054503`.

[23] A. Bazavov et al. “Equation of state in $(2+1)$-flavor QCD”. In: *Phys. Rev. D* 90 (9 Nov. 2014), p. 094503. DOI: `10.1103/PhysRevD.90.094503`. URL: `https://link.aps.org/doi/10.1103/PhysRevD.90.094503`.

[24] A. Beraudo and M. Nardi. “QGP lecture”. In: (). DOI: `http://personalpages.to.infn.it/~beraudo/lezioni/hydro2017_short.pdf`.

[25] A. Beraudo et al. “Heavy flavors in heavy-ion collisions: quenching, flow and correlations”. In: *Eur. Phys. J.* C75.3 (2015), p. 121. DOI: `10.1140/epjc/s10052-015-3336-6`. arXiv: `1410.6082 [hep-ph]`.

[26] G. Bertsch and P. j. Siemens. “NUCLEAR FRAGMENTATION”. In: *Phys. Lett.* 126B (1983), pp. 9–12. DOI: `10.1016/0370-2693(83)90004-7`.

[27] Claudio Bonati et al. “Curvature of the chiral pseudocritical line in QCD: Continuum extrapolated results”. In: *Phys. Rev. D* 92 (5 Sept. 2015), p. 054503. DOI: `10.1103/PhysRevD.92.054503`. URL: `https://link.aps.org/doi/10.1103/PhysRevD.92.054503`.

[28] Szabolcs Borsanyi. *Fluctuations at finite temperature and density.* 2015. arXiv: `1511.06541 [hep-lat]`.

[29] Szabolcs Borsanyi et al. “QCD Crossover at Finite Chemical Potential from Lattice Simulations”. In: *Phys. Rev. Lett.* 125 (5 July 2020), p. 052001. DOI: `10.1103/PhysRevLett.125.052001`. URL: `https://link.aps.org/doi/10.1103/PhysRevLett.125.052001`.

[30] Wit Busza, Krishna Rajagopal, and Wilke van der Schee. “Heavy Ion Collisions: The Big Picture and the Big Questions”. In: *Annual Review of Nuclear and Particle Science* 68.1 (2018), pp. 339–376. DOI: `10.1146/annurev-nucl-101917-020852`. eprint: `https://doi.org/10.`

`1146/annurev-nucl-101917-020852`. URL: `https://doi.org/10.1146/annurev-nucl-101917-020852`.

[31] Paolo Cea, Leonardo Cosmai, and Alessandro Papa. “Critical line of $2+1$ flavor QCD: Toward the continuum limit”. In: *Phys. Rev. D* 93 (1 Jan. 2016), p. 014507. DOI: `10.1103/PhysRevD.93.014507`. URL: `https://link.aps.org/doi/10.1103/PhysRevD.93.014507`.

[32] STAR Collaboration and M. M. Aggarwal et al. *An Experimental Exploration of the QCD Phase Diagram: The Search for the Critical Point and the Onset of De-confinement.* 2010. arXiv: `1007.2613 [nucl-ex]`.

[33] J. C. Collins and M. J. Perry. “Superdense Matter: Neutrons or Asymptotically Free Quarks?” In: *Phys. Rev. Lett.* 34 (21 May 1975), pp. 1353–1356. DOI: `10.1103/PhysRevLett.34.1353`. URL: `https://link.aps.org/doi/10.1103/PhysRevLett.34.1353`.

[34] P. Costa et al. “Pseudoscalar mesons in hot, dense matter”. In: *Phys. Rev. C* 70 (2 Aug. 2004), p. 025204. DOI: `10.1103/PhysRevC.70.025204`. URL: `https://link.aps.org/doi/10.1103/PhysRevC.70.025204`.

[35] Pedro Costa. “Influence of the vector interaction and an external magnetic field on the isentropes near the chiral critical end point”. In: *Phys. Rev. D* 93 (11 June 2016), p. 114035. DOI: `10.1103/PhysRevD.93.114035`. URL: `https://link.aps.org/doi/10.1103/PhysRevD.93.114035`.

[36] Enrico Fermi. “High-energy nuclear events”. In: *Prog. Theor. Phys.* 5 (1950), pp. 570–583. DOI: `10.1143/PTP.5.570`.

[37] Márcio Ferreira, Pedro Costa, and Constan ça Providência. “Presence of a critical endpoint in the QCD phase diagram from the net-baryon number fluctuations”. In: *Phys. Rev. D* 98 (3 Aug. 2018), p. 034006. DOI: `10.1103/PhysRevD.98.034006`. URL: `https://link.aps.org/doi/10.1103/PhysRevD.98.034006`.

[38] A. L. Fetter, John Dirk Walecka, and L. Kadanoff. *Quantum Theory of Many-Particle Systems.* 1971.

[39] Richard P. Feynman. "Very High-Energy Collisions of Hadrons". In: *Phys. Rev. Lett.* 23 (24 Dec. 1969), pp. 1415–1417. DOI: `10.1103/PhysRevLett.23.1415`. URL: `https://link.aps.org/doi/10.1103/PhysRevLett.23.1415`.

[40] Eduardo S. Fraga, Maurício Hippert, and Andreas Schmitt. "Surface tension of dense matter at the chiral phase transition". In: *Phys. Rev.* D99.1 (2019), p. 014046. DOI: `10.1103/PhysRevD.99.014046`. arXiv: `1810.13226 [hep-ph]`.

[41] Wei-jie Fu, Zhao Zhang, and Yu-xin Liu. "2 + 1 flavor Polyakov–Nambu–Jona-Lasinio model at finite temperature and nonzero chemical potential". In: *Phys. Rev. D* 77 (1 Jan. 2008), p. 014006. DOI: `10.1103/PhysRevD.77.014006`. URL: `https://link.aps.org/doi/10.1103/PhysRevD.77.014006`.

[42] Kenji Fukushima. "Chiral effective model with the Polyakov loop". In: *Physics Letters B* 591.3 (2004), pp. 277–284. ISSN: 0370-2693. DOI: `https://doi.org/10.1016/j.physletb.2004.04.027`. URL: `http://www.sciencedirect.com/science/article/pii/S0370269304006203`.

[43] Kenji Fukushima. "Phase diagrams in the three-flavor Nambu–Jona-Lasinio model with the Polyakov loop". In: *Phys. Rev. D* 77 (11 June 2008), p. 114028. DOI: `10.1103/PhysRevD.77.114028`. URL: `https://link.aps.org/doi/10.1103/PhysRevD.77.114028`.

[44] Richard J. Furnstahl and Brian D. Serot. "Covariant mean-field calculations of finite-temperature nuclear matter". In: *Phys. Rev.* C41 (1990), pp. 262–279. DOI: `10.1103/PhysRevC.41.262`.

[45] G.Jaeger. "The Ehrenfest Classification of Phase Transitions: Introduction and Evolution". In: *Archive for History of Exact Sciences* 53 (1). DOI: `10.1007/s004070050021`.

[46] R. V. Gavai and Sourendu Gupta. "On the critical end point of QCD". In: *Physical Review D* 71.11 (June 2005). ISSN: 1550-2368. DOI: `10.1103/physrevd.71.114014`. URL: `http://dx.doi.org/10.1103/PhysRevD.71.114014`.

[47] N. K. Glendenning, Laszlo P. Csernai, and J. I. Kapusta. "Liquid-gas phase separation in nuclear collisions". In: *Phys. Rev.* C33 (1986), pp. 1299–1302. DOI: `10.1103/PhysRevC.33.1299`.

[48] Rajan Gupta. *Introduction to Lattice QCD*. 1998. arXiv: `hep-lat/9807028 [hep-lat]`.

[49] Lisa M. Haas et al. "Improved Polyakov-loop potential for effective models from functional calculations". In: *Phys. Rev. D* 87 (7 Apr. 2013), p. 076004. DOI: `10.1103/PhysRevD.87.076004`. URL: `https://link.aps.org/doi/10.1103/PhysRevD.87.076004`.

[50] J. Hamilton, W. Heitler, and H. W. Peng. "Theory of Cosmic-Ray Mesons". In: *Phys. Rev.* 64 (3-4 Aug. 1943), pp. 78–94. DOI: `10.1103/PhysRev.64.78`. URL: `https://link.aps.org/doi/10.1103/PhysRev.64.78`.

[51] H. Hansen et al. "Mesonic correlation functions at finite temperature and density in the Nambu–Jona-Lasinio model with a Polyakov loop". In: *Phys. Rev. D* 75 (6 Mar. 2007), p. 065004. DOI: `10.1103/PhysRevD.75.065004`. URL: `https://link.aps.org/doi/10.1103/PhysRevD.75.065004`.

[52] Urs M. Heller. "Recent progress in finite temperature lattice QCD". In: *PoS* LAT2006 (2006), p. 011. DOI: `10.22323/1.032.0011`.

[53] Heuser, J.M. "The Compressed Baryonic Matter Experiment at FAIR". In: *EPJ Web of Conferences* 13 (2011), p. 03001. DOI: `10.1051/epjconf/20111303001`. URL: `https://doi.org/10.1051/epjconf/20111303001`.

[54] Bilandzic A Hirano T. van der Kolk N. *Hydrodynamics and Flow. In: Sarkar S., Satz H., Sinha B. (eds) The Physics of the Quark-Gluon Plasma.* Vol. 785. Lecture Notes in Physics. Springer, Berlin, Heidelberg, 2009.

[55] Edmond Iancu. “QCD in heavy ion collisions”. In: arXiv:1205.0579 (May 2012). Based on lectures presented at the 2011 European School of High-Energy Physics, 7-20 September 2011, Cheile Gradistei, Romania. 73 pages, many figures, 197–266. 73 p. DOI: `10.5170/CERN-2014-003.197`. URL: `https://cds.cern.ch/record/1445976`.

[56] Werner Israel, J. M. Stewart, and Stephen William Hawking. “On transient relativistic thermodynamics and kinetic theory. Il”. In: *Proceedings of the Royal Society of London. A. Mathematical and Physical Sciences* 365.1720 (1979), pp. 43–52.

[57] Sangyong Jeon and Ulrich Heinz. “Introduction to Hydrodynamics”. In: *Int. J. Mod. Phys. E* 24.10 (2015), p. 1530010. arXiv: `1503.03931 [hep-ph]`.

[58] J. B. Johnson. “Thermal Agitation of Electricity in Conductors”. In: *Phys. Rev.* 32 (1 July 1928), pp. 97–109. DOI: `10.1103/PhysRev.32.97`. URL: `https://link.aps.org/doi/10.1103/PhysRev.32.97`.

[59] O. Kaczmarek et al. “Heavy quark anti-quark free energy and the renormalized Polyakov loop”. In: *Phys. Lett. B* 543 (2002), pp. 41–47. DOI: `10.1016/S0370-2693(02)02415-2`. arXiv: `hep-lat/0207002`.

[60] Olaf Kaczmarek. “Screening at finite temperature and density”. In: *PoS* CPOD07 (2008), p. 043. DOI: `10.22323/1.047.0043`.

[61] J. I. Kapusta and Charles Gale. *Finite-temperature field theory: Principles and applications.* Cambridge Monographs on Mathematical Physics. Cambridge University Press, 2011.

[62] F. Karsch. “Lattice results on QCD thermodynamics”. In: *Nuclear Physics A* 698.1 (2002). 15th Int. Conf. on Ultra-Relativistic Nucleus-Nucleus Collisions (Quark Matter 2001), pp. 199–208. ISSN: 0375-9474. DOI: `https://doi.org/10.1016/S0375-9474(01)01365-3`.

URL: `https://www.sciencedirect.com/science/article/pii/S0375947401013653`.

[63] S. P. Klevansky. “The Nambu—Jona-Lasinio model of quantum chromodynamics”. In: *Rev. Mod. Phys.* 64 (3 July 1992), pp. 649–708. DOI: `10.1103/RevModPhys.64.649`. URL: `https://link.aps.org/doi/10.1103/RevModPhys.64.649`.

[64] S. Klimt et al. “Generalized SU(3) Nambu-Jona-Lasinio model: (I). Mesonic modes”. In: *Nuclear Physics A* 516.3 (1990), pp. 429–468. ISSN: 0375-9474. DOI: `https://doi.org/10.1016/0375-9474(90)90123-4`. URL: `https://www.sciencedirect.com/science/article/pii/0375947490901234`.

[65] Peter F. Kolb and Ulrich Heinz. “Hydrodynamic description of ultrarelativistic heavy-ion collisions”. In: *Quark–Gluon Plasma 3*, pp. 634–714.

[66] L.Landau. In: *Izv. Akad. Nauk Ser. Fiz* (1953), 15:51.

[67] M. van Leeuwen. “High-p_T results from ALICE”. In: (2012). arXiv: `1201.5205 [nucl-ex]`.

[68] A D Linde. “Phase transitions in gauge theories and cosmology”. In: *Reports on Progress in Physics* 42.3 (Mar. 1979), pp. 389–437. DOI: `10.1088/0034-4885/42/3/001`. URL: `https://doi.org/10.1088/0034-4885/42/3/001`.

[69] Pok Man Lo et al. “Polyakov loop fluctuations in SU(3) lattice gauge theory and an effective gluon potential”. In: *Phys. Rev. D* 88 (2013), p. 074502. DOI: `10.1103/PhysRevD.88.074502`. arXiv: `1307.5958 [hep-lat]`.

[70] M. Lutz, S. Klimt, and W. Weise. “Meson properties at finite temperature and baryon density”. In: *Nuclear Physics A* 542.4 (1992), pp. 521–558. ISSN: 0375-9474. DOI: `https://doi.org/10.1016/0375-9474(92)90256-J`. URL: `https://www.sciencedirect.com/science/article/pii/037594749290256J`.

[71] Matthew Luzum and Paul Romatschke. “Conformal Relativistic Viscous Hydrodynamics: Applications to RHIC results at s(NN)**(1/2) = 200-GeV”. In: *Phys. Rev.* C78 (2008). [Erratum: Phys. Rev.C79,039903(2009)], p. 034915. DOI: `10.1103/PhysRevC.78.034915,10.1103/PhysRevC.79.039903`. arXiv: `0804.4015 [nucl-th]`.

[72] Mauricio Martinez et al. “Initial state fluctuations of QCD conserved charges in heavy-ion collisions”. In: (Nov. 2019). arXiv: `1911.10272 [nucl-th]`.

[73] Mauricio Martinez et al. “Toward Initial Conditions of Conserved Charges Part II: The ICCING Monte Carlo Algorithm”. In: (Nov. 2019). arXiv: `1911.12454 [nucl-th]`.

[74] T. Matsui and H. Satz. “J/ψ Suppression by Quark-Gluon Plasma Formation”. In: *Phys. Lett. B* 178 (1986), pp. 416–422. DOI: `10.1016/0370-2693(86)91404-8`.

[75] Peter N. Meisinger and Michael C. Ogilvie. “Polyakov Loops, Z(N) Symmetry, and Sine-Law Scaling”. In: *Nuclear Physics B - Proceedings Supplements* 140 (2005). LATTICE 2004, pp. 650–652. ISSN: 0920-5632. DOI: `https://doi.org/10.1016/j.nuclphysbps.2004.11.120`. URL: `http://www.sciencedirect.com/science/article/pii/S0920563204006863`.

[76] Georgy Melkumov. “Recent results of strong interaction program from NA61/SHINE experiment at CERN SPS”. In: *EPJ Web of Conferences* (). DOI: `https://doi.org/10.1051/epjconf/201920401010`.

[77] Bruno W. Mintz et al. “Phase diagram and surface tension in the three-flavor Polyakov-quark-meson model”. In: *Phys. Rev.* D87.3 (2013), p. 036004. DOI: `10.1103/PhysRevD.87.036004`. arXiv: `1212.1184 [hep-ph]`.

[78] M. Motta et al. “Exploration of the phase diagram and the thermodynamic properties of QCD at finite temperature and chemical potential with the PNJL effective model”. In: *J. Phys. Conf. Ser.* 1667.1 (2020).

Ed. by Marco Destefanis et al., p. 012029. DOI: `10.1088/1742-6596/1667/1/012029`. arXiv: `1909.05037 [hep-ph]`.

[79] Mario Motta et al. "Isentropic evolution of the matter in heavy-ion collisions and the search for the critical endpoint". In: *Eur. Phys. J. C* 80.8 (2020), p. 770. DOI: `10.1140/epjc/s10052-020-8218-x`. arXiv: `2003.04734 [hep-ph]`.

[80] Y. Nambu and G. Jona-Lasinio. "Dynamical Model of Elementary Particles Based on an Analogy with Superconductivity. I". In: *Phys. Rev.* 122 (1 Apr. 1961), pp. 345–358. DOI: `10.1103/PhysRev.122.345`. URL: `https://link.aps.org/doi/10.1103/PhysRev.122.345`.

[81] H. Nyquist. "Thermal Agitation of Electric Charge in Conductors". In: *Phys. Rev.* 32 (1 July 1928), pp. 110–113. DOI: `10.1103/PhysRev.32.110`. URL: `https://link.aps.org/doi/10.1103/PhysRev.32.110`.

[82] Denis Parganlija et al. "Masses of Axial-Vector Resonances in a Linear Sigma Model with Nf=3". In: *AIP Conf. Proc.* 1343 (2011), pp. 328–330. DOI: `10.1063/1.3575019`. arXiv: `1011.6104 [hep-ph]`.

[83] Pereira, Renan Câmara, Moreira, João, and Costa, Pedro. "The strange critical endpoint and isentropic trajectories in an extended PNJL model with eight Quark interactions". In: *Eur. Phys. J. A* 56.8 (2020), p. 214. DOI: `10.1140/epja/s10050-020-00223-8`. URL: `https://doi.org/10.1140/epja/s10050-020-00223-8`.

[84] J. Perrin. "Mouvement Brownien et Réalité Moléculaire". In: *Annales de chimie et de Physique* 18 (8), pp. 5–114.

[85] Marcus B. Pinto, Volker Koch, and Jorgen Randrup. "The Surface Tension of Quark Matter in a Geometrical Approach". In: *Phys. Rev.* C86 (2012), p. 025203. DOI: `10.1103/PhysRevC.86.025203`. arXiv: `1207.5186 [hep-ph]`.

[86] Robert D. Pisarski. "Quark-gluon plasma as a condensate of $Z(3)$ Wilson lines". In: *Phys. Rev. D* 62 (11 Nov. 2000), p. 111501. DOI: `10.1103/PhysRevD.62.111501`. URL: `https://link.aps.org/doi/10.1103/PhysRevD.62.111501`.

[87] G. Policastro, D. T. Son, and A. O. Starinets. “Shear Viscosity of Strongly Coupled $N = 4$ Supersymmetric Yang-Mills Plasma”. In: *Phys. Rev. Lett.* 87 (8 Aug. 2001), p. 081601. DOI: `10.1103/PhysRevLett.87.081601`. URL: `https://link.aps.org/doi/10.1103/PhysRevLett.87.081601`.

[88] A.M. Polyakov. “Thermal properties of gauge fields and quark liberation”. In: *Physics Letters B* 72.4 (1978), pp. 477–480. ISSN: 0370-2693. DOI: `https://doi.org/10.1016/0370-2693(78)90737-2`. URL: `http://www.sciencedirect.com/science/article/pii/0370269378907372`.

[89] “Production of Meson Showers”. In: *Nature* 164 (). DOI: `10.1038/164065c0`. URL: `https://doi.org/10.1038/164065c0`.

[90] Jorgen Randrup. “Phase transition dynamics for baryon-dense matter”. In: *Phys. Rev.* C79 (2009), p. 054911. DOI: `10.1103/PhysRevC.79.054911`. arXiv: `0903.4736 [nucl-th]`.

[91] Claudia Ratti, Michael A. Thaler, and Wolfram Weise. “Phases of QCD: Lattice thermodynamics and a field theoretical model”. In: *Phys. Rev. D* 73 (1 Jan. 2006), p. 014019. DOI: `10.1103/PhysRevD.73.014019`. URL: `https://link.aps.org/doi/10.1103/PhysRevD.73.014019`.

[92] P. Rehberg, S. P. Klevansky, and J. Hufner. “Hadronization in the SU(3) Nambu-Jona-Lasinio model”. In: *Phys. Rev. C* 53 (1996), pp. 410–429. DOI: `10.1103/PhysRevC.53.410`. arXiv: `hep-ph/9506436`.

[93] P. Romatschke. “new developments in relativistic viscous Hydrodynamics”. In: *International Journal of Modern Physics E* 19.01 (2010), pp. 1–53.

[94] S. Rößner, C. Ratti, and W. Weise. “Polyakov loop, diquarks, and the two-flavor phase diagram”. In: *Phys. Rev. D* 75 (3 Feb. 2007), p. 034007. DOI: `10.1103/PhysRevD.75.034007`. URL: `https://link.aps.org/doi/10.1103/PhysRevD.75.034007`.

[95] A.M.Blundell S.J.Blundell. *Concepts in Thermal Physics.* Cambridge University Press, 2006.

[96] O. Scavenius, A. Dumitru, and J. T. Lenaghan. "The K/π ratio from condensed Polyakov loops". In: *Phys. Rev. C* 66 (3 Sept. 2002), p. 034903. DOI: `10.1103/PhysRevC.66.034903`. URL: `https://link.aps.org/doi/10.1103/PhysRevC.66.034903`.

[97] W. Schottky. "Über spontane Stromschwankungen in verschiedenen Elektrizitätsleitern". In: *Annalen der Physik* 362.23 (1918), pp. 541–567. DOI: `10.1002/andp.19183622304`. eprint: `https://onlinelibrary.wiley.com/doi/pdf/10.1002/andp.19183622304`. URL: `https://onlinelibrary.wiley.com/doi/abs/10.1002/andp.19183622304`.

[98] Huichao Song and Ulrich Heinz. "Causal viscous hydrodynamics in 2 + 1 dimensions for relativistic heavy-ion collisions". In: *Phys. Rev. C* 77 (6 June 2008), p. 064901.

[99] Michael Strickland. "Anisotropic Hydrodynamics: Three Lectures". In: *Acta Physica Polonica B* 45 (Oct. 2014). DOI: `10.5506/APhysPolB.45.2355`.

[100] Benjamin Svetitsky and Laurence G. Yaffe. "Critical Behavior at Finite Temperature Confinement Transitions". In: *Nucl. Phys. B* 210 (1982), pp. 423–447. DOI: `10.1016/0550-3213(82)90172-9`.

[101] V.Toneev. In: *Proc. Sci.* CPOD 07:057 (2007).